LAWRENCE
LIVERMORE
NATIONAL
LABORATORY

LLNL-TR-483651

Hydrologic Source Term Processes and Models for the Clearwater and Wineskin Tests, Rainier Mesa, Nevada National Security Site

S. F. Carle

May 11, 2011

Disclaimer

This work performed under the auspices of the U.S. Department of Energy by Lawrence Livermore National Laboratory under Contract DE-AC52-07NA27344.

LLNL-TR-483651

Hydrologic Source Term Processes and Models for the CLEARWATER and WINESKIN Tests, Rainier Mesa, Nevada National Security Site

Steven F. Carle

1/24/2018

Lawrence Livermore National Laboratory

This work was performed under the auspices of the U.S. Department of Energy by Lawrence Livermore National Laboratory under Contract DE-AC52-07NA27344

Table of Contents

List of Figures

List of Tables

Hydrologic Source Term Processes and Preliminary Models for the CLEARWATER and WINESKIN Tests at Rainier Mesa, Nevada National Security Site

1 Introduction

This report describes the development, processes, and results of a hydrologic source term (HST) model for the CLEARWATER (U12q) and WINESKIN (U12r) tests located on Rainier Mesa, Nevada National Security Site, Nevada (Figure 1.1). Of the 61 underground tests (involving 62 unique detonations) conducted on Rainier Mesa (Area 12) between 1957 and 1992 (USDOE, 2015), the CLEARWATER and WINESKIN tests present many unique features that warrant a separate HST modeling effort from other Rainier Mesa tests.

1.1 Uniqueness and Significance of CLEARWATER and WINESKIN Tests

The CLEARWATER and WINESKIN tests were unique to Rainier Mesa in several respects:

- The only two tests conducted in vertical shafts
- The two tests with largest maximum of the announced yield range (USDOE, 2015),
- The two most westerly tests, well outside N and T-Tunnel flow and transport model areas
- One (WINESKIN) of only two tests with a surface collapse feature on the top of Rainier Mesa (Figure 1.2).

The unique features of the CLEARWATER and WINESKIN tests are significant to assessment of radionuclide transport at Rainier Mesa:

- In terms of announced test yield or maximum of the test yield range (USDOE, 2015), WINESKIN and CLEARWATER, are the two largest tests conducted on Rainier Mesa and comprise about 25% of the total of the maximum test yield for the Corrective Action Unit (CAU) 99: Rainier Mesa/Shoshone Mountain.
- The vertical shaft tests are located 600 m to 1,000 m from the nearest tunnel complex, and no flow and transport interaction with the tunnels is expected (unlike the tunnel tests).

- The westerly test locations cause the Redrock Valley aquifer (RVA) to be the most likely regional aquifer impacted in the CAU domain instead of the upper carbonate aquifer (LCA3), as assumed in the N and T-Tunnel flow and transport or "sub-CAU" models (Navarro, 2017a).
- The WINESKIN test is located vertically above the Mesozoic granitic confining unit (MGCU), which is assumed to be impermeable in the saturated flow and transport model for the CAU (the SZ model). Transport of radionuclides from the WINESKIN exchange zone to the boundary of the SZ model requires a lateral flow component in the volcanic flow system to maintain consistency with the MGCU no-flow conditions of the SZ model (Navarro, 2017a).
- In earlier source term investigations (Tompson et al., 2010), concern was raised over potential for enhanced precipitation and higher recharge to the surface collapse feature (crater) of the WINESKIN test, as investigated by McNab (2008) for Yucca Flat tests. However, these concerns are no longer expected to be significant because (1) updated NET-INFIL3 models of surface infiltration (Navarro, 2017a) account for local infiltration near WINESKIN, and (2) the local watershed is small.

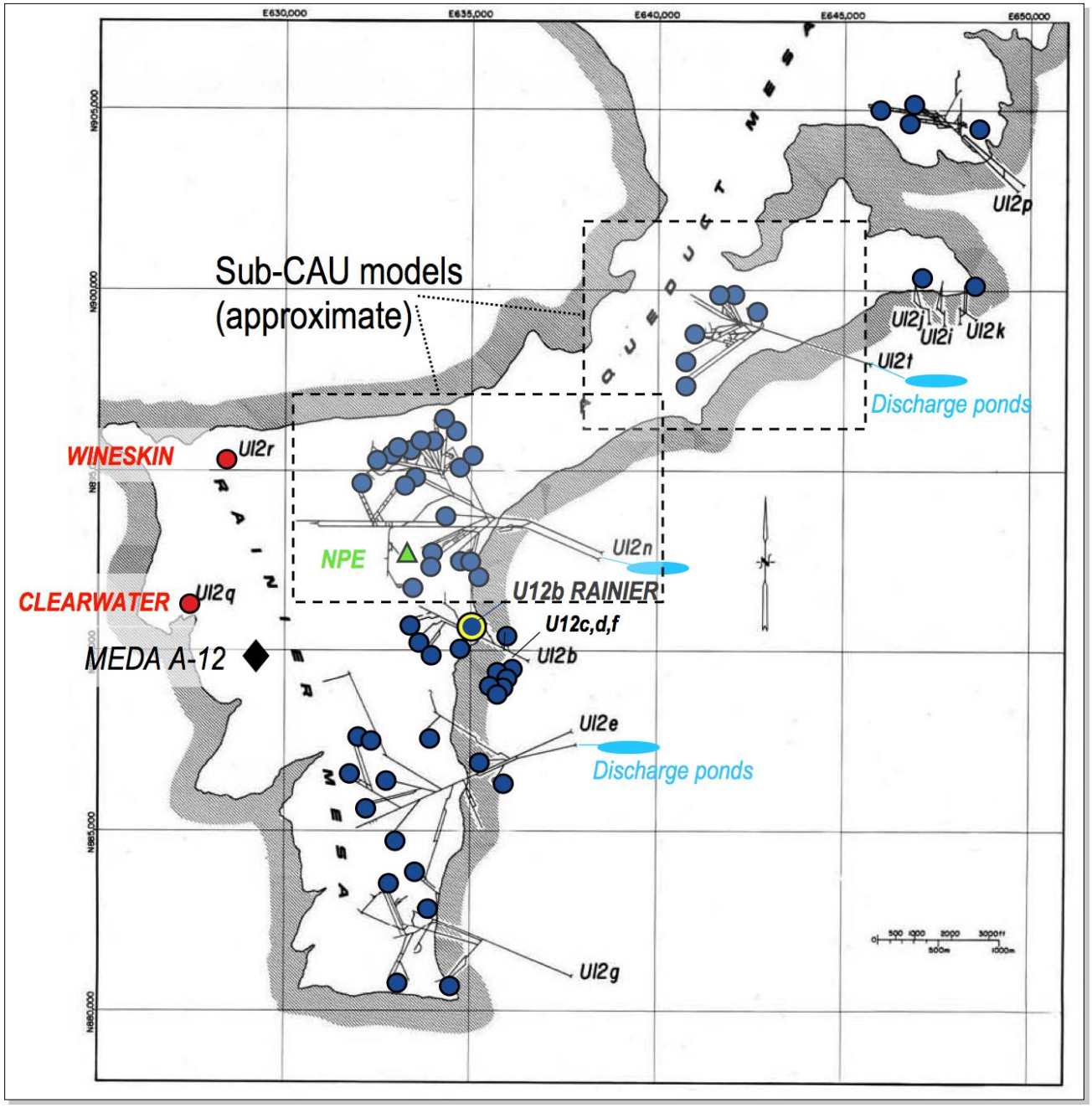

Figure 1.1 Locations of CLEARWATER (U12q) and WINESKIN (U12r) tests (red dots) relative to flow and transport model areas (dashed black lines), tunnel (solid black lines), tunnel test locations (blue dots), A-12 meteorological station (black diamond), 1993 Non-Proliferation Experiment (green triangle), and discharge ponds (light blue ovals) on Rainier Mesa.

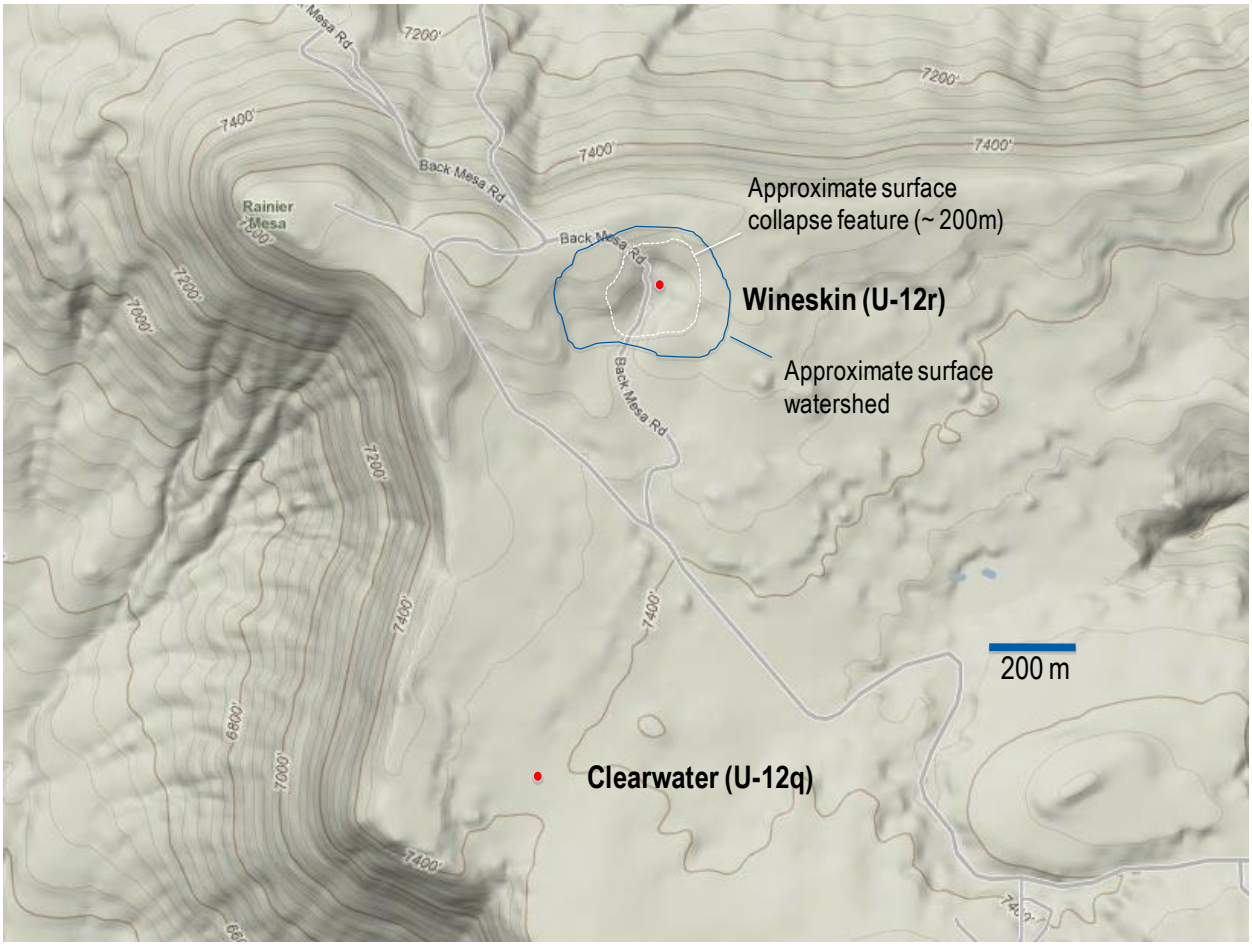

Figure 1.2 Locations of CLEARWATER and WINESKIN tests on the northwest portion of Rainier Mesa, showing outline of WINESKIN surface collapse feature.

1.2 Purpose of HST Modeling and Assessment

1.2.1 Objectives

The main objective of the CLEARWATER and WINESKIN HST modeling and assessment is to provide both water and radionuclide fluxes, with uncertainty, as boundary conditions to the SZ regional-scale flow and transport model. Several other objectives are intrinsic to the source term modeling:

- Address in-situ rock property heterogeneity by using a hydrostratigraphic framework model (NSTec, 2007) and subsequent updates (Navarro, 2017b)
- Integrate fracture-matrix interactions into flow and transport processes
- Directly utilize spatially variable infiltration models (Navarro, 2017a)
- Include impacts of test effects, particularly rock properties for test-altered zones and flow transients caused by post-test changes in rock properties

- Address complexities arising from the test location relative to SZ model boundaries, particularly with respect to variably saturated and upper saturated groundwater flow conditions not addressed by the SZ model
- Produce flow and transport models that are consistent with observed saturation, pressure, and radionuclide transport observations
- Assess HST processes in a three-dimensional (3-D) framework to address combined spatial influences of hydrostratigraphy, test effects, and test location relative to the SZ model.

1.2.2 Main Processes, Parameters, and Uncertainties to Assess

There is a wide range of uncertainty in the processes, parameters, and outcomes for the HST models. Expert judgment is needed to bound the model parameters and focus on the processes that produce the most uncertainty. For example, a considerable effort has been placed on bounding the matrix flow properties of the model and calibrating the flow model to observations. The CLEARWATER and WINESKIN HST modeling effort recognizes large uncertainties in initial radionuclide source term distribution and major processes affecting radionuclide transport including fracture-matrix interaction, matrix diffusion, and sorption. The assessment of uncertainty focuses mainly on fracture-matrix transport parameters and initial radionuclide source term distribution.

1.2.3 Limitations

The main limitations of the 3-D CLEARWATER and WINESKIN HST models compared to 2-D source term models of the RAINIER and CLEARWATER tests (Zavarin et al., 2011) are simplification of effects from complex early-time processes:

- thermal effects,
- gaseous flow and transport, and
- non-linear aspects of reactive chemistry.

The results of the 2-D CLEARWATER and RAINIER HST process models are used to account for complex early-time source term processes that impact radionuclide redistribution. This more detailed process modeling of radionuclide redistribution guides source term initialization for the 3-D CLEARWATER and WINESKIN HST models, which assess radionuclide transport to the SZ model boundary.

1.3 Comparison to Other RM Flow and Transport Models

1.3.1 Similarities

The CLEARWATER and WINESKIN HST models can be viewed as similar to the N and T-Tunnel flow and transport models (Navarro, 2017a) in several respects:

- **Variably Saturated Flow** – Radionuclide migration is assessed for variably saturated flow of water with aqueous phase transport.
- **Fracture-Matrix Interactions** - Fracture-matrix interactions are assessed.
- **Linear Sorption (Kd)** - Reactive chemistry is modeled assuming a linear sorption (Kd) process in the rock matrix only
- **Dual-Permeability Model** - The CLEARWATER and WINESKIN HST and flow and transport models address fracture-matrix flow and transport processes with similar dual-continuum models. Like the N and T-Tunnel flow and transport models, a dual-permeability model is used to address fracture-matrix interactions instead of a dual-porosity model. A dual- permeability model enables advective transport in the matrix unlike a dual porosity model.

1.3.2 Differences

CLEARWATER and WINESKIN HST model domain sizes are different than N and T-Tunnel flow and transport models for the following reasons:

- **Test-Specific Lateral Extent** - By focusing on only two tests individually, the CLEARWATER and WINESKIN modeling domains do not require the lateral extensiveness of the N and T-Tunnel flow and transport model domains.
- **Top of Model at Ground Surface** - The vertical extent is higher in the HST model domain than in the T-Tunnel flow and transport model domain because surface infiltration is directly integrated as the inflow boundary condition instead of using a separate "recharge distribution model" to project infiltration to the top level of an assumed horizontal plane of saturation in the perched zone of the operational flow and transport flow model.
- **Bottom of Model Based on RVA Discharge Location** - The lowermost HST model flow discharge boundary is the RVA and, therefore the lower extent of the HST model is not as low in elevation or deep in the stratigraphic section as the concurrent N and T-Tunnel flow and transport models, which use the LCA3 as the lowermost discharge boundary into the regional aquifer system.
- **No LCA3 Directly Beneath the Tertiary Volcanics, No flow in LCCU1, and No Flow in MGCU** – Unlike the N and T-Tunnel flow and transport model domains, the LCA3 is not present directly below the Tertiary volcanic sequence in any part of the CLEARWATER and WINESKIN HST domains. As a result, the CLEARWATER and WINESKIN HST model domains do not extend below the Tertiary volcanic sequence. Confining units, either MGCU or LCCU1, underlie the Tertiary volcanic sequence throughout the CLEARWATER and WINESKIN HST model domains (See Figures 2.2, 2.3, and 3.1 for the model domain hydrostratigraphic settings). Because the concurrent SZ model assumes the MGCU is impermeable and the LCCU1 isolates flow between the Tertiary volcanic and the LCA3, the CLEARWATER and WINESKIN

HST models do not extend into the LCCU1 or MGCU except into test-altered zones. The outflow boundary conditions or "flux planes" for the CLEARWATER and WINESKIN model domains progressed through interactions and agreement with SZ modelers.

Differences in flow conditions lead to differences in the hydrogeologic conceptual models, boundary conditions, and SZ model flux input locations:

- **Flow Transients Included** - The CLEARWATER and WINESKIN HST models include flow transients resulting from rock property changes caused by the tests (test effects), whereas the concurrent N and T-Tunnel flow and transport models rely on steady-state flow conditions. Flow transients are associated with enhanced drainage along test-induced fractures, funneling of flow through the chimney, and test-enhanced permeability and porosity in in-situ rocks.
- **Impermeable MGCU** - Because the WINESKIN test is located vertically above an impermeable MGCU, the WINESKIN HST model of transport of radionuclides from the WINESKIN exchange zone to the SZ model requires a large lateral flow component discharging to the RVA. Concurrent N and T-Tunnel flow and transport models assume no significant lateral flow component discharging to volcanic aquifers.
- **Lateral Discharge to Welded Tuff Aquifers** - Because both the CLEARWATER and WINESKIN HST models assume discharge to the SZ model via the RVA, a laterally extensive and vertically confined volcanic aquifer, lateral flow within the Tertiary volcanic aquifers is fundamentally allowed to occur, unlike the concurrent N and T-Tunnel flow and transport models which assume 100% discharge to the LCA3 and no lateral discharge to volcanic aquifers.
- **Variably Saturated Lateral Flow and Discharge to Vitric Tuff Aquifers** - The CLEARWATER and WINESKIN HST models allow for variably saturated lateral flow and discharge at the vitric tuff – zeolitic tuff (VTA/TCU) interface because of decreased vertical conductance at the interface between matrix-dominated and fracture dominated flow (Kwicklis, 2010a and b). Allowance for discharge at the VTA/TCU interface eases calibration of perched water levels, which tend to reside near or below the VTA/TCU interface on Rainier Mesa, as discussed in Section 2.4.3.
- **Flux to Regional Volcanic Aquifer** - Considering the westerly test locations (see Figure 3.1), SZ model flux inputs from the CLEARWATER and WINESKIN HST models are directed to vertical and horizontal planes associated with the lateral and vertical extents, respectively, of the volcanic aquifers as delineated by Fenelon et al. (2008) rather than the regional carbonate aquifer as assumed in the concurrent N and T-Tunnel flow and transport models. These flux planes establishing interfaces between the HST and SZ models were chosen by the SZ modeling team following

interactions with LLNL to ensure that the HST models can deliver fluxes to the SZ model boundaries.

Although fracture-matrix interactions are assessed in the HST and flow and transport models, the modeling approaches for addressing fracture networks have some fundamental differences:

- **No Faults** - No faults are assumed in the CLEARWATER and WINESKIN HST models because no faults exist in the HST modeling domains according to the base case Hydrostratigraphic Framework Model (NSTec, 2007), unlike the N and T-Tunnel flow and transport model domains.
- **No Discrete Fracture Modeling** - Similar to the N-Tunnel flow and transport model; no small-scale heterogeneity of fracture properties derived from discrete fracture modeling is introduced as in the T-Tunnel flow and transport model.

1.4 Summary

The flow and transport simulation approach for the CLEARWATER and WINESKIN HST model is reviewed here to introduce the HST modeling approach (Chapters 2 through 5) and modeling results (Chapter 6):

- Chapter 2 describes the hydrogeologic conceptual models, with emphasis on customization of each of the CLEARWATER and WINESKIN HST models to site specific characteristics and the hydrostratigraphic framework model (HFM), the NET-INFIL3 recharge model, and the SZ flow and transport model of the CAU. Conceptualization of fracture-matrix interactions and test-altered zones is also covered.
- Chapter 3 describes the flow processes, properties, and calibration involved with modeling variably saturated flow. Key aspects of the Rainier Mesa flow system, development of matrix and fracture flow properties for hydrostratigraphic units (HSUs) and test-altered zones, and calibration to water levels and saturation observations are discussed.
- Chapter 4 describes the methods for implementing the radionuclide source term into the HST models, including details on the relevant radionuclides and partitioning into different source zones.
- Chapter 5 describes radionuclide transport processes and properties, including sorption, matrix diffusion, uncertainty of transport properties, and interpretation of the initial time of HST simulation.
- Chapter 6 presents the HST model approach and results, including sensitivities to initial source zone distribution, source magnitude, and transport mobility parameters, total radionuclide fluxes to the SZ model, and description of HST model source inputs to the concurrent (as of July 2011) SZ model. The evental HST model

inputs to the final SZ model, consisting of lists of water and radionuclide fluxes over time at multiple locations of the SZ and HST model interface, were provided separately in electronic files and documented further in Navarro (2017a).

- Chapter 7 is conclusions and recommendations for the HST models.
- Chapter 8 is references.
- Appendices A through D provide details and descriptions of the development of rock properties for the HST models.

2 Hydrogeologic Conceptual Model

2.1 Model Domains and Interface with SZ Model

The CLEARWATER and WINESKIN HST model domains were designed individually to each test with consideration of source term spatial distribution, cell size, computational feasibility, hydrogeologic setting, proximity to the SZ model boundaries, and the hydrogeologic conceptual model used by the SZ model (Navarro, 2017a).

2.1.1 CLEARWATER Test

The CLEARWATER test location is situated vertically above the top boundary of the SZ model. The interface between the CLEARWATER HST model and the SZ model is a horizontal plane at an elevation of 1,500 m locally within the domain of the CLEARWATER HST model. The CLEARWATER model domain extends 375 m laterally to the north south, west, and east of the test location, forming a 750 by 750 m square box centered at the working point. The HST model domain extends vertically to encompass the base of the Redrock Valley aquifer (RVA) (1,187 m at bottom) and one cell thickness above the ground surface (2,297 m at top). Table 2.1 provides the details of the CLEARWATER HST model domain and locations of the test and interface with the SZ model. The lower clastic confining unit (LCCU1) is treated as a no-flow condition and, therefore, effectively outside the CLEARWATER HST model domain.

Table 2.1 CLEARWATER HST model domain locations for working point, domain extent, domain size, and SZ model interface.

CLEARWATER HST Model	Easting - UTM11 NAD27 (m)	Northing – UTM11 NAD27 (m)	Elevation (m)
Working Point	568,379	4,116,931	1711
Domain Extent	568,004 to 568,754	4,116,556 to 4,117,306	1,187 to 2,297
Domain Size	750	750	1,110
SZ Model Interface	568,004 to 568,754	4,116,556 to 4,117,306	1,500

2.1.2 WINESKIN Test

Several factors complicate design of the WINESKIN HST model domain:

- **Underlying MGCU** - The WINESKIN test overlies the Mesozoic granitic confining unit (MGCU), which is assumed to be impermeable in the SZ model. To maintain consistency between HST and SZ models, the HST model also assumes the in-situ, non-test-altered rock of the MGCU is impermeable and, therefore, treats in-situ MGCU as effectively outside the HST model domain except for test-altered zones.
- **Test Location North of the SZ Model Extent** - The WINESKIN test location is over 400 m north and 200 m above of the SZ model extent near the WINESKIN test (see Figure 2.1). Therefore, flow and transport from the WINESKIN test to the SZ model requires both vertical and lateral components.
- **Recharge and Hydrogeology** – Preliminary NET-INFIL2 recharge models provided in 2010 by Los Alamos National Laboratory (LANL) for HST modeling indicated high rate of recharge to vitric tuffs on the north face of Rainier Mesa. The hydrogeological combination of southward-dipping stratigraphy and high recharge on the north mesa face caused most of the groundwater flow through the WINESKIN test to originate from vitric tuffs exposed on the north mesa face. Therefore, the WINESKIN model domain extends northward to include vitric tuffs exposed on the north mesa face.

Considering that the WINESKIN test location is situated north of the lateral extent of the SZ model and vertically above the top boundary of the SZ model, a “stair step” boundary was developed in conjunction with the SZ modeling team as the interface between the WINESKIN HST and SZ model as shown in Figure 2.1. The top of the stair step is a horizontal plane at an elevation of 1550 m locally within the domain of the WINESKIN HST model. The north face of the stair step is a west-east vertical plane located at a northing of 4,117,625 m. The WINESKIN model domain extends 225 m to the west and east and 615 m to the south and north of the test location, forming a 450 m by 1,230 m rectangular box centered at the working point. The HST model domain extends vertically to encompass the base of the RVA (1,307 m at bottom) and one cell thickness above the ground surface (2,327 m at top). Table 2.2 and Figure 2.1 provide the details of the WINESKIN HST model domain and interface with the SZ model. To be consistent with the concurrent SZ flow model, the LCCU1 and MCCU are treated as a no-flow condition and, therefore, effectively outside the WINESKIN HST model domain except in the test-altered zones (Section 2.7).

Table 2.2 WINESKIN HST model locations for working point, domain extent, domain size, and SZ model boundary.

WINESKIN HST Model	Easting - UTM11 NAD27 (m)	Northing - UTM11 NAD27 (m)	Elevation (m)
Working Point	568,734	4,118,150	1,771
Domain Extent	568,509 to 569,959	4,117,535 to 4,118,765	1,307 to 2,327
Domain Size	450.0	1,230	1,020
SZ Model Boundary -Top of Stairstep	568,509 to 568,959	4,117,535 to 4,117,625	1,550
SZ Model Boundary -Face of Stairstep	568,509 to 568,959	4,117,625	1,307 to 1,550

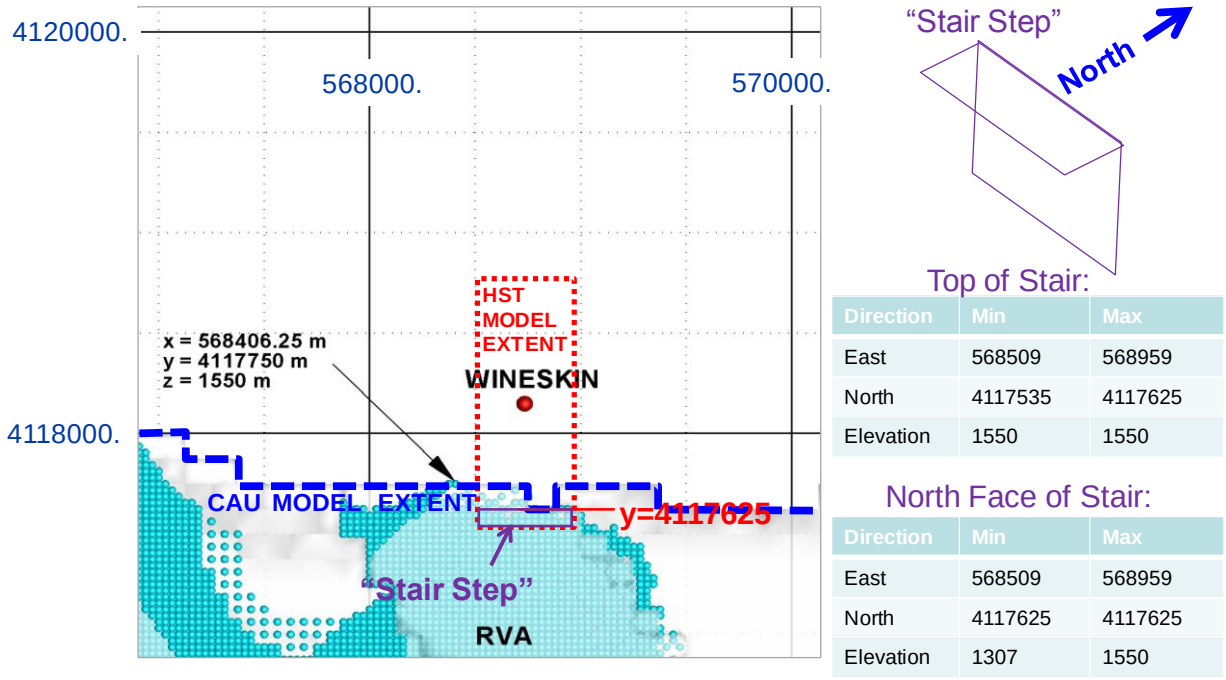

Figure 2.1 Location of WINESKIN HST model domain relative to SZ or "CAU" model extent in lateral directions with details showing location of "stair step" interface between HST and SZ models. All east and north values are given in UTM11 NAD27 coordinate system.

2.2 Model Discretization

HST model discretization is uniform with cell sized fixed at Δx=30 m, Δy = 30 m, and Δz = 15 m. The Δx=30 m and Δy = 30 m horizontal cell size is consistent with the 30 m by 30 m northing and easting cell size of NET-INFIL3 surface infiltration models (Section 2.4.1). The Δz = 15 m discretization enables vertical resolution of hydrostratigraphic units (HSUs). While finer discretization would be desirable, computational feasibility restricted further refinement of grid cell size.

2.3 Hydrostratigraphy

The spatial distribution of in-situ rock properties for the CLEARWATER and WINESKIN HST models is based on the hydrostratigraphy defined by the Hydrostratigraphic Framework Model (HFM) for Rainier Mesa (NSTec, 2007). The HFM addresses the geometric heterogeneities in rock properties of the groundwater flow system associated with major hydrogeologic flow units such as vitric tuff aquifers (VTA), welded tuff aquifers (WTA), tuff confining units (TCU), and clastic and granitic confining units (CCU and GCU). The locations of HSUs specified by the HFM are used to assign the spatial distribution of in-situ rock properties for the CLEARWATER and WINESKIN HST models. The HFM also includes major faults, however, no faults were mapped within the CLEARWATER and WINESKIN HST model domains. Figures 2.2 and 2.3 show cutaway views of the hydrostratigraphy within the HST model domains for CLEARWATER and WINESKIN, respectively.

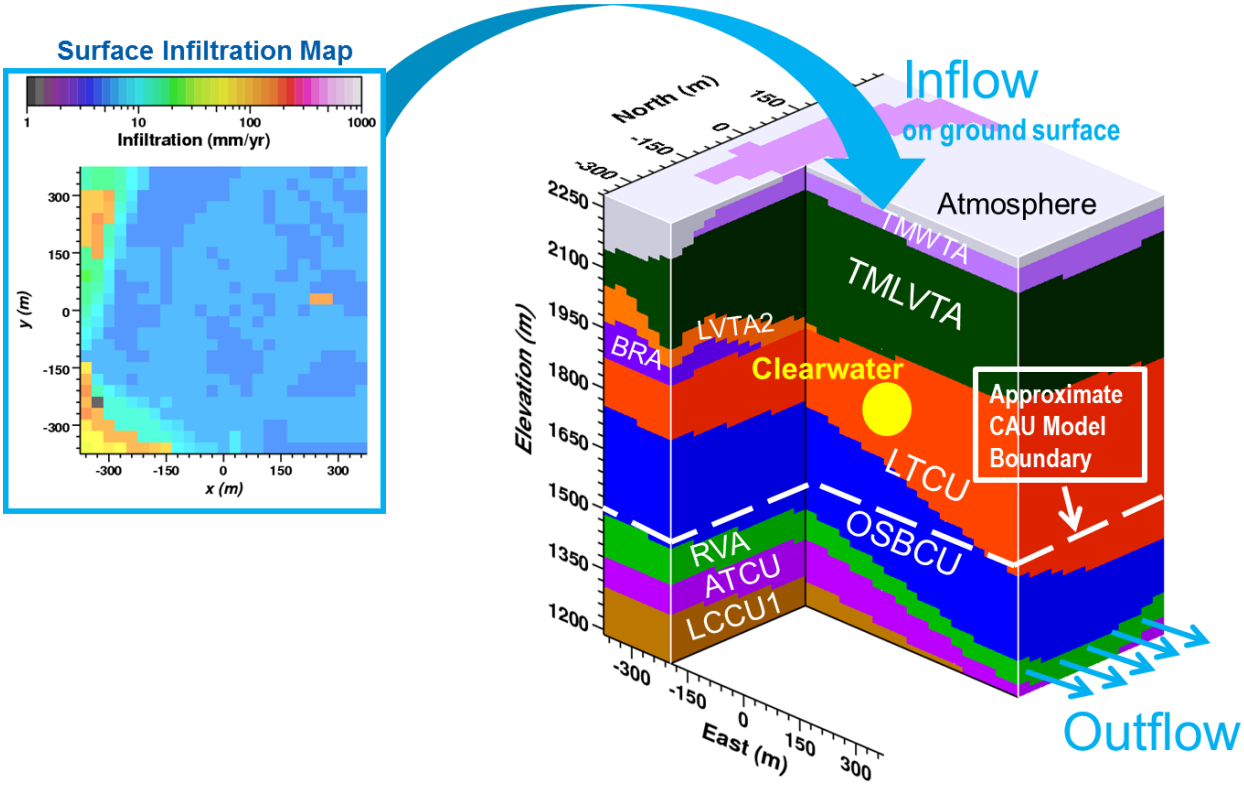

Figure 2.2 Cutaway view of CLEARWATER HST model domain, showing CLEARWATER test location, hydrostratigraphy, map of NET-INFIL3 surface infiltration values applied to HST model, and locations of lateral outflow fluxes.

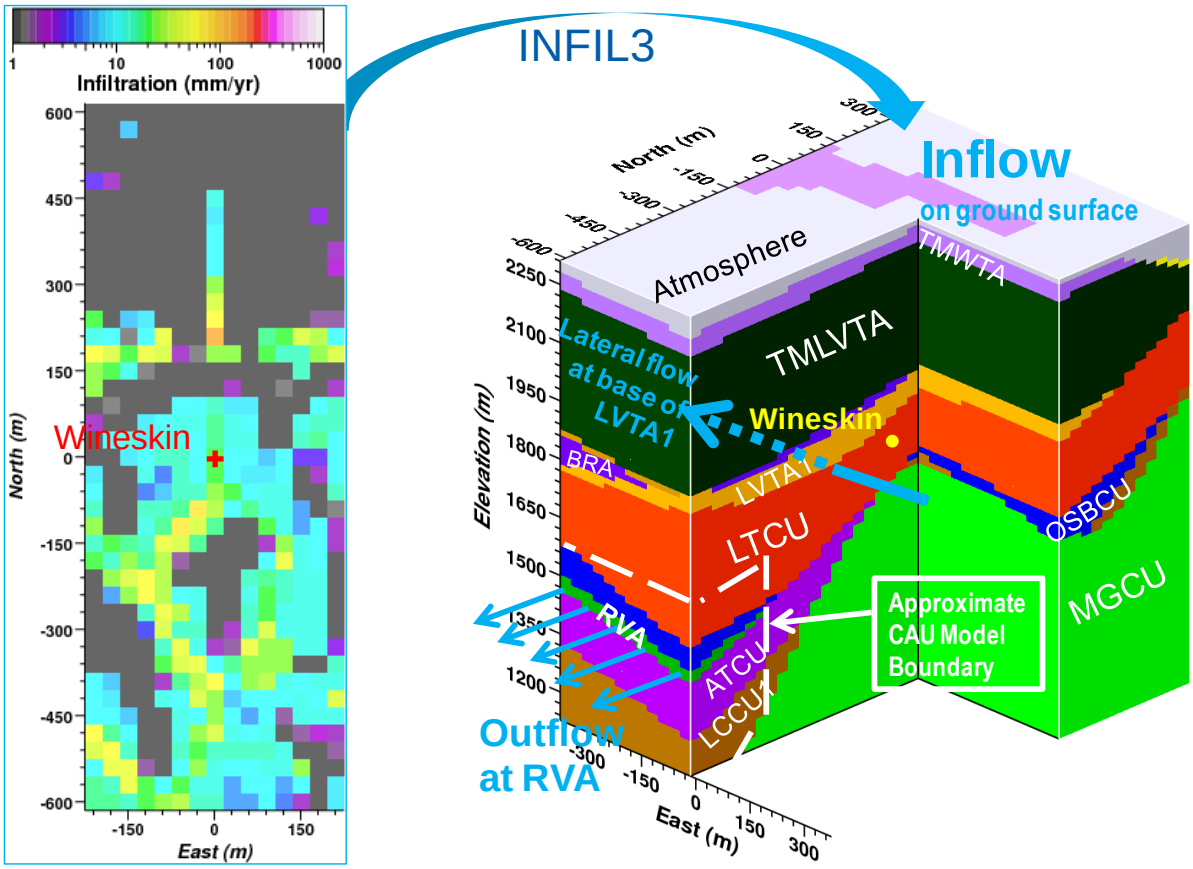

Figure 2.3 Cutaway view of WINESKIN HST model domain, showing WINESKIN test location, hydrostratigraphy, map of NET-INFIL3 surface infiltration values applied to HST model, and locations of outflow fluxes.

2.4 Boundary Conditions

Boundary conditions are based on inflow, outflow, and potentiometric head conditions. Inflow boundaries include recharge at the ground surface. Outflow boundaries include discharge to aquifers. Potentiometric head conditions are used in establishing discharge and drainage boundary conditions.

2.4.1 Infiltration and Recharge Models

Inflow to the CLEARWATER and WINESKIN HST models is implemented by applying surface infiltration rates to the uppermost cells immediately below the ground surface of the models. In this manner, spatial redistribution of recharge to the saturated perched zone is integrated directly within the HST models by variably saturated flow processes. For the HST modeling of inflow at the ground surface, six realizations (3, 7, 11, 23, 29, and 42) of the NET-INFIL3 infiltration models from Los Alamos National Laboratory (Navarro, 2017a) are imparted directly on a cell-by-cell basis to the ground surface sells of the HST flow

model at a 30 m by 30 m spacing; both the HST model and NET-INFIL3 models have cell x:y spacing of 30 m by 30 m.

2.4.2 Potentiometric Head in Regional Volcanic Aquifer and RVA Discharge

Potentiometric head conditions assigned to the HST model for the regional volcanic aquifer are largely inferred from interpretations by Fenelon et al. (2008), as discussed in further detail in Section 3.1. Local to the CLEARWATER and WINESKIN HST model domains, potentiometric heads in the RVA are estimated at 1,600 m (see Figure 3.1) and 1,550 m (see Figure 3.2) elevation above mean sea level, respectively. These potentiometric heads are used as fixed head boundary conditions at the location of outflow to the RVA in the HST models (Figures 2.2 and 2.3). The CLEARWATER HST model assumes generally eastward flow in the RVA based on the dip of the underlying synclinal structure. The WINESKIN HST model assumes generally southerly flow in the RVA based on southerly dip and proximity to the SZ model boundary. These fixed head boundary conditions impart lateral flow in the RVA with discharge from the HST model domain to the SZ model domain.

Ideally, outflow boundary conditions for the CLEARWATER and WINESKIN HST models would have been specified either by head or flux conditions provided from SZ modeling results. However, the concurrent SZ flow model calibration was not completed during the timeframe of CLEARWATER and WINESKIN HST modeling. Consequently, no specified boundary conditions for flux, flow direction, or hydraulic head were provided to the HST models by the SZ modeling team. SZ modelers have indicated that the data and interpretations of potentiometric head provided in Fenelon et al. (2008) are used as a calibration target for the SZ model. Therefore, the HST model boundary assumptions are consistent with the concurrent SZ model objectives, but may not be consistent with the eventual SZ model results.

2.4.3 Drainage Condition for Recharge Redistribution

The contact between vitric and zeolitic tuffs also imparts a transition from porous (interstitial) to fracture-dominated flow. The vitric-zeolitic tuff interface is amenable to lateral recharge redistribution because of decreased vertical hydraulic conductance between matrix and fracture flow across the interface (Kwicklis, 2010a and b). The CLEARWATER and WINESKIN HST models assume that a portion of the recharge can be directed laterally along the vitric-zeolitic interface. The CLEARWATER and WINESKIN HST flow models indicate variably saturated lateral flow is possible at the base of the vitric tuffs above the vitric-zeolitic tuff interface. Lateral flow in the shallow volcanic flow system may also occur where welded tuff of the BRA overlies the zeolitized tuff of the LTCU.

Alternatively, if the lateral recharge distribution at the vitric-zeolitic interface is constrained by a no-flow boundary (such as the edge of the model domain), the recharge distribution will unrealistically pond up above vitric-zeolitic surface within the model

domain, which was not observed during drilling of U12q based on water-related observations in Townsend et al. (2007):

> The drill hole started making water at 646.5 m (2,121 ft). By the time the hole had reached the depth of 653.5 m (2,144 ft), it was making 30 barrels of water per hour. A second reference mentions 30 gallons per hour, and a third reference states that "the hole filled with water at a rate of 4.6–6.1 m (15–20 ft) an hour." Water inflow into the hole created "extreme" drilling problems and the hole was terminated 108.5 m (356 ft) above planned TD of 762 m (2,500 ft).

These flow observations are well below the CLEARWATER working point depth of 584.6 m and below the LTCU-OSBCU interface at a depth of 627.9 m (NSTec, 2007).

The CLEARWATER and WINESKIN HST models enable a lateral drainage (or shallow lateral flow) process as a component of recharge redistribution through a lateral "drainage" boundary condition. The lateral drainage boundary condition imparts saturated and hydrostatic potentiometric head conditions on model vitric tuff side elements having the lowest elevation (i.e., the "downstream" location of vitric tuffs on the model domain).

In both the CLEARWATER and WINESKIN models, the drainage condition enables recharge to redistribute along the vitric-zeolitic interface without producing saturated conditions except at the boundary or near the trough of synclinal features of the vitric-zeolitic interface. These flow conditions are entirely consistent with water level data and stratigraphy on Rainier Mesa that indicate perched zone water levels are typically below the vitric-zeolitic interface except near the base of a syncline where saturated conditions may persist above the zeolitic tuff (Section 2.4.4).

Figure 2.4 compares total water flux discharge at the two outflow boundaries of the CLEARWATER and WINESKIN models – RVA and base of LVTA – for each of six NET-INFIL3 realizations (noted as 3.1 through 3.6). The CLEARWATER model produces on the order of 75%-80% discharge to the RVA and 20-25% discharge to the base of the LVTA2 for long-term flow. The WINESKIN model produces approximately 40% discharge to the RVA and 60% discharge to the LVTA2 in the long term. The discharge pattern at WINESKIN is consistent with a different hydrogeologic setting compared to CLEARWATER, including steeper slopes on the vitric-tuff interface, more steeply dipping hydrostratigraphy combined with less laterally extensive RVA and no flow conditions in the MGCU. If alternative SZ flow models include flow in the MGCU, the WINESKIN HST model outflow pattern would change for those alternatives.

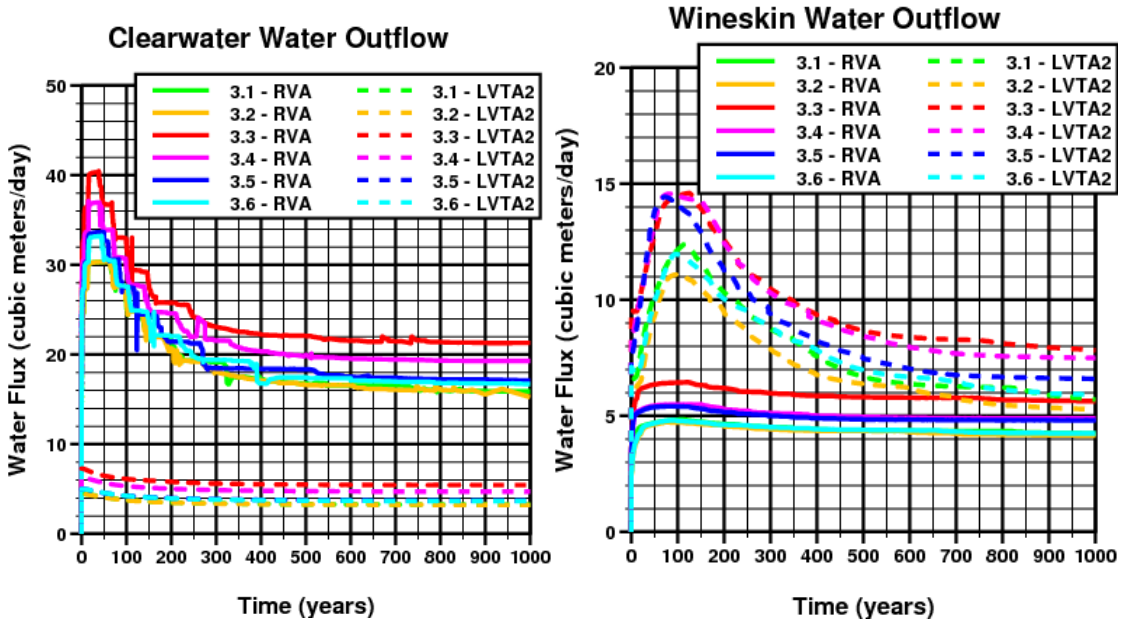

Figure 2.4 Comparison of water outflow fluxes to the RVA and base of LVTA1 in the CLEARWATER and WINESKIN HST models for six NET-INFIL3 realizations of infiltration.

2.4.4 Evidence for Storage and Lateral Flow Near the Base of Synclines

The vitric-zeolitic interface represents a large contrast in flow properties, from dominantly interstitial flow in the vitric tuffs, to very low matrix permeability and fracture flow in the zeolitic tuffs (Thordarson, 1965; Townsend, 2008). Observations of unusually high rates of groundwater flow can be related to the synclinal structure on the top of pervasively zeolitized tuffs (Figure 2.5), as represented by a trough in the elevation contours of the vitric-zeolitic interface passing through the N and T-Tunnel complexes. Recharge redistribution along the vitric-zeolitic interface may cause accumulation and lateral flow of perched groundwater above the vitric-zeolitic interface near the base of synclines. Evidence for this includes:

- The map of the top of the zeolitization surface (Figure 2.4, modified from NSTec, 2010) emphasizes the structural importance of a synclinal feature passing through the N and T-Tunnel complexes. The axis and slope of the synclinal troughs indicates potential directions of flow along a zeolitic-vitric tuff interface – southwest at N-Tunnel and east-northeast at T-tunnel.

  "Major amounts of perched water were found … in the north-central portion of N-Tunnel near the axis of the depositional syncline…" (Townsend et al., 2007)

  "…the depositional syncline that bisects Rainier Mesa, could be important if the syncline directs recharge …" (Townsend et al., 2007)

"…contaminants can travel along depositional bedding planes preferentially along the syncline axis…" (Townsend et al., 2007)

- At N-Tunnel, there is evidence of perched zone water above the top of the zeolitization surface:
  - During construction of the U12n.03 drift in 1966, several direct observations indicated that groundwater flow in N-Tunnel was associated with the syncline:

    "*The U12n.03 drift was the first indication that the syncline in this region is associated with extensive clay alteration of the tuff…*" (Ege et al., 1980)

    "Construction was stopped in that drift because of problems with water and poor ground conditions due to local alteration of the tuffs in that area by groundwater. Workers at that time believed that the presence of a structural syncline had caused tension fractures in the more brittle beds, and also funneled perched water into the area of the synclinal axis." (Russell et al., 2003)

    "…,the U12n.03 drift produced large volumes of water over a period of many years. The drift was abandoned because of the water flow, and the heavy (clay-rich) ground…" (Townsend et. al., 2007)

    "…entire potential test areas have been deemed unsuitable because of large volumes of water found during exploratory work." (Townsend et al., 2007)

  - The upward trend of water levels inside the plugged N-Tunnel indicate potential for flow into the LVTA1 vitric tuff aquifer. With the plugging of N-Tunnel in 1994 and subsequent re-filling with percolating groundwater, N-tunnel functions like a horizontal well for measuring water levels in the perched zone. The most recent (10/31/2006) N-Tunnel water pressure measurement of 29.5 psi at the Main Gas-Seal-Plug (GSP) pressure gauge (Stoller-Navarro, 2007a) indicates a water level elevation of 6,114 ft (1863.5 m) using the formula of Russell et al. (2003) combined with the 6,044 ft (1842.2 m) tunnel elevation at Main GSP location (Russell et al., 2003). Where the main extension drift of N-Tunnel crosses the syncline, the elevation of the top of zeolitization surface is about halfway between the 1,850 and 1,875 m contour, or about 1,862.5 m (Figure 2.5). These data indicate that the rising N-Tunnel water level in 2006 was near or slightly

higher than the base of the LVTA1 aquifer, which is constrained by the stratigraphic data for UE12n#1 near the N-Tunnel main extension drift (NSTec, 2007). Continued rise and eventual stabilization of N-Tunnel water levels at or slightly above the elevation of the vitric-zeolitic interface could be explained by redistribution of a portion of the recharge to lateral flow along vitric-zeolitic interface.

- Similar to N-Tunnel, T-Tunnel functions like a well for monitoring water levels in the perched zone since plugging of T-Tunnel in 1993 and subsequent re-filling with percolating groundwater (Russell et al., 2003). At T-Tunnel, a GSP gauge pressure measurement from 2006 indicates a water level of about 5,665 ft, which is below the top of the perched zone at ER-12-4 near T-Tunnel. However, a continuing rise of T-tunnel water levels and nearby water levels measurements indicate the "perched zone" water table could be above the top of the zeolitization surface near the syncline:
  - The perched zone water level is above the base of the vitric tuff aquifer in the ER-12-4 piezometer near T-Tunnel (NNSA, 2006; Stoller-Navarro, 2006b). The mean water level altitude is 5,967 feet (1,818.7 m) in the ER-12-4 piezometer (Fenelon et al., 2008), which is higher than the elevation of the top of zeolitization surface of 1806 m shown in Figure 2.5.
  - Horizontal drilling measurements during T-Tunnel development provide further evidence of perched zone water levels extending into the vitric tuffs at T-tunnel. During development of the U-12t.03 shaft as it crossed the base of the syncline, pressure measurements of flow from faults into horizontal cores drilled in T-Tunnel indicate a water level surface above the vitric-zeolitic interface near the base of the syncline (Figure 2.4):

    " Prior to U-12t.03 construction, five underground horizontal exploratory holes were drilled from the northern end of T-tunnel. All holes encountered water, and flow-rates of 38 to757 L/min (10 to 200 gpm) were measured. Testing of the flow-rates from hole to hole proved that the water-bearing faults and fractures were interconnected. Hydrostatic pressure was measured to be 1.14 MPa (165 psi) after two months' time." (Townsend et al., 2007)

    The 1.14 MPa hydrostatic pressure corresponds to about 116 m of hydrostatic head. Based on the basal U-12t.03 shaft elevation of 5,618 feet or 1712.4 m (Russell et al., 2003), the water level surface above U-12t.03 shaft can be estimated at 1,826 m. According to the map of the top of the zeolitization surface in Figure 2.5 (NSTec, 2010), the elevation of the vitric-zeolitic tuff interface is about 1,770 m at the intersection of the synclinal axis and the U-12t.03 shaft. Therefore, the combined U-12t.03 fault water

pressure measurement and the top of zeolitization surface mapping (NSTec, 2010) indicates that vitric tuffs were saturated to depths of 56 m (or greater if a vertical gradient for downward flow is considered) prior to completion of tunnel construction and testing at T-Tunnel. It would be useful to find out the exact elevation of the U-12t.03 fault pressure measurement location to better constrain the water level estimate associated with the pressure measurement. It is interesting that the pressure measurement was made "after two months' time" suggesting sustained high water pressure was available from a reservoir of groundwater much larger than TCU fracture volumes, such as saturated vitric tuff.

- There is evidence of large volumes of stored water above three T-Tunnel tests – larger than typical of Rainier Mesa tests - based on drill back observation of water present in the cavity and chimney. Perched water in overlying units with significant water storage, such as vitric tuff, could provide a source of water that could drain directly into the cavity and chimney if the chimney extends into the vitric tuffs, which is likely the case for T-tunnel tests. For example, the collapse chimney for the MIDAS MYTH T-Tunnel test extended all the way through the overlying zeolitic, vitric, and welded tuffs to the ground surface (Townsend, 2008). The process of drainage of perched water into the cavity and chimney (chimney drainage) was evaluated for the NASH test in Yucca Flat by Carle et al. (2008) using a variably saturated flow and transport model with constraints to water level mounding and tritium data at a satellite well. In consideration of a chimney drainage process, tests that are situated near the near the syncline will be more likely to show evidence of free water in the cavity and chimney. As noted by Townsend et al. (2007), for Rainier Mesa tests "free water is not frequently found within the chimney rubble during reentry operations." However, three T-Tunnel tests located near the synclinal trough appear to be an exception based on other information provided in Townsend et al. (2007) and summarized in Table 2.3. Five of six T-Tunnel tests are near the synclinal axis. Of these five tests near the syncline, three had drilling or reentry observations that penetrated the cavity or chimney. All three of these tests located near the syncline and having drilling or reentry operations penetrating the cavity or chimney showed evidence of free water in the cavity or chimney unlike most tests on Rainier Mesa. Assuming a chimney drainage process as described in Carle et al. (2008) can occur at Rainier Mesa, the water-related observations in the cavity and chimney on Rainier Mesa suggest that groundwater is more likely stored in vitric tuffs above tests located near the synclinal axis. As mentioned above, piezometer water level measurements in ER-12-4 near T-Tunnel and water pressure measurements within U-12t.03 horizontal shaft drilling also

support the presence of perched water within vitric tuff near the synclinal axis passing across T-Tunnel.

- The compilation of post-test water flow information in Table 2.3 shows that for all three cases where a T-Tunnel test was near the base of the syncline and had post-test drilling or mining into the cavity or chimney, evidence for flow or accumulation of water in the chimney or cavity was present (unusual on Rainier Mesa). The description that this water was heated and/or contained fission products indicates mixing with water passing through the cavity and radionuclide source exchange zones. A question to be resolved at T-Tunnel is what caused this unusual observation of water accumulation and circulation in the cavity and chimney water? Filling a portion of the cavity or chimney volume requires a large volume of water. Considering that the chimney can extend above the vitric-zeolitic interface, the chimney can provide a conduit for drainage of perched water into the cavity and chimney volumes. High-porosity friable vitric tuff provides more voluminous storage of rapidly drainable water compared to zeolitic tuff. Thus, the unusual post-test cavity and chimney water observations at the three T-Tunnel tests could be explained by groundwater stored in the vitric tuff above the vitric-zeolitic tuff interface that subsequently drained into collapse chimneys which propagated upward into the vitric tuff.
- The final exploratory horizontal drill hole in T-Tunnel triggered the highest sustained flow rates ever encountered on Rainier Mesa:

  …the final horizontal exploratory hole drilled by the DNA, just prior to closing U-12T-Tunnel, encountered the largest volume of water ever measured in Rainier Mesa, with flows measured at more than 1,514 L/min (400 gpm).(Townsend et al., 2007)

  Again, storage of groundwater in vitric tuffs above the T-Tunnel could provide explanation for this unusually high and sustained fault flow rate (for Rainier Mesa) at T-Tunnel (Townsend et al., 2007).
- The CLEARWATER and WINESKIN flow modeling indicates that inclusion of a drainage boundary condition for recharge redistribution on the vitric-zeolitic interface facilitates calibration to perched zone saturation and pressure/head conditions by enabling a portion of the infiltration to “run off” the top surface of the zeolitized tuffs and funnel into structural lows. With the limited model horizontal extent and lack of fault flow in the CLEARWATER and WINESKIN HST models, the recharge redistribution drainage condition is effectively assuming that some recharge is redistributed outside of the model vertical boundaries. The lateral drainage process at the base of the vitric tuffs prevents perched zone water levels from rising above the zeolitic-vitric tuff interface except in the trough of the syncline. The drainage boundary condition at the vitric-zeolitic

interface enables modeled perched water levels to be consistent with the drilling and water level observations in U12q (Sections 2.4.3 and 3.7.2). Section 3.8 provides further discussion of possible lateral flow processes in the Tertiary volcanics.

Table 2.3 Compilation of information about T-Tunnel tests relating location relative to synclinal axis and evidence for flow or accumulation of water in the cavity or chimney.

T-Tunnel Test	Near Base of Syncline?	Cavity or chimney penetrated by mining or drilling?	Evidence for flow or accumulation of water in chimney or cavity?	"Water Related Observations" relating to flow in the cavity and chimney given by Townsend et al., (2007)
MINT LEAF U-12t.01	Yes	No	Unknown	Not Available
DIAMOND SCULLS U-12t.02	No	Unknown	Unknown	Not Available
HUSKY PUP U-12t.03	Yes	No	Unknown	See second bullet above
MIDAS MYTH U-12t.04	Yes	Yes	Yes	The RE#3 hole, drilled into the lower portion of the chimney, unexpectedly produced very high-temperature water, eventually causing the termination of reentry work for MIDAS MYTH.
MIGHTY OAK U-12t.08	Yes	Yes	Yes	During the reentry operations no appreciable water was noted on any of the faults and fractures in the outer portions of the complex. However, many of the probe holes into the LOS and chimney areas made water for short periods of time (immediately plugged), with several being measured at about 19 L/min (5 gpm). During reentry operations water was observed flowing through the LOS drift at various locations.
MISSION GHOST U-12t.09	Yes	Yes	Yes	During the drilling of the chimney investigation hole RE-1, water was encountered at the initial rate of 379 L/min (100 gpm) and the flow maintained this rate for "several days." Eventually the rate stabilized at about 3.8 L/min (1 gpm). The temperature of the water ranged from 32 to 38 degrees C (90 to100 degrees F), and the water contained fission products.

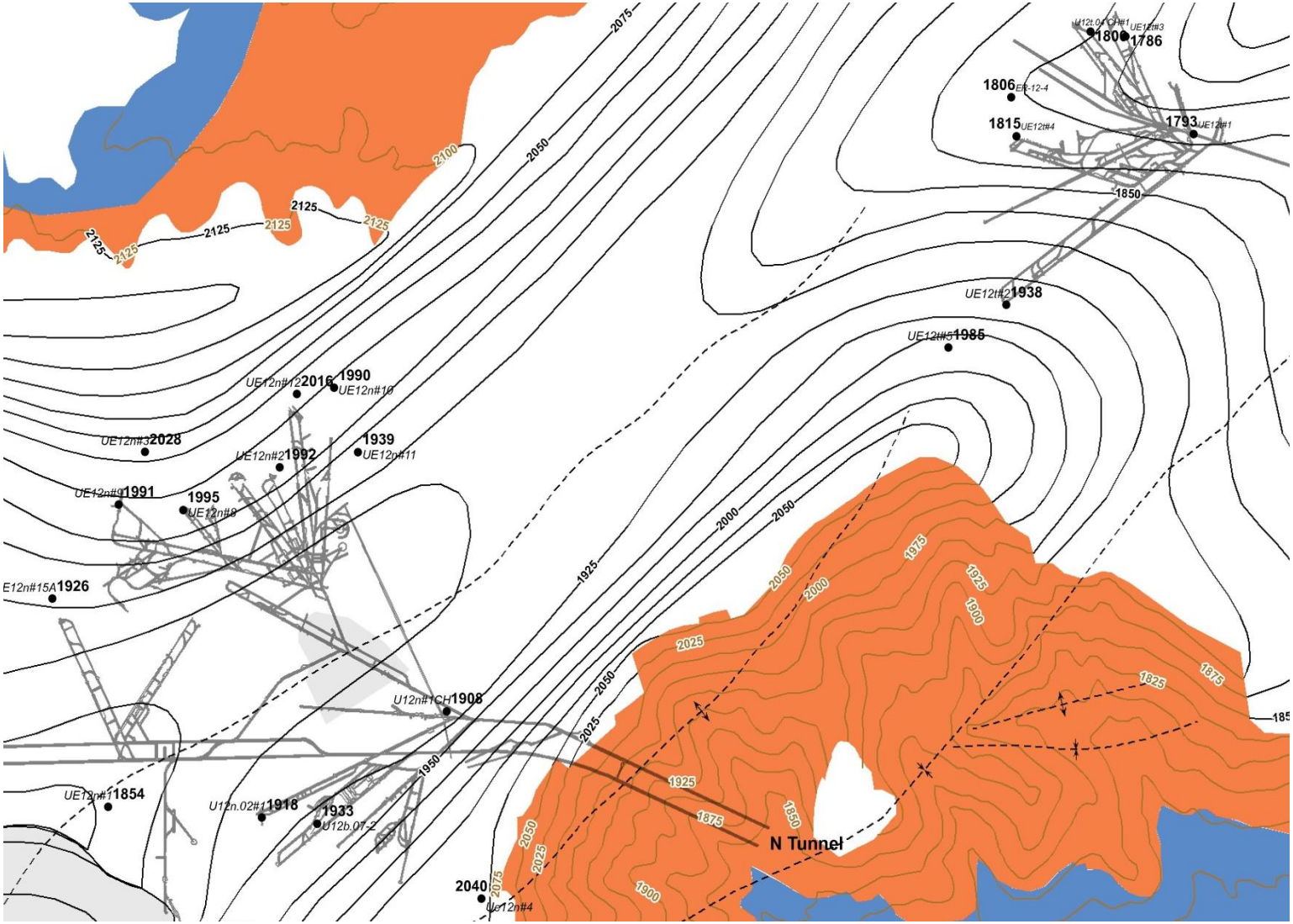

Figure 2.5 Portion of structure elevation contour map of the top zeolitization surface near N-Tunnel (to southwest) and T-Tunnel (to northeast) by NSTec (2010). Contour interval is 25 meters. The U-12t.03 shaft is the second shaft to the north of the main shaft relative to the portal, west of the shorter U-12t.09 shaft to the east.

2.5 Fracture-Matrix Continua and Dual-Permeability Model

The flow and transport model is conceptualized as a dual-permeability system with two continua operationally defined as "fracture" and "matrix". Conceptualization of processes and properties for the "fracture" and "matrix" continua depends on the flow and transport processes involved with rocks in the HSUs and test-altered zones, as discussed in Sections 3.3, 3.4, 4.3.2, 5.1, and 5.3.

The NUFT flow and transport modeling code used for the CLEARWATER and WINESKIN HST modeling enables multi-continua modeling, where each continuum has a complete set of flow and transport properties (Nitao, 2000a and b). All secondary continua (the continua additional to the primary continuum) are connected only to the primary continuum. Flow and transport connections between the secondary and primary continua are governed by areas per unit volume and lengths between the state condition nodes for pressure, saturation, and concentration.

For a fracture-matrix system modeled in the CLEARWATER and WINESKIN HST models, the matrix is designated the primary continuum and the fracture is designated as a single secondary continuum. Fracture area per unit volume, porosity, and aperture and mean matrix block size parameters are used to establish fracture-matrix connectivity of flow properties, as detailed in Section 3.4. As will be discussed in Section 5.3 on matrix diffusion, the transport properties for fracture area, fracture porosity, and matrix block radius should be adjusted for matrix diffusion dominated transport process with sorption.

2.6 Groundwater flow in the TCU

Conceptualization of flow in the tuff confining unit (TCU), the hydrogeologic unit where most Rainier Mesa tests are located including CLEARWATER and WINESKIN, is crucial to the hydrogeologic conceptual model for contaminant transport. The tunnel systems on Rainier Mesa provide unusual extensive temporal and spatial access to direct observation of groundwater flow in zeolitized tuffs of the TCU, particularly the lower tuff confining units (LTCU), the hydrostratigraphic unit where most Rainier Mesa tests were located. The prevalent hydrogeologic conceptual model for flow in the TCU involves groundwater flow dominated by fracture flow with insignificant matrix flow in nearly to fully saturated conditions (Thordarson, 1965; Carroll, 1990; Fenelon et al., 2008; Townsend, 2008). The following excerpts from hydrogeological and geophysical reports relevant to groundwater flow processes on Rainier Mesa describe the relative roles of fracture and matrix flow in the zeolitized tuffs of the TCU:

- "*The tuff is generally fully saturated interstitially hundreds of feet above the regional water table, yet no appreciable volume of water moves through the interstices because of the very low permeability. The only freely moving water observed in miles of*

underground workings occurred in fractures, usually fault zones. …This water is perched by the poor interconnection of the fractures themselves… The extremely low interstitial permeability of the interstitially saturated zeolitic-bedded tuff is principally through open fractures. Some water may move through interstices in the zeolitized tuff, but it is a very minor amount when compared to the amount of water that moves through fractures. …. The movement of interstitial water along bedding in the zeolitic tuff is negligible when compared with the movement of water along fractures." (Thordarson, 1965)

- "*The zeolitized tuffs generally do not produce interstitial water because of their extremely low permeability*." (Carroll, 1990)
- *"The less-permeable volcanic tuff present beneath Rainier Mesa and elsewhere beneath these upland areas impedes the downward movement of water through interconnected fractures, creating local zones of perched and semi-perched ground water."* (Fenelon et al., 2008)
- "*Matrix flow of radioactive contaminants through zeolitized tuff has been suggested by some investigators. Although the mechanics of such flow are possible, the calculated flow rates are extremely low. In my opinion, based on years of research into the microscopic properties of volcanic tuff and their zeolitic alteration, this method of transport is of negligible importance as a geologic pathway for any significant movement of radioactive contamination, compared to flow through fractures and faults.*" (Townsend, 2008)

2.7 Test Altered Zones

2.7.1 Altered Zone Terminology

The terminology used to describe the differing test-altered zones largely derives from the phenomenology of underground nuclear tests. The term "cavity" refers to volume occupied by a spherical void temporarily formed within milliseconds after an underground nuclear test formed by vaporization, melting, and shock compression of in-situ rocks. Shock compression induces fracturing and seismic displacement to distances of several cavity radii (U.S. Congress, 1989). As test-induced pressure subsides (largely from condensation of steam), in-situ rocks above the cavity collapse into the cavity void space within seconds to days after a test. A mixture of rock melt and collapsed rock material or "rubble" settles to the bottom of the cavity, forming a "melt glass zone." The collapse of rock material into the cavity void space propagates vertically above the cavity into a cylindrical form referred to as a "chimney."

2.7.2 Definition of Cavity Radius (Rc) for HST Models

The cavity radius (Rc) provides scaling for the size of test altered zones and spatial distribution of the radiologic source term (RST) discussed later in Chapter 4. Rc can be determined from measurements, if available (see Zavarin, 2014), or estimated by

calculation from yield (Pawloski, 1999). Rc measurements are not available for CLEARWATER and WINESKIN tests (Townsend, 2008; Zavarin, 2014). For the CLEARWATER and WINESKIN HST models, Rc is derived from a calculated value using Equation 1 from UCRL-ID-136003 (Pawloski, 1999):

$$\mathrm{Rc} = 70.2\frac{Y^{1/3}}{(\rho_{ob}WP)^{1/4}}$$

where Y is the announced yield or the maximum of the announced yield range (kt) from USDOE (2015), ρ_{ob} is an approximate overburden density (2.0 Mg/m^3), and WP is the working point depth (meters). The calculated Rc are 71.3 and 72.3 meters for CLEARWATER and WINESKIN, respectively, based on the 200 kt maximum of the 20 to 200 kt announced yield range for both tests (USDOE, 2015).

For simplicity and given the approximate nature of the calculated Rc value, the CLEARWATER and WINESKIN HST models assume Rc = 72 meters for both tests. All figures showing Rc and all references to Rc for the CLEARWATER and WINESKIN tests in this report are based on a 72-meter Rc assumed for the CLEARWATER and WINESKIN HST models as described above.

2.7.3 Definition of Test Altered Zones

Underground nuclear tests cause alteration of rock properties relative to the pre-test conditions. The general configuration of test-altered zones and properties is largely based on information compiled in U.S. Congress (1989) and Townsend (2008):

- Test-enhanced fracture permeability extends to 3 Rc (U.S. Congress, 1989).
- Test-enhanced microfracturing in rocks extends to 2 Rc (U.S. Congress, 1989).
- In-situ rock properties do not change beyond 3Rc, except in the chimney (U.S. Congress, 1989).
- Chimney height varies from 4.3 to 9.2Rc (Townsend, 2008).

The magnitude and extent of alteration of properties by the test will vary with the in-situ rock properties. For example, fracture permeability may not be enhanced in granular rock such as vitric tuffs. Chimney height will vary largely depending on the induration of the rock. For example, zeolitic and welded tuffs will have higher bulking than friable vitric tuffs leading to smaller chimney heights.

Figure 2.6 shows a schematic diagram for geometry of test-altered zones. For the CLEARWATER and WINESKIN HST models, the following concepts are used to define the test altered zones:

- **Cavity** – Within 1.0 Rc above the melt glass zone, the former cavity volume is assumed filled with TCU-derived rubble.
- **Melt Glass Zone** – The bottom of the former cavity is filled with a mixture of glass and rubble.
- **Chimney** – The chimney is assumed filled with rubble derived from the TCU, welded tuffs, or vitric tuffs, each of which will impart different properties.
- **Crush Zone** – The zone within 1.3 Rc is more intensely fractured or "pulverized" as described in Borg (1973).
- **Matrix to 2.0 Rc** – Matrix permeability is enhanced to 2.0 Rc as a result of microfracturing (U.S. Congress, 1989).
- **Fractures to 3.0 Rc -** Fracture permeability and porosity in in-situ rock is enhanced between 1.0 and 3.0 Rc, with increasing fracture permeability closer to the test (Boardman and Skrove, 1966; U.S. Congress, 1989).

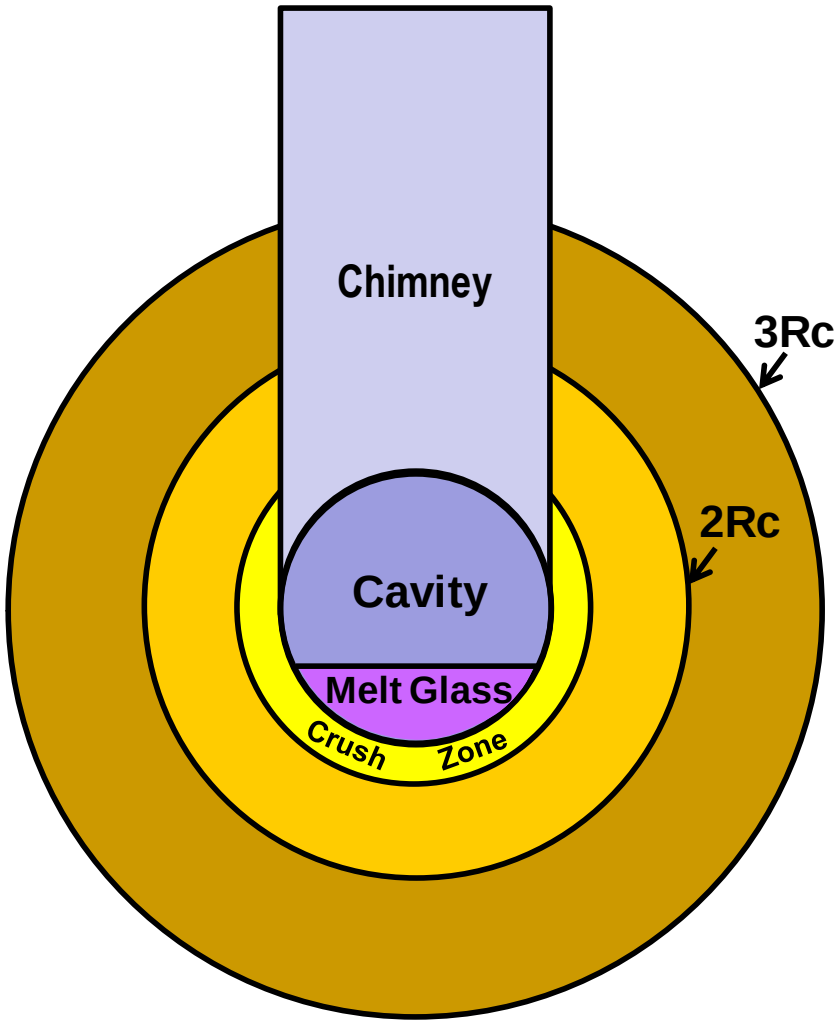

Figure 2.6 Schematic diagram for geometry of test-altered zones. All test-altered zones are assumed radially symmetric about the vertical axis.

Figure 2.7 shows the test-altered zones as implemented for the WINESKIN HST model, for example, using fracture permeability as the rock property in the background. Radial dependence on test alteration is accomplished by division of in-situ rock altered zones between cutoffs of 1.0, 1.3, 1.5, 2.0, 2.5, and 3.0 Rc. Table 2.4 compiles the conceptual models for fracture and matrix properties in each test-altered zone.

The time between test detonation and cavity collapse can range from minutes to days (U.S. Congress, 1989). The models use the geometric configuration of the test-altered zones beginning at "time zero" or time of detonation considering the long 1000-year modeling timeframe relative to time of cavity collapse (Section 5.5).

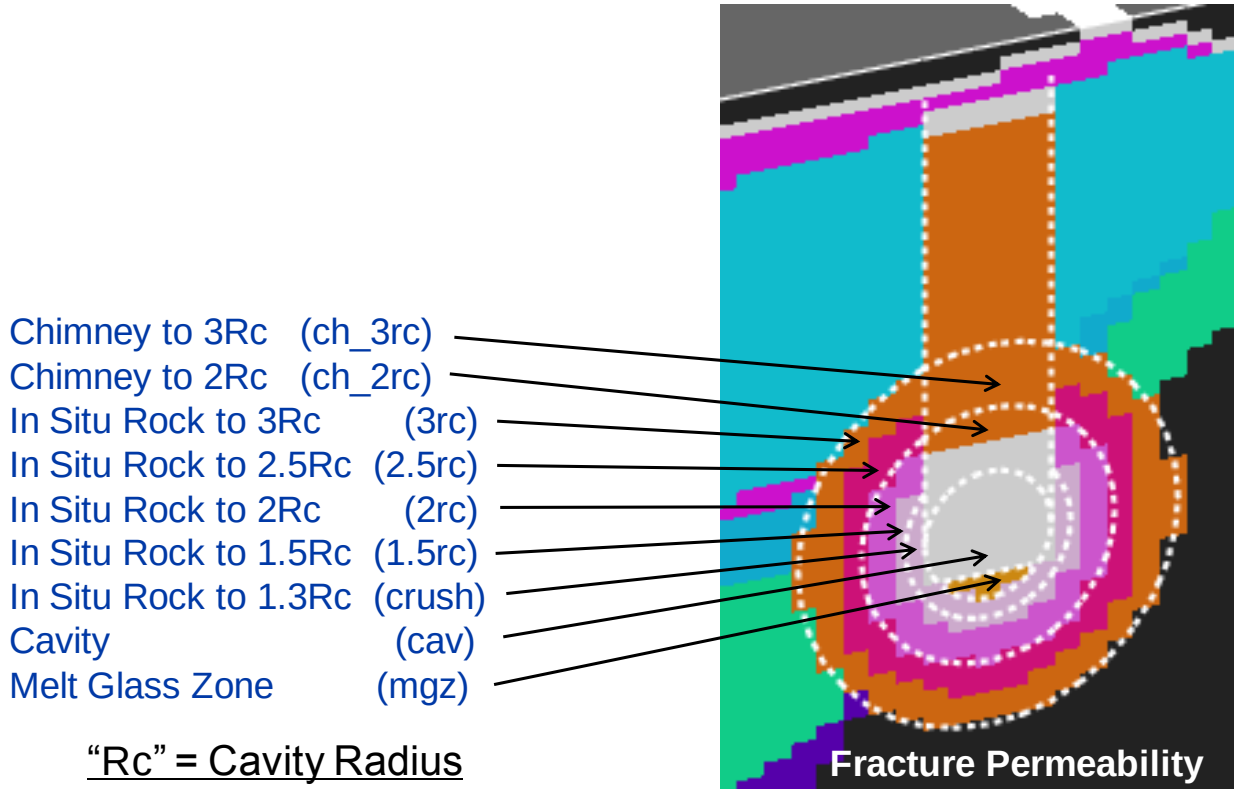

Figure 2.7 Definition of test-altered zones used in the CLEARWATER and WINESKIN HST models. Concentric circles of 1Rc, 1.3Rc, 2Rc, and 3Rc are shown, as well as the projected chimney height for the WINESKIN test. The example rock property is fracture permeability, showing enhancement in test-altered zones with "hotter" colors. The model Rc of 72 m is derived from maximum announced yield (USDOE, 2015) and Pawloski (1999) as detailed in Section 2.7.2.

Table 2.4 Conceptualization of test-altered zones for defining of matrix and fracture continua in the CLEARWATER and WINESKIN HST models.

Test-Altered Zone	Matrix	Fracture
Cavity	TCU blocks with enhanced permeability from microfracturing	Void or bulking space
Melt Glass	TCU blocks with enhanced permeability from microfracturing	Glass Zone
Chimney	TCU, vitric tuff, or welded tuff depending on stratigraphy	Void or bulking space
In-Situ to 1.3Rc	Enhanced permeability from microfracturing	Fractures with enhanced permeability and porosity
In-Situ to 1.5Rc		
In-Situ to 2Rc		
In-Situ to 2.5Rc	No change	
In-Situ to 3.0Rc		

2.7.4 Comparison to Previous Conceptualizations of Test –Altered Zones

Certain aspects of the conceptualization of the test-altered zones are different for the CLEARWATER and WINESKIN HST models compared to previous HST models (e.g., Pawloski et al., 2001; Carle et al., 2007; Carle et al., 2008, Maxwell et al., 2008). Differences in rock properties must be considered. Data availability varies with test setting. At Pahute Mesa, the HST models were designed for a test situated in rhyolitic lava and calibrated primarily to abundant thermal data (Pawloski et al., 2001). At Frenchman Flat, the HST models were designed for a test situated in alluvium and calibrated primarily to the radionuclide migration experiment and multi-well pumping test data (Carle et al., 2007). At Yucca Flat, HST models designed for carbonate tests were conceptualized by post-test characterization data and consideration of the unique properties of carbonate rocks, such as thermal decomposition prior to melting (Carle et al., 2008). Also at Yucca Flat, HST models used pore-water pressure data to infer post-test compression of test-altered rocks of the tuff confining unit (Maxwell et al., 2008). At Rainier Mesa, post-test characterization data of permeability and porosity, temperature, hydraulic testing, or pore pressure are lacking compared to previous HST model sites. However, U.S. Congress (1989) does provide a conceptual model specific to the test-altered zones of Rainier Mesa tests. This conceptual model can be applied to Rainier Mesa HST modeling with judicious use of indirect data. Nonetheless, considerable uncertainty in HST model transport predictions derives from uncertainty in the parameters used for the test-altered zones. The current CLEARWATER and WINESKIN HST models include assessment of uncertainty in properties of test-altered zones.

3 Flow Processes, Properties, and Calibration

3.1 Rainier Mesa Hydrogeologic System

The collective of hydrogeologic interpretations for Rainier Mesa (Thordarson, 1965; Carroll, 1990; NSTec, 2007; Fenelon et al., 2008) generally divide the Rainier Mesa area hydrogeologic system into five zones of groundwater flow (from top to bottom):

- The unsaturated zone – a variably saturated zone from the ground surface to the top of the (semi-) perched zone,
- The (semi-) perched zone – from the "top of saturated volcanic rocks" (Carroll, 1990) on Rainier Mesa to the base of the Tertiary volcanics (where perched) or to the "water–level surface" of the "regional volcanic aquifer" (where semi-perched) (Fenelon et al., 2008),
- The "Pahute Mesa-Timber Mountain volcanic aquifer" or "regional volcanic aquifer",
- A variably saturated zone below western Rainier Mesa between the "perched zone" and "upper carbonate aquifer"
- The saturated zone below the "water-level surface" or water table of the "upper carbonate aquifer" or "LCA3"

The WINESKIN and CLEARWATER HST and N and T-Tunnel flow and transport models address variably saturated flow processes in the unsaturated and (semi-) perched zones (see Section 3.2.1), whereas the SZ model addresses saturated flow processes below the water-level surfaces in the regional volcanic and upper carbonate aquifers. Water level (e.g., Fenelon et al., 2008), water pressure (e.g., Townsend et al, 2007), and saturation data provide flow calibration targets for HST, N and T-Tunnel, and SZ models of groundwater flow in the unsaturated, perched, and semi-perched, regional volcanic aquifer, upper carbonate aquifer zones.

Figure 3.1 shows a generalized hydrogeologic cross-section through Rainier Mesa modified from Fenelon et al. (2008) by adding the following information relevant to development of HST, N and T-Tunnel, and SZ flow and transport models:

- Major HSUs that comprise aquifers and confining units, from top to bottom:
    - TMWTA, TMLVTA, and LVTA volcanic aquifers in mostly unsaturated flow conditions (see Section 2.4.4 regarding saturated conditions in LVTA aquifers)
    - LTCU and OSBCU confining units in mostly perched or semi-perched flow conditions
    - RVA volcanic aquifer, which constitutes the main deep flowing zone of the regional volcanic aquifer near Rainier Mesa
    - ATCU confining unit (perched or semi-perched)

    - LCA3 upper carbonate aquifer
- Water level data
    - outlined in white for shallow or perched systems
    - outline in black for intermediate or deep systems
- Top of the perched zone
    - light blue dotted line
    - based on perched zone water level data
- Water-level surface of volcanic aquifer
    - approximate top of SZ model for volcanic aquifer system
- Water-level surface of carbonate aquifer
    - approximate top of SZ model for carbonate aquifer system
    - lower boundary condition for flow and transport models
- Variably saturated zone above in LCA3
    - included in flow and transport models
    - not included in CLEARWATER and WINESKIN HST models
- CLEARWATER HST model boundary
    - Model domain extends from base of RVA to ground surface.
    - 1,711 m water level data in U12q constrains head in perched zone.
    - Estimated 1,600 m water level in volcanic aquifer provides lower head boundary condition. This estimated 1,600 m water level is based on volcanic aquifer water level surface mapped by Fenelon et al. (2008) shown by dashed white line in Figure 3.1. At U12q (the CLEARWATER emplacement hole), Fenelon et al. (2008) shows the volcanic aquifer water level surface to be slightly below the bottom of U12q, which is at 5,269 (1,606 m) elevation (Figure 3.1).

3.1.1 Unsaturated Zone

Reference in this report to the "unsaturated zone" pertains to the portion of the Rainier Mesa hydrogeologic system from the ground surface down to the water table of the (semi-) perched zone where saturated conditions pervasively continue downward to the base of the Tertiary volcanics. In the unsaturated zone, saturation is persistently below unity in both fracture and matrix materials. However, saturated conditions may exist in some pockets of the unsaturated zone, particularly above interfaces between volcanic aquifers and confining units. At Rainier Mesa, unsaturated conditions exist in most of the TMWTA, TMLVTA, LVTA1, LVTA2, BRA, and SWA volcanic aquifers and upper portions of the LTCU confining unit. Water level and stratigraphy data suggest, however, that saturated conditions may exist near the base of BRA, LVTA1m and LVTA2 volcanic aquifers within synclinal structures (see Section 2.4.4).

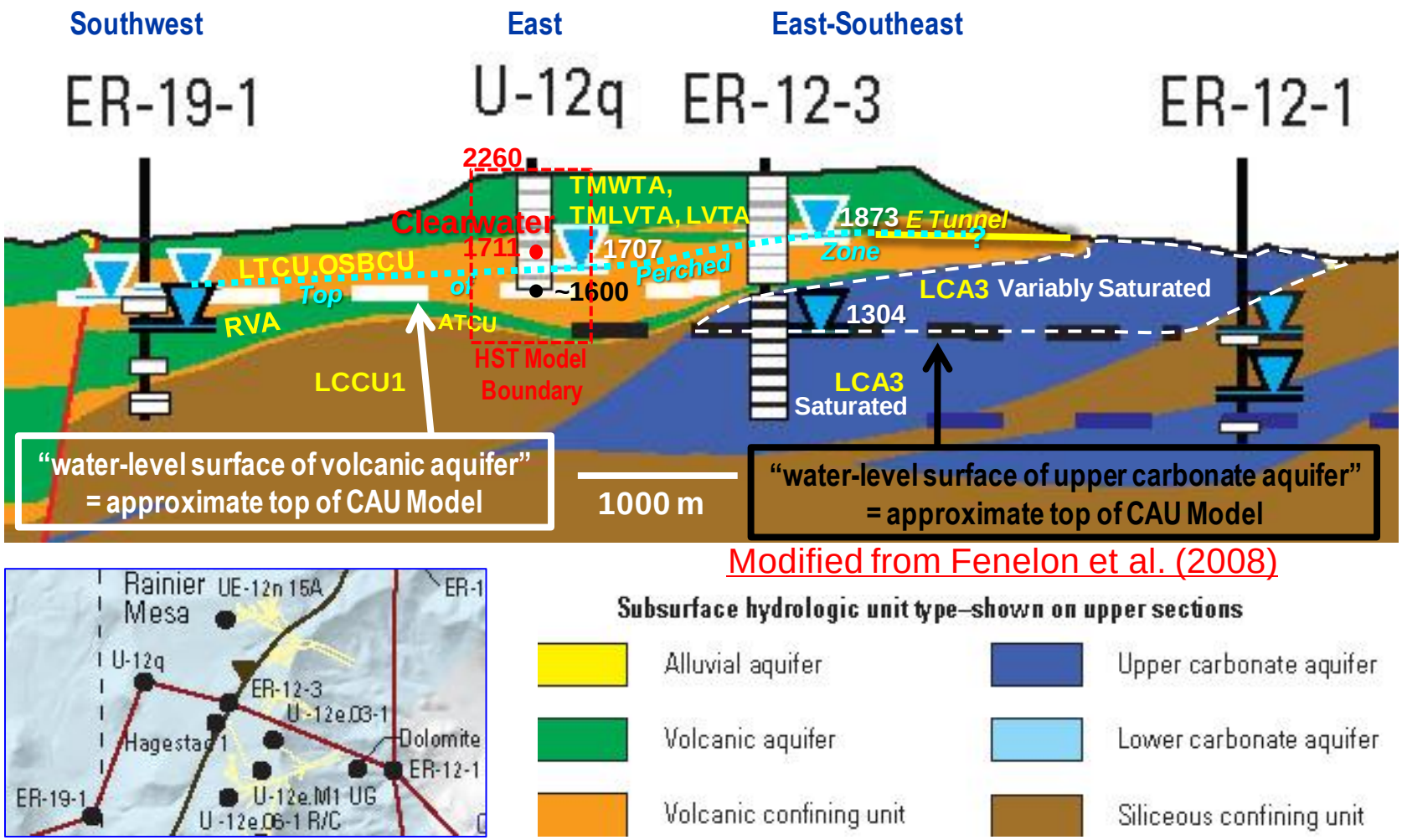

Figure 3.1 Generalized cross-section through Rainier Mesa and location of CLEARWATER test showing aquifers and confining units, water level surfaces for regional volcanic aquifer (white dashes), LCA3 carbonate aquifer (black dashes), and perched zone (light blue dotted line), and intermediate or deep systems (blue dashes). Red dot and red dashed lines show location of CLEARWATER test and HST model boundary, respectively. Variably saturated portion of LCA3 is outlined in thin white dashes. Figure modified from Fenelon et al. (2008).

3.1.2 Perched Zone

In hydrogeologic terms, "perched" refers to unconfined saturated conditions underlain by unsaturated conditions (as shown in Figure 3.1 for eastern Rainier Mesa) and "semi-perched" refers to unconfined saturated conditions overlying a (semi-)confined aquifer system of lower head (as shown for Figure 3.1 for western Rainier Mesa). For simplicity in this report, the term "perched zone" is referred to in generalized terms to represent the portion of the Rainier Mesa Tertiary volcanic hydrogeologic system where saturated conditions are pervasive in both fracture or matrix materials overlying carbonate rocks (as in western Rainier Mesa) or siliciclastic rocks (as in eastern Rainier Mesa). The term "perched zone" used in this report comprises both perched and semi-perched conditions described in Thordarson (1965) and Winograd and Thordarson (1975) and "shallow elevated water" described in Fenelon et al. (2008). As detailed in Section 2.6, bulk flow in the tuff confining unit (TCU) of the perched zone is controlled or dominated by the interconnectivity of fractures and faults dissecting the low-permeability and predominately zeolitized tuff matrix materials of the LTCU and OSBCU hydrostratigraphic units (Thordarson, 1965; Winograd and Thordarson, 1975; Carroll, 1990; Fenelon, 2008; Townsend, 2008).

3.1.3 Pahute Mesa-Timber Mountain Volcanic Aquifer

The Pahute Mesa-Timber Mountain (PMTM) volcanic aquifer extends from central Rainier Mesa to the west with increasing thickness. Near Rainier Mesa, Pahute Mesa-Timber Mountain volcanic aquifer corresponds to deeper the Redrock Valley aquifer (RVA) hydrostratigraphic unit, a welded tuff aquifer hydrogeologic unit (NSTec, 2007). Further west, the PMTM aquifer includes the saturated basal portion of the Belted Range aquifer (BRA). The PMTM volcanic aquifer receives recharge from Rainier Mesa, and regional flow moves laterally in westward to southwestward directions from Rainier Mesa and flow moves westward into the PMTM volcanic aquifer near the N, B, and E-Tunnels (Fenelon et al., 2008), as shown in Figure 3.2. Internal heterogeneity, discontinuities in aquifer extent, and structural features such faults and synclines will cause local variations in flow direction.

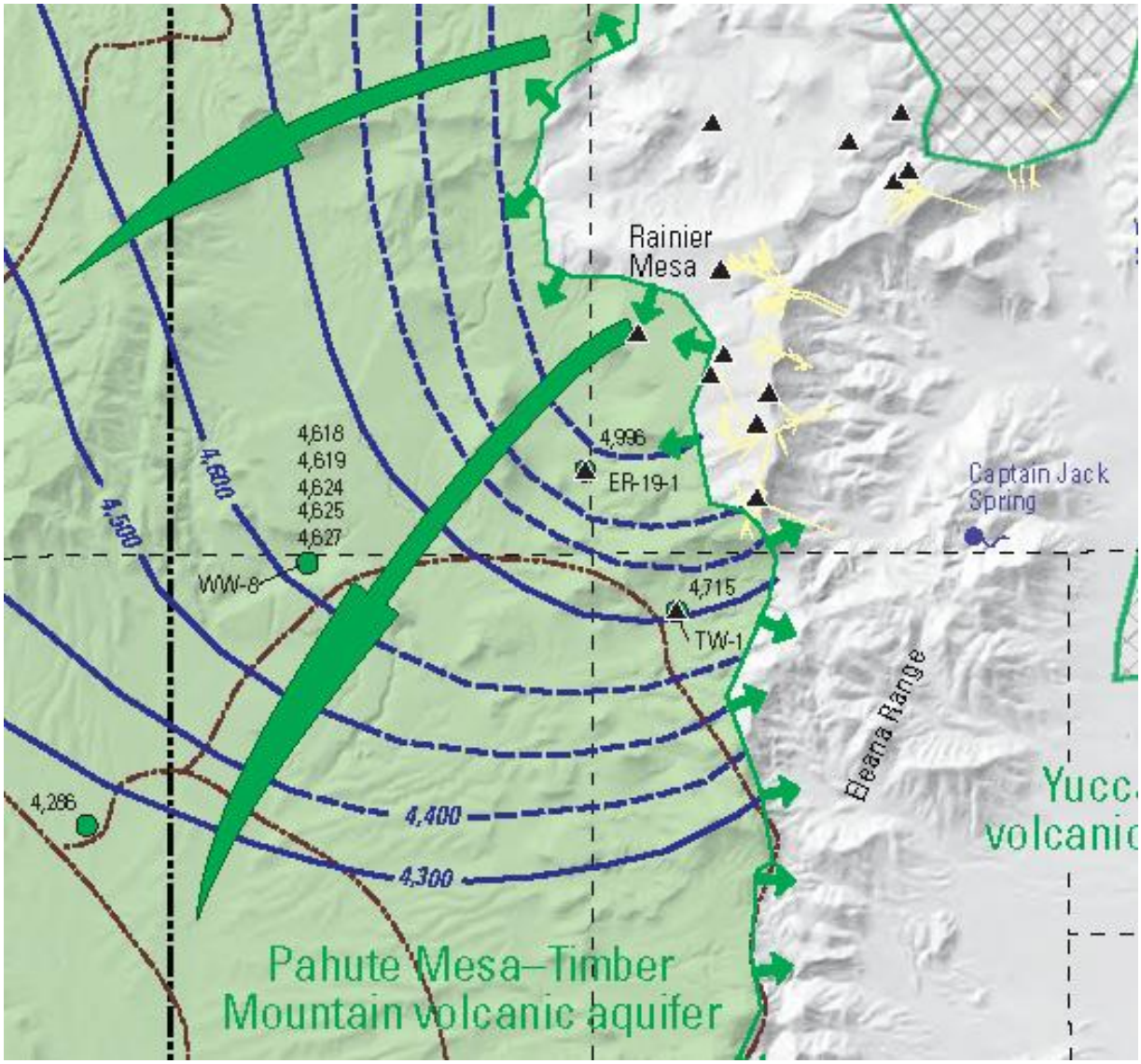

Figure 3.2 Water levels (blue contours), westward to southwestward flow directions (large arrows), and direction of flow into and out of (small arrows) the Pahute Mesa –Timber Mountain volcanic aquifer, as shown by map in Fenelon et al. (2008). Tunnel locations are shown in yellow.

Importantly, the full eastern extent of the RVA in relation to tunnel locations and vertical shaft test is not shown in the map of Figure 3.2 by Fenelon et al. (2008). Maps of RVA extent are provided by NSTec (2007, 2009a, and 2011). Figure 3.3 compares a map of RVA extent near N-Tunnel based on the NSTec (2007) report and a revised interpretation by NSTec (2009a). According to this map, the RVA extends beneath large portions of the N-Tunnel area in both the 2007 (shaded in green) and 2009 (outlined in red) interpretations. The borehole location U12r in the northwest portion of the map is the WINESKIN test

location. Both the NSTec (2007) and NSTec (2009a) interpretations indicate the RVA does not extend laterally to U12r. As discussed in Section 2.3, the southerly dipping hydrostratigraphy near WINESKIN indicates a southerly flow direction toward the RVA consistent with the location of small arrows directed south near the "Rainier Mesa" label in Figure 3.2 modified from Fenelon et al. (2008).

3.1.4 Choice of Hydrostratigraphic Framework Realization

The choice of a hydrostratigraphic framework realization for HST modeling can depend on evaluation of differences in data and interpretations, as well as considerations of consistency between different HST, N and T-Tunnel, and SZ flow and transport modeling efforts. NSTec (2007) documents the hydrostratigraphic framework model used by the SZ model. During review of geologic data for CLEARWATER and WINESKIN HST model development in early 2009, an inconsistency was pointed out between the stratigraphy and hydrostratigraphy used for borehole RME#1 by NSTec (2007) compared to Townsend and Townsend (2004). RME#1 is very important control point for definition of hydrostratigraphic models near the CLEARWATER and WINESKIN tests and the western side of E, G, and N-Tunnel areas. NSTec (2009b) confirmed that the RME#1 stratigraphy given in NSTec (2007) was erroneous, and revisions to the hydrostratigraphic model were made, including the revision of the RVA thickness and extent shown in Figure 3.3.

While Figure 3.3 illustrates that revisions to the hydrostratigraphic interpretation of the RVA could affect the N-Tunnel area, the UGTA Rainier Mesa Peer Review Committee concluded that the revisions would have little or no effect on the CLEARWATER and WINESKIN HST models. The Rainier Mesa Peer Review Committee advised the HST model development to *not* incorporate revised hydrostratigraphic interpretations (e.g., NSTec, 2009a and b, 2011) to maintain consistency with the concurrent flow and transport models.

The CLEARWATER and WINESKIN HST models use a hydrostratigraphic model provided by NSTec that is identical to the hydrostratigraphic model used in the concurrent SZ model. All hydrostratigraphic units provided in the hydrostratigraphic framework model by NSTec are directly applied to the CLEARWATER and WINESKIN HST models. No selective choosing of the hydrostratigraphic interpretations has been done during CLEARWATER and WINESKIN HST model development.

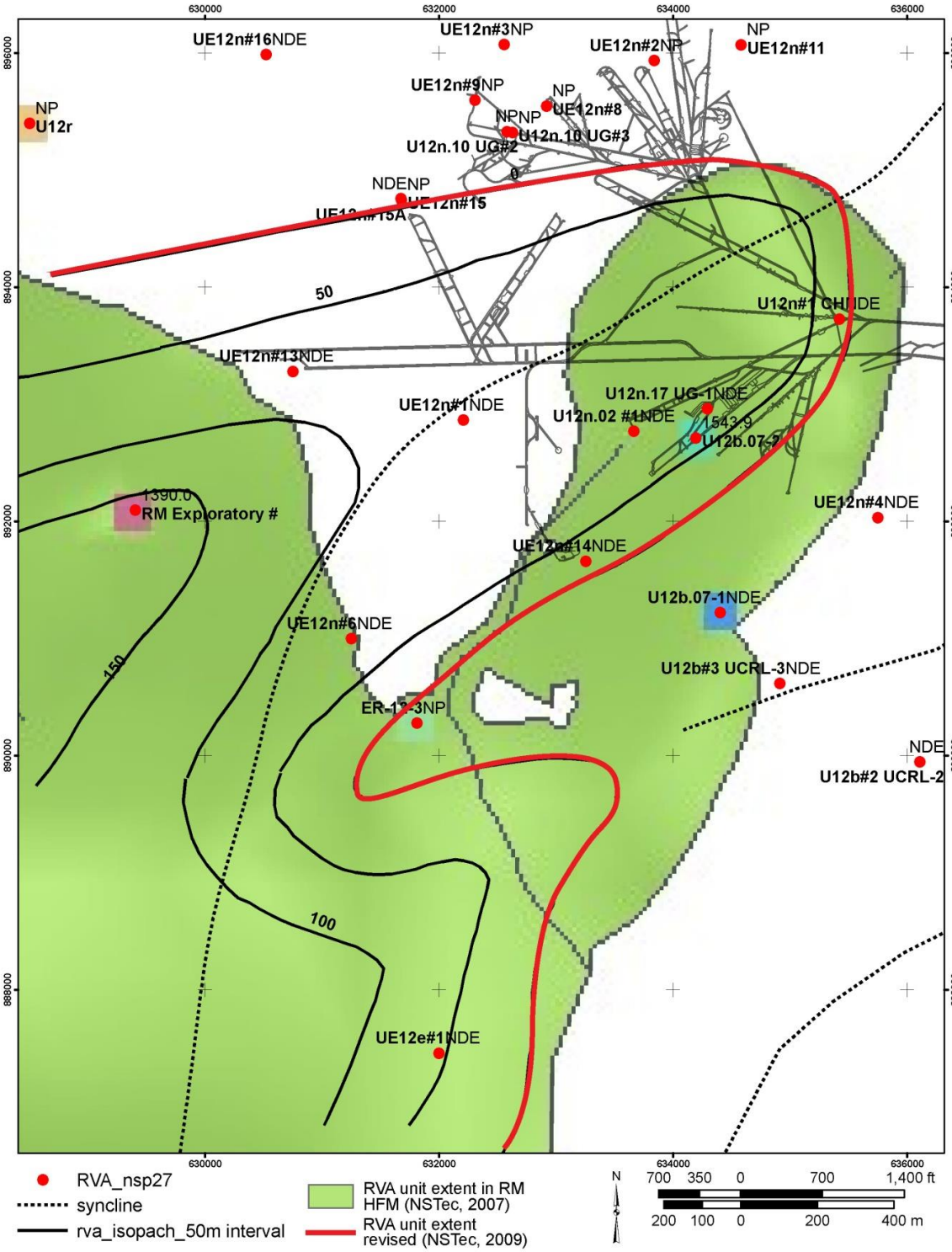

Figure 3.3 Map comparing RVA extent near N-Tunnel based on the NSTec (2007) and a revised interpretation by NSTec (2009a). Location marked "RM Exploratory #" is borehole RME#1. The borehole location U12r in the northwest corner of the map is the WINESKIN test location. "NDE"=not detected; "NP"=not present. Syncline axis shown by dotted line.

3.2 Water Level Data

Water level data are useful for HST flow model calibration, particularly for establishment of flow gradients through the perched zone near the CLEARWATER and WINESKIN tests. Only one water level datum is available within the CLEARWATER and WINESKIN HST model domains, a water level of 1,707 m (5,600 ft) from the CLEARWATER U12q emplacement hole (Fenelon et al., 2008). The U12q water level is considered representative of the perched or "shallow" zone of "elevated" groundwater (Fenelon et al., 2008), as the U12q borehole did not extend to the deeper RVA of the PMTM volcanic aquifer. Thus, the U12q water level can be used to calibrate perched zone potentiometric head and saturation in the CLEARWATER HST model.

During drilling of the WINESKIN emplacement hole U12r, water began to flow into the hole in the OSBCU at 598 m depth, about 79 m below the working point depth, which would be considered within the perched zone. No water level measurements were obtained and, thus, the perched zone water level near the WINESKIN test is unknown but likely within about 1Rc (~72 m) below the WINESKIN working point elevation based on the description of flow of water into the U12r hole 79 m below the working point.

As discussed in Section 3.1, the water level of the PMTM volcanic aquifer can be inferred from maps and cross-sections by Fenelon et al. (2008). PMTM volcanic aquifer water levels inferred as 1,600 m near CLEARWATER and 1,550 m near WINESKIN are used for outflow boundary conditions in the HST models.

3.3 Fracture-Matrix Interaction

Groundwater flow in in-situ rocks near the CLEARWATER and WINESKIN test locations is assumed to be dominated by fracture flow, as is interpreted for other Rainier Mesa tunnel tests situated in zeolitized tuff of the LTCU (Thordarson, 1965; Carroll 1990; Fenelon et al., 2008; Townsend, 2008). However, given low fracture porosity (Section 9.4.1 of Appendix A) and low fracture frequency in the tuff confining unit, on the order 0.1 per meter based on Reeves (2008) (Section 9.4.2), the in-situ rock matrix materials present a much larger available volume for immobilization by physical and geochemical processes compared to fracture pore space.

Within the CLEARWATER and WINESKIN HST model domain, flow in welded tuff (TMWTA, BRA, RVA), granitic (MGCU) HSUs is also dominated by fractures. Flow in alluvial (AA) and vitric tuff (TMLVTA, LVTA1, LVTA2) HSUs is dominated by matrix or "interstitial" flow (Thordarson, 1965). The degree of fracture flow in the argillic tuff confining unit (ATCU) and the lower clastic confining unit-thrust plate (LCCU1) is uncertain, but most likely lower than in the LTCU or OSBCU.

The test-altered zones present additional contrasts and considerations for modeling fracture and matrix properties:

- Microfractures and fractures are created out to 2Rc (U.S. Congress, 1989).
- Existing fractures are extended and connected out to 3Rc (U.S. Congress, 1989).
- Interconnected void spaces, analogous to fractures of very large aperture, are created in the collapsed cavity and chimney zones.
- Test-induced fracturing and chimney collapse processes decrease matrix block sizes relative to unaltered rock in the melt glass zone, cavity, chimney, and test-altered zones out to 2Rc.
- The melt glass zone is a mixture of glass and rubble blocks, which presents transport process issues for modeling radionuclides sources that originate in glass.

Fracture-matrix interaction undoubtedly plays a major role in prediction of flow and transport in all Rainier Mesa tests including CLEARWATER and WINESKIN. As such, a dual-continuum modeling approach is developed for CLEARWATER and WINESKIN HST modeling.

3.4 Flow Property Data

Flow properties for the CLEARWATER and WINESKIN HST models are based on data (in order of preference) relevant to Rainier Mesa, NNSS, and rocks of similar characteristics. The CLEARWATER and WINESKIN HST models use hydrostratigraphic units (HSUs) for spatial distribution of rock properties, similar to the SZ and the N and T-Tunnel flow and transport models. Therefore, the flow properties derived from data and used for model parameters are organized around HSUs. Further derivation of matrix properties for stratigraphic units, as used T-Tunnel flow and transport models, is detailed in Appendix B.

3.4.1 Matrix Properties

3.4.1.1 Matrix Property Data

Matrix unsaturated flow properties for HST model rock units are derived primarily from the RME#1 and UE12t#1 core measurement data from Kwicklis et al. (2008), with adjustments described in Appendices B, C, and D. The RME#1 and UE12t#1 matrix property data from Kwicklis et al. (2008) are more useful for HST and flow and transport modeling than the various property data sets on Rainier Mesa for several reasons:

- Data were collected and analyzed using the same techniques and analysts.
- Data locations span the entire volcanic section rather than a single unit (e.g. Norris et al., 1982).
- Individual permeability data values are available rather than ranges and arithmetic means (e.g., Thordarson, 1965).

- Data include core and mineralogic descriptions valuable to understanding property variation.
- Permeability ranges in altered tuffs are lower than the lower limit of gas permeability measurements of 0.1 millidarcy (1e-16 m^2 or 1e-9 m/s hydraulic conductivity) or greater provided in Townsend (2009). Data indicating altered tuff permeabilities can be much lower than 1e-16 m^2 include:
    - Norris et al. (1982) report permeabilities in the range of 2e-19 m^2 and 3e-18 m^2 for zeolitized bedded tuff of the Grouse Canyon member, and
    - Matrix permeability measurements detailed in Appendix B after applying corrections to data from Kwicklis et al. (2008) yield average permeabilities as low as 2e-18 m^2 in hydrostratigraphic units and 1e-18 m^2 in stratigraphic units (Tables 3.2 and 10.4).
- By combining knowledge of the specific rock property measurement techniques used and XRD data provided by Kwicklis et al. (2008), it is possible to correct matrix property data for dehydration associated with zeolite and smectite bearing rocks (Appendix C). This was not possible to do with older rock property data sets (e.g., Thordarson, 1965; Brethauer et al., 1980; Townsend, 2009) that do not have accompanying XRD or relative humidity box data as provided in Kwicklis et al. (2008).

3.4.1.2 Revised Hydrostratigraphy and Stratigraphy for RME#1

Much of the matrix property data from Kwicklis et al. (2008), particularly the more reliable rigid-wall matrix permeability measurements, are derived from drill hole RME#1. However, subsequent to the Kwicklis et al. (2008) report, NSTec (2009b) provided revised hydrostratigraphic and stratigraphic interpretation for RME#1 consistent with Townsend and Townsend (2004) but different from NSTec (2007), which the hydrostratigraphic framework model was derived from. Subsequently, differences in revised Ksat and van Genuchten model parameter values (van Genuchten, 1980) for hydrostratigraphic and stratigraphic units relative to values given in Kwicklis et al. (2008) result from differences in hydrostratigraphic and stratigraphic interpretations at RME#1.

Table 3.1 compares hydrostratigraphic and stratigraphic units for RME#1 sample depth intervals as given by Kwicklis et al. (2008) and NSTec (2009b). For the 32 samples from RME#1, the revised hydrostratigraphy and stratigraphy from NSTec (2009b) changes hydrostratigraphic units at 9 sample locations and stratigraphic units at 14 sample locations, as indicated by table entries shaded in yellow. Entries in Table 3.1 shaded in green indicate only change in the name of the same unit, which does not affect parameter values.

All matrix property data values derived in this section from the Kwicklis et al. (2008) data for the CLEARWATER and WINESKIN HST models are corrected for the revised RME#1

hydrostratigraphy provided by NSTec (2009b). Appendix B provides details to corrections to matrix properties to account revised RME#1 hydrostratigraphy and stratigraphy.

Table 3.1 Comparison of hydrostratigraphic and stratigraphic units assigned to samples from RME#1 by Kwicklis et al. (2008) and NSTec (2009b). Green shading denotes changes that reflect nomenclature only. Yellow shading denotes revised hydrostratigraphic or stratigraphic interpretations.

Sample Depth Range (ft)	Hydrostratigraphic Unit (HSU)		Stratigraphic Unit	
	Kwicklis et al. (2008)	NSTec (2009b)	Kwicklis et al. (2008)	NSTec (2009b)
886.3-886.6	TM-LVTA	TM-LVTA	Tp	Pre-Tmr, post Tbg
915.0-915.2	TM-LVTA	TM-LVTA	Tpc	
1027.6-1027.8	TM-LVTA	TM-LVTA	Tcbs	
1114.25-1114.4	TM-LVTA	BRA	Tbg	Tbg
1287.7-1288.0	TM-LVTA	LVTA1	Tbgb	Tbgb
1396.3-1396.6	BRCU	LTCU	Tn4	Tn4
1571.9-1572.2	BRCU	LTCU	Tn4	Tn4
1674.3-1674.6	BRCU	LTCU	Tn4	Tn4
1704.5-1704.8	BRCU	LTCU	Tn4	Tn4
1790.1-1790.4	BRCU	LTCU	Tn3	Tn3
1894.4-1894.7	BRCU	LTCU	Tn3	Tn3
1940.3-1940.6	BRCU	LTCU	Tn3	Tn3
1976.6-1980.0	BRCU	LTCU	Tub	Tub
1994.0-1994.2	OSBCU	LTCU	Ton2	Tub
2045.6-2046.0	OSBCU	OCBCU	Ton2	Ton2
2176.4-2176.8	OSBCU	OCBCU	Ton1	Ton2
2273.6-2274.0	OSBCU	OSBCU	Ton1	Toy
2479.6-2480.3	OSBCU	OSBCU	Ton1	Toy
2640.2-2640.45	OSBCU	OSBCU	To	Toy
2669.6-2670.0	OSBCU	OSBCU	To	Ton1
2742.1-2742.6	OSBCU	OSBCU	To	Ton1
2864.0-2864.4	OSBCU	RVA	Tor	Tor
2948.7-2948.9	OSBCU	RVA	Tor	To
3158.2-3158.5	OSBCU	RVA	Tor	Tot
3294.8-3195.2	RVA	RVA	Tor	Tot
3295.3-3295.6	RVA	RVA	Tor	Tot
3349.0-3349.4	RVA	RVA	Tor	Tot
3408.0-3408.4	OSBCU	RVA	Tf	Tot
3428.0-3428.2	OSBCU	LTCU1	Tf	Tot
3522.0-3522.3	OSBCU	LTCU1	Tf	Tot
3608.8-3609.1	ATCU	ATCU	Ttl	To
3630.4-3630.8	ATCU	ATCU	Ttl	To

3.4.1.3 Ksat

Saturated hydraulic conductivity (Ksat) parameters for matrix materials will be used in development of hydraulic conductivity and permeability values in HST, N and T-Tunnel, and SZ flow and transport models. Table 3.2 compares mean Ksat values in HSUs derived

from core data (Kwicklis et al., 2008) with revised Ksat values accounting for the factors considered in Appendices B and C and summarized above.

Kwicklis et al. (2008) derived Ksat parameter values for HSUs from the geometric mean of individual data within each HSU. Revised Ksat parameter values for HSUs include both geometric and harmonic mean to provide plausible effective matrix property ranges for both lateral and vertical flow directions in anisotropic media such as the layered volcanic sequences on Rainier Mesa.

Differences in number of data (N) within each HSU result from both: (1) differences in criteria for excluding data as detailed in Appendix B and (2) use of re-interpreted RME#1 stratigraphy by NSTec (2009b). Revised Ksat values are generally reduced by accounting for the effects of overestimation of Ksat by flexible-wall data from UE12t#1, but can also be raised or lowered as result of revised RME#1 stratigraphy.

The magnitudes of geometric mean Ksat values for HSUs differ relative to values from Kwicklis et al. (2008) as follows:

- Ksat is reduced by 58% in the TM-WTA welded tuff aquifer.
- Ksat values in vitric tuff aquifers (TM-LVTA and LVTA1) are raised 77% in TM-LVTA and reduced by 45% in LVTA1.
- Ksat values in tuff confining units are all reduced: 62% in the LTCU, 29% in the OSBCU, and 99% in the ATCU.
- Ksat in the RVA is raised by a factor of 22 in the RVA with addition of data in RVA (from 3 to 7), primarily based on revised RME#1 stratigraphy (NSTec, 2009b).
- One datum used for the revised Ksat value for the BRA welded tuff aquifer was added based on revised RME#1 stratigraphy (NSTec, 2009b).
- No revised Ksat value for the TUBA aquifer is provided because of the combination of flexible-wall Ksat data at UE12t#1 and high standard error in alpha (van Genuchten et al., 1991).

As discussed in Appendix B, Section 10.3, the harmonic mean provides a lower bound to the effective or upscaled "block averaged" hydraulic conductivity or permeability. Considering that permeability is usually lower in the vertical (z) direction than the horizontal (x) direction in units composed of elongate layers and beds, the ratio of the geometric to harmonic mean provides an estimate of the anisotropy ratio (K_x:K_z).

The anisotropy ratio in tuff confining units, particularly the ATCU and LTCU1, is pivotal in establishing whether groundwater perching can occur in the Tertiary volcanic section of Rainier Mesa. For example, the revised harmonic mean Ksat values in hydrostratigraphic units that compose the tuff confining units range from 0.6 to 7.5 mm/yr, well below a typically recharge rate of 24 mm/yr for Rainier Mesa and well below geometric mean

values in Kwicklis et al. (2008) ranging from 20 to 212 mm/yr. Assuming a low enough fracture permeability, the revised matrix Ksat values for the ATCU and LTCU1 can help justify an assumption of perching conditions sustained at the base of the Tertiary volcanics.

3.4.1.4 Van Genuchten Parameters

Dependence of hydraulic conductivity and capillary pressure on saturation in the matrix continuum is modeled by a van Genuchten function (van Genuchten, 1980). The van Genuchten model formulation for capillary pressure P_c and variably saturated hydraulic conductivity, $K(S)$, as a function of saturation, S, is

$$P_c = \frac{1}{\alpha}\left(S^{-1/m} - 1\right)^{1/n}$$

and

$$K(S) = K_{sat} S^{1/2}\left[1.0 - \left(1.0 - S^{1/m}\right)^m\right]^2$$

where:

P_c = capillary pressure
S = liquid saturation
α = alpha parameter
m =1/(1-n)
$K(S)$ = hydraulic conductivity as a function of saturation
K_{sat} =saturated hydraulic conductivity.

Table 3.3 shows revised van Genuchten model parameters for HSU matrix materials. Differences in van Genuchten parameters derived by Kwicklis et al. (2008) result from combined effects of:

- revised RME#1 stratigraphy (see Section 3.1.4),
- criteria for removing erroneous data (see Appendix B), and
- correction for zeolite and smectite dehydration (see Appendix C).

These differences in van Genuchten parameters will have secondary effects on matrix flow compared to the differences in Ksat.

Table 3.2 Ksat parameters for the matrix continuum of hydrostratigraphic units (HSUs) derived from geometric mean values by Kwicklis et al. (2008) compared to geometric and harmonic mean values derived from rigid-wall data and correlation with alpha. "N" denotes number of data within HSU included in mean calculations.

	Ksat			Ksat						
	N	(m^2)	(mm/yr)	N	(m^2)		(mm/yr)		(m/s)	
		geom	Geom.		Geom	harm	geom	harm	geom	harm
TM-WTA	2	1.20E-14	3,700	2	5.17E-15	1.43E-15	1,600	442	5.07E-8	1.40E-8
TM-LVTA	9	2.90E-14	8,960	7	5.12E-14	2.81E-14	15,900	8,710	5.03E-7	2.76E-7
BRA	1	-	-	1	6.47E-18	6.47E-18	2.0	2.0	6.35E-11	6.35E-11
LVTA1	1	3.53E-14	109,000	2	1.93E-14	1.24E-14	5,990	3,850	1.90E-7	1.22E-7
LTCU	12	6.32E-17	19.5	15	2.43E-17	2.43E-18	7.53	7.52	2.39E-10	2.38E-11
TUBA	1	6.57E-17	20.3	0	-	-	-	-	-	-
OSBCU	20	2.14E-16	66.1	14	1.52E-16	7.52E-18	47.2	2.33	1.50E-9	7.38E-11
RVA	3	1.83E-18	0. 6	7	4.07E-17	3.94E-18	12.6	1.22	3.99E-10	3.87E-10
LTCU1	0	-	-	2	6.16E-18	5.46E-18	1.91	1.69	6.05E-11	5.36E-11
ATCU	5	6.86E-16	212	3	7.23E-18	2.04E-18	2.24	0.633	7.09E-11	2.00E-11
LCA3	1	9.08E-17	28.0	1	9.08E-17	9.08E-17	28.0	28.0	8.88E-10	8.88E-10

Table 3.3 Mean van Genuchten model parameter values for the matrix continuum of hydrostratigraphic units (HSUs) including corrections for zeolite and smectite dehydration described in Appendix C. "N" denotes number of data within HSU included in mean calculations.

HSU	*alpha*			*n*		*m*		Volumetric Water Content		
	N	Geom.		arith	geom	arith	geom	N	arith	
		(m^{-1})	(Pa^{-1})						Residual	Saturated
TM-WTA	2	0.21	2.15E-5	1.57	1.57	0.37	0.36	2	0.015	0.206
TM-LVTA	7	0.622	6.35E-5	2.27	1.68	0.56	0.40	7	0.044	0.353
BRA	0	-	-	-	-	-	-	1	0	0.231
LVTA1	2	0.317	3.23E-5	2.38	2.37	0.58	0.58	2	0.065	0.411
LTCU	10	0.032	3.27E-6	1.62	1.57	0.38	0.36	15	0.012	0.264
TUBA	0	-	-	-	-	-	-	0	-	-
OSBCU	13	0.048	4.88E-6	1.44	1.43	0.30	0.30	14	0	0.258
RVA	5	0.025	2.52E-6	1.66	1.66	0.40	0.40	7	0.002	0.179
LTCU1	2	0.04	4.09E-6	1.27	1.27	0.21	0.21	2	0	0.241
ATCU	2	0.032	3.25E-6	1.25	1.25	0.20	0.20	3	0	0.162
LCA3	1	4.26	4.35E-4	1.28	1.28	0.22	0.22	1	0.010	0.053

3.4.1.5 Compressibility

The NUFT code used for HST modeling accounts for change in storage with pressure as a function of fluid and rock compressibility. Gas and liquid-phase compressibility variations are accounted for with pressure and temperature-dependent models of air and water compressibility. Rock compressibility is a NUFT model parameter (in units of Pa^{-1}) applied to each rock unit.

Compressibility values for hydrogeologic units (HGUs), HSUs, and stratigraphic units (Table 3.4) are inferred from bulk modulus data in the original files used for statistical evaluation of physical properties in Area 12, Nevada National Security Site (Brethauer et al., 1980). Bulk compressibility is the reciprocal of bulk modulus. These data, however, do not span all stratigraphic units in the Tertiary volcanic rocks of Rainier Mesa. Values of compressibility for HST model rock units are based on the Area 12 bulk modulus data where available. For HST model rock units without Area 12 data, compressibility values are inferred by lithology and alteration. For zeolitized or argillized ash fall tuff and welded tuff rock units, compressibility values inferred from the Area 12 data ranges from slightly over one order of magnitude from 7.8e-11 to 1.2e-9 Pa^{-1}.

Fredrich et al (1995) provides a compressibility value of 4e-9 Pa^{-1} for vitric tuffs. A compressibility value of 2e-11 Pa^{-1} for dolomite is inferred from data from Cherry et al., (1968).

3.4.1.6 HST Model Hydraulic Property Data

Where multiple data are available for one HST model rock unit, data values are averaged as appropriate to evaluate HST model hydraulic property data (Table 3.5):

Kx	geometric mean
Kz	harmonic mean
alpha	geometric mean
m	from geometric mean of *n*
S_R	arithmetic mean of θ_R divided by arithmetic mean of θ_S
θ_S	arithmetic mean

Table 3.4 Compressibility values for HGUs, HSUs, and stratigraphic units based on tunnel core data (Brethauer et al., 1980) and compressibility values for vitric tuffs (Fredrich et al., 1995) and dolomite (Cherry et al., 1968). Values in italics are inferred by lithology and alteration. "N" denotes number of compressibility data within rock HST rock units included in mean calculations.

HGU	HSU	Strat	Lithology (NSTec,2007)	Alter-ation	HST rock unit	Compressibility	
						N	(Pa^{-1})
WTA	TM-WTA	Tmr	MWT	Nr	Tmr-M	0	*1e-10*
			DWT	Nr	Tmr-W	0	*8e-11*
VTA	TM-LVTA	Tmr	PWT/NWT	Nr	Tmr-V	0	4e-9
		Post Tbg	BED/RWT	GL	VTA-t		
			NWT/PWT	GL	VTA-n		
WTA	BRA	Tbg	VITROPHYRE	Nr	BRA-VP	0	*8e-11*
			PWT/DWT	ZC	BRA-Z	0	*8e-10*
VTA	LVTA1	Tbgb	BED	GL	LVTA	0	4e-9
TCU	LTCU/ BRCU	Tn4	BED/RWT	ZC	Tn4-Z	59	7.7e-10
			BED/RWT	ZC	Tn4-Z2		
			BED/RWT	OP	Tn4-O		
		Tn3	BED/RWT	ZC	Tn3-Z	34	9.7e-10
			BED/RWT	ZC, AR	Tn3-ZA	6	2.6e-10
		Tub	NWT		Tub-ZA	0	*3e-10*
WTA	TUBA	Tub	DWT	Nr	TUBA	1	7.8e-11
TCU	OSBCU	Ton2	BED/RWT	ZC	Ton2-Z	6	8.3e-11
		Toy	NWT/RWT	AR	Toy-A	1	8.5e-10
			NWT/RWT	ZC	Toy-Z	1	6.7e-10
		Ton1	BED/RWT	AR	Ton1-A	0	*9e-10*
		To	BED/RWT	AR	To-A	0	*9e-10*
			PWT BED/RWT	AR, ZC	To-AZ	0	*5e-10*
WTA	RVA	Tor	PWT/MWT	Nr	Tor-M	0	*1e-10*
TCU		To	BED	ZC	RVA-Z	0	*8e-10*
WTA		Tot	PWT?	DV	RVA-M	0	*1e-10*
			DWT	DV	RVA-W	0	*8e-11*
TCU	LTCU1	Tot	PWT/NWT	ZC	LTCU1	1	1.2e-9
	ATCU	To	BED/RWT	AR	ATCU	0	*1e-9*
		Tl	PCL	AR	Tl-A	0	*1e-9*
CA	LCA3	Pz	breccia	AR	LCA-B	0	*1e-9*
			matrix	AR	LCA-M	0	2e-11

Table 3.5 Hydraulic property data for HST model rock units based on HSU, stratigraphy, lithology and alteration (NSTec, 2007) and composite RME#1 and UE12t#1 data (Kwicklis et al., 2008). Data source shaded as: RME#1 (yellow), UE12t#1 (blue), and both RME#1 and UE12t#1 (green). "N" denotes number of data within HST rock unit included in mean calculation. "na" denotes "not accurate."

HGU	HSU	Strat	Lithology	Alteration	HST Rock Unit	N	Ksat (m^2)		*alpha* (Pa^{-1}) geom	$m = 1-\frac{1}{n}$	S_R	θ_S
							Geom	harm				
WTA	TM-WTA	Tmr	MWT	nr	Tmr-M	1	3.7E-14	3.7E-14	4.3E-5	0.32	0.00	0.322
			DWT	nr	Tmr-D	1	7.3E-16	7.3E-16	1.2E-5	0.40	0.33	0.090
VTA	TM-LVTA	Tmr	PWT/NWT	nr	Tmr-V	2	2.0E-14	2.0E-14	3.4E-5	0.61	0.19	0.264
		Post Tbg	BED/RWT	GL	VTA-t	2	1.5E-13	6.5E-14	9.0E-5	0.53	0.08	0.430
			NWT/PWT	GL	VTA-n	3	4.6E-14	2.5E-14	7.7E-5	0.59	0.12	0.361
WTA	BRA	Tbg	VITROPHYRE	nr	BRA-VP	1	na	na	na	na	0.0	0.023
			PWT/DWT	ZC	BRA-Z	1	6.5E-18	6.5E-18	1.3E-6	0.21	0.0	0.239
VTA	LVTA1	Tbgb	BED	GL	LVTA	2	1.9E-14	1.2E-14	3.2E-5	0.58	0.06	0.411
TCU	LTCU/BRCU	Tn4	BED/RWT	ZC	Tn4-Z	6	4.4E-17	3.0E-17	3.6E-6	0.25	0	0.279
			BED/RWT	ZC	Tn4-Z2	1	5.0E-14	5.0E-14	3.8E-6	0.66	0.64	0.169
			BED/RWT	OP	Tn4-O	1	1.0E-13	1.0E-13	5.6E-5	0.43	0.25	0.310
		Tn3	BED/RWT	ZC	Tn3-Z	4	1.9E-18	1.7E-18	7.8E-7	0.35	0	0.250
			BED/RWT	ZC, AR	Tn3-ZA	1	6.7E-19	6.7E-19	5.7E-7	0.35	0	0.306
		Tub	NWT		Tub-ZA	2	1.2E-18	9.4E-19	6.8E-7	0.35	0	0.252
WTA	TUBA	Tub	DWT	nr	TUBA	1	1.8E-18	1.7E-18	8.6E-7	0.40	0	0.039
TCU	OSBCU	Ton2	BED/RWT	ZC	Ton2-Z	3	2.5E-17	2.0E-17	2.3E-6	0.35	0	0.265
		Toy	NWT/RWT	AR	Toy-A	1	3.7E-14	3.7E-14	4.3E-5	0.20	0	0.342
			NWT/RWT	ZC	Toy-Z	5	5.8E-17	2.5E-17	2.8E-6	0.34	0	0.289
		Ton1	BED/RWT	AR	Ton1	2	1.3E-17	2.0E-18	2.2E-7	0.21	0	0.222
		To	BED/RWT	AR	To-A	2	1.2E-13	1.2E-13	5.8E-5	0.18	0	0.230
			PWT BED/RWT	AR, ZC	To-AZ	2	8.1E-18	3.8E-18	8.5E-7	0.31	0	0.145
WTA	RVA	Tor	PWT/MWT	nr	Tor-M	1	3.8E-15	3.8E-15	2.3E-5	0.31	0	0.268
TCU		To	BED	ZC	RVA-Z	1	4.3E-17	4.3E-17	2.0E-6	0.45	0	0.135
WTA		Tot	PWT?	DV	RVA-M	2	4.2E-16	4.1E-16	2.8E-6	0.42	0	0.274
			DWT	DV	RVA-W	3	1.8E-18	1.7E-18	8.7E-7	0.40	0	0.100
TCU	LTCU1	Tot	PWT/NWT	ZC	LTCU1	2	6.2E-18	5.5E-18	4.1E-6	0.21	0	0.236
	ATCU	To	BED/RWT	AR	ATCU	2	1.5E-18	1.4E-18	2.2E-6	0.17	0	0.127
		Tl	PCL	AR	Tl-A	1	1.6E-16	1.6E-16	4.9E-6	0.22	0	0.234
CA	LCA3	Pz	Breccias	AR	LCA-B	1	inacc	inacc	inacc	Inac	0	0.151
			Matrix	AR	LCA-M	1	9.1E-17	9.1E-17	4.3E-4	0.22	0.20	0.053

3.4.1.7 Matrix Ksat and Porosity for LCA3

While the LCA3 is not present in the CLEARWATER and WINESKIN HST model domains, discussion of LCA3 rock properties is included here for completeness in relation to flow and transport modeling at RM. Thordarson (1965) provides permeability and porosity

ranges for LCA3 rocks based on four samples. The permeability and porosity ranges are lower than the LCA3 parameter values based on a single datum from Kwicklis et al. (2008). Therefore, the Thordarson (1965) data could substantiate use of lower matrix permeability and porosity values in LCA3 model units. Table 3.6 compares LCA3 porosity and permeability data. The Thordarson (1965) permeability range of 1.0 to 3.0 mm/yr for the LCA3 matrix rocks is well below a typical recharge rate of 24 mm/yr and the Kwicklis et al. (2008) permeability of 28.0 mm/yr.

Table 3.6 Comparison of permeability and porosity values for LCA3 matrix units from Kwicklis et al. (2008) and Thordarson (1965).

Unit	Permeability						Porosity	
	Kwicklis et al. (2008)			Thordarson (1965)			Kwicklis et al. (2008)	Thordarson (1965)
	(m^2)	(mm/yr)	(m/s)	(m^2)	(mm/yr)	(m/s)		
LCA3 matrix	9.08e-17	28.0	8.88e-10	3.4e-18 to 9.6e-18	1.0 to 3.0	3.3e-11 to 9.4e-11	0.085	0.006 to 0.011

3.4.2 Fracture Properties

3.4.2.1 Permeability and Porosity

Wide ranges of permeability and porosity are inferred from the limited fracture property data pertinent to Rainier Mesa. Stoller-Navarro (2008a) provides permeability ranges, and Stoller-Navarro (2008b) provides effective porosity ranges that depend on whether fracture or porous flow is expected to be dominant. According to hydrogeological studies of Rainier Mesa, bulk flow in WTA and TCU hydrogeologic units is dominated by fracture flow, whereas bulk flow in VTA hydrogeologic units is dominated by porous (or interstitial) flow (Thordarson, 1965; Fenelon et al., 2008; Townsend, 2008).

The "pumping-scale" permeability range $4.2e^{-13}$ to $1.4e^{-11}$ m^2 for WTA based on RM/SM area data (Stoller-Navarro, 2008a) is much higher than typical WTA matrix permeabilities on the order of 10^{-18} m^2. The higher pumping scale permeability relative to matrix permeability in the WTA indicates fracture flow can be expected to dominate bulk flow in most WTA hydrogeologic units and subunits.

The "pumping-scale" permeability range of $7.4e^{-18}$ to $2.6e^{-11}$ m^2 for the TCU based on NNSS area data (Stoller-Navarro, 2008a) spans a large permeability range, from a low permeability typical of matrix permeability for the TCU (on the order of 10^{-17} m^2 or less) to a high permeability typical of fracture permeability for a WTA. This wide range indicates either matrix or fracture flow can dominate flow at different spatial scales within the TCU depending on location and test conditions. The N-Tunnel flow and transport model

predicts a maximum fault flow permeability of $6.7e^{-13}$ m^2 (Kwicklis et al., 2009). Considering fault flow permeability is expected to be higher than fracture flow permeability, $6.7e^{-13}$ m^2 is a more reasonable upper limit to fracture flow permeability for TCU units compared to the $2.6e^{-11}$ m^2 given as maximum TCU permeability by Stoller-Navarro (2008a). Table 3.7 compiles fracture porosity and permeability ranges for HSUs and stratigraphic units. Fracture permeability ranges are based on ranges of pumping scale permeability in HGUs (Stoller-Navarro, 2008a) with comparison to matrix permeability data in the same HGUs. Flow calibration for concurrent N and T-Tunnel flow and transport modeling should further constrain fracture permeability ranges.

Prothro (2008) gives values of average open fracture spacing of 5.0 m and average aperture of 1.1 mm based on four boreholes in the TCU of Yucca flat. An average fracture porosity of 0.00022 (2.2e-4) is derived from these values. Based on fracture spacing and aperture data from individual boreholes, TCU fracture porosity values vary from 5.0e-5 to 5.7e-4. Prothro (2008) did not observe open fractures in the ATCU, suggesting that fracture permeability and porosity, if non-zero, are very low in the ATCU relative to the LTCU and OSBCU.

3.4.2.2 Van Genuchten Parameters

The dependency of hydraulic conductivity and capillary pressure on saturation in the fracture continuum is modeled by a van Genuchten function (van Genuchten, 1980) except in void space between chimney or cavity rubble, where unsaturated hydraulic conductivity is assumed linearly dependent on saturation, and capillary pressure is set to zero. Fracture van Genuchten model parameters are based on values used for fractures in flow and transport models (Ed Kwicklis and Matt Reeves, personal communications). No data for fracture van Genuchten parameters specific to Rainier Mesa are available.

3.4.3 MGCU and LCCU1 Rock Properties

Rock properties for clastic and granitic confining units are needed for the WINESKIN HST model because the WINESKIN test was located within 2Rc of the Mesozoic granitic confining unit (MGCU) and the lower clastic confining unit (LCCU1), assuming a cavity radius (Rc) of 72 m as described in Section 2.7.2. The SZ model treats the MGCU as a no-flow (zero permeability) unit. However, test effects can be expected to enhance fracture permeability within 2 to 3 Rc (U.S. Congress, 1989). Based on Rc calculated from the maximum of the yield range for the WINESKIN test (Pawloski, 1999; USDOE, 2015), the test-altered zones for the WINESKIN HST extend into both the LCCU1 and MGCU.

Table 3.7 Ranges of rock unit fracture permeability and porosity. Fracture permeabilities are based on difference between HGU total permeability ranges (Stoller-Navarro, 2008a) and values of HST rock unit matrix permeability. Fracture porosities for WTA and LCA3 HGUs are based on fracture porosities for Yucca Flat hydrogeologic units (HGUs) (Stoller-Navarro, 2008a). Fracture porosities for TCU units are based on mean aperture and fracture spacing for TCU in Yucca Flat (Prothro, 2008). Values of zero minimum and possible zero maximum fracture porosity and permeability in ATCU and LCA-B units based on no observations of open fractures (Prothro, 2008).

HGU	HSU	Strat	Lith, Alt	Permeability (m^2)					Fracture Porosity		
				Pumping Scale (Stoller-Navarro,2008a)		Matrix (geom. mean)	Fracture				
				Min	Max		Min	Max	Min	Max	Mode
WTA	TM-WTA	Tmr	NWT,GL	4.2E-13	1.4E-11	3.7E-14	3.8E-13	1.4E-11	1e-4	6e-3	3e-3
			NWT,P			7.3E-16	4.2E-13	1.4E-11			
VTA	TM-LVTA	Tmr	vitric	?	?	2.0E-14	0.0	>0?	0	>0?	0?
		Post Tbg	vitric			1.5E-13					
			NWT			4.6E-14					
WTA	BRA	Tbg	zeol	4.2E-13	1.4E-11	6.5E-18	4.2E-13	1.4E-11	1e-4	6e-3	3e-3
			vphere			inacc	4.2E-13	1.4E-11			
VTA	LVTA1	Tbgb	vitric	?	?	5.3E-14	0.0	>0?	0	>0?	0?
TCU	LTCU/ BRCU	Tn4	zeol	7.4E-18	2.6E-11	4.4E-17	0.0	6.7E-13	5e-5	6e-4	2.2e-4 (ave)
			zeol			5.0E-14	0.0	6.7E-13			
			opal			1.0E-13	0.0	6.7E-13			
		Tn3	zeol			1.9E-18	5.5E-18	6.7E-13			
			zeol,arg			6.7E-19	6.7E-18	6.7E-13			
		Tub	zeol,arg			1.2E-18	6.2E-18	6.7E-13			
WTA	TUBA	Tub	DWT	4.2E-13	1.4E-11	1.8E-18	4.2E-13	1.4E-11	1e-4	6e-3	3e-3
TCU	OSBCU	Ton2	zeol	7.4E-18	2.6E-11	2.5E-17	0.0	6.7E-13	5e-5	6e-4	2.2e-4 (ave)
		Toy	arg			3.7E-14	3.7E-14	6.7E-13			
			zeol			5.8E-17	0.0	6.7E-13			
		Ton1	zeol			1.3E-17	0.0	6.7E-13			
		To	arg			1.2E-13	0.0	6.7E-13			
			arg,zeol			8.1E-18	7.0E-19	6.7E-13			
WTA	RVA	Tor	NWT	4.2E-13	1.4E-11	3.8E-15	4.2E-13	1.4E-11	1e-4	6e-3	3e-3
TCU		To	zeol	7.4E-18	2.6E-11	4.3E-17	0.0	6.7E-13	?	?	2.2e-4
WTA		Tot	MWT	4.2E-13	1.4E-11	4.2E-16	4.2E-13	1.4E-11	1e-4	6e-3	3e-3
			DWT			1.8E-18	4.2E-13	1.4E-11			
TCU	LTCU1	Tot	LTCU1	7.4E-18	2.6E-11	6.2E-18	4.8E-18	6.7E-13	?	?	2.2e-4
	ATCU	To	arg	?	?	1.5E-18	0	0?	0	0?	0?
		Tl	arg	?	?	1.6E-16	0	0?	0	0?	0?
CA	LCA3	Pz	breccia	?	?	inacc	0	0?	0	0?	0?
			matrix	1.3E-15	1.5E-12	9.1E-17	1.3E-15	1.5E-12	2e-4	2e-2	5e-3

MCGU rock properties are based on a variety of data. Boardman et al. (1965) report pre-test permeability for the HARD HAT test in "highly jointed and fractured" granitic rock on the order of tenths to a few millidarcies (1 millidarcy = 9.9e-16 m^2). Murray (1980) reports permeabilities for Climax Stock granodiorite of 10-4 to 10-1 darcies (1 darcy = 9.9e-13 m^2) in moderately to highly fractured zones and less than 10^{-9} darcies (9.9e-22 m^2) in intact rock. Stoller-Navarro (2006a) reports a mean permeability of 3.2e-3 m/d (3.8e-15 m^2 at 20°C) based on one pumping-scale datum. Boardman et al. (1964) reports porosity of 0.9% for core data. Stoller-Navarro (2007b) reports porosity of 1.94+/-1.48%. Stoller-Navarro (2008b) suggests a fracture porosity range of 0.001% to 0.02% for the MGCU. Based on these data, pre-test MGCU permeability and porosity are assigned values of 1e-21 m^2 and 0.009 for the matrix and 3.8e-15 m^2 and 0.0001 for the fractures. The very low MGCU matrix permeability of 1e-21 m^2 supports the concept of no flow in the MGCU (Section 1.3.2) if fracture permeability is exceptionally low also.

LCCU1 rock properties are treated as no flow except within the test-altered zones. Stoller-Navarro (2008a) reports mean hydraulic conductivity of 6.2e-3 m/d (7.3e-15 m^2 at 20°C) for the LCCU based on one pumping-scale datum. Laboratory-scale data yield a mean hydraulic conductivity of 2.8e-8 m/d (3.1e-20 m^2 at 20°C). Porosity range is 3.26+/-2.52 percent (Stoller-Navarro, 2008a). Based on these data, mean pre-test LCCU1 matrix permeability and porosity are assigned values of 3.1e-20 m^2 and 0.03, respectively.

3.4.4 Test-Altered Rock Permeability and Porosity

Fracture permeability and porosity of test-altered rocks are key parameters for understanding flow and radionuclide mobility from initial radionuclide source zones. Fractures dominate flow in unaltered TCU (Thordarson, 1965; Carroll, 1990; Fenelon et al., 2008; Townsend, 2008) and, subsequently, should dominate flow in test-altered zones with test-enhanced fracture permeability. Unfortunately, no quantitative information on fracture permeability and porosity of test-altered rocks is available for test-altered zones of Rainier Mesa tests. The most quantitative information about the spatial distribution of fracture permeability in test-altered rock is found in post-test studies of the HARD HAT and PILE DRIVER tests in granitic rocks.

Based on field-scale measurements in boreholes located adjacent to the HARD HAT test, Boardman and Skrove (1966) report fracture permeabilities on the order of 0.1 to 3 darcies (1 darcy = 9.87e-13 m^2) decreasing radially between 125 to 215 feet (38.5 to 65.5 m) from the working point. Based on the Rc value of 19.2 m for the HARD HAT test given in Boardman et al. (1964), the zone of test-induced enhanced permeability extends from 2.0 to 3.4 Rc. Boardman (1966) reports permeability of 7 to 15 millidarcies (1 millidarcy = 9.87e-16 m^2) in "friable" rock within 4 m of the HARD HAT cavity edge. Stoller-Navarro (2007b) summarizes permeability data from the HARD HAT test (Figure 3.4).

While chimney property studies (e.g., Patch and Lie, 1975) have been performed on two Rainier Mesa tests, MING BLADE and DINING CAR, these studies did not produce quantitative direct measurements of bulk permeability and porosity for the chimney and cavity.

For the PILE DRIVER test, Borg (1971) reports shock-induced microfracturing to 2.7 Rc and "extensive fracturing" to 1.3 Rc. Enhanced permeability from microfracturing is estimated at greater than 0.1 darcy. These radial limits correspond to distances given in Borg (1973), which describes a Rc of 40 m, a pulverized zone from 40 to 52 m, and a fractured zone from 52 to 110 m for the PILE DRIVER test.

Fracture porosity in test-altered zones is not well constrained. Nilson (1989) reports fracture porosity induced by a nuclear explosion is 0.001 or less. However, effective porosity could be higher than 0.001 in test-altered rocks closest to the cavity edge.

Several studies suggest that rocks closest to the cavity edge, particularly below the cavity, could be more extensively fractured or crushed. For the HARD HAT test, Short (1966) reports porosity ranging between 0.095 to 0.112 for three samples from "strongly shocked material just below the base of the explosion cavity …differentiated from all samples beyond the innermost 3.0 to 4.5 meters around the cavity by its chalky white appearance and notable reduction in density." These samples correspond to "high porosity material below cavity" noted in Figure 3.4 and to "friable" rock within 4 m of the HARD HAT cavity edge reported by Boardman (1966). For the PILE DRIVER test, Borg et al. (1976) states that a zone of highly crushed rock extends to a distance of about 1.3 cavity radii. For the CHESHIRE test situated in rhyolitic lavas, Pawloski et al. (2001) calibrated melt glass zone permeability of 4e-14 m^2 (3.9e-7 m/s) and crush zone permeability 4e-12 m^2 (3.9e-5 m/s) to temperature data. This study refers to a "crushed zone" to distinguish test-altered in-situ rocks with the highest alteration of fracture and matrix properties outside the cavity and chimney.

3.5 HST Model Flow Properties

The CLEARWATER and WINESKIN HST model flow properties are developed from matrix and fracture property data (Section 3.4) and calibration to saturation (Section 3.6) and potentiometric head (Section 3.7). The flow properties listed in this section represent a base case set of parameters for the different rock types used in the HST models. Section 3.10 discusses uncertainty of flow properties.

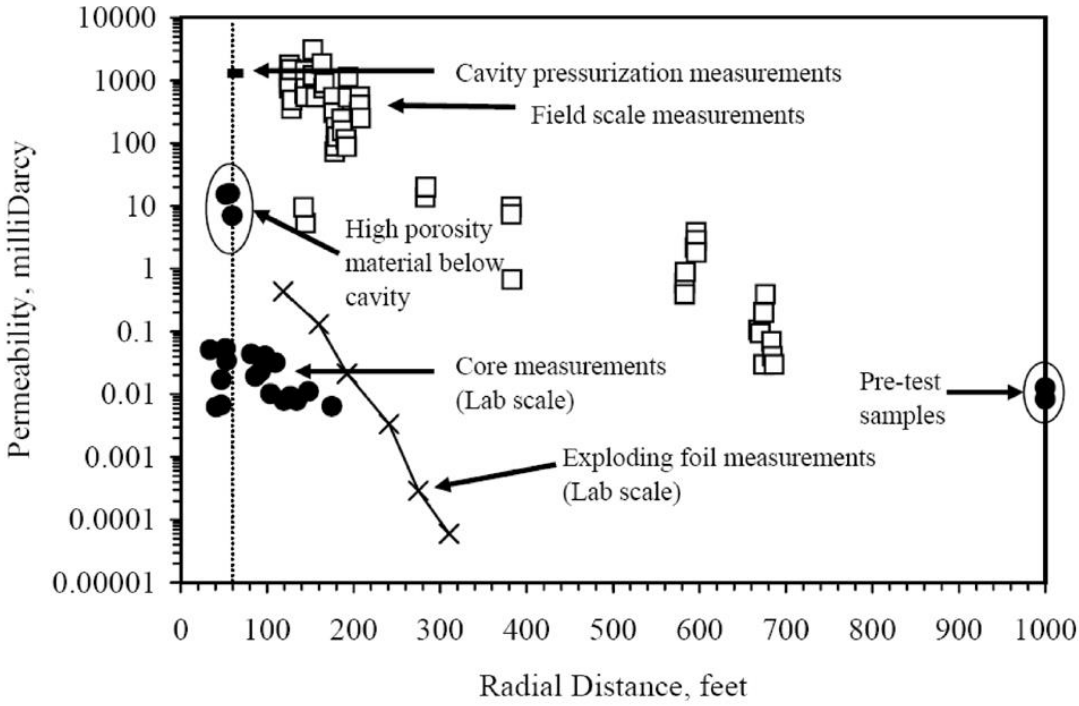

Figure 3.4 Permeability data from the HARD HAT test (Stoller-Navarro, 2007).

3.5.1 Rock Type Names

Rock type names are needed to identify zones in the HST models corresponding to different rock types with different properties based on hydrostratigraphy (Section 2.3), fracture and matrix continua (Section 2.5 and 3.4), and test-altered zones (Section 2.7). Rock type names are developed with a convention as follows:

continuum - altered zone - HSU

where:

continuum =	m (matrix) or f (fracture)
altered zone =	blank (not altered), CH (chimney), CAV (cavity), CRUSH (crush zone), MGZ (melt glass zone), 1.5Rc (between crush zone and 1.5Rc), 2Rc (between 1.5Rc and 2Rc), 2.5Rc (between 2Rc and 2.5Rc), and 3Rc (between 2.5Rc and 3Rc).
HSU =	hydrostratigraphic units described in NSTec (2007).

3.5.2 Matrix Continuum

Model flow properties for the matrix continuum of in-situ and test-altered rock units are derived from the matrix property data (Section 3.4.1) and the conceptual model for test-altered zones (Section 2.7).

The "Length" parameter corresponds to a representative length of a hydraulic connection for matrix flow within a matrix element to the edge of fracture element as derived from fracture spacing or block radius. The "Length" parameter is set as follows:

- 6 m for tuff confining units based on mean fracture spacing of 12 m.
- 6 m as default value in matrix flow dominated units such as vitric tuff aquifers.
- 0.5 m in welded tuff aquifers based on 1 m size blocks
- 0.25 m in welded tuff or zeolitized tuff chimney rubble
- 0.1, 1, and 2 m in the crush zone, 1.5Rc, and 2Rc based on test-induced fracturing and microfracturing.

Matrix porosity is an *effective* variably saturated matrix flow porosity derived largely from reanalysis of matrix property data of Kwicklis et al. (2008) as detailed in Appendix B. Matrix "Kx" and "Kz" are saturated hydraulic conductivity (Ksat) in the lateral direction and vertical directions, as largely derived from geometric and harmonic mean data values (Section 3.4.1.3). Van Genuchten parameters of residual saturation (Sr) and the fitting parameters "m" and "alpha" are derived from matrix property data (Section 3.4.1.3) with corrections to data from Kwicklis et al. (2008) as described in Appendix B.

Table 3.8 compiles base case CLEARWATER and WINESKIN HST model matrix continuum flow properties. Matrix flow properties have not been changed for uncertainty analysis assuming that matrix properties are relatively well constrained by site-specific data (Section 3.4.1) compared to other flow and transport properties. Moreover, the TCU fracture and matrix model properties are consistent with previous hydrogeological observations in the TCU that fracture flow is dominant and matrix flow is insignificant (Thordarson, 1965; Carroll, 1990; Fenelon et al., 2008; Townsend, 2008) as discussed in Section 2.6. Figure 3.5 shows base case matrix permeability for the CLEARWATER HST model in hydraulic conductivity units.

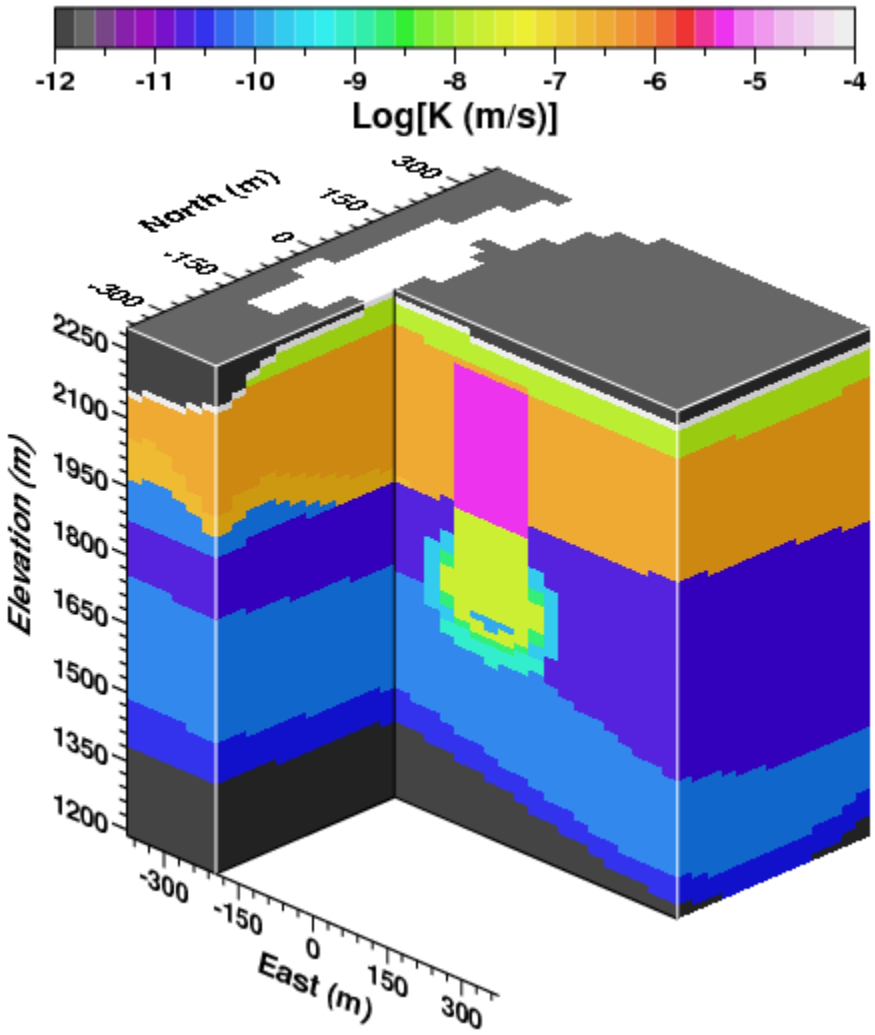

Figure 3.5 Base case matrix permeability distribution for CLEARWATER HST model. The model Rc of 72 m is derived from maximum announced yield (USDOE, 2015) and Pawloski (1999) as detailed in Section 2.7.2.

Table 3.8 Base-case matrix continuum flow properties.

Rock_type	Length (m)	Porosity	Kx (m/s)	Kz (m/s)	Sr	m	alpha (m^{-1})
ATM	6	1	0	1.00E-01	0	-1	-1
m-TMWTA	0.5	0.206	5.07E-08	1.40E-08	7.28E-02	3.60E-01	2.10E-01
m-BRA	0.5	0.231	6.35E-11	6.35E-11	0	4.00E-01	2.47E-02
m-SWA	0.5	0.231	6.35E-11	6.35E-11	0	4.00E-01	2.47E-02
m-RVA	0.5	0.179	4.00E-10	3.87E-11	0	4.00E-01	2.47E-02
m-CH-WTA	0.25	0.206	5.07E-08	1.40E-08	7.28E-02	3.60E-01	2.10E-01
m-TMLVTA	6	0.353	5.02E-07	2.76E-07	1.25E-01	4.00E-01	6.17E-01
m-AA	6	0.353	5.02E-07	2.76E-07	1.25E-01	4.00E-01	6.17E-01
m-LVTA1	6	0.411	1.89E-07	1.89E-07	1.58E-01	5.80E-01	3.15E-01
m-LVTA2	6	0.411	1.89E-07	1.89E-07	1.58E-01	5.80E-01	3.15E-01
m-CH-VTA	0.25	0.353	5.02E-06	5.02E-06	1.25E-02	4.00E-01	6.17E-01
m-UTCU1	6	0.264	2.39E-10	2.39E-10	4.55E-02	3.60E-01	3.20E-02
m-LTCU	6	0.264	2.38E-10	2.38E-11	4.55E-02	3.60E-01	3.20E-02
m-1.5RC-LTCU	1	0.264	2.38E-08	2.38E-09	4.55E-02	3.60E-01	3.20E-02
m-2RC-LTCU	2	0.264	2.38E-09	2.38E-10	4.55E-02	3.60E-01	3.20E-02
m-CH-TCU	0.25	0.224	2.38E-08	2.38E-08	4.55E-02	3.60E-01	3.20E-02
m-OSBCU	6	0.258	1.49E-09	7.38E-11	0	3.00E-01	4.78E-02
m-1.5RC-OSBCU	1	0.258	1.49E-07	7.38E-09	0	3.00E-01	4.78E-02
m-2RC-OSBCU	2	0.258	1.49E-08	7.38E-10	0	3.00E-01	4.78E-02
m-ATCU	6	0.162	7.09E-11	2.00E-11	0	2.00E-01	3.18E-02
m-1.5RC-ATCU	1	0.162	7.09E-09	2.00E-09	0	2.00E-01	3.18E-02
m-2RC-ATCU	2	0.162	7.09E-10	2.00E-10	0	2.00E-01	3.18E-02
m-LCCU1	6	0.241	6.04E-11	5.36E-11	0	2.10E-01	4.00E-02
m-1.5RC-LCCU1	1	0.241	6.04E-09	5.36E-09	0	2.10E-01	4.00E-02
m-2RC-LCCU1	2	0.241	6.04E-10	5.36E-10	0	2.10E-01	4.00E-02
m-MGCU	6	0.03	6.04E-11	5.36E-11	0	2.10E-01	4.00E-02
m-1.5RC-MGCU	1	0.03	6.04E-09	5.36E-09	0	2.10E-01	4.00E-02
m-2RC-MGCU	2	0.03	6.04E-10	5.36E-10	0	2.10E-01	4.00E-02
m-CAV	0.25	0.224	2.38E-08	2.38E-08	4.55E-02	3.60E-01	3.20E-02
m-CAV-LTCU	0.25	0.224	2.38E-08	2.38E-08	4.55E-02	3.60E-01	3.20E-02
m-MGZ	0.25	0.132	1.19E-10	1.19E-10	4.55E-02	3.60E-01	3.20E-02
m-CRUSH	0.1	0.259	2.38E-08	2.38E-08	4.55E-02	3.60E-01	3.20E-02

3.5.3 Fracture Continuum

Model flow properties for the fracture continuum of in-situ and test-altered rock units are derived from the fracture property data (Section 3.4.2), properties compiled by Stoller-Navarro (2008a) and summarized in Appendix A, and the conceptual model for test-altered zones (Section 2.7).

The "Length" parameter corresponds to a representative length of hydraulic connection for fracture flow within a fracture element to the edge of a matrix element, as derived from fracture half-aperture or void space size. The "Length" parameter is derived as follows:

- 0.0005 m for welded tuff, based on half of the fracture aperture of 0.001 m,
- 0.0011 m for tuff confining units, based on half of the fracture aperture of 0.0022 m,
- 0.0011 m for fractures in altered zones, based on a concept of similar sized fractures in the altered zones compared to in-situ rock,
- 0.001 m for void space in the cavity and chimney rubble considering close proximity of void water to the rubble blocks, and
- 0.05 m for the half-thickness of melt glass between rubble blocks in the melt glass zone.

Fracture area per unit volume (Area/Volume) refers to the surficial area of the fracture continuum per cubic meter. The fracture Area/Volume is derived as follows:

- 6 m^2/m^3 in welded tuff aquifers based on three-dimensional fracture spacing of 1 m,
- 0.2 m^2/m^3 in tuff confining units based on two-dimensional fracture-spacing of 12 m in the vertical and 50 m in the horizontal,
- Larger values of 0.4 to 4.4 m^2/m^3 in test-altered zones within tuff confining units outside the cavity to account for test-induced fracturing, and
- 12 m^2/m^3 in rubble to represent the surface area of rubble blocks per unit volume.

Fracture porosity in in-situ fractured rocks is based on data from Stoller-Navarro (2008a) and Prothro (2008). Fracture porosity values given for matrix-flow dominated rock units, such as vitric tuffs and alluvial aquifers, are scaled with hydraulic conductivity to give equivalent matrix flow in the fracture elements. Fracture porosity for chimney rubble is set to 0.15 to represent void space between rubble blocks. Fracture porosity in the melt glass zone is set to 0.068 in conjunction with 0.132 matrix porosity in the melt glass zone to produce 0.200 total melt glass zone porosity, as calibrated in Pawloski et al. (2001) for the CHESHIRE test situated in rhyolitic lava.

Fracture "Kx" and "Kz" are saturated hydraulic conductivity (Ksat) in the lateral direction and vertical directions, with values based on ranges given in Stoller-Navarro (2008a) and calibration to saturation and potentiometric head. Van Genuchten parameters of residual saturation (Sr) and the fitting parameters "m" and "alpha" are derived fracture properties given by E. Kwicklis (written communication, 2010) or from matrix properties in matrix-flow dominated rock types.

Table 3.9 compiles fracture continuum flow properties for the base-case CLEARWATER and WINESKIN HST models. Future uncertainty analysis may include variation of fracture permeability in tuff confining units, which is the flow parameter that dominates advective

flow between test locations and the SZ model interfaces. Figure 3.6 shows base case fracture permeability for the CLEARWATER HST model.

Table 3.9 Base-case fracture continuum flow properties. Where "Pc=0" is specified, capillary pressure is set to zero, and a van Genuchten model is not used, so "m" and "alpha" parameters not relevant.

Rock Type	Length (m)	Area/Volume (m^2/m^3)	Porosity	Kx (m/s)	Kz (m/s)	Sr	m	alpha (m^{-1})
f-TMWTA	0.0005	6	0.003	4.02E-06	4.02E-06	1.00E-02	6.30E-01	9.79E+00
f-BRA	0.0005	6	0.003	4.12E-06	4.12E-06	1.00E-02	6.30E-01	1.27E+01
f-SWA	0.0005	6	0.003	4.12E-06	4.12E-06	1.00E-02	6.30E-01	1.27E+01
f-RVA	0.0005	6	0.003	4.12E-06	4.12E-06	1.00E-02	6.30E-01	1.27E+01
f-TMLVTA	0.0018	0.2	0.000353	5.02E-10	2.76E-10	1.25E-01	4.00E-01	6.17E-01
f-AA	0.0018	0.2	0.000353	5.02E-10	2.76E-10	1.25E-01	4.00E-01	6.17E-01
f-LVTA1	0.0022	0.2	0.000411	1.89E-10	1.89E-10	1.58E-01	5.80E-01	3.15E-01
f-LVTA2	0.0022	0.2	0.000411	1.89E-10	1.89E-10	1.58E-01	5.80E-01	3.15E-01
f-LTCU	0.0011	0.2	0.00022	1.00E-09	1.00E-09	1.00E-02	6.30E-01	1.27E+01
f-OSBCU	0.0011	0.2	0.00022	1.00E-09	1.00E-09	1.00E-02	6.30E-01	1.27E+01
f-ATCU	0.0011	0.2	0.00022	1.18E-11	1.18E-11	1.00E-02	6.30E-01	1.27E+01
f-LCCU1	0.0011	0.2	0.00022	1.18E-11	1.18E-11	1.00E-02	6.30E-01	1.27E+01
f-MGCU	0.0011	0.2	0.00022	1.18E-11	1.18E-11	1.00E-02	6.30E-01	1.27E+01
f-3RC	0.0011	0.2	0.00022	1.00E-07	1.00E-07	1.00E-02	6.30E-01	1.27E+01
f-2.5RC	0.0011	0.4	0.00044	3.20E-07	3.20E-07	1.00E-02	6.30E-01	1.27E+01
f-2RC	0.0011	0.8	0.00088	1.00E-06	1.00E-06	1.00E-02	6.30E-01	1.27E+01
f-1.5RC	0.0011	1.6	0.00176	3.20E-06	3.20E-06	1.00E-02	6.30E-01	1.27E+01
f-CRUSH	0.0011	4.4	0.0048	3.90E-05	3.90E-05	1.00E-02	6.30E-01	1.27E+01
f-CAV	0.001	12	0.15	1.00E-03	1.00E-03	1.00E-02	Pc=0	Pc=0
f-MGZ	0.05	12	0.068	3.90E-07	3.90E-07	1.25E-01	4.00E-01	6.17E-01
f-CH-WTA	0.001	12	0.15	1.00E-03	1.00E-03	0	Pc=0	Pc=0
f-CH-TCU	0.001	12	0.15	1.00E-03	1.00E-03	0	Pc=0	Pc=0
f-CH-VTA	0.001	12	0.05	7.11E-07	7.11E-07	0	4.00E-01	6.17E-01

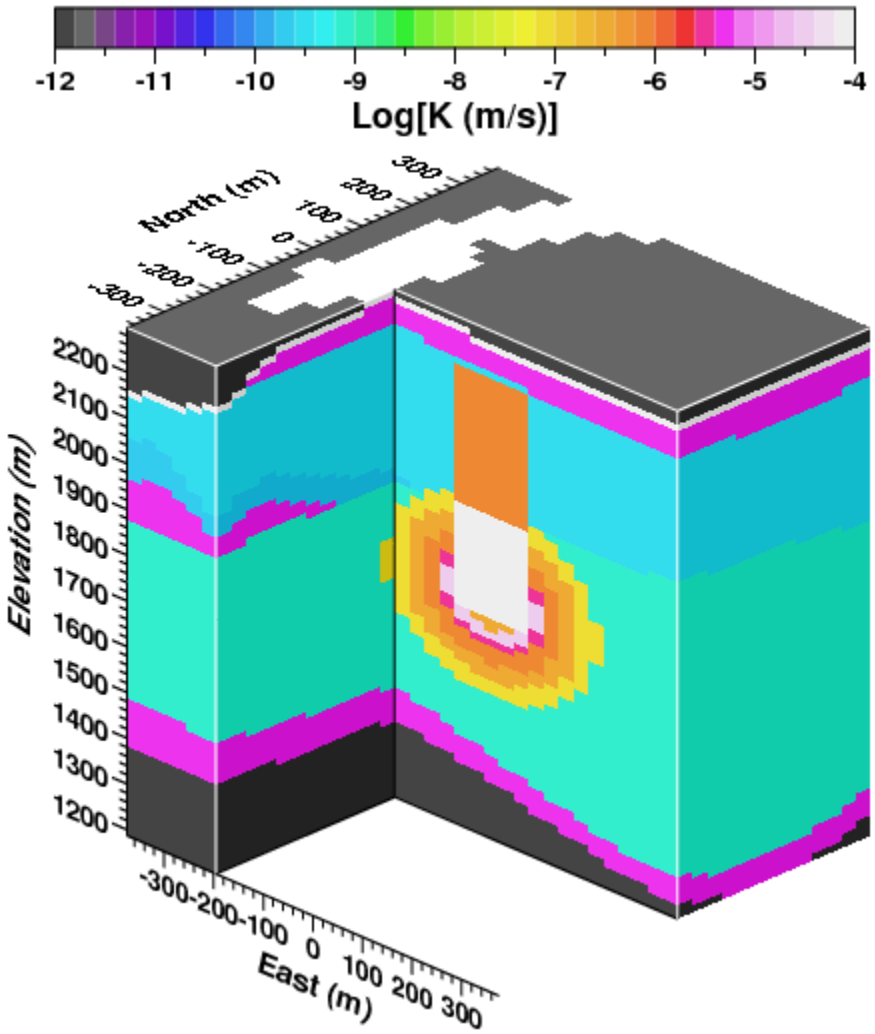

Figure 3.6 Base case fracture permeability for the CLEARWATER HST model. The model Rc of 72 m is derived from maximum announced yield (USDOE, 2015) and Pawloski (1999) as detailed in Section 2.7.2.

3.6 Saturation

The dual-continuum CLEARWATER and WINESKIN HST models simulate saturation in the fracture and matrix continua independently within each mesh element. For example, in modeling variably saturated conditions within a mesh element, the matrix and fracture saturations are usually different except where matrix flow is expected to dominate groundwater flow, such as in vitric tuffs. In vitric tuffs, the dual-continuum flow and transport models assume purely porous or interstitial flow (no fracture flow) such that the modeled matrix and fracture properties and saturations are equivalent to a matrix only or interstitial flow process. In zeolitic tuffs where fracture-matrix interactions are accounted

for and matrix permeability is very low, it is possible for the matrix to be saturated, and the fracture to be unsaturated.

In the unsaturated zone, data indicate matrix saturations close to 1.0 in the tuff confining units and within range of 0.3 to 0.8 in vitric tuff aquifers. Fracture saturation in the tuff confining units can be highly variable in the upper 120 m (400 feet) of zeolitized tuffs above the perched zone water table (Thordarson, 1965; Winograd and Thordarson, 1975).

In terms of modeling flow within the perched zone, however, the HST models assume saturated conditions for both the matrix and fracture continua. The model assumption of saturated conditions for both matrix and fractures in the perched zone is hydraulically consistent with observed water levels in the perched zone. A model assumption of saturated conditions, however, does not rule out the actual existence of unsaturated hydraulically disconnected fractures or voids within the perched zone on Rainier Mesa, as described in Thordarson (1965). The CLEARWATER and WINESKIN HST models fundamentally assume that hydraulically disconnected fractures or voids do not to contribute to the effective flow system.

A goal of HST model calibration is to reproduce the general saturation observations at Rainier Mesa. This has been achieved by carefully analyzing fracture and matrix properties (Section 3.4 and Appendices A through D), implementation of boundary conditions with allowance for lateral flow (Section 2.4), and calibration to water level measurements (Sections 3.2 and 3.7).

3.6.1 Transient Flow

For both the CLEARWATER and WINESKIN HST models, transient flow results from two test-related effects:

- Redistribution of ground water by thermal and pressure effects of test phenomenology, and
- Test-induced change in permeability and porosity.

The CLEARWATER and WINESKIN HST models do not explicitly model complexities of test phenomenology including test-related thermal and pressure transients as do the 2-D CLEARWATER and RAINIER HST models (Zavarin et al., 2011). Phenomenological effects are abstracted to the initial conditions of the CLEARWATER and WINESKIN HST models.

Test-induced change in permeability and porosity are included in the CLEARWATER and WINESKIN HST models (see Section 3.4.4) and can produce several significant transient flow effects:

- Enhanced permeability in the chimney and cavity induces drainage of water within the chimney and cavity material and focuses infiltration toward the cavity and melt glass zone.
- Enhanced porosity in the chimney and cavity provides a large volume of storage for drainage toward the source zones.
- Enhanced permeability to 3Rc increases fracture flow connectivity between the source zones and outlying in-situ rocks.
- Rubble blocks within the chimney, cavity, and melt glass zone provide capacity for matrix diffusion.
- Increased fracturing and microfracturing enhances the areal connection between fractures and matrix material and, as a result, enhances capacity for matrix diffusion.
- The combined effects of test-altered zone geometry, test-enhanced permeability, and drainage causes long-term reduction of matrix saturation in test-altered zones such as the cavity, chimney, and in-situ rocks within 3Rc.

3.6.2 Initial Saturation Conditions

For both the CLEARWATER and WINESKIN HST models, the initial steady state saturation field prior to the test is determined by implementing rock properties (Section 3.5) and boundary conditions (Section 2.4) and running the model for sufficient time (several ten-thousand years) to achieve steady-state flow conditions. The post-test initial saturation condition at 0 years model time or time zero (Sections 2.7.3 and 5.5) adopts the steady-state initial saturation condition with the following exceptions for the test-altered zones:

- Both fracture and matrix continua of the melt glass zone are assigned initial saturation of 1.0 assuming boiling conditions have ceased and post-test transient flow has caused water to pool at the bottom of the cavity and infiltrate into the melt glass zone.
- For cavity rubble derived from zeolitized or welded tuff, initial saturation is set at 0.012 in the fracture continuum consisting of 0.15 porosity void space. This cavity void space saturation is derived from conservation of mass of pre-test water within rocks vaporized to approximately 0.1 Rc. Initial saturation in the matrix is set to 0.99 for zeolitized tuff (assuming zeolitic tuff is nearly saturated) and to pre-test conditions for welded tuff.
- For chimney rubble derived from zeolitized tuff, initial saturation is set at 0.0015 in the fracture continuum consisting of 0.15 porosity void space, which equates to 0.00022 volumetric water content. This chimney void space saturation is derived from conservation volumetric water content assuming fully saturated pre-test fractures with a porosity of 0.00022.

- For chimney rubble derived from welded tuff (for WINESKIN only at top of chimney), initial saturation is set at 0.0024 in the fracture continuum consisting of 0.15 porosity void space, which equates to 0.0004 volumetric water content for fracture. This chimney void space saturation is derived from conservation of fracture volumetric water content assuming pre-test fracture saturation of 0.12 and a porosity of 0.003. Saturation of the welded tuff chimney rubble matrix is maintained at pre-test conditions.
- For chimney rubble derived from vitric tuff, initial saturation is set at 0.0045 in the fracture continuum consisting of 0.05 porosity void space, which equates to volumetric water content 0.00022. The 0.0045 saturation and 0.05 porosity values maintain conservation of volumetric water content in the fracture continuum.
- For in-situ rocks out to 3Rc, the fracture saturation is set at 1.0 assuming test-induced pressures and heat drive water from the cavity into fractures out to 3Rc. Matrix saturation in-situ rock out to 3Rc is maintained at pre-test conditions, assuming test-induced pressure and heat mainly impact fractures.

3.6.3 CLEARWATER

Pre-test saturation conditions for the CLEARWATER HST model reflect results of applying the matrix and fracture rock properties (Section 3.5) and boundary conditions (Section 2.4), as follows, from top to bottom:

- Simulated saturation ranges from about 0.05 to 0.20 in fractures and 0.6 to 0.8 in the matrix in welded tuffs of the TMWTA HSU that cap Rainier Mesa near CLEARWATER.
- The HST models treat flow in vitric tuffs as dominated by matrix flow and, therefore, simulated matrix and fracture continua saturation are identical in vitric tuffs, ranging from 0.45 to 0.60 near CLEARWATER.
- In the LTCU, matrix saturation is high, from above 0.98 to 1.0. Above the perched water table, fracture saturation varies from 0.25 to 0.90.
- Below the perched zone water table, simulated fracture and matrix saturation is 1.0.

Increased fracture and matrix saturation can occur along interfaces of rock units with different properties, particularly the interface between vitric and zeolitic tuff. This transition from matrix- to fracture-dominated flow causes a decrease in conductance because of the limited hydraulic connection between porous and fracture flow conduits (Section 2.4.4).

Figure 3.7 shows simulated saturation for the CLEARWATER HST model at pre-test and post-test initial conditions (time zero). The red lines indicate the outline of the plane intersecting the SZ model boundary. The white lines overprinted on the saturation field

indicate the location of test-altered zones, including 1.0, 1.3, 2.0, and 3.0 Rc outlines assuming a Rc of 72 m as presented in Section 2.7 and Figure 2.6 based on calculation from the maximum of the yield range (Pawloski, 1999; USDOE, 2015). Initial saturation conditions in the post-test 0-year time (time zero) are only different from the pre-test condition in test-altered zones as described above. Figures 3.8 and 3.9 show simulated saturation at 1, 10, 100, and 1,000 years after the CLEARWATER test. Comparison of saturation conditions from 0 to 1,000 years indicates the following flow transients:

- Water in the vitric tuff portion of the chimney drains rapidly within 1 year and, later, more slowly over time.
- Water in zeolitic tuff rubble drains slowly over a 1000-year time frame.
- Enhanced fracture permeability out to 3Rc induces drainage of fractures and possibly some water stored along the vitric-zeolitic tuff interface.
- Perched zone water levels have three transient stages: (1) a drop because of storage created in the cavity (~1-year timeframe), (2) a rise from test-induced drainage (~10 to 100-year timeframe), and (3) a drop as a result of test-induced permeability enhancement between the perched zone and regional aquifer (~100 to 1,000-year timeframe).

The CLEARWATER HST model includes all flow transients described above in calculation of water and radionuclide fluxes to the SZ model boundary.

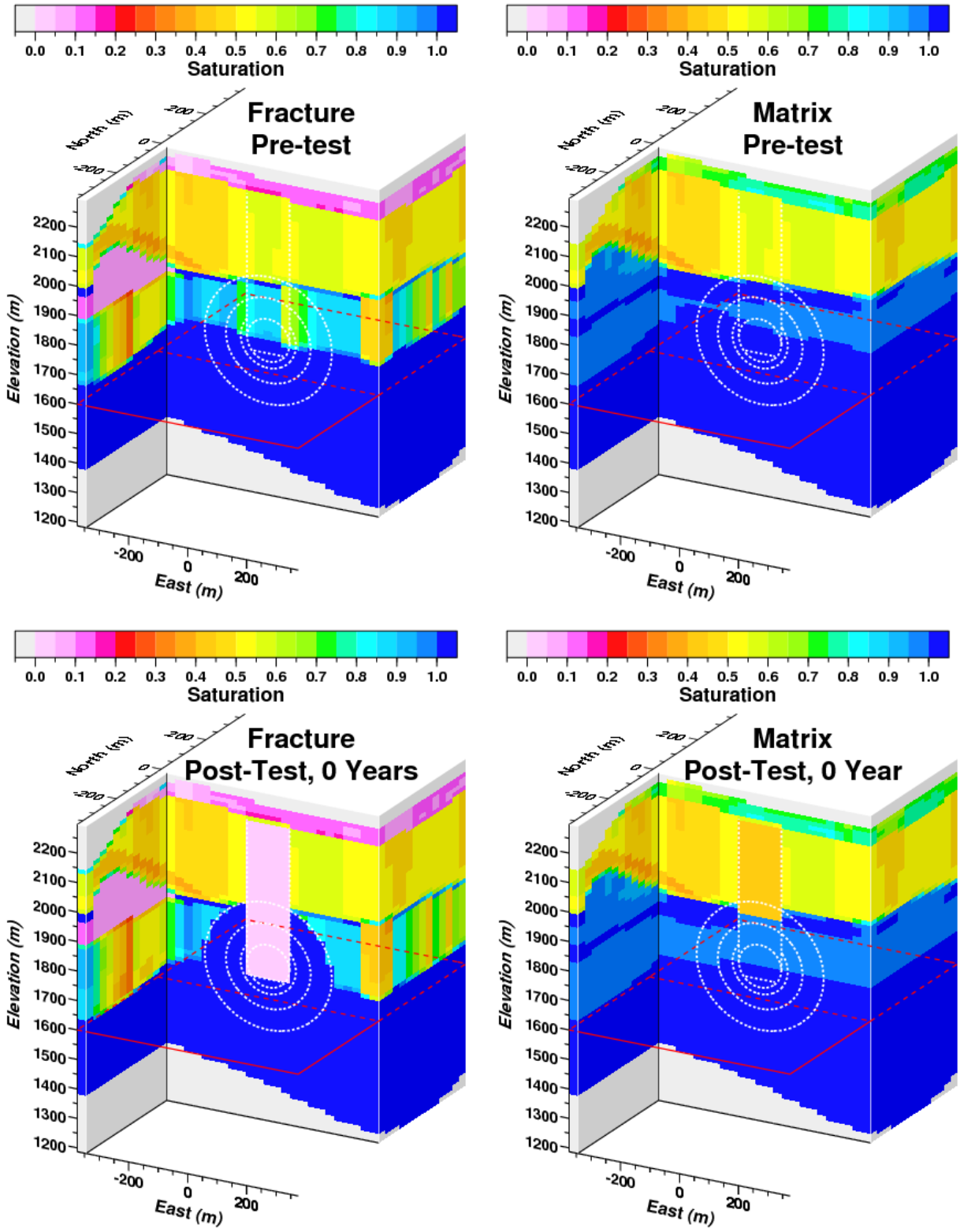

Figure 3.7 CLEARWATER HST model fracture and matrix saturation at pre-test and 0 year (initial condition) post-test times. The model Rc of 72 m is derived from maximum announced yield (USDOE, 2015) and Pawloski (1999) as detailed in Section 2.7.2.

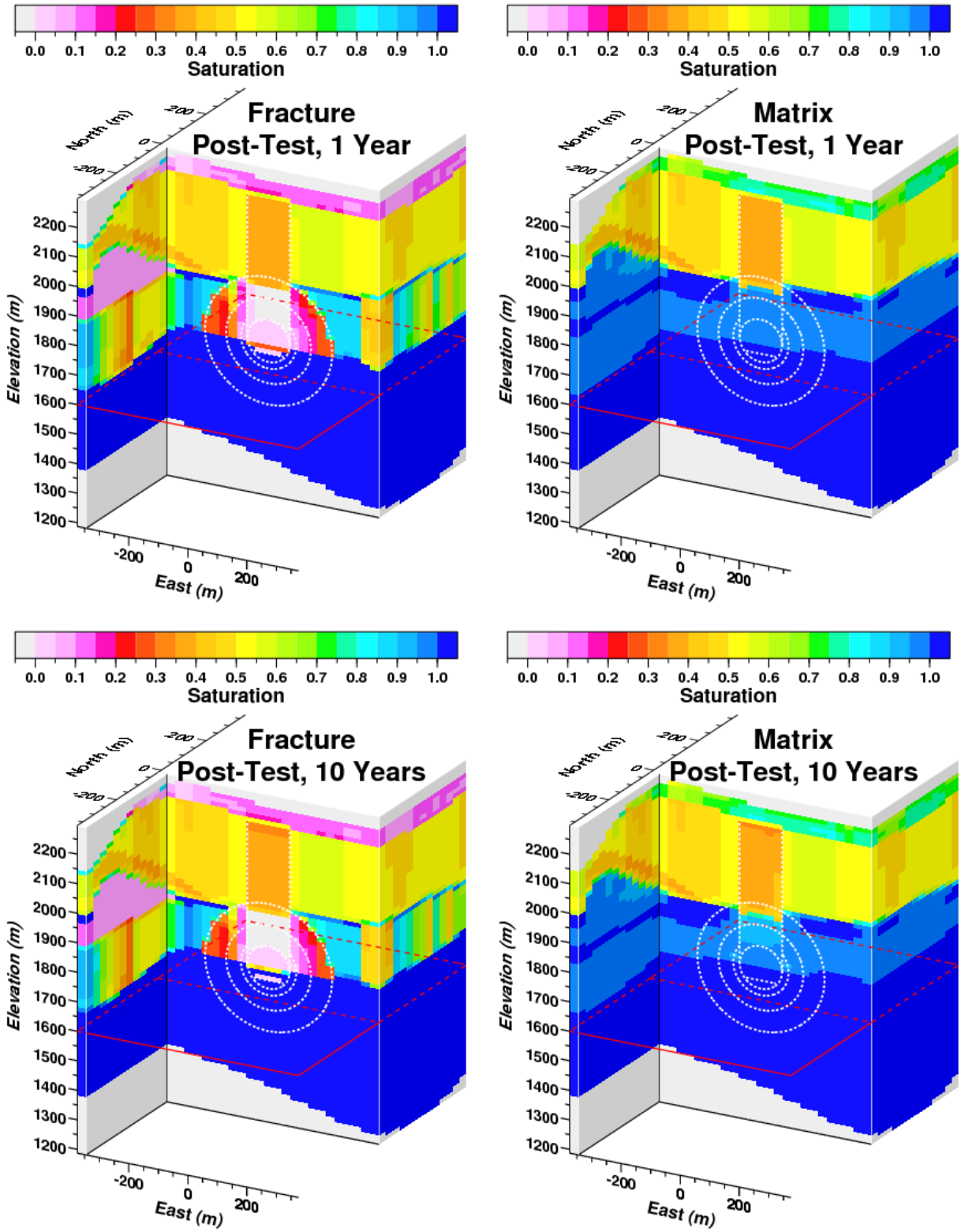

Figure 3.8 CLEARWATER HST model fracture and matrix saturation at 1 year and 10 year post-test times. The model Rc of 72 m is derived from maximum announced yield (USDOE, 2015) and Pawloski (1999) as detailed in Section 2.7.2.

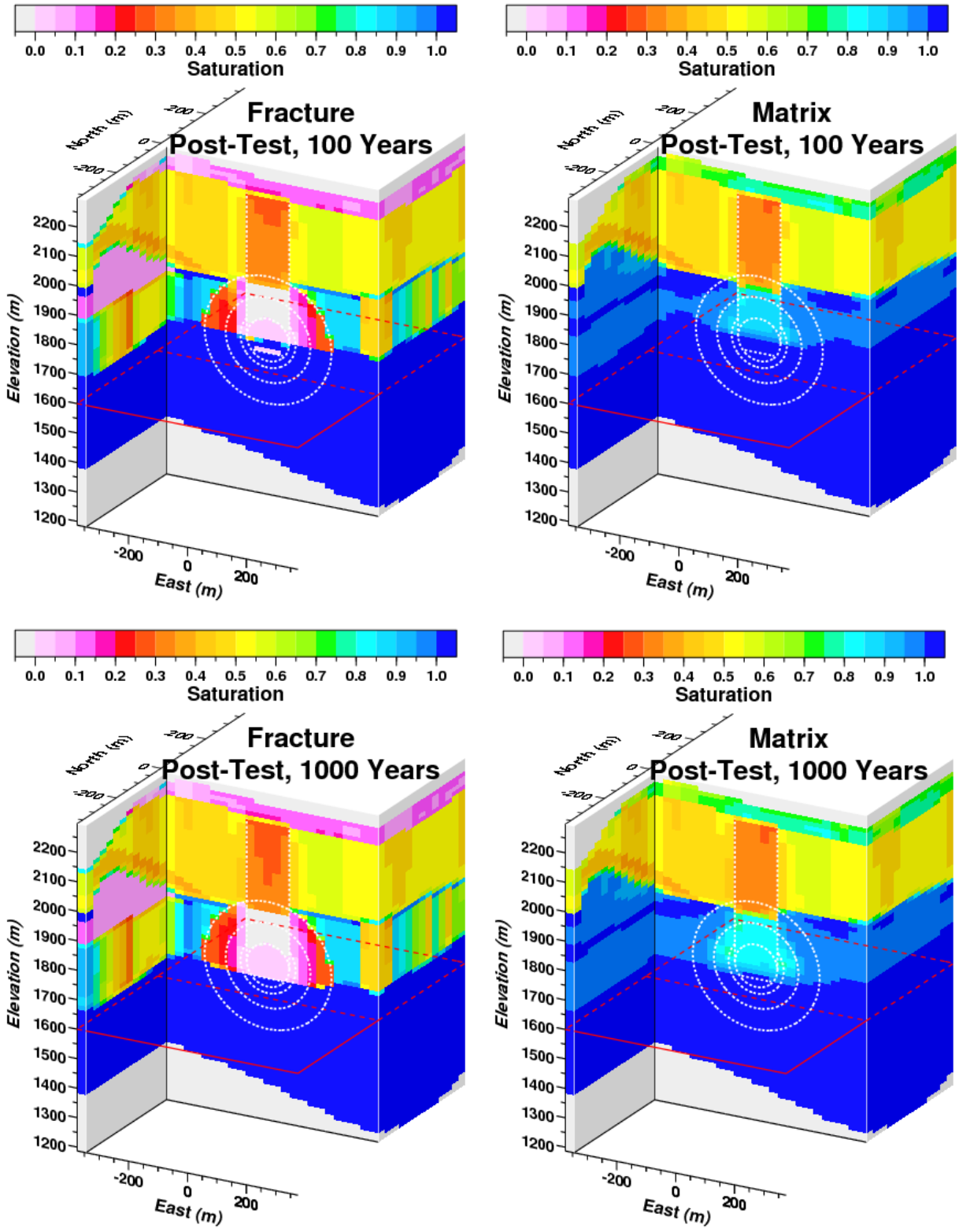

Figure 3.9 CLEARWATER HST model fracture and matrix saturation at 100 and 1,000year post-test times. The model Rc of 72 m is derived from maximum announced yield (USDOE, 2015) and Pawloski (1999) as detailed in Section 2.7.2.

3.6.4 WINESKIN

Pre-test saturation conditions for the WINESKIN HST model reflect the matrix and fracture rock properties (Section 3.5) and boundary conditions (Section 2.4), as follows, from top to bottom:

- Simulated saturation ranges from about 0.05 to 0.15 in fractures and 0.55 to 0.8 in the matrix in welded tuffs of the TMWTA HSU that cap the Rainier Mesa near WINESKIN.
- The HST models treat flow in vitric tuffs as dominated by matrix flow and, therefore, simulated matrix and fracture continua saturation are identical in vitric tuffs, ranging from 0.40 to 0.65 near WINESKIN.
- Welded tuffs of the BRA cause saturation variability and potential for variably saturated lateral flow above the TCU.
- In the LTCU, matrix saturation is very high, from above 0.98 to 1.0, except to the north where saturation declines to as low as 0.80. Above the perched water table, fracture saturation varies from 0.45 to 0.90.
- Below the perched zone water table, simulated fracture and matrix saturation is 1.0.

As for CLEARWATER, increased fracture and matrix saturation can occur along interfaces, particularly the interface between vitric, welded, and zeolitic tuff. Transitions from matrix- to fracture-dominated flow causes a decrease in conductance because of the limited hydraulic connection between porous and fracture flow conduits.

Figure 3.10 shows simulated saturation for the WINESKIN HST model at pre-test and post-test initial conditions (time zero). The red lines indicate the outline of the "stair step" intersection with the SZ model boundary. The white lines overprinted on the saturation field indicate the location of test-altered zones, including 1.0, 1.3, 2.0, and 3.0 Rc outlines assuming a Rc of 72 m as presented in Section 2.7 and Figure 2.6 based on calculation from the maximum of the yield range (Pawloski, 1999; USDOE 2015). Initial saturation conditions in the post-test 0-year time (time zero) are only different from the pre-test condition in test-altered zones as described above. Figures 3.11 and 3.12 show simulated saturation at 1, 10, 100, and 1,000 years after the WINESKIN test. Comparison of saturation conditions from 0 to 1,000 years indicates the following flow transients:

- Water in the vitric tuff portion of the chimney drains rapidly within 1 year and, later, drains more slowly over time.
- Water in zeolitic tuff rubble drains slowly over a 1000-year time frame.

- Enhanced fracture permeability out to 3Rc induces drainage of fractures and possibly some water stored along the vitric-zeolitic and vitric-welded tuff interfaces.
- Perched zone water levels will rapidly change near the test, from a strong north-to-south gradient to a sub-horizontal level as a result of test-enhanced permeability.
- Perched zone water levels rise from test-induced drainage in an approximately 10 to 100-year timeframe and subsequently drop in 100 to 1,000-year timeframe.

The WINESKIN HST model includes all flow transients described above in calculation of water and radionuclide fluxes to the SZ model boundary.

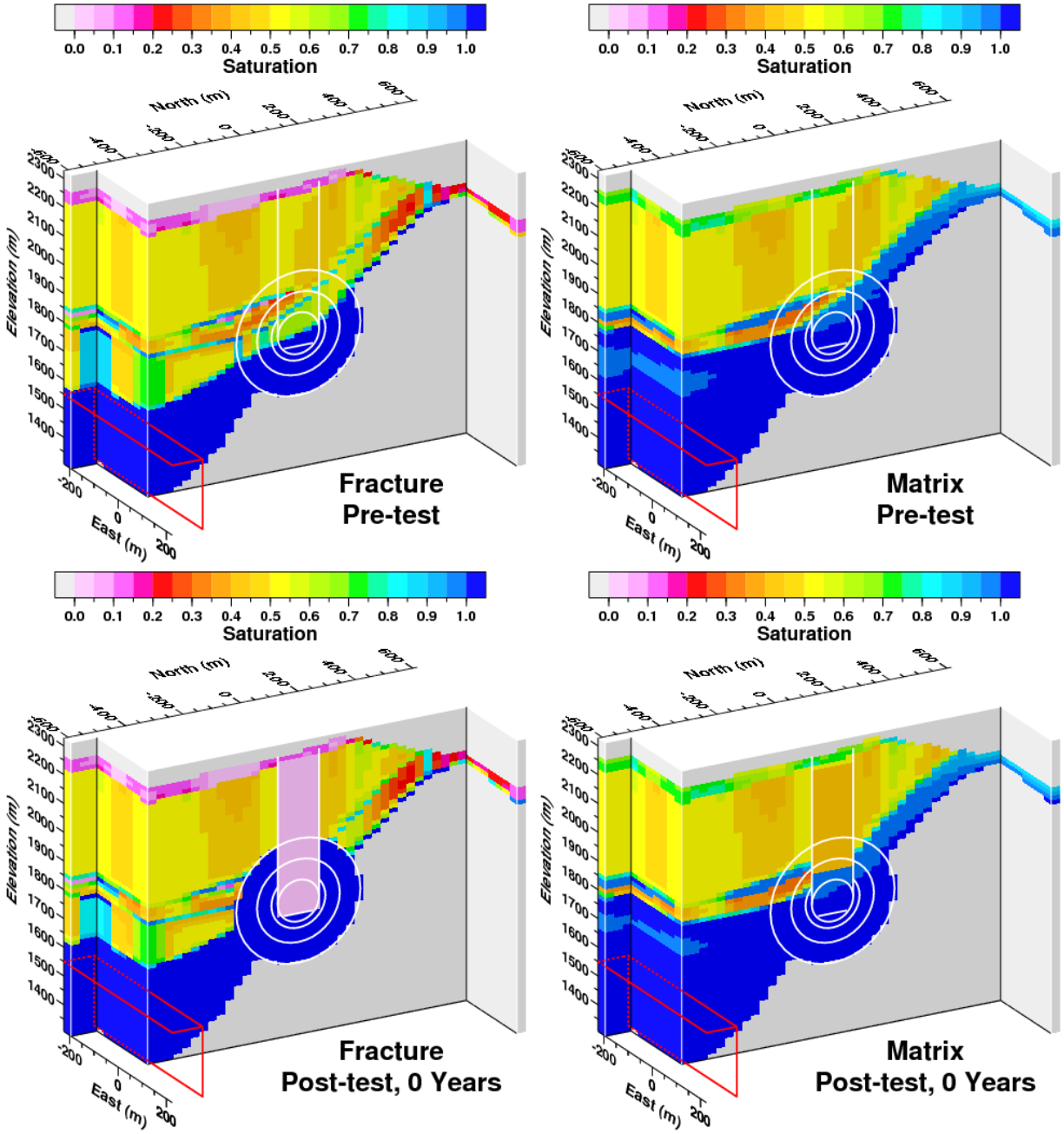

Figure 3.10 WINESKIN HST model fracture and matrix saturation at pre-test and (initial condition) post-test times. The model Rc of 72 m is derived from maximum announced yield (USDOE, 2015) and Pawloski (1999) as detailed in Section 2.7.2.

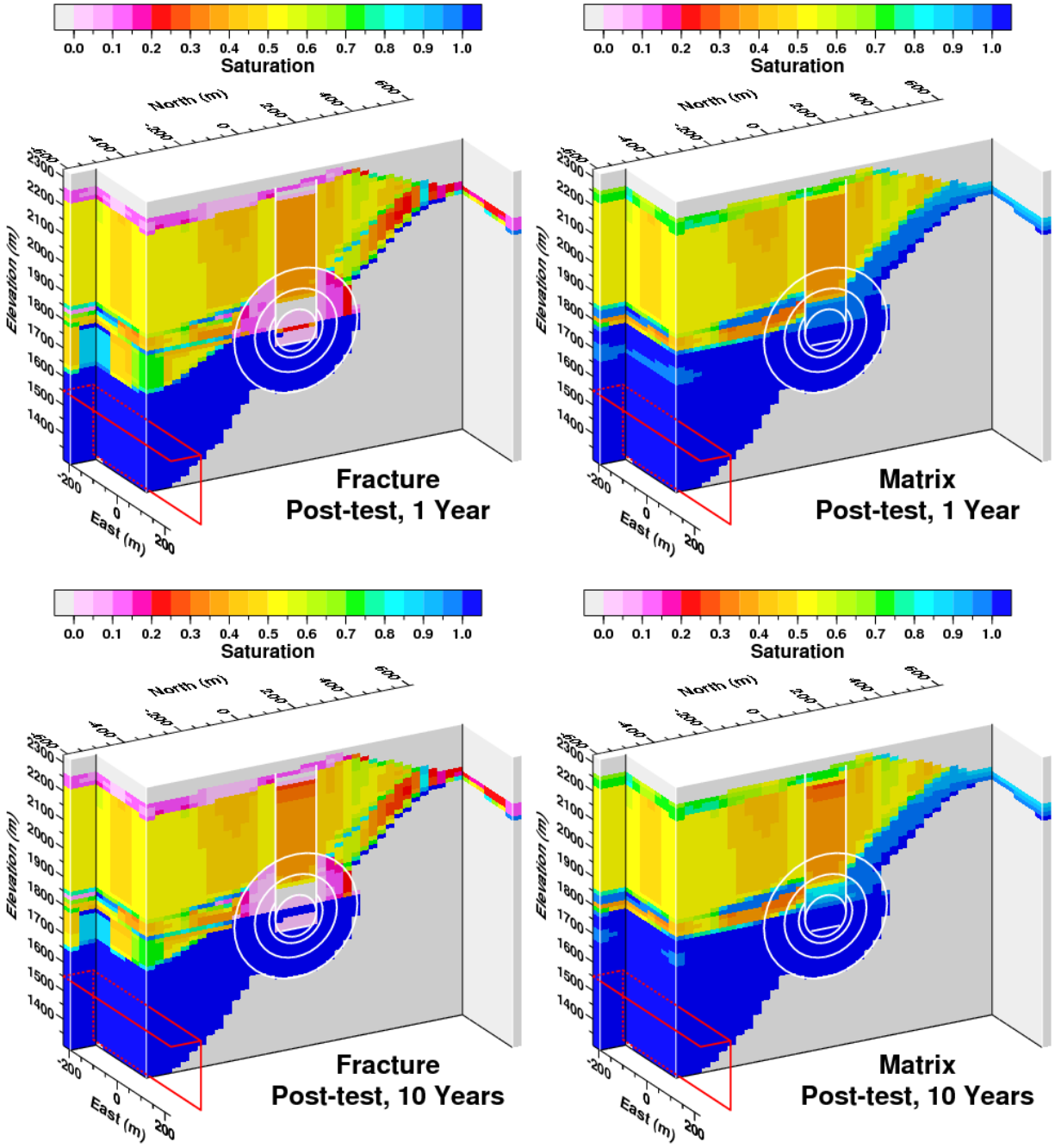

Figure 3.11 WINESKIN HST model fracture and matrix saturation at 1 and 10 year post-test times. The model Rc of 72 m is derived from maximum announced yield (USDOE, 2015) and Pawloski (1999) as detailed in Section 2.7.2.

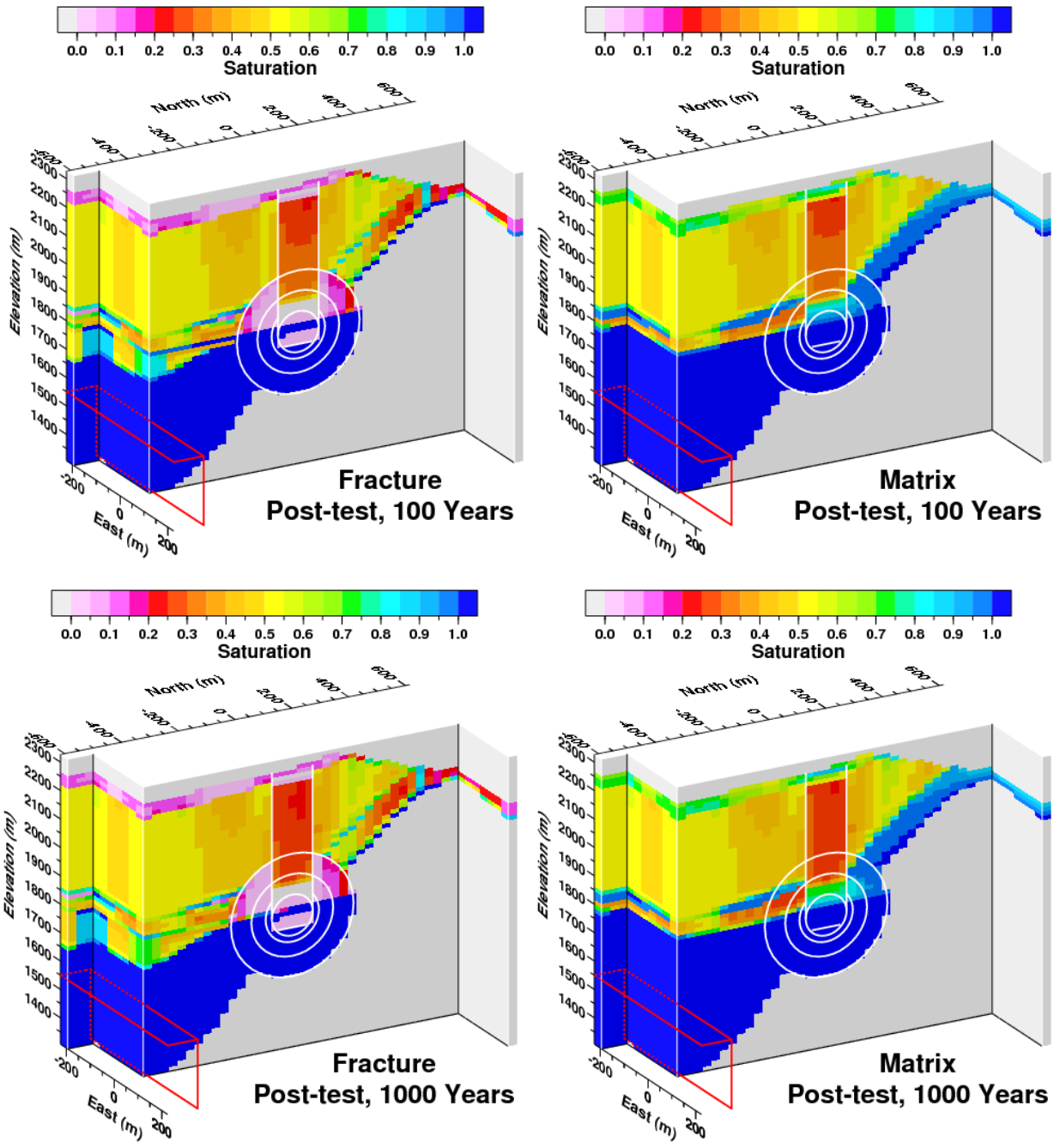

Figure 3.12 WINESKIN HST model fracture and matrix saturation at 100 and 1,000 year post-test times. The model Rc of 72 m is derived from maximum announced yield (USDOE, 2015) and Pawloski (1999) as detailed in Section 2.7.2.

3.7 Potentiometric Head

In the CLEARWATER and WINESKIN HST models, potentiometric heads are referenced to elevation above sea level to facilitate calibration to data for water levels and hydraulic gradients. As described in Section 2.4.2, potentiometric heads are also used to integrate HST boundary conditions with the upper boundary of the SZ model. Since the CLEARWATER and WINESKIN HST models include flow transients, potentiometric head is also transient.

3.7.1 Initial Conditions

As for saturation conditions, initial conditions for potentiometric head are also based on the steady state flow conditions of the pre-test flow stage. Pre-test head is also applied as initial conditions (at time zero) for all test-altered zones. The NUFT code automatically re-computes pressure (or potentiometric head) if cells become unsaturated, for example, as a result of changing initial saturation conditions to account for test effects in the post-test zero-year model time representing the initial condition at time zero (Section 2.7.3).

3.7.2 CLEARWATER

Figure 3.13 shows potentiometric head for the CLEARWATER HST model's pre-test conditions and post-test times of 1, 100, and 1,000 years. Comparison of potentiometric head at pre-test and 1-year times shows how the test-altered zones affect hydraulic gradients and perched zone water levels. The enhanced fracture permeability to 3Rc dampens hydraulic gradients within the test-altered zones with saturated conditions. Vertical hydraulic gradients increase below the test-altered zones. The perched zone water level falls initially in a 1-year timeframe. Perched water levels rise in 100-year timeframe and subsequently fall in a 1,000-year timeframe. As interpreted above for saturation, perched zone water levels initially decline near the test because of cavity and chimney infilling, subsequently rise because of test-induced drainage, and finally decline over the long term from test-enhanced permeability out to 3Rc.

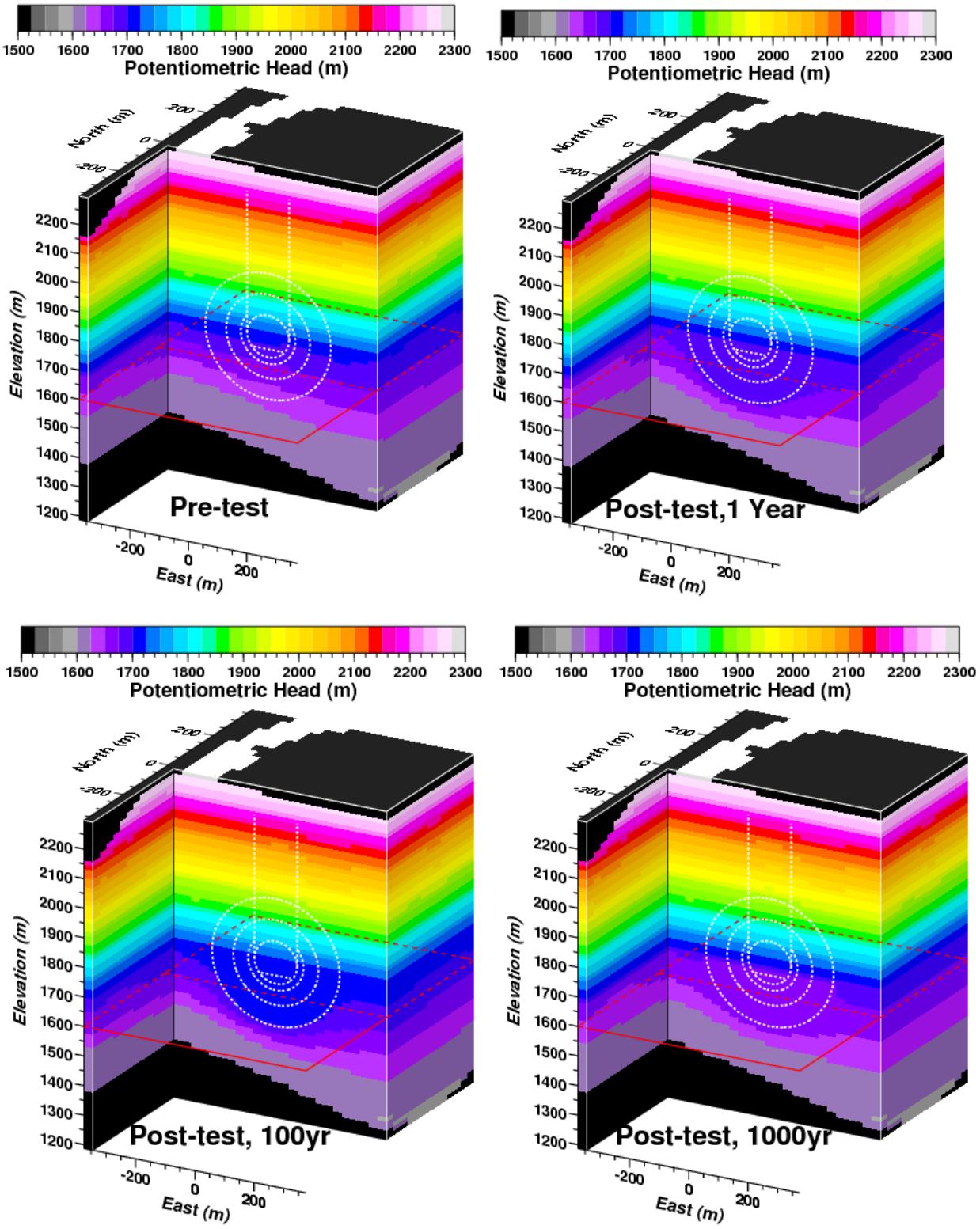

Figure 3.13 Potentiometric head for the CLEARWATER HST model's pre-test conditions and post-test times of 1, 100, and 1,000 years. The model Rc of 72 m is derived from maximum announced yield (USDOE, 2015) and Pawloski (1999) as detailed in Section 2.7.2.

3.7.3 WINESKIN

Figure 3.14 shows potentiometric head for the WINESKIN HST model pre-test conditions and post-test times of 1, 100, and 1,000 years. In the WINESKIN HST model, initial potentiometric head in the upper chimney for the pre-test condition at the model time of 0 years (time zero) is overwritten to consider connection to the atmosphere, since the WINESKIN chimney collapse propagated to the ground surface (Townsend et al., 2007). Comparison of potentiometric head at pre-test and 1-year times shows how the test-altered zones affect hydraulic gradients and perched zone water levels. The enhanced fracture permeability to 3Rc dampens hydraulic gradients within the test-altered zones with saturated conditions. Hydraulic gradients increase downgradient of the test-altered zones. The perched zone water level initially rises in a 1-year to 100-year timeframe, and subsequently declines in a 1,000-year timeframe. As interpreted above for saturation, perched zone water levels initially rise because of test-induced drainage, then decline over the long term from equilibration to the test-enhanced permeability.

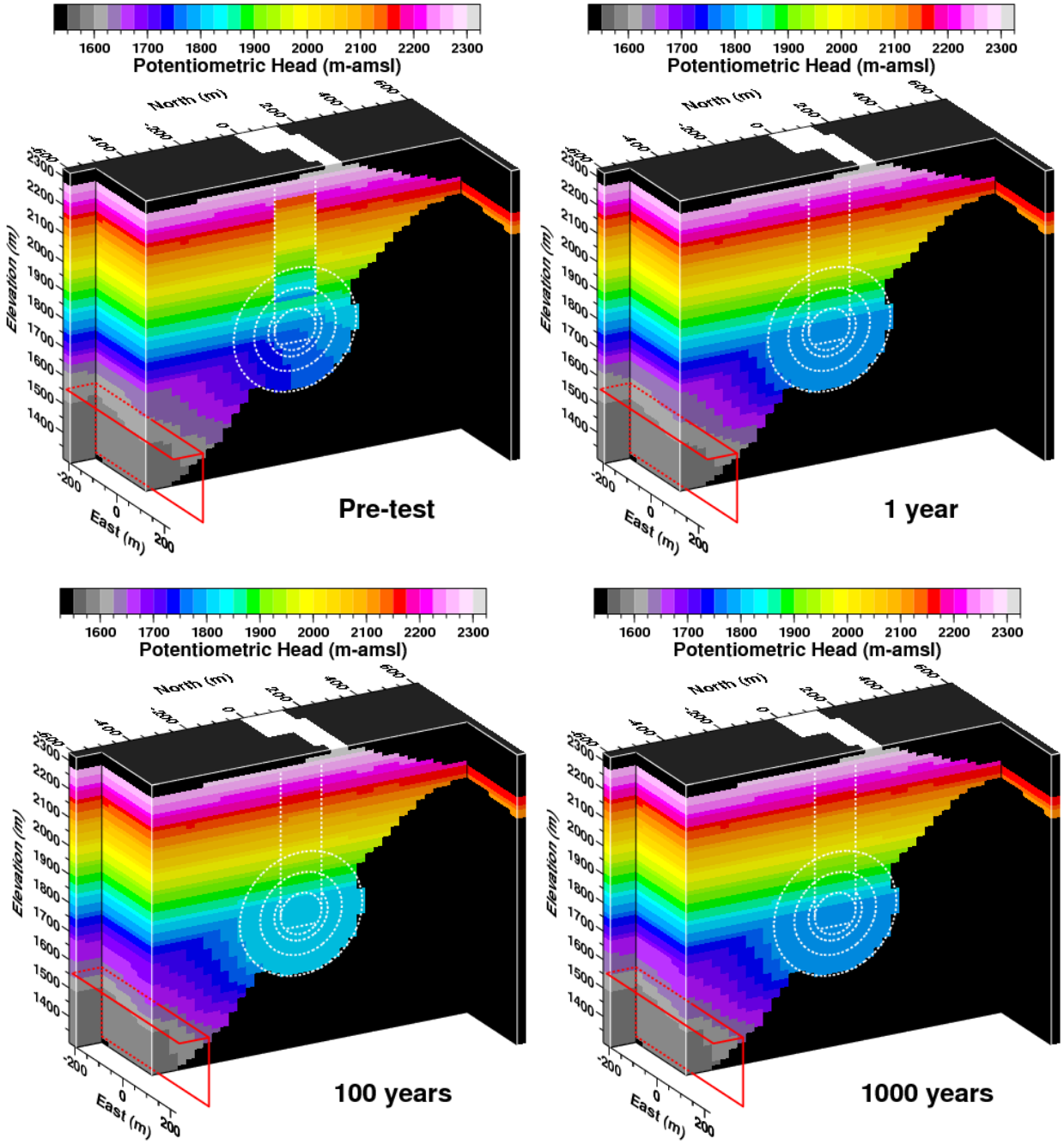

Figure 3.14 Potentiometric head for the WINESKIN HST model's pre-test conditions and post-test times of 1 year, 100 year, and 1,000 years. The model Rc of 72 m is derived from maximum announced yield (USDOE, 2015) and Pawloski (1999) as detailed in Section 2.7.2.

3.8 Lateral Flow

The CLEARWATER and WINESKIN HST models allow for lateral flow from hydraulic heterogeneities, particularly at the vitric-zeolitic interface and locations for discharge boundary conditions into the Redrock Valley aquifer (RVA) (Section 2.4). Lower vitric tuff aquifers (LVTA) are usually situated within synclines above the vitric-zeolitic tuff interface or upper limit of pervasive zeolitization (NSTec, 2007; Townsend, 2008). Fenelon et al. (2008) map out directions of lateral flow in the regional volcanic aquifer including areas where the RVA is near CLEARWATER and WINESKIN.

Fenelon et al. (2008) point out that lateral flow also plays a role in perched and semi-perched zones on Rainier Mesa:

"Water contained within these perched and semi-perched zones moves laterally until encountering conditions that allow downward flow into an underlying aquifer."

Zavarin et al. (2011) further reviews evidence for lateral flow mechanisms within the Tertiary volcanic sequence, including lateral flow in welded tuff aquifers and at the base of synclines filled by vitric tuff aquifers, such as the LVTA1 and LVTA2. Presence of welded tuff aquifers such as the BRA, TUBA, or RVA above or below test locations indicate potential for lateral transport of contaminants within HST and flow and transport model domains, as noted by Townsend (2008):

"…the presence of a welded unit below the WP [working point], with the additional porosity and potentially greater water availability, could enhance the downward (or lateral) movement of contaminants liberated from the cavity/chimney area."

"Densely welded volcanic tuff is located both above and below most WPs within the mesas. It has been shown that these units have a considerably higher fracture porosity and increased permeability compared to the surrounding zeolitized tuff, and in some areas, considerable perched water resides within these rocks. If contaminants reach these layers, it is possible that their movement could be enhanced within the welded units, both vertically and laterally."

The CLEARWATER and WINESKIN HST models are designed to permit lateral flow in vitric tuff and welded tuff units. Allowing for lateral flow at the base of synclines filled by vitric tuff aquifers provides a mechanism for stabilizing water levels in the perched zone to near or below the vitric-zeolitic tuff interface, which facilitates flow calibration to potentiometric head measured in the perched zone (Section 2.4.3). Allowing for lateral flow in the RVA is consistent with consideration of lateral flow processes in the regional volcanic aquifers as indicated by maps of groundwater flow direction (Fenelon et al., 2008) and as implemented in the SZ model (Navarro, 2017a).

3.9 Flow Uncertainty

Uncertainty in the NET-INFIL3 infiltration model (Navarro, 2017a) contributes to assessment of uncertainty in the HST flow models. Six flow realizations for both the CLEARWATER and WINESKIN HST models were calibrated to the six realizations of NET-INFIL3 infiltration provided by LANL in 2011. HST flow model results indicate the different NET-INFIL3 realizations using the same hydraulic properties produced different flow behavior in terms of total flux and head distribution for the same hydrostratigraphic model used throughout the CLEARWATER and WINESKIN HST models.

Prior to the flow uncertainty analysis, the Rainier Mesa Review Committee decided in March 2011 to require that NET-INFIL3 realization 11 would establish the base case for HST modeling. In subsequent flow uncertainty analysis, NET-INFIL3 realization 7 was found to produce the lowest overall fluxes, while NET-INFIL3 realizations 29 produced intermediate flux, less the base case realization 11. Figures 3.14 and 3.15 compare water fluxes to the RVA produced by the six calibrated CLEARWATER and WINESKIN HST model flow realizations using the six different NET-INFIL3 realizations. Figure 2.4 shows the effect of different NET-INFIL3 realizations on total water fluxes at model discharge locations – the RVA and the base of vitric tuff aquifer LVTA2. As discussed in Section 2.4.3, including consideration of variably saturated lateral flow at the zeolitic-vitric tuff interface has a stabilizing effect on calibration to perched zone water levels. For the CLEARWATER and WINESKIN HST models, perched zone water levels are more easily calibrated by including lateral flow processes along the zeolitic-vitric tuff interface. Some NET-INFIL3 realizations produced very similar flow results. For the current HST model uncertainty analysis, three NET-INFIL3 realizations were selected to span the range of uncertainty in the infiltration model and to address uncertainty in fracture permeability of the TCU.

Flow calibration to the single water level measurement at U12q (5,600 feet) could be achieved for all six flow realizations by adjusting fracture permeability for the LTCU and OSBCU (Table 3.10). Without any water level data for flow calibration at WINESKIN, the same fracture permeability values obtained from the CLEARWATER calibrations were applied the WINESKIN HST flow models based on the NET-INFIL3 realization. Thus, the CLEARWATER and WINESKIN HST models address uncertainty in the infiltration model and groundwater flow rates by allowing for uncertainty in the LTCU and OSBCU fracture permeability, which is the most important flow uncertainty parameter affecting water flux between the radionuclide source areas and the regional volcanic aquifer. Transport of radionuclides from the CLEARWATER and WINESKIN tests to the SZ model interface requires extensive migration through LTCU and OSBCU tuff confining units, where overall water flux is dominated by fractures. Calibration of flow realizations for the HST models has focused on adjusting fracture permeability in the tuff confining units. The calibration target was to maintain consistency between the water level of 5,600 feet (1,707 m)

measured in U12q and the estimated water level in the regional volcanic aquifer of 1,600 m (Fenelon et al, 2008) beneath the CLEARWATER test (see Figure 3.1). Additionally, the perched water level at WINESKIN was checked for consistency with U12r drilling records indicating a water level elevation near or below the working point. Assuming the same matrix properties for all realizations, the flow calibration exercise resulted in three sets of fracture permeability values for the tuff confining units (Table 3.10).

The fracture permeability range of 7e-17 to 1e-16 used for the CLEARWATER and WINESKIN HST models falls in the middle of ranges of heterogeneous fracture permeability ranges determined for the T-Tunnel flow and transport model (Navarro, 2017a): vertical fracture permeability ranging from 4e-17 to 4.3e-16 and north-south fracture permeability ranging from 3.7e-17 to 2.9e-16. An east-west fracture permeability range of 2.5e-18 to 2.0e-17 determined for the T-Tunnel flow and transport model could be used to impart anisotropy into the fracture permeability values used in the CLEARWATER and WINESKIN HST models. However, these permeability ranges were not available at the time of the CLEARWATER and WINESKIN HST modeling work.

Importantly, the CLEARWATER and WINESKIN HST model matrix and fracture permeability ranges are consistent with the T-Tunnel matrix and fracture permeability ranges (Navarro, 2017a), suggesting that certain rock properties are transferable across different testing areas of Rainier Mesa.

Table 3.10 HST model fracture permeability values for the LTCU and OSBCU calibrated to six NET-INFIL3 realizations.

NET-INFIL3 Realization	HST Model LTCU and OSBCU Fracture Permeability	
	m/s	m^2
3	7e-10	7e-17
7	7e-10	7e-17
11	1e-9	1e-16
23	8e-10	8e-17
29	8e-10	8e-17
42	7e-10	7e-17

Alternative flow models based on different hydrostratigraphy or flow assumptions in confining units such as the MGCU or LCCU1 were not investigated because the base case SZ model assumed “no flow” conditions in these units. Updated hydrostratigraphy (NSTec, 2009a and b) was not considered upon guidance from the Rainier Mesa Review Committee. At the time of the current HST modeling of July 2011, SZ models had not investigated any alternative flow models or interpretations, and the base case SZ flow model remained uncalibrated (Chen, 2011).

3.10 Flow Code

The HST models use the "US1P" module of the NUFT numerical simulation code to model variably saturated flow in a dual-continuum (with dual permeability and dual porosity fracture and matrix continua) integrated finite-difference mesh. The NUFT code is documented by Nitao (2000a and b). Specifics of the US1P module are documented in Nitao (2004). The version date for the NUFT code used is 11-17-04. Quality assurance for the NUFT code is documented in Carle et al. (2014).

4 Source Term Implementation

4.1 Radiologic Source Term (RST)

The radiologic source term (RST) for the CLEARWATER and WINESKIN tests is determined from a yield-weighted division of the Bowen et al. (2001) inventory for Rainier Mesa/Shoshone Mountain Principle Geographic Test Center, using announced yields or the maximum of announced yield ranges from USDOE (2015) and a September 23, 1992 date of distribution. Zavarin et al. (2011) provides further details on source term distribution.

4.1.1 Relevant Radionuclides

For the CLEARWATER and WINESKIN tests and other Rainier Mesa radionuclide sources, a limited number of radionuclides are considered relevant to flow and transport in the SZ model. The relevant radionuclides are selected by expected or observed radionuclide activity relative to the maximum contaminant limit (MCL). Zavarin et al. (2011) provides details on selection of the relevant radionuclides for all Rainier Mesa tests. Eleven relevant radionuclides are identified and abbreviated as given in Table 4.1 with MCL and half-life for each radionuclide.

In June 2011, at the time of HST transport model set up and execution for the CLEARWATER and WINESKIN tests, the list of relevant radionuclides for Rainier Mesa tests was not finalized. For CLEARWATER and WINESKIN HST modeling, Table 4.1 lists the preliminary eleven relevant radionuclides with MCL and half-life. Ni-63 in lieu of Am-241 is the only difference between the more recent list given for all Rainier Mesa tests by Zavarin et al. (2011). Subsequent HST modeling of Am-241 transport for CLEARWATER and WINESKIN is described in Navarro (2017a).

Table 4.1 List of names and abbreviations for eleven radionuclides included in CLEARWATER and WINESKIN HST models and their maximum contaminant limit (MCL) and radioactive half-life, as determined in Zavarin et al. (2011). Future models replace Ni-63 with Am-241 (Navarro, 2017a).

Relevant Radionuclides			MCL (pCi/L)	Half-life
Name	Abbreviations			
Tritium	^{3}H	H-3	20,000	12.3
Carbon-14	^{14}C	C-14	2,000	5,730
Chlorine-36	^{36}Cl	Cl-36	700	301,000
Technetium-99	^{99}Tc	Tc-99	900	213,000
Iodine-129	^{129}I	I-129	1	15,700,000
Nickel-63	^{63}Ni	Ni-63	50	100
Strontium-90	^{90}Sr	Sr-90	8	29.1
Uranium-238	^{238}U	U-238	30	4,470,000,000
Plutonium-238	^{238}Pu	Pu-238	15	87.7
Plutonium-239	^{239}Pu	Pu-239	15	24,100
Plutonium-240	^{240}Pu	Pu-240	15	6,560

4.1.2 Source Term Units

The CLEARWATER and WINESKIN HST models use picocuries (pCi) as units for the source term. Aqueous concentration units for the source term are given in pCi per cubic meter (pCi/m^3). Water flux units are given in meters cubed per second (m^3/s).

4.1.3 Exchange Volume and Glass Zone Partitioning

The "exchange volume" is defined as the volume into which the RST is initially located at "time zero" (Section 2.7.3). The exchange volume for a given radionuclide is largely based on observed data from other tests, but does not necessarily correspond to the maximum detectable extent. The exchange volume is a practical maximum initial extent of contamination relative to the maximum contaminant limit (MCL). The extent of contamination is uncertain spatially and in magnitude of total activity according to the RST. Depending on the radionuclide, the radionuclide sources partition into melt glass and other portions of the exchange volume with different fractions and radial extent.

The "melt glass zone" consists of a mixture of rubble and melt glass. The amount of radionuclide source released from the melt glass depends on the glass dissolution rate over time. For the CLEARWATER and WINESKIN HST models, a concept of "instantaneous release" of glass zone radionuclide sources is implemented considering that the glass release rate is highest at early times because of test-generated thermal effects on glass dissolution rate (Pawloski et al. 2001; Zavarin et al., 2011). The model concept of instantaneous release assumes the entire available portion of the radionuclide source eventually dissolved from the glass zone is released at time zero.

The fraction of the source term available for instantaneous release from the melt glass zone is the product of the glass partition fraction (fraction of source term in the glass) and the glass dissolution fraction (fraction of glass dissolved). The fraction of the source term initialized into the exchange zone outside the melt glass zone is the complement of the glass partition fraction.

4.1.4 Radionuclide Source Term Model Values, Decay Rates, and Uncertainty

Table 4.2 summarizes radionuclide sources used to investigate preliminary RST total radionuclide activity and ranges of uncertainty for glass partitioning, glass dissolution, and exchange zone radius for eleven radionuclides investigated in this report, 10 of 11 of which are as given in Zavarin et al. (2011). For each test, the initial radionuclide source value in picocuries at "time zero" is corrected for decay based on the September 23, 1992 date of distribution of the Bowen inventory. However, the CLEARWATER and WINESKIN tests were detonated at well before 9/12/92: CLEARWATER on 10/16/63 and WINESKIN on 1/15/69 (USDOE, 2015). Accordingly, the initial HST model radionuclide source is larger at the time of test detonation for CLEARWATER than WINESKIN, depending on the radioactive decay rate, even though both tests have the same announced yield range of 20 to 200 Kt (USDOE, 2015).

Uncertainty in source term distribution for the CLEARWATER and WINESKIN HST models arises largely from the following factors:

- The source term values are normalized to the Bowen et al. (2001) inventory applied to the time of September 23, 1992, but the tests were executed on different dates - October 16, 1963 and January 15, 1969.
- The yield is uncertain.
- The fractions of non-volatile radionuclides partitioned into glass of the melt glass zone are uncertain.
- The fraction of melt glass dissolved into the aqueous phase is uncertain.
- The exchange volume radius for each radionuclide source is uncertain.
- The amount of partitioning of radionuclide sources with relatively high volatility and low solubility (e.g. C-14) into the gas phase is uncertain.

Zavarin et al. (2011) provides details on derivation of the RST model and uncertainty. Table 4.3 shows radionuclide source decay rates and uncertainty of radionuclide sources as characterized by minimum, mean, and maximum values.

Table 4.2 Summary of radionuclide source mean values and ranges of uncertainty for glass partitioning, glass dissolution, and exchange zone radius for the eleven relevant radionuclides.

Radionuclide Source* (pCi) Mean Values			Glass Partition (%)		Glass Dissolution (%)		Exchange Volume (Rc)	
Relevant Radionuclide	CLEAR-WATER 10/16/63	WINESKIN 1/15/69	min	max	min	max	min	max
H-3	4.9E+17	3.7E+17	0	0	0.0002	0.027	1.5	3.0
C-14	1.4E+13	1.4E+13	0	0	0.0002	0.027	3.0	5.0
Cl-36	1.4E+12	1.4E+12	50	50	0.0002	0.027	1.5	3.0
Tc-99	3.3E+13	3.2E+13	95	95	0.0002	0.027	1.5	3.0
I-129	4.1E+15	3.6E+15	35	35	0.0002	0.027	1.5	3.0
Ni-63	9.9E+11	9.9E+11	80	80	0.0002	0.027	1.0	1.5
Sr-90	3.7E+09	3.7E+09	50	50	0.0002	0.027	1.5	3.0
U-238	8.8E+10	8.8E+10	90	90	0.0002	0.027	1.0	1.5
Pu-238	4.2E+14	4.1E+14	95	100	0.0002	0.027	1.0	1.5
Pu-239	1.4E+15	1.4E+15	95	100	0.0002	0.027	1.0	1.5
Pu-240	3.5E+14	3.5E+14	95	100	0.0002	0.027	1.0	1.5

*Source term component value corrected for decay to date of test based on inventory of Bowen et al. (2001) at 9/23/92.

Table 4.3 Radionuclide decay rate and minimum, mean, and maximum source values for CLEARWATER and WINESKIN tests.

Radio-nuclide Source	Decay Rate (y^{-1})	Minimum (pCi)		Mean (pCi)		Maximum (pCi)	
		CLEAR-WATER	WINESKIN	CLEAR-WATER	WINESKIN	CLEAR-WATER	WINESKIN
H-3	5.65e-2	1.65E+17	1.22E+17	4.94E+17	3.67E+17	1.48E+18	1.10E+18
C-14	1.21e-4	1.40E+12	1.40E+12	1.40E+13	1.40E+13	1.40E+14	1.40E+14
Cl-36	2.30e-6	1.43E+11	1.43E+11	1.43E+12	1.43E+12	1.43E+13	1.43E+13
Ni-63	6.93e-3	3.28E+12	3.17E+12	3.28E+13	3.17E+13	3.28E+14	3.17E+14
Sr-90	2.38e-2	3.12E+15	2.75E+15	4.05E+15	3.57E+15	5.27E+15	4.64E+15
Tc-99	3.25e-6	7.63E+11	7.63E+11	9.92E+11	9.92E+11	1.29E+12	1.29E+12
I-129	4.41e-8	2.85E+09	2.85E+09	3.70E+09	3.70E+09	4.81E+09	4.81E+09
U-238	1.55e-10	7.31E+10	7.31E+10	8.78E+10	8.78E+10	1.05E+11	1.05E+11
Pu-238	7.90e-3	3.53E+14	3.39E+14	4.24E+14	4.07E+14	5.09E+14	4.88E+14
Pu-239	2.88e-5	1.15E+15	1.15E+15	1.38E+15	1.38E+15	1.65E+15	1.65E+15
Pu-240	1.06e04	2.93E+14	2.93E+14	3.51E+14	3.51E+14	4.22E+14	4.22E+14

4.2 HST Model Source Zone Definitions

For the CLEARWATER and WINESKIN HST models, the radionuclide source term is partitioned into five zones containing the volumes defined as follows:

- Melt glass = a "puddle" like volume at the bottom of a sphere with 1Rc radius
- Cavity = the portion a sphere with 1Rc radius above the melt glass zone
- 1.5Rc = a spherical shell between 1 and 1.5 Rc radii excluding the chimney
- 3Rc = a spherical shell between 1.5 and 3 Rc radii excluding the chimney
- Chimney = a cylinder of 1Rc radius extending above the cavity to a radius of 2Rc for non-volatile radionuclides and 3Rc for volatile radionuclides

The chimney source zone is subdivided into two volumes called "Chimney-2Rc" and "Chimney-3Rc", to account differences in the volatility of the radionuclide sources. Volatile radionuclides will tend to migrate higher up the chimney by gaseous transport, whereas non-volatile radionuclides will tend to be down-dropped with in-fallen rock debris by cavity collapse. Figure 4.1 shows a schematic diagram of the five HST model source zones. The five source zones are designed to account for uncertainty in the spatial distribution of the radionuclide sources.

Notably, HST model source zones do not correspond exactly to the HST model altered zones (See Section 2.7.3 and Figure 2.4). The HST model source zones are designed to address the range of variability in source distribution given in Zavarin et al. (2011), while the test-altered zones are designed to address rock property spatial distributions.

To demonstrate how the HST model implements the radionuclide source zones on the 3-D numerical mesh, Figure 4.2 overlays the HST model source zone boundaries (shown in gray) onto the WINESKIN HST model numerical mesh for fracture permeability.

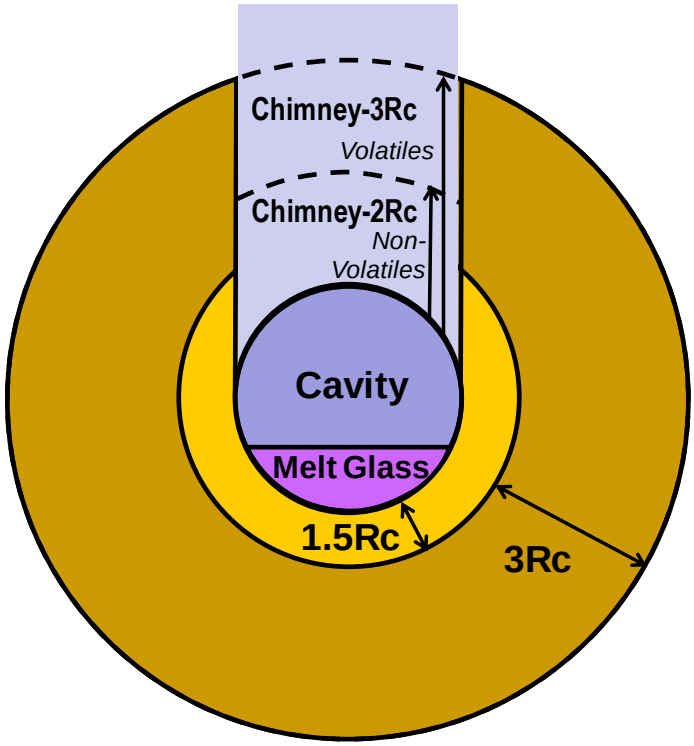

Figure 4.1 Schematic diagram of the five radionuclide source zones used for CLEARWATER and WINESKIN HST models.

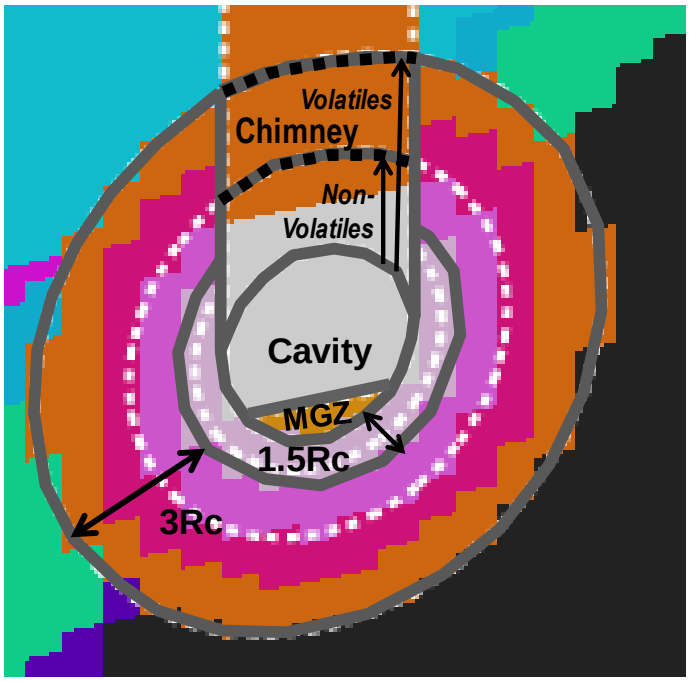

Figure 4.2 Overlay of boundaries of the five radionuclide source zones onto the 3-D WINESKIN HST model numerical mesh for fracture permeability.

4.3 Partitioning and Distribution of the RST into HST Source Zones

4.3.1 Consideration of Test Phenomenology

In addition to direct observations of radionuclide spatial distributions from Rainier Mesa tests (e.g. Townsend et al., 2007; Zavarin et al., 2011), test phenomenology is considered in partitioning and distribution of the RST into HST source zones. Both the CLEARWATER and WINESKIN tests were located in fractured zeolitized tuffs with relatively indurated matrix blocks. About 10% of the mass in the cavity volume is spatially redistributed by vaporization and melting of in-situ rock and fluids, and the remaining 90% is displaced by compression or block motion (U.S. Congress, 1989; Townsend et al., 2007).

As discussed in Section 2.7, test shock induces fractures out to 2Rc and enhances permeability of fractures out to 3Rc (U.S. Congress, 1989). Within hard or fractured rocks on Rainier Mesa such as zeolitized or welded tuffs, fractures provide the main conduits in in-situ rock for early-time redistribution of radionuclides from the cavity to the outer extent of the exchange zones. Cavity collapse causes chimney formation with approximately 15% void space or "bulking" between in-fallen zeolitized tuff blocks. After cavity collapse, gaseous processes transport volatile radionuclides into chimney void space, whereas falling chimney rubble transports non-volatile radionuclides in the exchange zone downward as the chimney and cavity void space is filled with rubble. In consideration of test phenomenology summarized above, the radionuclide sources are initially partitioned into the "fracture", "void space", or "glass zone" portions of the five HST source zones as discussed below.

4.3.2 Operational Characteristics of Fracture-Matrix Continua

In the dual-continuum CLEARWATER and WINESKIN HST modeling framework, each HST source zone contains two continua operationally defined as "fracture" and "matrix" as discussed in Section 2.5. All HST source zones have corresponding test-altered zones (Section 2.7) where fracture and matrix rock properties are different than pre-test in-situ rock properties except for matrix materials beyond 2Rc. Within HST source zones, rock properties of the "fracture" and "matrix" continua depend on the rock types and characteristics of the test-altered zones. Similarly, implementation of the HST into source zones also depends on the characteristics of the test-altered zones and consideration of HST processes (Zavarin et al., 2011).

The operational characteristics of the "fracture" and "matrix" continua for the five HST source zones are summarized in Table 4.4. The RST components are distributed into the operationally defined "fracture" continuum of the HST source zones only. The dual continuum model enables diffusive and advective transport processes to re-distribute the RST from "fracture" to "matrix" continua over time. Consequently, the impact of matrix diffusion on radionuclide transport subsequent to source term implementation or "time

zero" (Section 5.5) is explicitly accounted for in the CLEARWATER and WINESKIN HST models as follows:

- Radionuclide sources distributed into fractures can diffuse into adjacent matrix material.
- Radionuclide sources distributed into void space of the cavity and chimney source zones can diffuse into rubble blocks composed of zeolitic or welded tuffs or a matrix composed of vitric tuff having bulk density of in-situ rock.
- Radionuclide sources released from melt glass can diffuse into rubble blocks within the melt glass zone or "puddle" at the base of the cavity.

Table 4.4 Operational characteristics of the "fracture" and "matrix" continua for the five HST source zones.

HST Source Zone	Operational Characteristics	
	"Fracture" Continuum	"Matrix" Continuum
Melt Glass Zone	Melt Glass	Rubble blocks
Cavity	Void Space	Rubble blocks
1.5Rc	Fractures	Matrix
3Rc	Fractures	Matrix
Chimney in zeolitic tuff	Void space of 15% space	Rubble blocks
Chimney in vitric tuff	Void space of5% bulking of in-	vitric tuff having volume of in-

4.3.3 Mass-Based Radionuclide Partitioning into HST Source Zones

Difficulties arise in estimating initial HST source zone radionuclide concentrations, for example:

- Radionuclide concentrations in source zones are typically measured months to years after a test.
- Sorption affects rates of matrix diffusion, thereby affecting fracture concentration over time.
- Conceptual models and properties for addressing fracture-matrix interactions differ in the various source term and flow and transport models used at Rainier Mesa.

Alternative to initializing and assessing uncertainty in source term distributions through radionuclide concentrations, the CLEARWATER and WINESKIN HST models partition the radionuclide sources into the HST source zones based on mass fractions of the source term components. This approach ensures conservation of radionuclide source mass (or total activity) and enables transferability of HST results to other radionuclide transport model

applications such as the N and T-Tunnel flow and transport models regardless of the conceptual model for fracture-matrix interactions.

4.3.4 Scaling of Initial Radionuclide Concentrations

For the fracture continuum of a source zone, the volumetric water content, derived from the product of porosity and saturation, is used to scale the source term distribution to initial radionuclide solute concentrations in the fractures, melt glass, or rubble void space. The HST model initially assumes zero radionuclide concentration in the matrix continuum of all source zones. The matrix diffusion process in the HST model enables redistribution of the radionuclide sources from the fracture continuum to the matrix continuum. The matrix diffusion process has the capacity to reduce initial source term radionuclide concentrations within the fracture continuum by several orders of magnitude within a timeframe of one year or less.

The total amount of redistribution of the source term distribution into the matrix, however, can be limited by the diffusion accessible porosity or maximum penetration depth (Neretnieks, 1980). Therefore, two key parameters for relating radionuclide concentrations to the spatial distribution of the source term in the exchange zone are fracture water volume and diffusive accessible water volume, which are derived from source zone volumes, fracture porosity and saturation, and diffusion accessible matrix porosity and saturation. The concept and model setup for diffusion accessible matrix porosity is further discussed in Sections 5.3.6, 5.3.7, and 5.3.8.

Table 4.5 compiles CLEARWATER and WINESKIN HST model source zone properties for partitioning of the RST into the “fracture” continuum. The “bulk volume” refers to the total volume that contains the “fracture” continuum. The “volume fraction” refers to the fraction of the bulk volume within which the “fracture” continuum occurs. The porosity refers to the porosity of the fracture continuum contained within the volume fraction. For fractured rock, “volume fraction” is set to 1.0 corresponding to fractures occupying 100% of the bulk volume. For the melt glass zone, a volume fraction of 0.50 is set assuming melt glass occupies 50% of the melt glass zone (the other 50% is rubble) with a porosity of 0.136. For the cavity, the volume fraction of voids is set to 0.15 assuming the CLEARWATER cavity rubble is derived from zeolitic tuffs of the LTCU; cavity voids are assigned a porosity of 1.0. Volume fraction and porosity for the chimney fracture continuum are derived similarly to the cavity, depending on whether the rubble originates from zeolitic or vitric tuff.

Table 4.5 CLEARWATER and WINESKIN HST model source zone properties for partitioning of the RST into the "fracture" continuum.

Source Zone	Bulk Volume (m^3)	HST Source Zone Fracture Continuum Properties			
		Volume Fraction	Porosity	Saturation	Initial Water Volume (m^3)
Melt Glass	1.35e5	0.5	0.136	1.0	9,180
Cavity	1.62e6	0.15	1.0	0.012	2,920
1.5Rc	1.09e6(crush) 1.53e6(1.5Rc)	1.0 1.0	0.0048 0.00176	1.0 1.0	7,940
3Rc	6.41e6(2Rc) 1.12e7(2.5Rc) 1.70e7(3Rc)	1.0 1.0 1.0	0.00088 0.00044 0.00022	1.0 1.0 1.0	15,940
Chimney	1.11e6	0.15 (zeolitic) 0.05 (vitric)	1.0 1.0	0.0015 0.0045	695

5 Transport Processes and Properties

5.1 Fracture-Matrix Conceptualization for Transport

The dual-continuum conceptualization for transport is similar to flow (Section 2.5), except with scaling factors to account for the spatial and temporal scales of sorption diffusive transport. The matrix continuum functions as the primary continuum, such that the area of connection of the fracture continuum to the matrix is specified by units of area per unit volume. Matrix and fracture continua are connected to each other within each element, allowing for both advective and diffusive transport in fracture-matrix interactions. All matrix elements are connected to each other, and all fracture elements are connected to each other. This allows for advective transport both within and between the matrix and fracture continua.

Temporal and spatial scales of diffusive transport are important factors to consider in HST modeling. Given large fracture spacing in confining units at Rainier Mesa, it is unlikely that the entire volume of matrix pore space is accessible to diffusive processes, either because of physical barriers (e.g. heterogeneity of porosity and permeability structure) or lengthy fracture spacing.

5.2 Radionuclide Retardation and Matrix Sorption

The CLEARWATER and WINESKIN HST models assume that retardation of radionuclide transport occurs only in the matrix continuum. Therefore, the retardation factor for all

radionuclides is 1.0 in the fracture continuum. Retardation factors for radionuclide transport in the matrix continuum are determined from sorption coefficients (Kd_{rn}), porosity ($\emptyset$), and bulk density (ρ) values determined for radionuclides and matrix materials of hydrostratigraphic units (HSUs) and test altered zones, as follows:

$$R_{rn} = 1 + Kd_{rn}\frac{\rho}{\phi}$$

In the CLEARWATER and WINESKIN HST transport models, radionuclide retardation values are assigned to each matrix rock unit based on Kd_{rn} values specific to radionuclides and HSUs. Table 5.1 provides a range of Kd_{rn} values to address uncertainty, specifically "low," "base case," and "high" values, for sorbing radionuclides in HSUs (Zavarin, 2011a). The base case Kd_{rn} values are based on the mean of the log[Kd_{rn}] distribution, and low and high Kd_{rn} values are based on one standard deviation from the mean of log[Kd_{rn}]. All non-sorbing radionuclides (H-3, C-14, Cl-36, Tc-99, and I-129) are assigned Kd_{rn}values of zero. For HSUs lacking sufficient Kd data, Kd_{rn} is assigned based on hydrogeologic unit (HGU) as defined in NSTec (2007). Table 5.2 provides "low," "base case," and "high" Kd_{rn} values for HGUs (Zavarin, 2011a).

Data or estimates of Kd_{rn} for the LCCU1 are not available. The HST models assign conservative values of $Kd_{rn}$to the LCCU1. However, the LCCU1 unit is only included in the WINESKIN HST model within 3Rc of the working point; elsewhere the LCCU1 is assigned no-flow conditions.

Table 5.1 Kd_{rn}values for HSUs, with minimum, base case, and maximum HST model values given for non-sorbing radionuclides.

Radio-nuclide	Low, Base Case, and High *Kd* (ml/g) Values in HSUs										
	TMLVTA	LVTA	LTCU	OSBCU	RVA	ATCU	LCCU1	LCA3	MGCU	TMWTA	BRA
H-3	0.0	0.0	0.0	0.0	0.0	0.0	0.0	0.0	0.0	0.0	0.0
C-14	0.0	0.0	0.0	0.0	0.0	0.0	0.0	0.0	0.0	0.0	0.0
Cl-36	0.0	0.0	0.0	0.0	0.0	0.0	0.0	0.0	0.0	0.0	0.0
Tc-99	0.0	0.0	0.0	0.0	0.0	0.0	0.0	0.0	0.0	0.0	0.0
I-129	0.0	0.0	0.0	0.0	0.0	0.0	0.0	0.0	0.0	0.0	0.0
Ni-63	76.3 178.7 418.7	346.1 811.2 1901	128.1 300.2 703.4	486.0 1139 2688	25.1 58.9 138.1	1482 3324 7789	- 100.0 -	761.2 1784 4180	8.4 32.7 127.4	11.0 23.5 55.1	42.6 99.9 234.1
Sr-90	3.5 8.1 19.0	14.4 33.7 79.3	811.9 1902 4462	565.0 1324 3105	161.2 377.7 886.1	176.6 413.2 970.3	- 100.0 -	65.5 153.1 359.8	9.3 55.0 323.6	7.3 17.0 39.9	542.9 1272 2984
U-238	0.6 1.1 2.1	2.8 5.1 9.4	1.2 2.4 4.8	4.2 7.9 15.1	1.0 2.4 6.2	12.3 23.4 45.1	- 1.0 -	6.9 13.3 26.1	1.2 3.5 9.8	0.1 0.1 0.3	0.3 0.6 1.2
Pu-238, 239, 240	43.8 102.6 240.2	198.6 465.8 1091	74.7 175.2 410.3	280.6 657.9 1541	19.7 46.1 108.0	820.2 1923 4503	- 100.0 -	1876 4329 9966	1000 3236 10471	5.8 13.5 31.6	24.5 57.4 134.3

Table 5.2 Kd_{rn} values for HGUs, with minimum, base case, and maximum HST model values given for non-sorbing radionuclides.

Radionuclide	Low, Base Case, and High *Kd* (ml/g) Values in HGUs				
	WTA	VTA	TCU	CA	GCU
H-3	0.0	0.0	0.0	0.0	0.0
C-14	0.0	0.0	0.0	0.0	0.0
Cl-36	0.0	0.0	0.0	0.0	0.0
Tc-99	0.0	0.0	0.0	0.0	0.0
I-129	0.0	0.0	0.0	0.0	0.0
Ni-63	22.4 52.5 123.1	153.4 359.4 842.1	425.6 997.3 2337	761.2 1784 4180	8.4 32.7 127.4
Sr-90	172.0 403.0 945.3	6.6 15.4 39.9	630.6 1477 3465	65.5 153.1 359.8	9.3 55.0 323.6
U-238	0.7 1.8 4.7	1.2 2.3 4.2	3.7 7.0 13.6	6.9 13.3 26.1	1.2 3.5 9.8
Pu-238, 239, 240	16.8 39.3 92.0	88.0 206.4 483.2	246.2 577.1 1351	1876 4329 9965	1000 3236 10471

5.3 Matrix Diffusion Processes

Matrix diffusion is an essential transport process to consider in the CLEARWATER and WINESKIN HST models. As conceptualized in the dual continuum flow and transport simulations for the HST models, radionuclide transport from sources initialized in fractures will not be significantly impeded by physical and chemical properties of the matrix unless a matrix diffusion process is included. Simulation of diffusive exchange between fracture and matrix elements is a crucial component of the HST model.

5.3.1 Effective Diffusive Flux

The quantities of "apparent diffusive flux" and "effective diffusive flux" are important to distinguish in models of fracture-matrix interaction (Neretnieks, 1980). Effective diffusive flux accounts for the total diffusive flux between fracture and matrix elements; apparent diffusive flux accounts for the diffusive flux in the aqueous phase. In the NUFT dual continuum formulation for the CLEARWATER and WINESKIN HST models, the effective diffusive flux from the edge of a fracture element into a matrix element is computed by

$$q_{D,effective} = \frac{A_{trans,rn}\phi_{m,\,flow}S_m\tau_{rn}D_{rn}}{L_{m.trans}}\Delta C$$

where:

$A_{trans,rn}$ = effective area of transport between fracture and matrix for the radionuclide
$\phi_{m,\,flow}$ = matrix porosity for flow,
S_m = matrix saturation,
τ_{rn} = tortuosity factor for the radionuclide,
D_{rn} = free molecular diffusivity for the radionuclide,
$L_{m,trans}$ = effective length for diffusive transport into matrix, and
ΔC = difference in concentration from fracture to matrix.

With respect to flow processes, the transport processes can be modeled with different "effective" properties of porosity, area of exchange, and length to account for differences in scale and effective flux for transport components compared to groundwater flow. Importantly, the simulated effects of matrix diffusion strongly depend on the effective properties used in the transport model.

5.3.2 Molecular Diffusivity

Molecular diffusivity varies between about 1.2 to 2.4e-9 m^2/s for radionuclides relevant to source term modeling (Zavarin et al., 2007). With perspective of the uncertainty and variability of other molecular diffusion parameters, the variation in molecular diffusivity between different radionuclides is relatively small. For simplicity, all CLEARWATER and WINESKIN HST models assume a constant molecular diffusivity of 2e-9 m^2/s for all radionuclides.

5.3.3 Tortuosity Factor

Tortuosity decreases bulk matrix diffusivity by increasing the effective length of pathways for diffusion. Stoller-Navarro (2007b) developed a relationship between matrix porosity, ϕ_m and the tortuosity factor, τ, from NNSS data

$$\log\tau = 3.068\phi_m - 1.979\,.$$

For the CLEARWATER and WINESKIN HST modeling, this tortuosity-porosity relationship is applied to the matrix porosity values of the model rock units to obtain base case transport simulation tortuosity factors. For low and high mobility transport simulation cases, the base case transport tortuosity factors are multiplied and divided, respectively, by

factors of 3.0, which represents a typical range of variability of tortuosity data presented in Stoller-Navarro (2007b).

5.3.4 Consideration of Colloidal Transport

Colloids may transport certain sorbing radionuclides and effectively lessen impacts of matrix diffusion. Approximately 90% of the plutonium source term can be expected to be transported by colloids, and thus plutonium can be expected to be relatively more mobile in fractures compared to matrix materials (Zavarin et al., 2011). To account for the effects of approximately 90% colloidal phase plutonium and 10% aqueous phase plutonium in fracture flow conditions pertinent to the CLEARWATER and WINESKIN HST models, tortuosity factors for plutonium species are multiplied by a factor of 0.1 relative to other radionuclides. This decreases the diffusive flux for plutonium by a factor of ten compared to other radionuclide sources for HST cases using the same sets of flow and transport parameters. Zavarin et al. (2011) further discusses colloidal transport processes affecting HST prediction.

5.3.5 Penetration Thickness

A purely diffusive transport process from fracture to matrix is transient along the profile of penetration into the matrix – the longer the matrix diffusion process occurs, the greater the penetration into the matrix material. The length or "thickness" of penetration by diffusive processes can be limited by physical heterogeneity in the pore structure and sorption properties within the matrix material.

To address differences in the length scale of fracture to matrix diffusion because of porosity heterogeneity and different radionuclide matrix sorption values, we adopt the concept of a "penetration thickness", $\tilde{\eta}_{m,rn}$, defined by Neretnieks (1980). $\tilde{\eta}_{m,rn}$ is a hypothetical distance into a rock matrix, m, at which concentrations of a sorbed radionulicide, rn, are at equilibrium between fracture and matrix. The concept of penetration thickness has been used previously in HST modeling by Pawloski et al. (2001) to develop effective transport porosity for single continuum model.

Assuming the fracture-to-matrix diffusive flux is caused by a constant fracture concentration adjacent to homogeneous matrix material for a contact time, Δt, the penetration thickness, $\tilde{\eta}_{m,rn}$, is calculated by

$$\tilde{\eta}_{m,rn} = \frac{2}{\pi^{1/2}} \left(D_{rn} \frac{S_m \tau_{rn}}{R_{rn}} \Delta t \right)^{1/2} \qquad (5.1).$$

Importantly, $\tilde{\eta}_{m,rn}$ is dependent on the radionuclide transport retardation factor, R_{rn}, for the matrix rock, with a larger retardation coefficient producing smaller penetration

thickness. The concept of penetration thickness highlights relationships between the timescale of matrix diffusion and length scales used in dual-continuum modeling:

- Fracture to matrix contact time, Δt, can be used to estimate an effective penetration thickness assuming parameter values for molecular diffusivity, saturation, tortuosity factor, and retardation.
- Uncertainty in the volume of matrix material accessible to matrix diffusion, which relates to the product of penetration thickness and fracture surface area per unit volume, can be addressed for all radionuclides and rock type by varying the contact time parameter, Δt.
- Given the 1,000-year timeframe of the HST model, contact time should not exceed 1,000 years.

5.3.6 Maximum Penetration Thickness and Diffusion Accessible Matrix

Matrix diffusion can be limited by the effective depth of diffusion accessible matrix or "maximum penetration thickness" because of limits to contact time (how long the component in the solute in the fracture contacts the matrix) or matrix porosity connectivity (Moreno and Crawford, 2009). In terms of contaminant transport modeling, the depth of diffusion accessible matrix represents the maximum effective distance to which contamination originating within fractures penetrates the matrix. The concept of diffusion accessible matrix in a fractured rock is similar to the concept of "effective porosity" discussed in Stoller-Navarro (2007b) for welded tuffs, where effective porosity for tracer transport is found to be greater than fracture porosity and less than matrix porosity.

The modeling timeframe for matrix diffusion processes may also limit the length scale for matrix diffusion. Importantly, the penetration thickness for matrix diffusion with contact time of 1,000 years, the UGTA modeling time, may be less than the length scales of matrix blocks. Thus, in the modeling timeframe, matrix diffusion cannot necessarily be expected to produce concentrations in equilibrium between fracture and the entire volume of matrix materials within the same model grid block.

In terms of modeled matrix porosity for transport simulation, the depth of diffusion accessible matrix limits the amount of porosity available for matrix diffusion. Only the portion of matrix porosity that can be penetrated by contamination is considered by the transport model as matrix porosity accessible to diffusion. It is possible for certain model rock types and radionuclide classes, however, that the entire matrix porosity is accessible to matrix diffusion, depending on matrix block size and maximum penetration thickness.

There is some evidence that the penetration depth is largely determined by physical aspects of the pore structure. According a modeling study for radionuclide waste repositories by Moreno and Crawford (2009),

"…the impact of limited pore connectivity is similar for all the radionuclides, independent of the sorption constant. It is mainly determined by the depth of the diffusion accessible rock…the effective penetration depth associated with retardation is independent of sorption capacity for the radionuclides."

Using this concept, maximum penetration thickness and, therefore, the effective matrix transport porosity can be reasonably assigned the same value for all radionuclides in the same rock type if the impact of pore connectivity is similar for all radionuclides. In this case, the depth of diffusion accessible matrix into the NUFT dual-continuum model or maximum penetration thickness, $\eta_{m,\max}$, is calculated from the penetration thickness for a non-sorbing tracer, $\tilde{\eta}_{m,tracer}$, assuming a contact time, Δt. Implementation of maximum penetration thickness requires two adjustments to the effective transport properties:

- The effective matrix transport length, $L_{m,trans}$, must be scaled relative to the effective matrix flow length by a factor of $0.5\times\left(\eta_{m,\max} / L_{m,flow}\right)$, where $L_{m,flow}$ is the "block radius" or half-length between fractures in the matrix. This defines $L_{m,trans}$ equivalent to the distance from the edge of the fracture to the center of the volume of matrix-diffusion accessible porosity.
- The effective matrix transport porosity is scaled relative to the matrix porosity considering a factor of $\left(\eta_{m,\max} / L_{m,flow}\right)$.

However, given the 1000-year timeframe of the UGTA modeling, the maximum penetration thickness for a sorbing radionuclide could be time-limited and, therefore, smaller compared to maximum penetration of a non-sorbing radionuclide limited by pore connectivity. Penetration depth for sorbing radionuclides is also calculated using Equation 5.1 with the radionuclide retardation coefficient and contact time of 1000 years. The model uses this radionuclide specific penetration depth if it is smaller than the penetration depth for a tracer with a given contact time.

Figure 5.1 is a schematic diagram for how the diffusion accessible porosity parameter relates to the maximum penetration depth and matrix block parameters used in the HST model for the situation of parallel fractures. The block radius parameter scales according to fracture spacing in in-situ rock and to rubble block radius in the melt glass, cavity, and chimney zones.

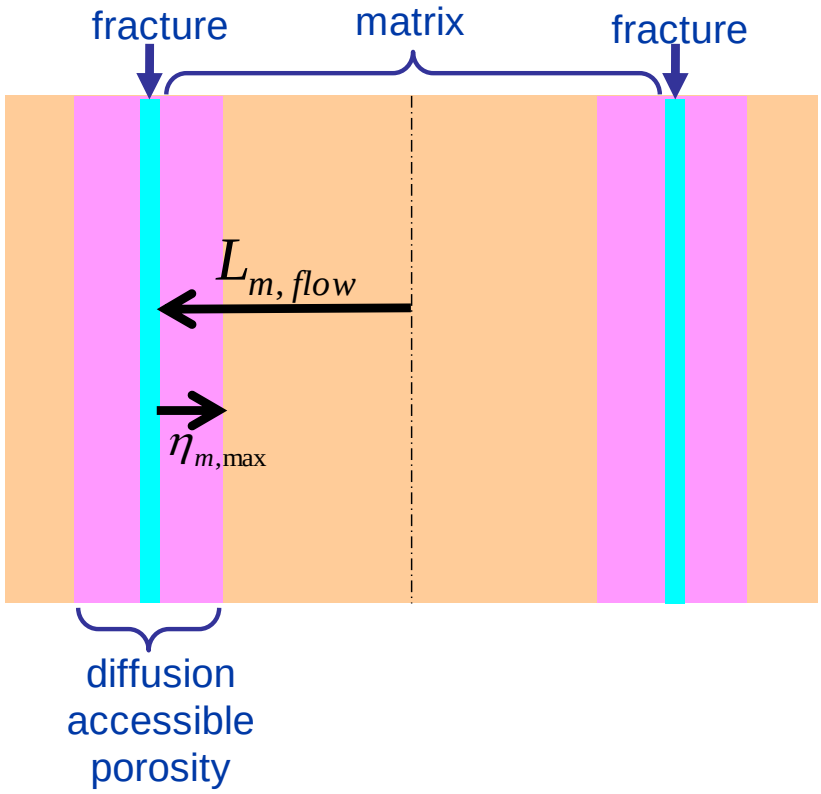

Figure 5.1 Schematic diagram showing how diffusion accessible portion of matrix relates to matrix block radius, L_m, and maximum penetration depth, $\eta_{m,\max}$.

5.3.7 Effective Matrix Transport Porosity and Dimensionality

The effective porosity value for transport in the matrix, $\phi_{m,trans}$, accounts for both (1) the finite penetration thickness and (2) the dimensionality of the fracture matrix system. The dimensionality accounts for the dependence of the volume of diffusion accessible matrix on both shape of matrix blocks and maximum penetration thickness. For example, parallel planar fractures represent a dimensionality of 1.0, whereas fracture surfaces that envelop the matrix at all angles, such as void space around rubble, represent a dimensionality of 3.0.

In the CLEARWATER and WINESKIN HST models, the effective matrix transport porosity, $\phi_{m,trans}$, is derived from the maximum penetration thickness, $\eta_{m,\max}$, and dimensionality, d, by

$$\phi_{m,trans} = \phi_{m,\,flow}\left[1 - \frac{\left(L_{m,\,flow} - \eta_{m,\max}\right)^d}{\left(L_{m,\,flow}\right)^d}\right]$$

When $d = 1$, as for parallel fractures with constant dip and strike, the relationship between $\phi_{m,\,flow}$ and $\phi_{m,trans}$ reduces to

$$\phi_{m,trans} = \phi_{m,\,flow} \frac{\eta_{m,\max}}{L_{m,\,flow}}$$

The effective matrix transport porosity also scales component concentrations in the matrix to the volume of matrix occupied by the maximum penetration thickness.

5.3.8 Effective Area of Transport Between Fracture and Matrix

The effective diffusive flux of a sorbing radionuclide is greater than the apparent diffusive flux because of partitioning to the solid phase. To account for the effect of Kd on effective diffusive flux, the effective area of transport between fracture and matrix per unit volume, $A_{trans,rn}$, is obtained by multiplying the fracture area per unit volume for flow, A_{flow}, by the radionuclide retardation factor, R_{rn}

$$A_{trans,rn} = A_{flow} R_{rn}$$

Apparent diffusivity from fracture to matrix materials, which accounts for the apparent aqueous phase concentration profile in a matrix with non-zero *Kd*, is a factor of R_{rn} lower than the effective diffusivity, which accounts for the total flux from fracture to matrix materials (Neretnieks, 1980).

5.4 HST Model Transport Properties

5.4.1 Base Case Matrix Transport Properties

The base case HST model transport simulations are based on the HST flow model properties (Section 3.5) and the base case matrix transport properties. In all HST model simulations, fracture transport properties are not changed from the fracture flow properties assuming sorption occurs only in the matrix continuum. Fracture retardation factors and tortuosity factors are set to 1.0 for all radionuclides. Transport model rock type names are derived in the same manner as for flow model rock type names (Section 3.5.1).

The base case matrix transport properties for the model matrix continuum of each model rock type (Table 5.3) consist of effective length, effective porosity, tortuosity factor, and retardation factors for Ni, Sr, Pu, and U radionuclide classes. The effective length for transport is based on the effective matrix transport length (Section 5.3.5) assuming a contact time of 1 year. Sensitivity studies on "contact time" were carried out to determine contact time values that yield simulated radionuclide concentrations consistent with observed data from sampling of test cavities and exchange zones ("hot well" data) and

tunnel discharge (Chapter 6). The effective transport porosity is based on the porosity accessible to matrix diffusion, as derived from the dimensionality and effective lengths for flow and transport (Section 5.3.7). The tortuosity factor is derived from a correlation relationship to porosity (Section 5.3.3) developed by Stoller-Navarro (2007b). For Pu radionuclide classes, tortuosity is lowered by a factor of ten to account for effects of colloidal transport (Section 5.3.3). Retardation factors are calculated from the base case Kd values, matrix porosity, and bulk density (Section 5.2).

Table 5.3 Base case effective flow and transport length scales and porosity, tortuosity, and retardation factors for the matrix continuum of model rock types.

		Effective Length		Effective Porosity			Retardation Factor			
Rock	d	Flow	Transport	Flow	Transport	τ	Ni	Sr	Pu	U
m-TMWTA	2	0.5	0.064	0.206	0.0925	0.01	285.2	206.2	164.2	2.8
m-BRA	2	0.5	0.068	0.231	0.1089	0.01	1013.2	12886	582.2	7.4
m-SWA	2	0.5	0.068	0.231	0.1089	0.01	635.7	4872	475.7	23.3
m-RVA	2	0.5	0.060	0.179	0.0757	0.01	836.3	5360	655.5	35.3
m-CH-WTA	3	0.25	0.064	0.206	0.1826	0.01	635.7	4872	475.7	23.3
m-TMLVTA	3	6	6	0.353	0.353	0.01	1180.4	54.3	678.2	8.4
m-AA	3	6	6	0.353	0.353	0.01	1180.4	54.3	678.2	8.4
m-LVTA1	3	6	6	0.411	0.411	0.01	4619.2	193.1	2652.7	30.1
m-LVTA2	3	6	6	0.411	0.411	0.01	4619.2	193.1	2652.7	30.1
m-CH-VTA	3	0.25	0.25	0.353	0.353	0.01	2373.2	102.7	1363	16
m-UTCU1	1	6	0.0723	0.264	0.0064	0.01	8916.4	13206.2	5160	64
m-LTCU	1	6	0.073	0.264	0.0064	0.01	2684.5	17004.6	1567.5	22.2
m-BRCU	1	6	0.073	0.264	0.0064	0.01	2684.5	17004.6	1567.5	22.2
m-1.5RC-LTCU	2	1	0.073	0.264	0.0714	0.01	2684.5	17004.6	1567.5	22.2
m-2RC-LTCU	1.5	2	0.073	0.264	0.0284	0.01	2684.5	17004.6	1567.5	22.2
m-CH-TCU	3	0.25	0.073	0.264	0.2450	0.01	2684.5	17004.6	1567.5	22.2
m-OSBCU	1	6	0.072	0.258	0.0062	0.01	10815	12570	6248.9	75.7
m-1.5RC-OSBCU	2	1	0.072	0.258	0.0691	0.01	10815	12570	6248.9	75.7
m-2RC-OSBCU	1.5	2	0.072	0.258	0.0274	0.01	10815	12570	6248.9	75.7
m-ATCU	1	6	0.057	0.162	0.0031	0.01	51529	6531.1	30389	370.4
m-1.5RC-ATCU	2	1	0.057	0.162	0.0349	0.01	51529	6531.1	30389	370.4
m-2RC-ATCU	1.5	2	0.057	0.162	0.0137	0.01	51529	6531.1	30389	370.4
m-LCCU1	1	6	0.070	0.241	0.0056	0.01	3003	4133	1753	25
m-1.5RC-LCCU1	2	1	0.070	0.241	0.0625	0.01	3003	4133	1753	25
m-2RC-LCCU1	1.5	2	0.070	0.241	0.0248	0.01	3003	4133	1753	25
m-MGCU	1	6	0.025	0.03	0.00025	0.01	2947	4946.8	291235	313
m-1.5RC-MGCU	2	1	0.025	0.03	0.0029	0.01	2947	4946.8	291235	313
m-2RC-MGCU	1.5	2	0.025	0.03	0.0011	0.01	2947	4946.8	291235	313
m-CAV	3	0.25	0.073	0.264	0.2450	0.01	2684.5	17004.6	1567.5	22.2
m-CAV-LTCU	3	0.25	0.073	0.264	0.2450	0.01	2684.5	17004.6	1567.5	22.2
m-MGZ	3	0.25	0.052	0.132	0.1053	0.01	2684.5	17004.6	1567.5	22.2
m-CRUSH	2.5	0.1	0.072	0.259	0.259	0.01	2684.5	17004.6	1567.5	22.2

5.4.2 Low and High Mobility Properties

Three matrix properties – diffusion accessible matrix porosity, Kd_{rn}, and tortuosity – are controlling factors for radionuclide mobility in the CLEARWATER and WINESKIN HST models. As discussed in Sections 5.3.5 and 5.3.6, diffusion accessible porosity can be scaled by the maximum penetration thickness for a given contact time, which was assigned a value of 1 year for the base case transport simulations. Ranges of Kd_{rn} are provided in Tables 5.1 and 5.2, and ranges of tortuosity factors are discussed in Section 5.3.3.

For the low mobility transport simulation case, the following changes are applied to matrix properties:

- Diffusion accessible matrix porosity is increased, where available, by a factor of $\sqrt{10}$, reflecting an increase of contact time from 1 to 10 years (Equation 5.1).
- The upper range value of Kd_{rn} from Table 5.1 is used, reflecting a one log-scale standard deviation increase from the base case Kd_{rn} values.
- Tortuosity factors are increased by a factor of 3.0 relative to the base case values.

For the high mobility transport simulation case, the following changes are applied to matrix properties:

- Diffusion accessible matrix porosity is decreased, where available, by a factor of $\sqrt{10}$, reflecting a decrease of contact time from 1 to 0.1 years (Equation 5.1).
- The lower range value of Kd_{rn} from Table 5.1 is used, reflecting a one log-scale standard deviation decrease from the base case Kd_{rn} values.
- Tortuosity factors are decreased by a factor of 3.0 relative to the base case values.

The low and high mobility matrix transport parameters are selected to provide reasonable ranges to account for the composite uncertainty of the most sensitive transport properties in the CLEARWATER and WINESKIN HST models.

5.4.3 Comparison of Matrix Flow Porosity, Matrix Effective Transport Porosity, and Fracture Porosity

In the current HST model, the matrix effective transport porosity is lower than or equal to the matrix flow porosity where matrix-fracture interactions occur, such as in welded and zeolitic tuffs. In addition, the interior of rubble blocks may not be entirely accessible to diffusion.

Figure 5.2 (upper left) shows matrix porosity used in the CLEARWATER HST flow model. In the flow model, the matrix is entirely accessible to flow. Figure 5.2 (upper right) shows matrix effective transport porosity, which is identical to matrix flow porosity in vitric tuffs, for example, but lower than matrix flow porosity in welded and zeolitic tuffs because of limited volume of exchange within the matrix. Figure 5.2 (lower) shows fracture porosity.

Comparison of the matrix effective transport porosity to matrix and fracture porosity shows that matrix effective transport porosity values generally falls between fracture and matrix porosity, depending on the rock type and fracture spacing. In the HST model, the effective porosity for transport is the sum of the fracture porosity and the matrix effective transport porosity. Importantly, in dual-permeability approach used in the HST models, flow and transport exchanges between the fracture and matrix are accounted for (Section 2.5).

In zeolitic tuffs where fracture spacing can average on the order of 10 m (Reeves, 2008), the matrix effective porosity can be very small relative to the total matrix porosity because of the limited surface area of fractures per unit volume and large distances between fractures (Section 5.3). Importantly, the "matrix effective transport porosity" is largely a model conceptualization resulting from limited model resolution (i.e. 30 m by 30 m by 15 m scale grid blocks). Particle-based transport methods can account for multi-scale fracture-matrix transport processes in a more detailed fashion typically by assuming steady-state flow. However, the CLEARWATER and WINESKIN HST models are set up to account for transient flow as has been done in previous HST modeling (Pawloski et al., 2001; Carle et al., 2007; Carle et al., 2008; Maxwell et al., 2008). Moreover, available particle-based methods are not set up for transient flow in dual-permeability systems. The matrix effective transport porosity addresses cumulative effects of matrix diffusion on radionuclide transport and, subsequently, significantly reduces the fraction of source term present in the more mobile fracture transport pathways (Section 4.1.4). Matrix effective transport porosity is a key calibration and uncertainty parameter for the CLEARWATER and WINESKIN HST models.

5.4.4 Comparison to Previously Published Models

Ebel and Nimmo (2009, 2010) take an alternative extreme viewpoint to maximize radionuclide transport by ignoring effects of matrix diffusion in assessment of the CLEARWATER, WINESKIN, and other underground nuclear tests at Rainier Mesa and Shoshone Mountain. The Ebel and Nimmo (2009, 2010) models effectively assume zero matrix porosity accessible to diffusion in zeolitic tuff, welded tuff, and carbonate rocks. The CLEARWATER and WINESKIN HST models could assess this "alternative" conceptual model of zero matrix porosity accessible to diffusion. However, such an extreme case is not considered realistic for current HST and flow and transport models.

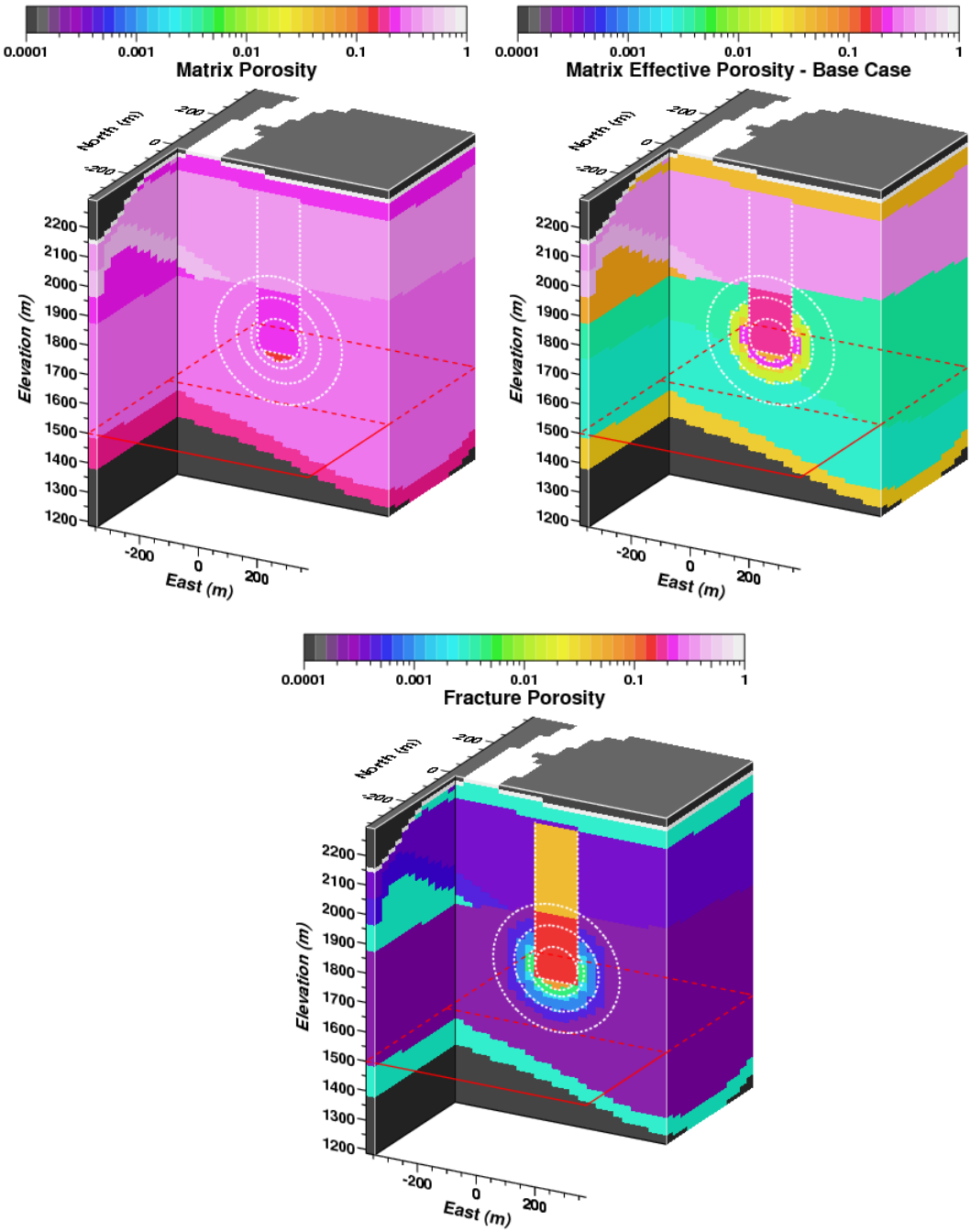

Figure 5.2 Three porosities: (1) matrix, (2) matrix effective transport, and (3) fracture porosity used in current CLEARWATER HST model. The model Rc of 72 m is derived from maximum announced yield (USDOE, 2015) and Pawloski (1999) as detailed in Section 2.7.2.

5.5 Definition of Time Zero

The CLEARWATER and WINESKIN HST models must establish a "time zero" to relate the time of flux input to the SZ model to the time the HST model outputs. The 2-D CLEARWATER HST process modeling results, including thermal and gas-phase flow and transport, indicate that early time test-related transients affecting source-term re-distribution are largely complete within one day for tritium and carbon-14 (Zavarin et al., 2011). Early time test-related transients will have more effect on redistribution of volatile radionuclides compared to non-volatile radionuclides. In the 1,000-year timeframe of HST and SZ modeling, it is reasonable to assume that initial radionuclide distributions in the CLEARWATER HST model pertain to the time of the test. Therefore, the "time zero" of the CLEARWATER and WINESKIN HST models is the time of test detonation for each test.

5.6 Transport Code

The HST models use the "US1C" module of the NUFT numerical simulation code to model single-component transport with variably saturated flow in a dual-continuum (fracture and matrix) integrated finite-difference mesh. The NUFT code is documented by Nitao(2000a and b), and specifics of the US1C module are documented in Nitao (2005). The version date is 11-17-04. Quality assurance for the NUFT code is documented in Carle et al. (2014).

The US1C module of NUFT was selected because this transport code is directly compatible with the US1P module of NUFT (Section 3.10), the variably saturated flow code used in the CLEARWATER and WINESKIN HST modeling and the T-Tunnel flow and transport modeling (Section 3.10). The US1C transport code has the important capability to handle both fracture-matrix interactions and transient flow, which occurs in the CLEARWATER and WINESKIN HST models from post-test effects on the rock porosity, permeability, and saturation in the test-altered zones (Section 2.6).

The main reason for using the US1P-US1C package of NUFT codes is to enable an integrated evaluation of transient variably-saturated groundwater flow and transport in a fracture-matrix system from ground surface to aquifer systems using a dual-permeability conceptual model. Additionally, US1P-US1C NUFT model setup is complementary to other HST models which use the USNT NUFT module to simulate and evaluate coupled thermal gas-liquid phase flow and multi-component transport, such as the 2-D HST models of the CLEARWATER and RAINIER tests (Zavarin et al., 2011).

6 HST Transport Modeling Approach and Results

6.1 HST Transport Modeling Approach

The HST transport modeling approach follows a stepwise procedure:

- Establish matrix rock properties (Section 3.4.1 and Appendices A through D).
- Develop a hydrogeologic conceptual model using the hydrostratigraphic framework model (HFM) to establish the geometry of rock units in the hydrogeologic setting.
- Consider the observations of flow processes at Rainier Mesa, including fracture-dominated flow in tuff confining units and potential for lateral flow in saturated welded tuff aquifers (e.g., the RVA) and along interfaces between of vitric tuff aquifers and tuff confining units (e.g. LTCU and LVTA1 or LVTA2).
- Develop flow models calibrated to NET-INFIL3 by LANL or other infiltration models, SZ model potentiometric head and flux values, observed head values (only U12q available), and saturation observations.
- Define locations and properties of test-altered zones based on data, observations, and descriptions in literature.
- Simulate and calibrate variably saturated flow in a fracture-matrix flow system, using bulk fracture permeability as the major parameter for calibration to flow for all six NET-INFIL3 realizations.
- Define radionuclide source zones, including spatial ranges of uncertainty for each radionuclide class.
- Initialize radionuclide sources for each radionuclide class by applying a unit concentration to the liquid phase in the fracture continuum of a source zone.
- Simulate radionuclide transport separately for each radionuclide class and source zone using matrix diffusion and sorption parameters specific to the different HST model rock types.
- Address the spatial variability of the source term based on the RST, observations of aqueous radionuclide activity in similar hydrogeologic settings, and detailed HST process modeling (Zavarin et al., 2011)
- Address spatial variability in radionuclide source distribution by linearly combining source zone-specific transport simulations normalized by the total radionuclide isotope activity given in the RST (Zavarin et al., 2011).
- Address uncertainty in the radionuclide source distribution by applying a range of radionuclide source mass fractions in each source zone bounded by the spatial limits specified by Zavarin et al. (2011).
- Address uncertainty in transport parameters by repeating the HST simulations with sets of lower and higher radionuclide mobility parameter values (e.g., Kd, tortuosity, and porosity accessible to matrix diffusion).

- Compare simulated radionuclide concentrations to observational data (Section 6.5). Adjust transport parameters to be consistent with the range of observed aqueous radionuclide activities in similar hydrogeologic settings.
- Assume that for a given SZ model head condition driving the HST model discharge flow boundary conditions, HST model uncertainty in radionuclide source distribution and transport parameters is much greater than HST model uncertainty in flow parameters. Assessment of uncertainty of flow parameters is not considered except for the most sensitive and uncertain flow parameter - fracture permeability in the LTCU and OSBCU.

Transport simulation for each radionuclide class is run separately for each source zone using an initial unit concentration in the source zone and zero elsewhere within the HST model domain. This method requires 21 transport simulations for each test and set of flow and transport parameters, based on 5 tracer source zones and 4 sorbing radionuclide source zones for each of the 4 sorbing radionuclide classes (the chimney zone is combined into the 3Rc zone for non-volatile sorbing radionuclides).

6.2 Implementation of Transport Sensitivity and Uncertainty Analysis

As discussed above, HST simulations of radionuclide concentration are computed from linear combinations of the radionuclide class transport simulations for each source zone normalized by the RST applied at model time zero. This enables an efficient sensitivity and uncertainty analysis, particularly for magnitude and spatial distribution of radionuclide sources.

The parameters for CLEARWATER and WINESKIN HST model sensitivity and uncertainty analysis are:

- Source Term Parameters
  - Radionuclide isotope source value (pCi)
  - Fraction of source in melt glass
  - Fraction of melt glass source released
  - Radial range of source distribution (Rc)
- Radionuclide Mobility
  - Groundwater flow
  - Tortuosity factor
  - Kd
  - Effective matrix transport porosity

6.2.1 Source Term Parameters

The CLEARWATER and WINESKIN HST model enables continuous variation of the range of source parameters specified in the HST source model (Zavarin et al., 2011). Therefore,

given probability distributions for the source parameters, percentiles of uncertainty associated with the source parameters can be propagated into evaluation of uncertainty of the CLEARWATER and WINESKIN HST fluxes delivered to the SZ model boundaries.

6.2.2 Radionuclide Mobility Parameters

The combined effects of uncertainty in groundwater flow, tortuosity, Kd, and effective matrix transport porosity are difficult to quantify. While reasonable ranges of values for tortuosity (Stoller-Navarro, 2007b, 2008b) and Kd (Zavarin, 2011a; Zavarin et al., 2011) for Rainier Mesa or similar rocks can be established, uncertainties in the groundwater flow and the effective matrix transport porosity remain difficult to quantify. Evaluation of uncertainties derived from different radionuclide mobility parameters are also intertwined with non-linear effects on transport processes including early-time test-induced transients.

Another complication in evaluation of radionuclide mobility parameters is that a separate transport simulation is required to evaluate any sensitivity to a single radionuclide mobility parameter. This makes HST uncertainty analysis of radionuclide mobility parameters far more computationally intensive than evaluation of radionuclide source term parameters (Section 6.2.1).

To efficiently assess sensitivity and uncertainty of radionuclide mobility parameters, the CLEARWATER and WINESKIN HST models investigate three sets of radionuclide mobility parameters – low mobility, base case, and high mobility (Table 6.1). For groundwater flow, flow realizations derived from three NET-INFIL3 surface infiltration realizations are used, with lowest water flux (NET-INFIL3 Realization 7) in the low mobility case, a mid-range water flux (NET-INFIL3 Realization 11) for the base case, and highest water flux (INFIL3 Realization 29) in the high mobility case. For tortuosity factor, the base case parameters are established from a porosity-dependent model given in Stoller-Navarro (2007b) with uncertainty factors of 3.0 for low and high mobility cases and a 0.1 multiplier for colloidal transport (Section 5.3.3). For Kd, the base case parameters are established from mid-range values, and the low and high mobility cases are established from 1.0 standard deviation values (Zavarin, 2011a) where available (Section 5.2). Effective matrix porosity values are derived from contact times (Section 5.4.2) consistent with effective tracer porosities given in Stoller-Navarro (2007b), with a factor of $\sqrt{10}$ multiplied for the low mobility case (higher effective matrix porosity) and a factor of $\sqrt{10}$ divided for the high-mobility case (lower effective matrix porosity).

6.2.3 Further Work

Further work could focus on effects of two main variables affecting radionuclide transport prediction for the CLEARWATER and WINESKIN HST models: (1) the groundwater flow model, and (2) effective matrix transport porosity.

Table 6.1 Radionuclide mobility parameters used for low mobility, base case, and high mobility sensitivity cases.

Radionuclide Mobility Set	Groundwater Flow	Tortuosity	Kd	Matrix Effective Porosity for Transport
Low Mobility	NET-INFIL3 Realization 7	Base Case multiplied by 3.0	Mid-range plus 1.0 Standard Deviation	0.316 year tracer contact (Neretnieks, 1980)
Base Case	NET-INFIL3 Realization 11	Calculated (Section 5.3.3)	Mid-range value	1 year tracer contact time (Neretnieks,1980)
High Mobility	NET-INFIL3 Realization 29	Base Case divided by 3.0	Mid-range minus 1.0 Standard Deviation	3.16 year tracer contact time (Neretnieks, 1980)

The SZ flow model calibration was not completed before the CLEARWATER and WINESKIN HST modeling occurred, so uncertainty related to the regional flow system was not completely assessed. No boundary conditions for regional groundwater flow were provided by the SZ flow model. Only a range of fixed head boundary conditions were implemented thus far in HST modeling (Section 2.4.2). Ideally, the SZ model could have provided a probability distribution or limited range for the head boundary conditions at the HST-SZ model interfaces.

The effective matrix transport porosity is a key parameter for quantifying radionuclide concentrations – too low will lead to overprediction of fluxes and concentrations, and too high will lead to underprediction of fluxes and concentrations at the SZ model interfaces. Since direct measurements of radionuclide concentration for the CLEARWATER and WINESKIN tests are not available, calibration of matrix effective transport porosity cannot be directly constrained. Alternatively, reasonable ranges of concentration for model calibration can be inferred from radionuclide concentration data from similar hydrogeologic settings. These include other tests situated in tuff confining units at NNSS or Rainier Mesa tunnel water and discharge (Section 6.5).

If final SZ flow model results become available, the CLEARWATER and WINESKIN HST models could be re-calibrated for flow, and sensitivity studies on radionuclide transport could be re-run. The results of the sensitivity studies could improve the accuracy of matrix effective transport porosity values based on comparison to modeled and observed values of radionuclide concentrations. Uncertainty in the predictions of CLEARWATER and WINESKIN HST radionuclide transport fluxes would be reduced, although the RST will remain the largest uncertainty factor for some radionuclides.

6.3 Concentration Evolution for Radionuclide Sources

This section reviews concentration results from the CLEARWATER and WINESKIN HST model base case transport simulations for radionuclide transport for eleven radionuclides: H-3, C-14, Cl-36, I-129, Tc-99, Ni-63, Sr-90, U-238, Pu-238, Pu-239, and Pu-240. Review of

concentration evolution for radionuclide sources provided in this section is not exhaustive and is intended to highlight and illustrate general HST model results for the radionuclide transport simulations.

6.3.1 Current HST Model Radionuclide Sources

The eleven radionuclide sources included in the current CLEARWATER and WINESKIN HST model results do not correspond exactly to the HST radionuclide source term list derived from most recent RST documentation (Zavarin et al., 2011) as discussed in Section 4.1.1. The HST model radionuclide source term list was finalized after an interim list was provided for the CLEARWATER and WINESKIN HST model calculations were completed for this report. The only differences from the HST model radionuclide source term list are that Ni-63 is included and Am-241 is not. Future CLEARWATER and WINESKIN HST model calculations will include Am-241 (Navarro, 2017a). Inclusion of the Ni-63 CLEARWATER and WINESKIN HST model results obtained so far is, nonetheless, useful for comparison to the final RST evaluation that Ni-63 is not a radionuclide source of concern for HST and SZ transport model evaluation.

6.3.2 CLEARWATER

6.3.2.1 H-3

The initial tritium or H-3 source term varies in a radial spatial distribution around the detonation point between 1.5 and 3Rc as prescribed by the RST model (Zavarin et al., 2011). Compared to a source term contained within 1.5Rc, a 3Rc source distribution will project a portion of the source term closer to the SZ model interface. Figure 6.1 shows temporal evolution of CLEARWATER HST model simulation of H-3 concentration at 0, 1, 10, and 100 years for base case transport parameters and initial 3Rc distribution of a mean H-3 source in liquid phase of the fracture continuum. Initial concentrations (at time zero) in the fractures are over 100,000 MCL (1 MCL = 20,000 pCi/L). By one year, a noticeable drop in H-3 fracture concentrations is evident in the cavity and upper portions of the source zones within 3Rc because of matrix diffusion and advective transport. H-3 transport moves primarily downward toward and below the SZ model interface (red outlined horizontal plane at 1,500 meters elevation). By 10 years, an H-3 plume is approaching the Redrock Valley aquifer (RVA). Maximum plume concentrations are on the order of 10,000 MCL. By 100 years, effects of radioactive decay have greatly reduced H-3 concentrations – to about 100 MCL or less. Radioactive decay alone reduces H-3 concentrations by a factor of 66 per 100 years. This base case set of model parameters predicts H-3 flux above the MCL at the SZ model interface lasting for up to 200 years.

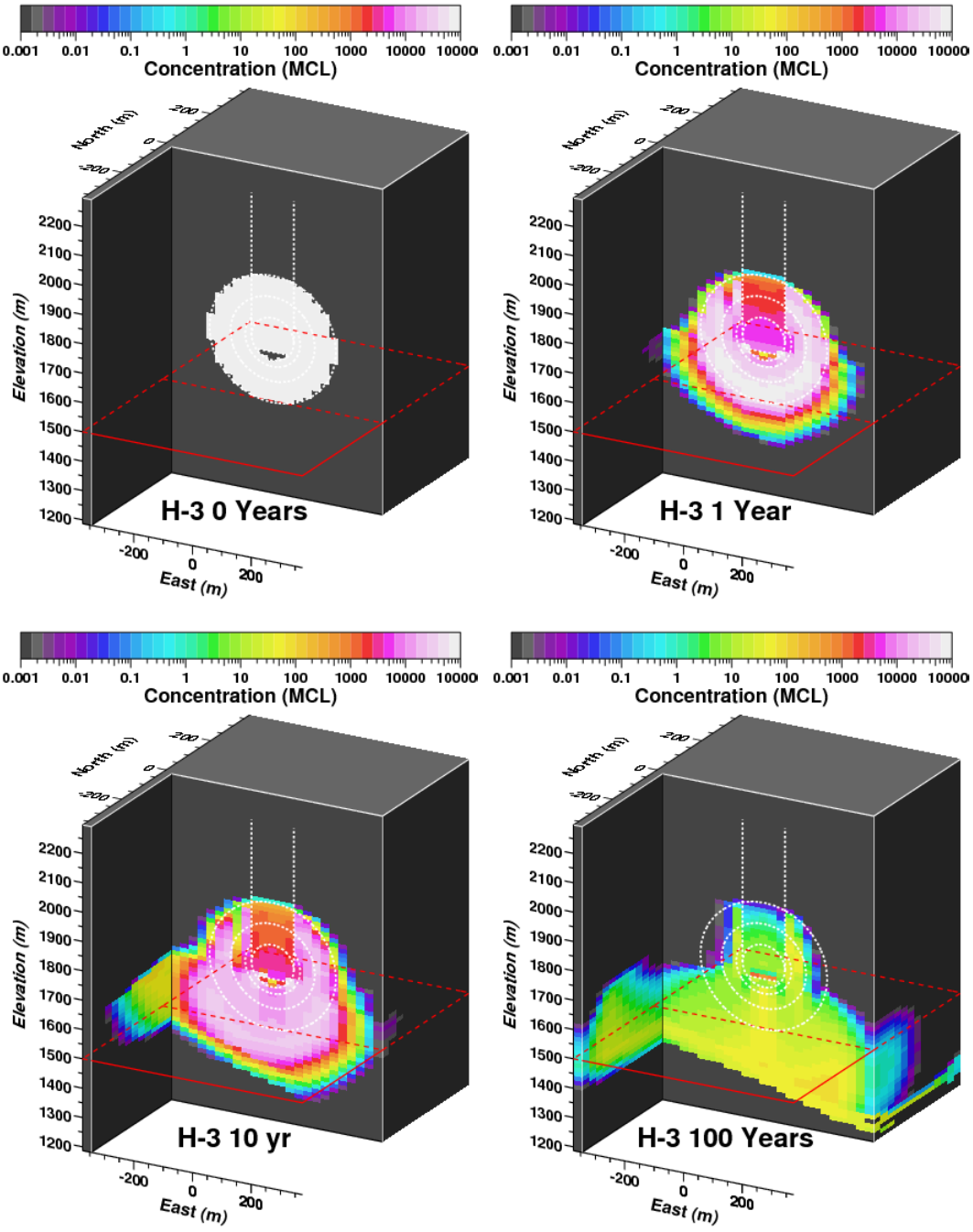

Figure 6.1 Temporal evolution of CLEARWATER HST model simulation of H-3 concentration at 0, 1, 10, and 100 years for a base case transport parameters and initial 3Rc distribution of a meanH-3 source in the liquid phase of fractures. The model Rc of 72 m is derived from maximum announced yield (USDOE, 2015) and Pawloski (1999) as detailed in Section 2.7.2.

6.3.2.2 C-14

Figure 6.2 shows CLEARWATER HST model simulation of C-14 concentration at 10 years for base case transport parameters and initial 3Rc distribution of a mean C-14 source in liquid phase of the fracture continuum. Because the CLEARWATER HST model treats the C-14 source as a tracer, the C-14 concentration distribution is similar to H-3 at 10 years, but scaled to the C-14 total source activity and MCL. In the long term, the longer C-14 half-life causes the model to show persistence of C-14 above the MCL through 1000 years. However, the CLEARWATER HST model results in this report do not include consideration of the thermal, gaseous, and chemical processes that account for early-time C-14 redistribution into the vadose zone. Future 2-D CLEARWATER HST model results extended beyond those presented in Zavarin et al. (2011) could be used to justify reduction of aqueous C-14 activity in HST models.

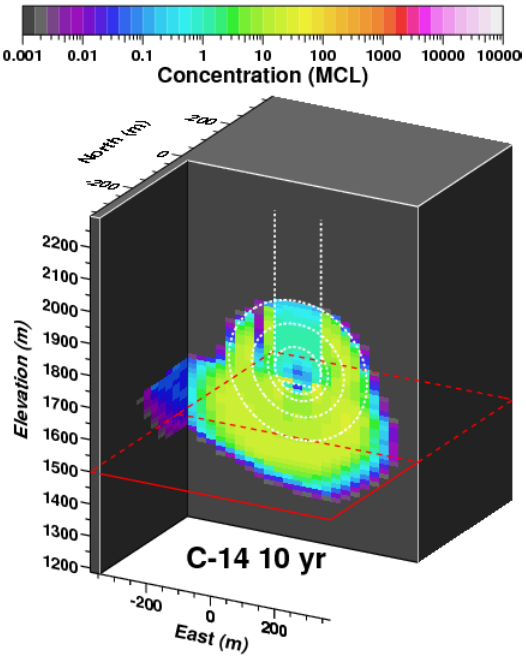

Figure 6.2 CLEARWATER HST model simulation of C-14 concentration at 10 years for base case transport parameters and initial 3Rc distribution of a mean C-14 source in the liquid phase of fractures. The model Rc of 72 m is derived from maximum announced yield (USDOE, 2015) and Pawloski (1999) as detailed in Section 2.7.2.

Cl-36

Figure 6.3 shows CLEARWATER HST model simulation of Cl-36 concentration from 10 years for base case transport parameters and initial 3Rc distribution of a mean Cl-36 source in liquid phase of the fracture continuum. Because the CLEARWATER HST model treats the Cl-36 source as a tracer, the Cl-36 concentration distribution is similar to H-3 at 10 years, but scaled to the Cl-36 source magnitude and MCL. In the long term, the CLEARWATER HST model simulation indicates Cl-36 concentrations at the SZ model interface can persist at maximum concentrations of a few MCL for over 100 years.

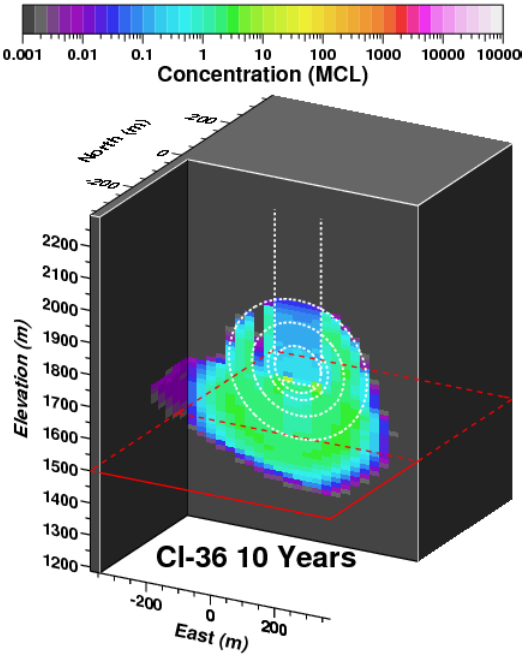

Figure 6.3 CLEARWATER HST model simulation of Cl-36 concentration at 10 years for a base case transport parameters and initial 3Rc distribution of a mean Cl-36 source in the liquid phase of fractures. The model Rc of 72 m is derived from maximum announced yield (USDOE, 2015) and Pawloski (1999) as detailed in Section 2.7.2.

6.3.2.3 I-129

Figure 6.4 shows CLEARWATER HST model simulation of I-129 concentration at 10 years for base case transport parameters and initial 3Rc distribution of a mean I-129 source in liquid phase of the fracture continuum. Because the CLEARWATER HST model treats the I-129 source as a tracer, the I-129 concentration distribution is similar to other tracer results at 10 years, but scaled to the I-129 source magnitude and MCL. In the long term, the CLEARWATER HST model simulation indicates I-129 concentrations at the SZ model interface can persist at maximum concentrations of a few MCL for over 100 years, similar to Cl-36.

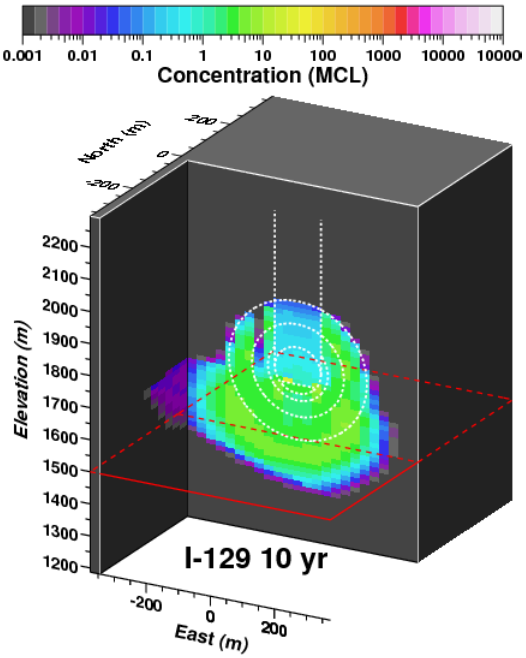

Figure 6.4 CLEARWATER HST model simulation of I-129 concentration at 10 years for a base case transport parameters and initial 3Rc distribution of a mean I-129 source in the liquid phase of fractures. The model Rc of 72 m is derived from maximum announced yield (USDOE, 2015) and Pawloski (1999) as detailed in Section 2.7.2.

6.3.2.4 Tc-99

Figure 6.5 shows CLEARWATER HST model simulation of Tc-99 concentration at 10 years for base case transport parameters and initial 3Rc distribution of a mean Tc-99 source in liquid phase of the fracture continuum. Because the CLEARWATER HST model treats the Tc-99 source as a tracer, the Tc-99 concentration distribution is similar to other tracers at 10 years, but scaled to the Tc-99 source magnitude and MCL. In the long term, the CLEARWATER HST model simulation indicates Tc-99 concentrations at the SZ model interface will fall near or below the MCL.

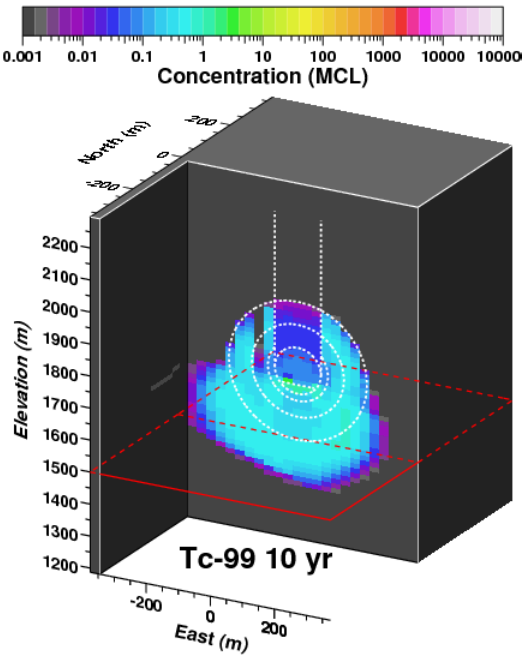

Figure 6.5 CLEARWATER HST model simulation of Tc-99 concentration at 10 years for a base case transport parameters and initial 3Rc distribution of a mean Tc-99 source in the liquid phase of fractures. The model Rc of 72 m is derived from maximum announced yield (USDOE, 2015) and Pawloski (1999) as detailed in Section 2.7.2.

6.3.2.5 Ni-63

Figure 6.6 shows CLEARWATER HST model simulation of Ni-63 concentration at 10 years for base case transport parameters and initial 1.5Rc distribution of a mean Ni-63 source in liquid phase of the fracture continuum. The CLEARWATER HST model accounts for sorption of Ni-63 in the rock matrix, which causes strong retardation of Ni-63 and reduction of Ni-63 fracture concentrations below the MCL within a few years. As a result, the CLEARWATER HST model indicates that Ni-63 will not be a significant radionuclide source for the SZ transport model, as predicted in the radiologic source term analysis by Zavarin et al. (2011).

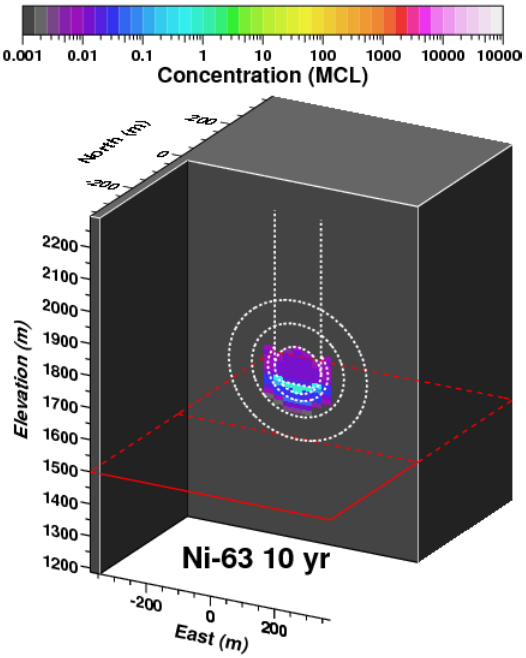

Figure 6.6 CLEARWATER HST model simulation of Ni-63 concentration at 10 years for base case transport parameters and initial 3Rc distribution of a mean Ni-63 source in the liquid phase of fractures. The model Rc of 72 m is derived from maximum announced yield (USDOE, 2015) and Pawloski (1999) as detailed in Section 2.7.2.

6.3.2.6 Sr-90

Figure 6.7 shows CLEARWATER HST model simulation of Sr-90 concentration at 10 and 100 years for base case transport parameters and initial 3Rc distribution of a mean Sr-90 source in liquid phase of the fracture continuum. The CLEARWATER HST model accounts for sorption of Sr-90 in the rock matrix, which causes strong retardation of Sr-90 in zeolitic rocks. At 10 years, the CLEARWATER HST model shows Sr-90 concentrations in the zeolitic altered zones ranging from 10 to 100 MCL. Sr-90 concentrations continue to decline mainly as a result of radioactive decay. In the strongly sorbing conditions within zeolitic tuff, Sr-90 transport is highly retarded in both test-altered and in-situ rocks between the CLEARWATER source zones and the SZ model interface. While Sr-90 fluxes may exceed the MCL at the SZ model interface for 3Rc radial distributions, the CLEARWATER HST model indicates Sr-90 transport will be highly retarded immediately below the SZ model interface. For practical purposes, the CLEARWATER HST model indicates that Sr-90 will not be a significant radionuclide source for the SZ transport model because Sr-90 transport will not come close to reaching the Redrock Valley aquifer (RVA).

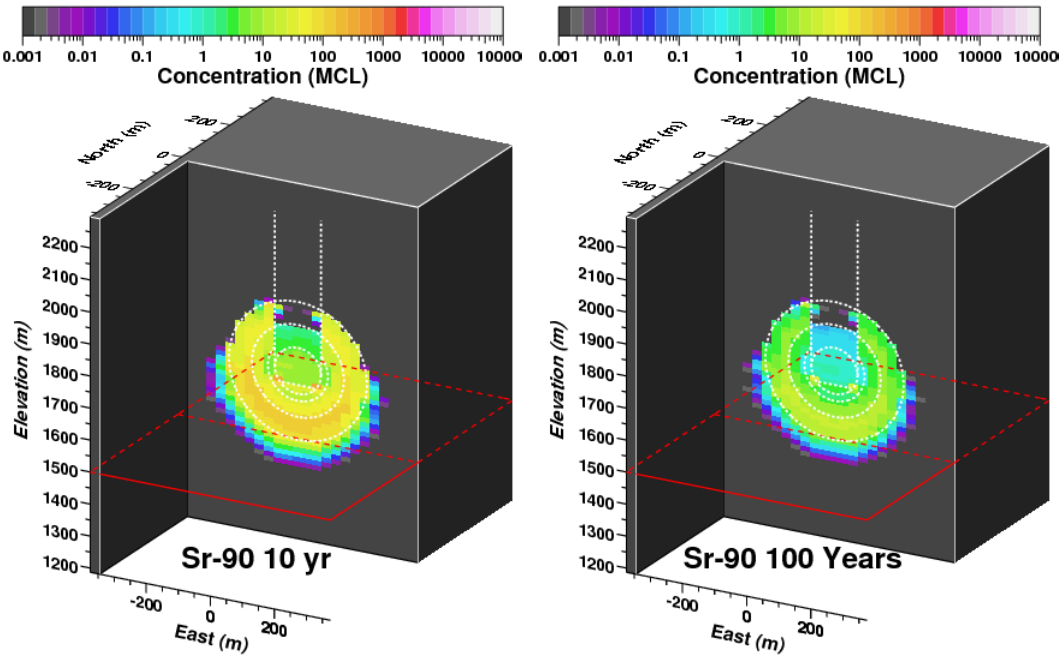

Figure 6.7 CLEARWATER HST model simulation of Sr-90 concentration at 10 and 100 years for base case transport parameters and initial 3Rc distribution of a mean Ni-63 source in the liquid phase of fractures. The model Rc of 72 m is derived from maximum announced yield (USDOE, 2015) and Pawloski (1999) as detailed in Section 2.7.2.

6.3.2.7 U-238

Figure 6.8 shows CLEARWATER HST model simulation of U-238 concentration at 10 years for base case transport parameters and initial 1.5Rc distribution of a mean U-238 source in liquid phase of the fracture continuum. The CLEARWATER HST model accounts for sorption of U-238 in the rock matrix, which causes relatively weak retardation of U-238 transport compared to other radionuclides. At 10 years, the CLEARWATER HST model shows U-238 concentrations well below the MCL within 2Rc except possibly the melt glass zone. The simulation results indicate U-238 is indeed mobile, but concentrations are well below the MCL. The CLEARWATER HST model indicates that U-238 from the CLEARWATER test will not be a significant radionuclide source for the SZ transport model.

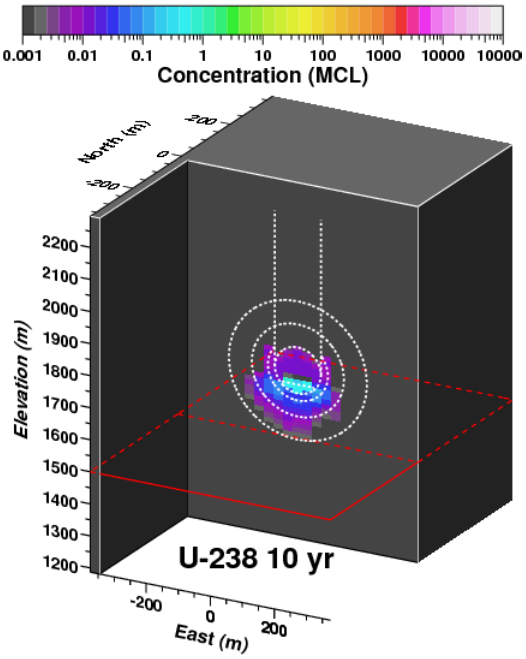

Figure 6.8 CLEARWATER HST model simulation of U-238 concentration at 10 years for base case transport parameters and initial 1.5Rc distribution of a mean U-238 source in the liquid phase of fractures. The model Rc of 72 m is derived from maximum announced yield (USDOE, 2015) and Pawloski (1999) as detailed in Section 2.7.2.

6.3.2.8 Pu-238

Figure 6.9 shows CLEARWATER HST model simulation of Pu-238 concentration at 10 and 1,000 years for base case transport parameters and initial 1.5Rc distribution of a mean Pu-238 source in liquid phase of the fracture continuum. The CLEARWATER HST model accounts for sorption of Pu-238 in the rock matrix. A 90% fraction of Pu-238 colloidal transport is accounted for by multiplying the Pu-238 tortuosity factor by 0.10 as described in Section 5.3.4. At 10 years, the CLEARWATER HST model shows Pu-238 concentrations as high as 10 MCL within 2Rc and higher in the melt glass zone. Diffusion, sorption and radioactive decay retard and reduce Pu-238 concentrations over time. By 1,000 years, Pu-238 concentrations are well below the MCL. While the CLEARWATER HST model indicates that Pu-238 concentrations may exceed the MCL at the SZ model interface, the Pu-238 plume will not come close to the Redrock Valley aquifer (RVA). As a result, the CLEARWATER HST model indicates that Pu-238 may not be a significant radionuclide source for the SZ transport model.

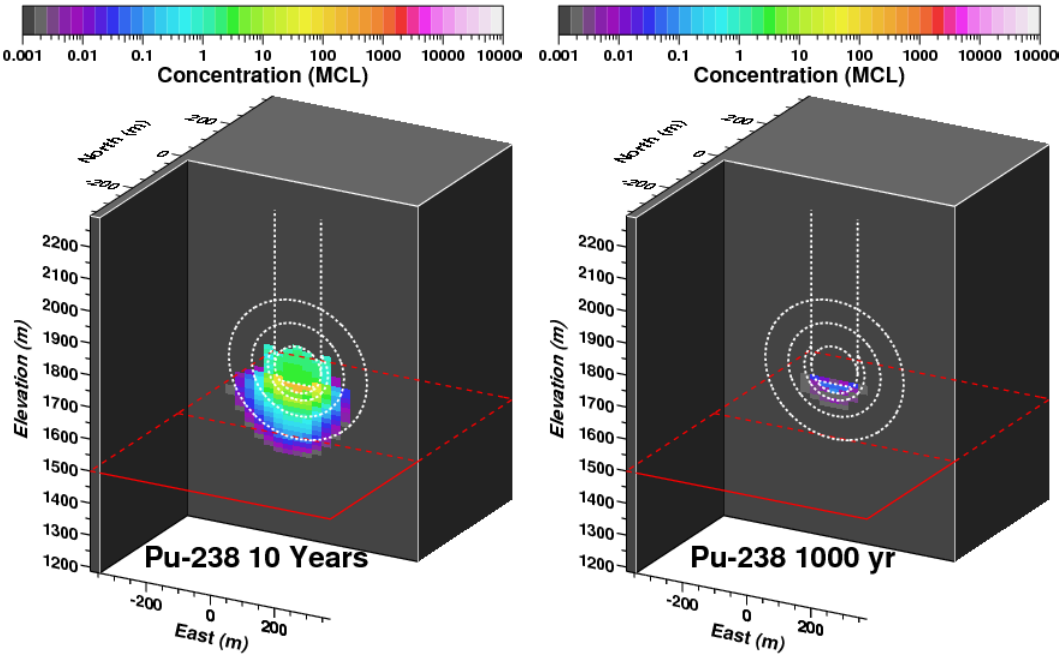

Figure 6.9 CLEARWATER HST model simulation of Pu-238 concentration at 10 and 1,000 years for base case transport parameters and initial 1.5Rc distribution of a mean Pu-238 source in the liquid phase of fractures. The model Rc of 72 m is derived from maximum announced yield (USDOE, 2015) and Pawloski (1999) as detailed in Section 2.7.2.

6.3.2.9 Pu-239

Figure 6.10 shows CLEARWATER HST model simulation of Pu-239 concentration at 10 and 1,000 years for base case transport parameters and initial 1.5Rc distribution of a mean Pu-239 source in liquid phase of the fracture continuum. The CLEARWATER HST model accounts for sorption of Pu-239 in the rock matrix. A 90% fraction of Pu-239 colloidal transport is accounted for by multiplying the Pu-239 tortuosity factor by 0.10 as described in Section 5.3.4. At 10 years, the CLEARWATER HST model shows Pu-239 concentrations over 10 MCL within 2Rc and higher concentrations in the melt glass zone. As the Pu-239 slowly migrates in a mostly downward direction, diffusion, sorption and radioactive decay retard and reduce Pu-239 concentrations over time. By 1,000 years, Pu-239 concentrations near the source zones remain over the MCL, but the Pu-239 plume largely remains in a suspended state. As a result, the CLEARWATER HST model indicates that Pu-239 from the CLEARWATER test may not be a significant radionuclide source for the SZ transport model.

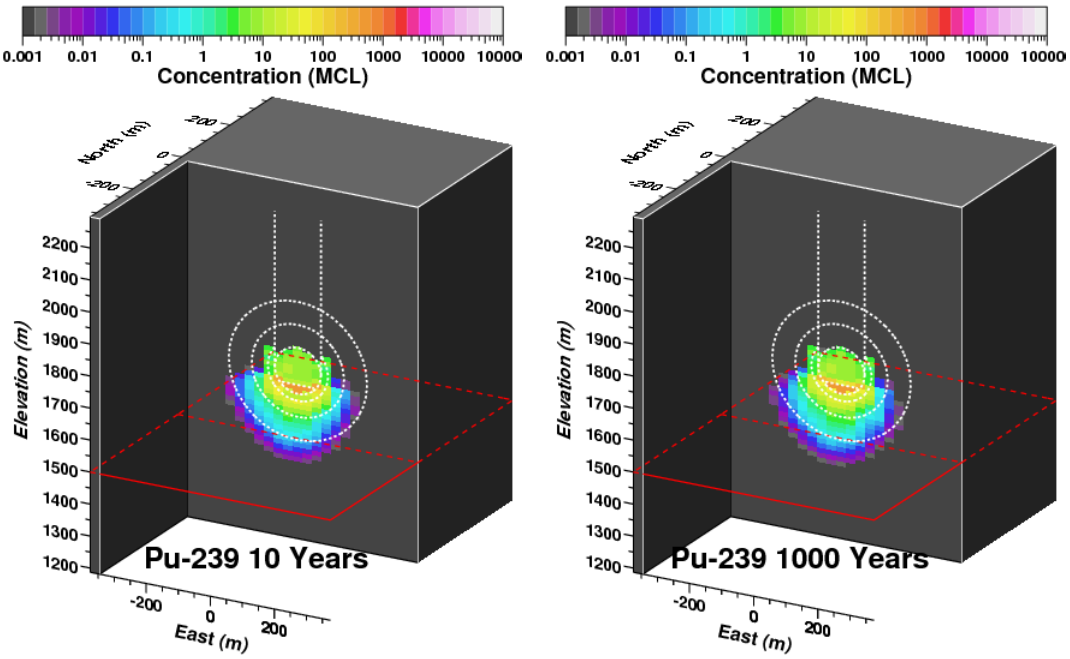

Figure 6.10 CLEARWATER HST model simulation of Pu-239 concentration at 10 and 1,000 years for base case transport parameters and initial 1.5Rc distribution of a mean Pu-239 source in the liquid phase of fractures. The model Rc of 72 m is derived from maximum announced yield (USDOE, 2015) and Pawloski (1999) as detailed in Section 2.7.2.

Pu-240

Figure 6.11 shows CLEARWATER HST model simulation of Pu-240 concentration at 10 and 1,000 years for base case transport parameters and initial 1.5Rc distribution of a mean Pu-240 source in liquid phase of the fracture continuum. The CLEARWATER HST model accounts for sorption of Pu-240 in the rock matrix. A 90% fraction of Pu-240 colloidal transport is accounted for by multiplying the Pu-240 tortuosity factor by 0.10 as described in Section 5.3.4. At 10 years, the CLEARWATER HST model shows Pu-240 concentrations approaching 10 MCL within 2Rc and higher concentrations in the melt glass zone. Once the Pu-240 enters the in-situ rock, diffusion, sorption and radioactive decay retard and reduce Pu-240 concentrations over time. As Pu-240 slowly migrates in a mostly downward direction, diffusion, sorption and radioactive decay retard and reduce Pu-240 concentrations over time. By 1,000 years, Pu-240 concentrations near the source zones remain over the MCL, but the Pu-240 plume largely remains in a suspended state. As a result, the CLEARWATER HST model indicates that Pu-240 from the CLEARWATER test may not be a significant radionuclide source for the SZ transport model.

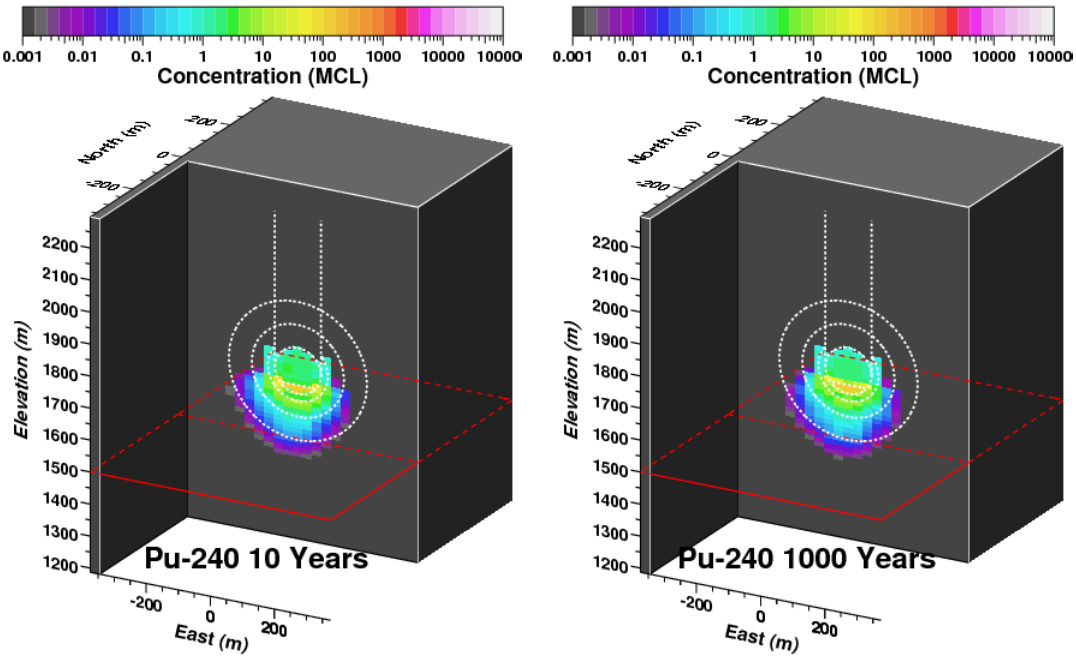

Figure 6.11 CLEARWATER HST model simulation of Pu-240 concentration at 10 and 1,000 years for base case transport parameters and initial 1.5Rc distribution of a mean Pu-240 source in the liquid phase of fractures. The model Rc of 72 m is derived from maximum announced yield (USDOE, 2015) and Pawloski (1999) as detailed in Section 2.7.2.

6.3.3 WINESKIN

6.3.3.1 H-3

The initial tritium or H-3 source term varies in radial distribution between 1.5 and 3Rc according to the limits of the RST model (Zavarin et al., 2011). Compared to a source term contained within 1.5Rc, a 3Rc source distribution will project a portion of the source term closer to the SZ model interface. Figure 6.12 shows temporal evolution of WINESKIN HST model simulation of H-3 concentration at 0, 1, 10, and 100 years for base case transport parameters and initial 3Rc distribution of a mean H-3 source in liquid phase of the fracture continuum. Initial concentrations (at time zero) in the fractures are over 100,000 MCL (1 MCL = 20,000 pCi/L). By one year a noticeable drop in H-3 fracture concentrations is evident in the cavity and upper portions of the source zones within 3Rc as a result of matrix diffusion and advection. H-3 transport moves south toward the SZ model interface (red outlined stairstep at lower left of each plot). By 10 years, an H-3 plume is approaching the SZ model interface. H-3 concentrations in altered zones within granitic rocks remain the highest because the model tends to trap H-3 directly above the assumed impermeable unaltered MGCU (consistent with SZ flow model assumptions), where flow is relatively stagnant. Tritium concentrations in the initial source zones outside the granitic rocks range from 100 to 10,000 MCL. By 100 years, effects of radioactive decay have greatly reduced H-3 concentrations – to about 200 MCL or less. Radioactive decay alone brings H-3 concentrations by a factor of 66 per 100 years. This base case set of model parameters predicts H-3 breakthrough above the MCL at the SZ model interface largely between 10 and 200 years.

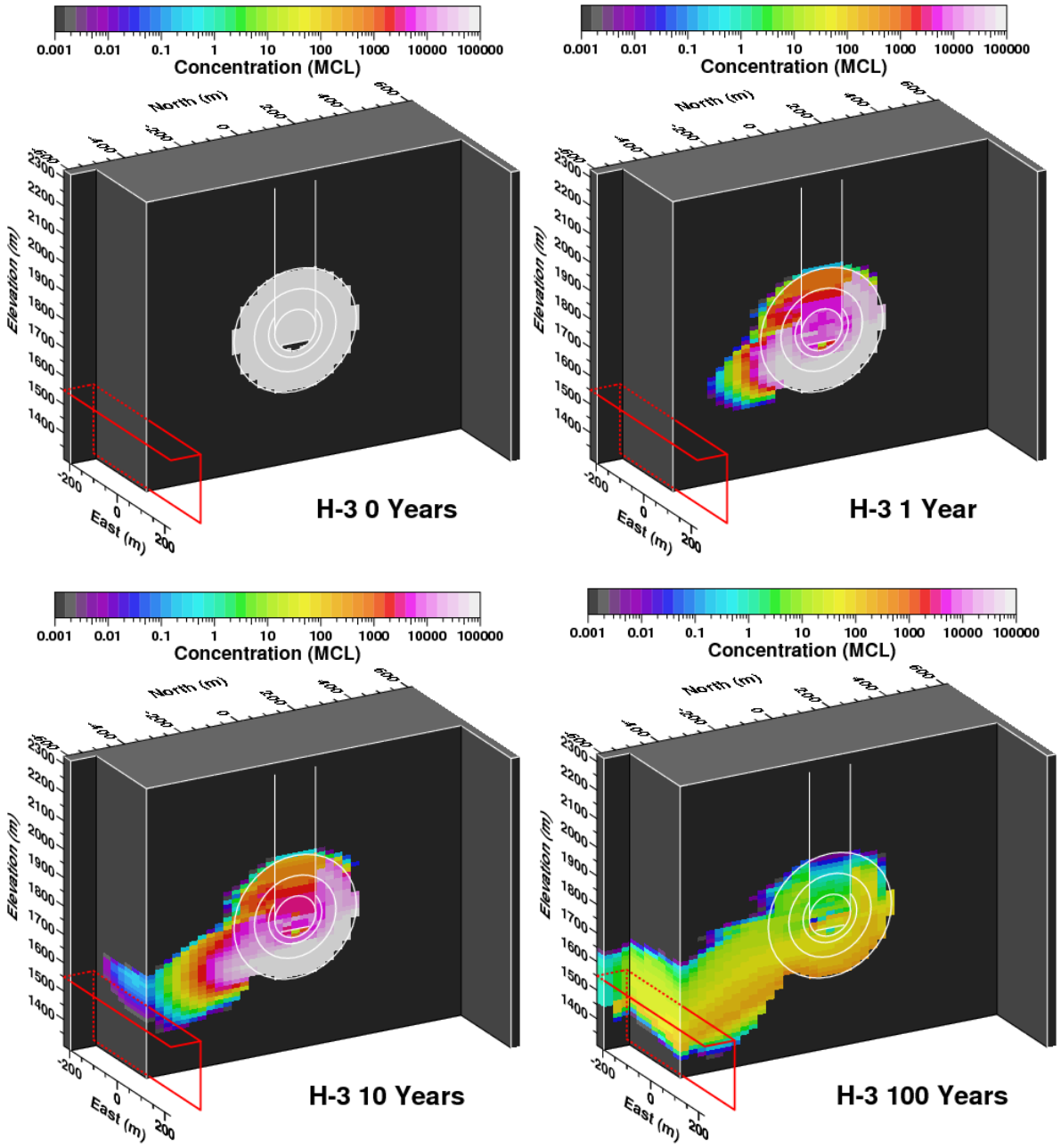

Figure 6.12 Temporal evolution of WINESKIN HST model simulation of H-3 concentration at 0, 1, 10, and 100 years for a base case transport parameters and initial 3Rc distribution of a mean H-3 source in the liquid phase of fractures. The model Rc of 72 m is derived from maximum announced yield (USDOE, 2015) and Pawloski (1999) as detailed in Section 2.7.2.

6.3.3.2 C-14

Figure 6.13 shows temporal evolution of WINESKIN HST model simulation of C-14 concentration at 10 years for base case transport parameters and initial 3Rc distribution of a mean C-14 source in liquid phase of the fracture continuum. Because the WINESKIN HST model treats the C-14 source as a tracer, the C-14 concentration distribution is similar to H-3 at 10 years, but scaled to the C-14 source magnitude and MCL. In the long term, the longer C-14 half-life causes the model to show persistence of C-14 above the MCL through 1000 years. However, the WINESKIN HST model results in this report do not include consideration of the thermal, gaseous, and chemical processes that favor early-time C-14 redistribution into the vadose zone. Future 2-D CLEARWATER HST model results extended beyond those presented in Zavarin et al. (2011) could be used to justify reduction of aqueous C-14 activity in source term models.

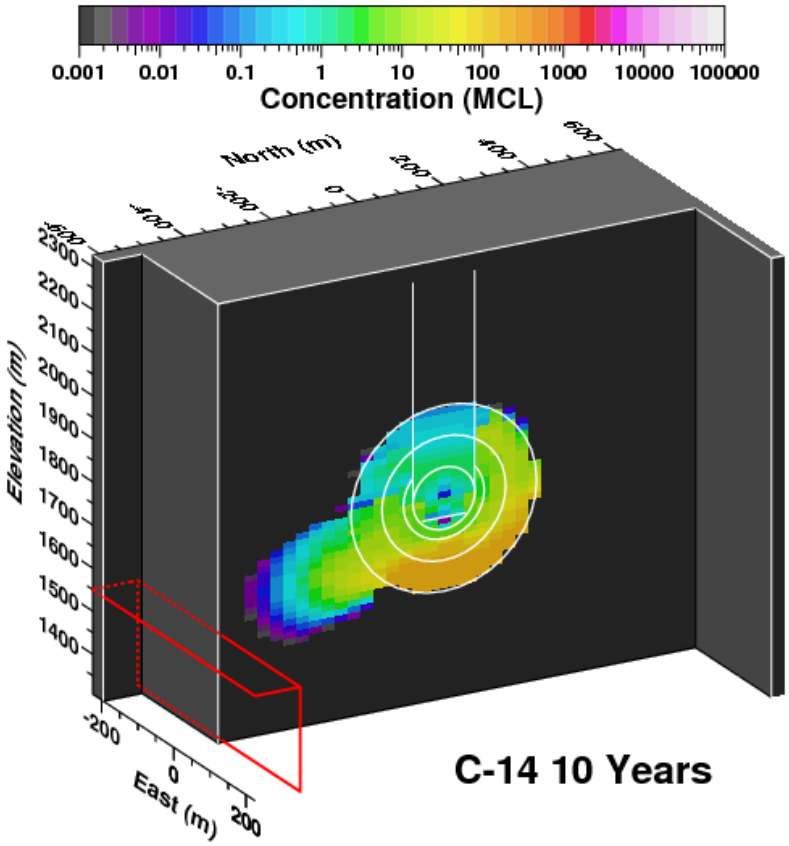

Figure 6.13 WINESKIN HST model simulation of C-14 concentration at 10 years for a base case transport parameters and initial 3Rc distribution of a mean C-14 source in the liquid phase of fractures. The model Rc of 72 m is derived from maximum announced yield (USDOE, 2015) and Pawloski (1999) as detailed in Section 2.7.2.

6.3.3.3 Cl-36

Figure 6.14 shows temporal evolution of WINESKIN HST model simulation of Cl-36 concentration from 10 to 100 years for base case transport parameters and initial 3Rc distribution of a mean Cl-36 source in liquid phase of the fracture continuum. Because the WINESKIN HST model treats the Cl-36 source as a tracer, the Cl-36 concentration distribution is similar to H-3 at 10 years, but scaled to the Cl-36 source magnitude and MCL. In the long term, the WINESKIN HST model simulation indicates Cl-36 concentrations at the SZ model interface can persist at maximum concentrations up to a few MCL for over 100 years.

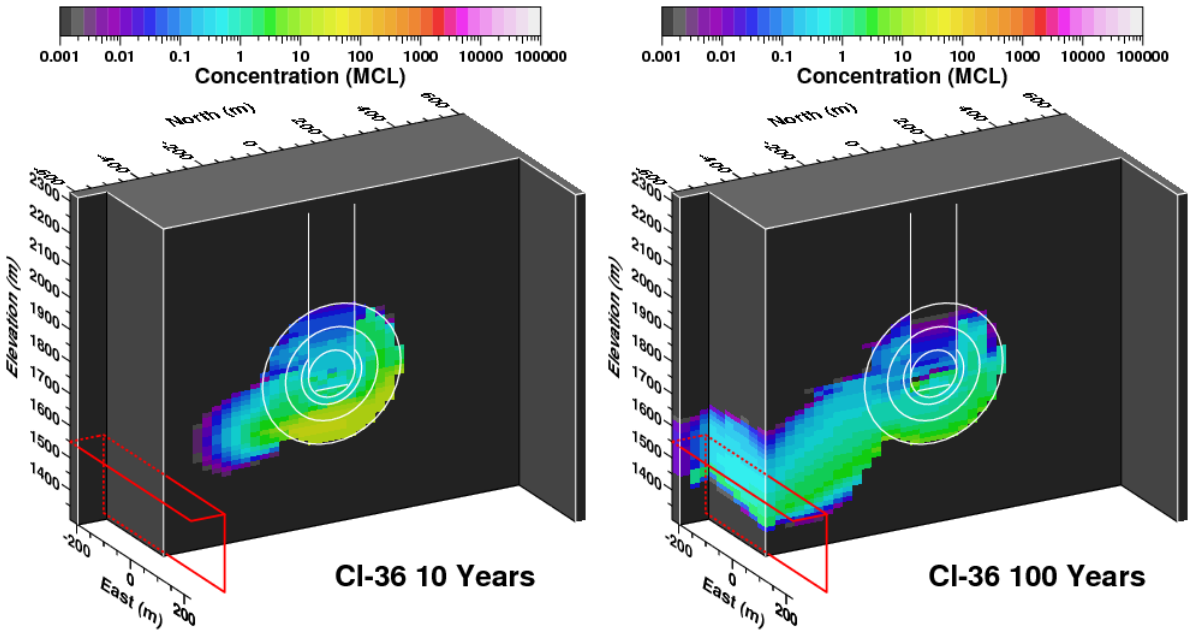

Figure 6.14 WINESKIN HST model simulation of Cl-36 concentration at 10 and 100 years for a base case transport parameters and initial 3Rc distribution of a mean Cl-36 source in the liquid phase of fractures. The model Rc of 72 m is derived from maximum announced yield (USDOE, 2015) and Pawloski (1999) as detailed in Section 2.7.2.

6.3.3.4 I-129

Figure 6.15 shows temporal evolution of WINESKIN HST model simulation of I-129 concentration from 10 to 100 years for base case transport parameters and initial 3Rc distribution of a mean I-129 source in liquid phase of the fracture continuum. Because the WINESKIN HST model treats the I-129 source as a tracer, the I-129 concentration distribution is similar to other tracers at 10 years, but scaled to the I-129 source magnitude and MCL. In the long term, the WINESKIN HST model simulation indicates I-129 concentrations at the SZ model interface can persist at maximum concentrations of a few MCL for over 100 years, similar to Cl-36.

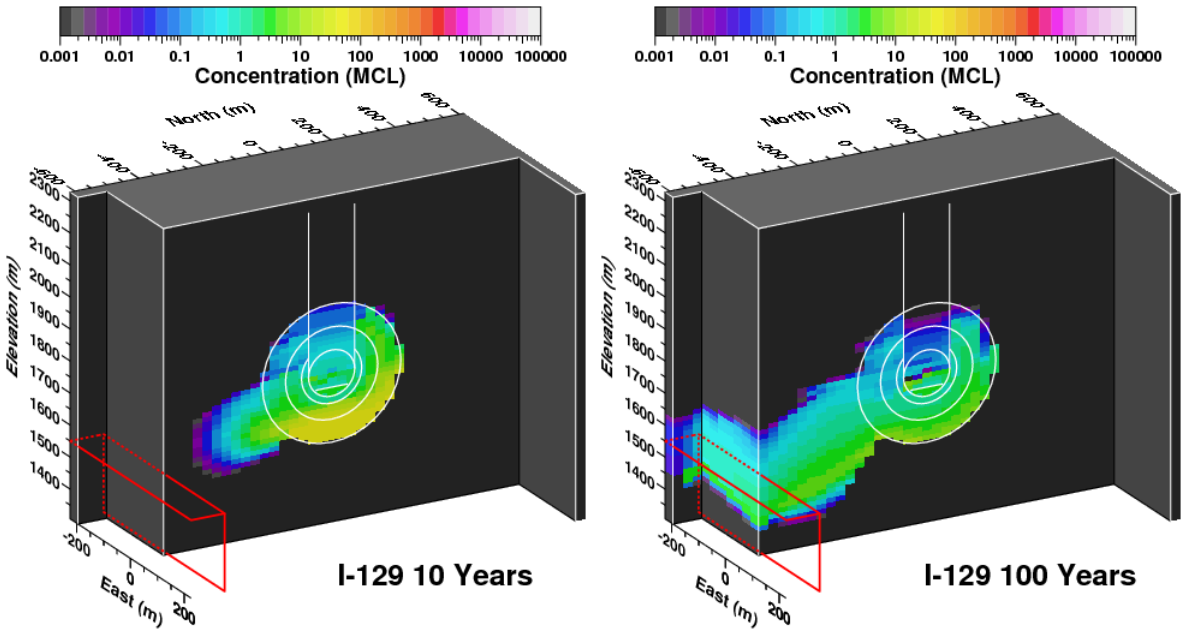

Figure 6.15 WINESKIN HST model simulation of I-129 concentration at 10 and 100 years for a base case transport parameters and initial 3Rc distribution of a mean I-129 source in the liquid phase of fractures. The model Rc of 72 m is derived from maximum announced yield (USDOE, 2015) and Pawloski (1999) as detailed in Section 2.7.2.

Tc-99

Figure 6.16 shows temporal evolution of WINESKIN HST model simulation of Tc-99 concentration from 10 to 100 years for base case transport parameters and initial 3Rc distribution of a mean Tc-99 source in liquid phase of the fracture continuum. Because the WINESKIN HST model treats the Tc-99 source as a tracer, the Tc-99 concentration distribution is similar to other tracers at 10 years, but scaled to the Tc-99 source magnitude and MCL. In the long term, the WINESKIN HST model simulation indicates Tc-99 concentrations at the SZ model interface will fall below the MCL.

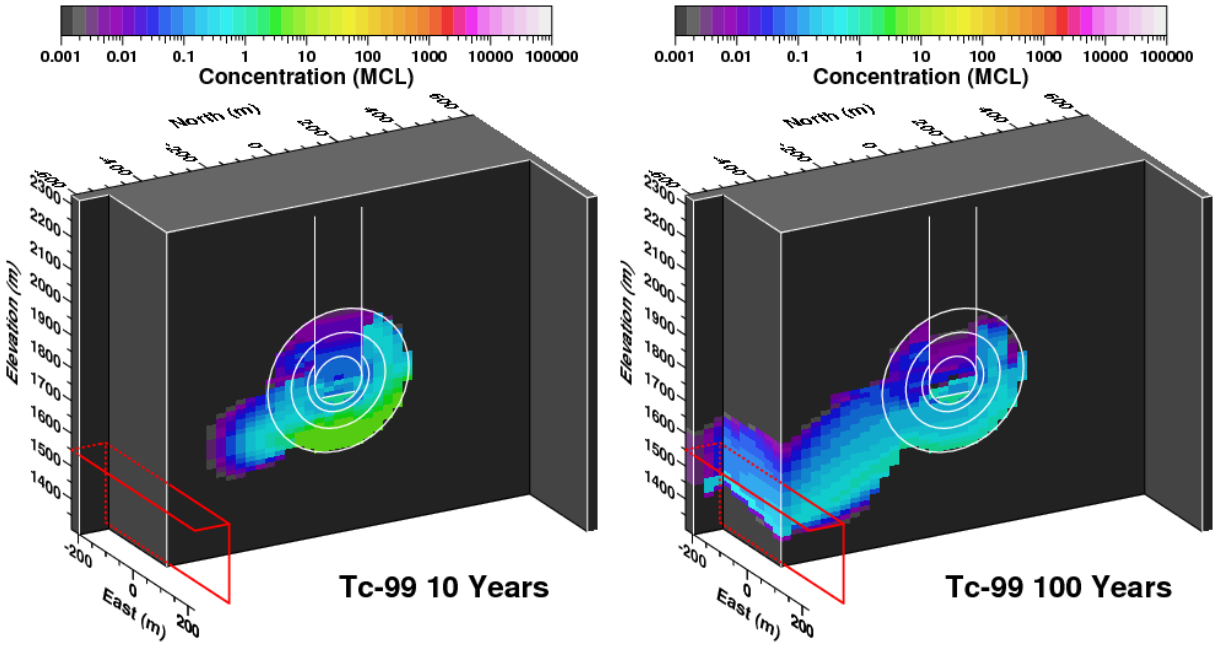

Figure 6.16 WINESKIN HST model simulation of Tc-99 concentration at 10 and 100 years for a base case transport parameters and initial 3Rc distribution of a mean Tc-99 source in the liquid phase of fractures. The model Rc of 72 m is derived from maximum announced yield (USDOE, 2015) and Pawloski (1999) as detailed in Section 2.7.2.

6.3.3.5 Ni-63

Figure 6.17 shows WINESKIN HST model simulation of Ni-63 concentration at 10 years for base case transport parameters and initial 1.5Rc distribution of a mean Ni-63 source in liquid phase of the fracture continuum. The WINESKIN HST model accounts for sorption of Ni-63 in the rock matrix, which causes strong retardation of Ni-63 and reduction of Ni-63 fracture concentrations below the MCL within a few years. As a result, the WINESKIN HST model indicates that Ni-63 will not be a significant radionuclide source for the SZ transport model, as predicted in the radiologic source term analysis by Zavarin et al. (2011).

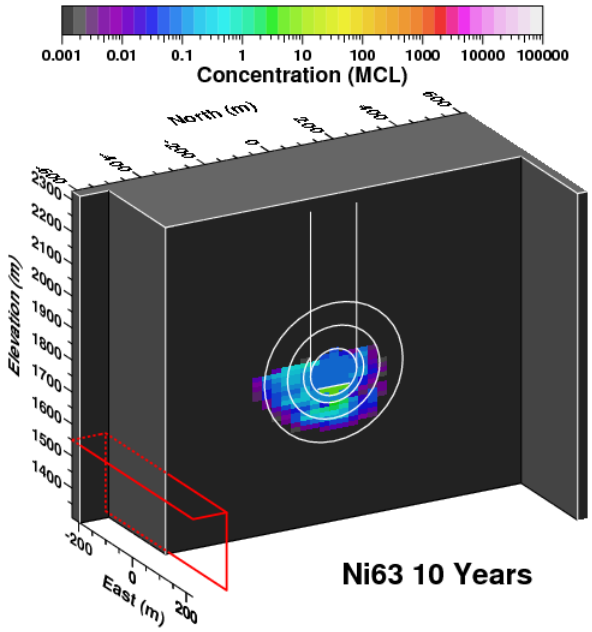

Figure 6.17 WINESKIN HST model simulation of Ni-63 concentration at 10 years for base case transport parameters and initial 3Rc distribution of a mean Ni-63 source in the liquid phase of fractures. The model Rc of 72 m is derived from maximum announced yield (USDOE, 2015) and Pawloski (1999) as detailed in Section 2.7.2.

Sr-90

Figure 6.18 shows WINESKIN HST model simulation of Sr-90 concentration at 10 and 100 years for base case transport parameters and initial 3Rc distribution of a mean Sr-90 source in liquid phase of the fracture continuum. The WINESKIN HST model accounts for sorption of Sr-90 in the rock matrix, which causes strong retardation of Sr-90 in zeolitic rocks. At 10 years, the WINESKIN HST model shows Sr-90 concentrations in the zeolitic altered zones ranging from 10 to 100 MCL and much higher Sr-90 concentrations in the granitic altered zone, mainly as a result lower Kd. Sr-90 concentrations continue to decline mainly as a result of radioactive decay. In the strongly sorbing conditions of zeolitic tuff, Sr-90 transport is highly retarded in in-situ rocks between the WINESKIN source zones and the SZ model interface. As a result, the WINESKIN HST model indicates that Sr-90 will not be a significant radionuclide source for the SZ transport model.

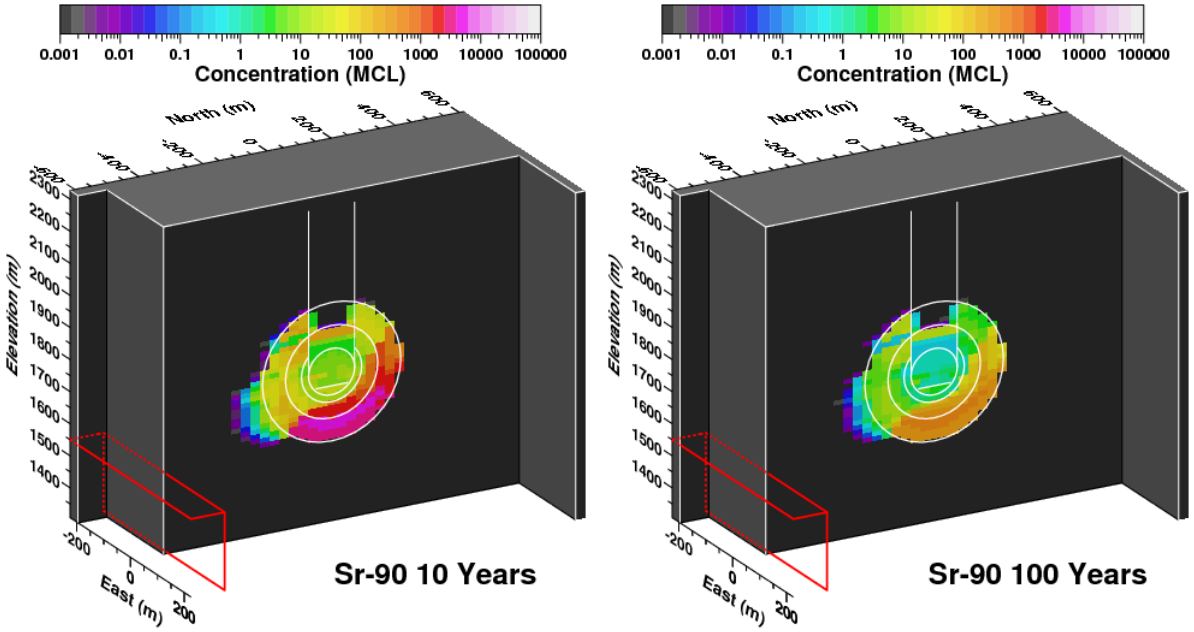

Figure 6.18 WINESKIN HST model simulation of Sr-90 concentration at 10 and 100 years for base case transport parameters and initial 3Rc distribution of a mean Ni-63 source in the liquid phase of fractures. The model Rc of 72 m is derived from maximum announced yield (USDOE, 2015) and Pawloski (1999) as detailed in Section 2.7.2.

6.3.3.6 U-238

Figure 6.19 shows WINESKIN HST model simulation of U-238 concentration at 10 and 100 years for base case transport parameters and initial 1.5Rc distribution of a mean U-238 source in liquid phase of the fracture continuum. The WINESKIN HST model accounts for sorption of U-238 in the rock matrix, which causes relatively weak retardation of U-238 transport compared to other radionuclides. At 10 years, the WINESKIN HST model shows U-238 concentrations well below the MCL within 2Rc except possibly the melt glass zone. The simulation results at 100 years indicate U-238 is indeed mobile, but concentrations are well below the MCL. The WINESKIN HST model indicates that U-238 from the WINESKIN test will not be a significant radionuclide source for the SZ transport model.

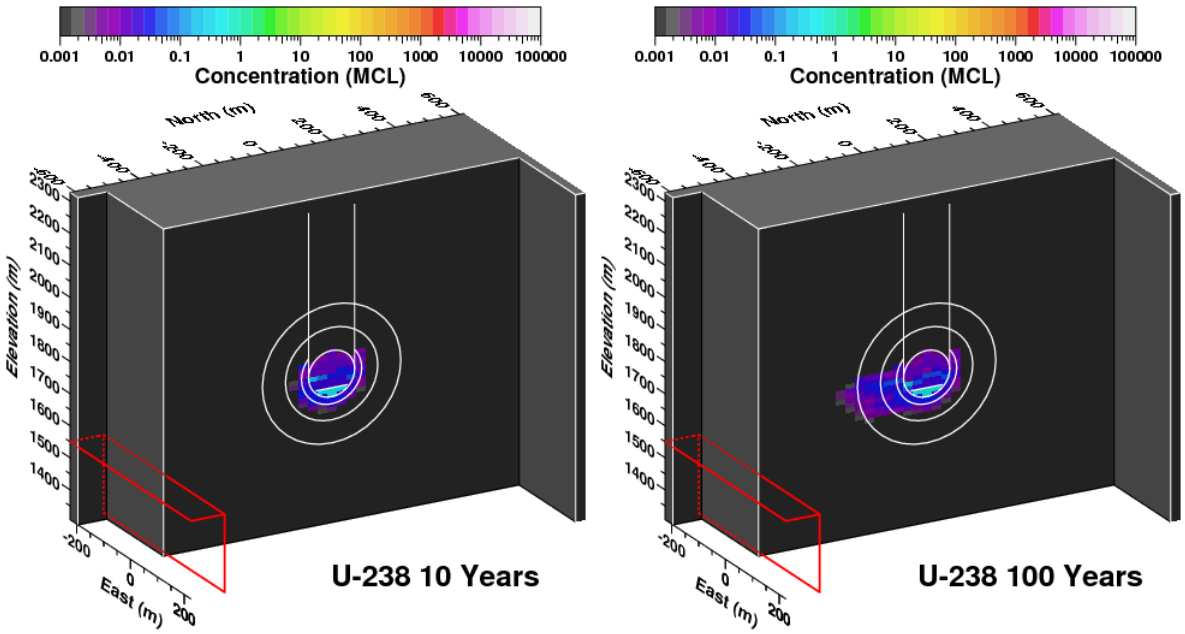

Figure 6.19 WINESKIN HST model simulation of U-238 concentration at 10 and 100 years for base case transport parameters and initial 1.5Rc distribution of a mean U-238 source in the liquid phase of fractures. The model Rc of 72 m is derived from maximum announced yield (USDOE, 2015) and Pawloski (1999) as detailed in Section 2.7.2.

6.3.3.7 Pu-238

Figure 6.20 shows WINESKIN HST model simulation of Pu-238 concentration at 10 and 1,000 years for base case transport parameters and initial 1.5Rc distribution of a mean Pu-238 source in liquid phase of the fracture continuum. The WINESKIN HST model accounts for sorption of Pu-238 in the rock matrix. A 90% fraction of Pu-238 colloidal transport is accounted for by multiplying the Pu-238 tortuosity factor by 0.10 as described in Section 5.3.4. At 10 years, the WINESKIN HST model shows Pu-238 concentrations as high as 100 MCL within 3Rc. Once the Pu-238 enters the in-situ rock, diffusion, sorption and radioactive decay retard and reduce Pu-238 concentrations over time. By 1,000 years, Pu-238 concentrations are well below the MCL, and the Pu-238 plume has not come close to the SZ model interface. As a result, the WINESKIN HST model indicates that Pu-238 will not be a significant radionuclide source for the SZ transport model.

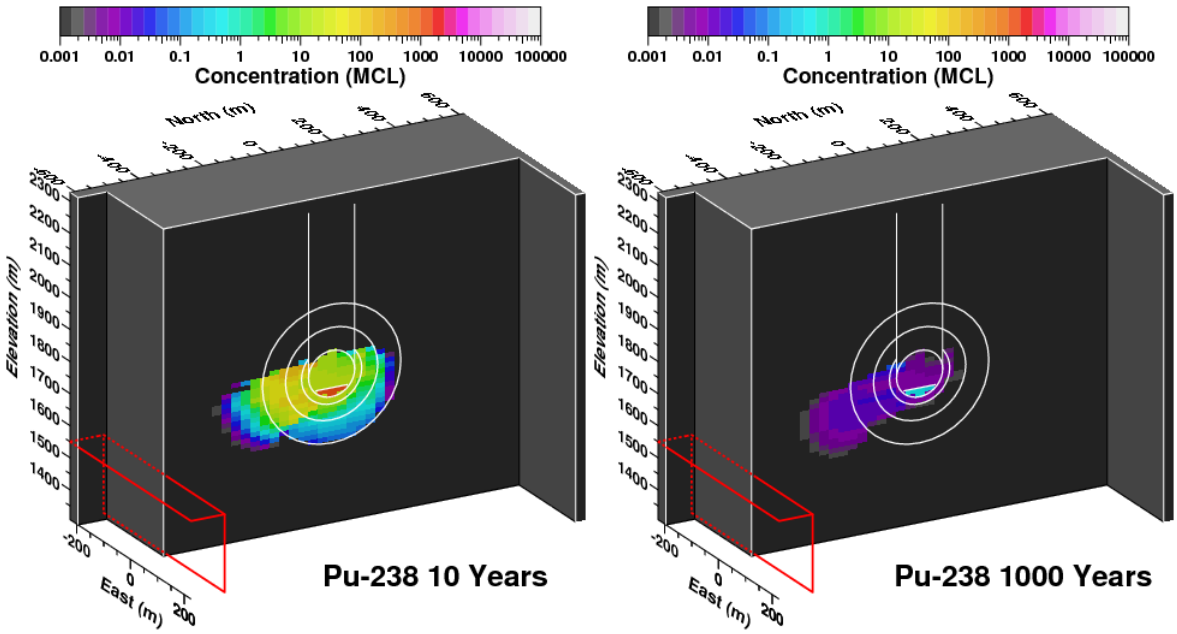

Figure 6.20 WINESKIN HST model simulation of Pu-238 concentration at 10 and 1,000 years for base case transport parameters and initial 1.5Rc distribution of a mean Pu-238 source in the liquid phase of fractures. The model Rc of 72 m is derived from maximum announced yield (USDOE, 2015) and Pawloski (1999) as detailed in Section 2.7.2.

6.3.3.8 Pu-239

Figure 6.21 shows WINESKIN HST model simulation of Pu-239 concentration at 10 and 1,000 years for base case transport parameters and initial 1.5Rc distribution of a mean Pu-239 source in liquid phase of the fracture continuum. The WINESKIN HST model accounts for sorption of Pu-239 in the rock matrix. A 90% fraction of Pu-239 colloidal transport is accounted for by multiplying the Pu-239 tortuosity factor by 0.10 as described in Section 5.3.4. At 10 years, the WINESKIN HST model shows P-239 concentrations over 100 MCL within 3Rc. Once the Pu-239 enters the in-situ rock, diffusion, sorption and radioactive decay retard and reduce Pu-239 concentrations over time. By 1,000 years, Pu-239 concentrations near the source remain over the MCL, but the Pu-239 plume has not reached the SZ model interface. As a result, the WINESKIN HST model indicates that Pu-239 will not be a significant radionuclide source for the SZ transport model. However, of the Pu species, Pu-239 shows the greatest potential for a radionuclide source to the SZ transport model.

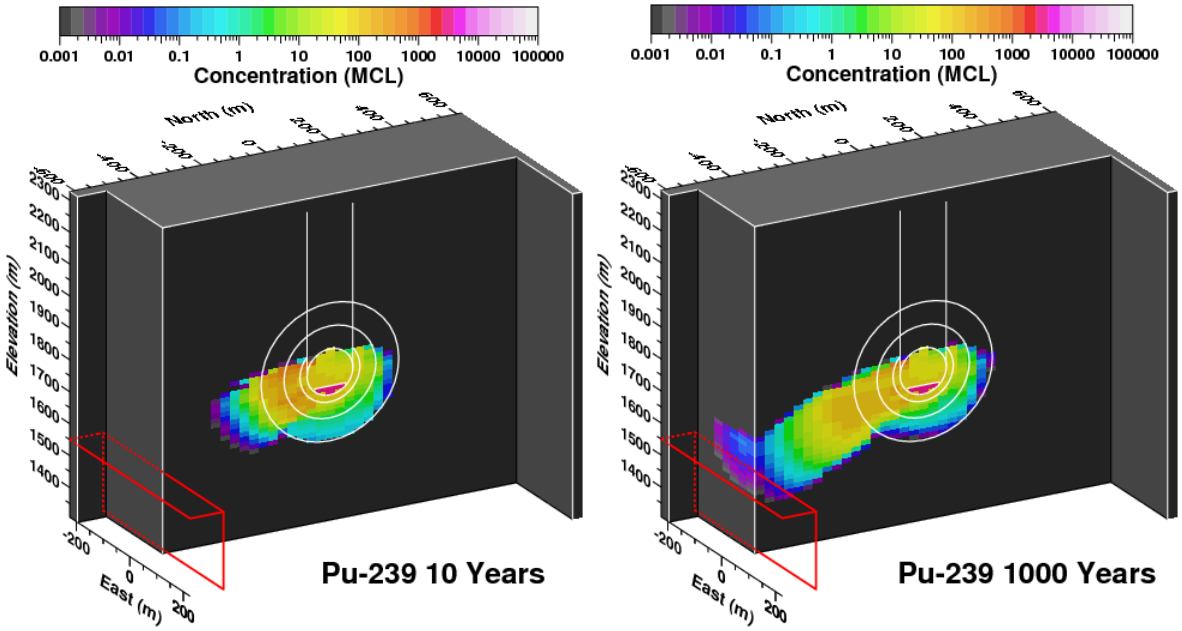

Figure 6.21 WINESKIN HST model simulation of Pu-239 concentration at 10 and 1,000 years for base case transport parameters and initial 1.5Rc distribution of a mean Pu-239 source in the liquid phase of fractures. The model Rc of 72 m is derived from maximum announced yield (USDOE, 2015) and Pawloski (1999) as detailed in Section 2.7.2.

6.3.3.9 Pu-240

Figure 6.22 shows WINESKIN HST model simulation of Pu-240 concentration at 10 and 1,000 years for base case transport parameters and initial 1.5Rc distribution of a mean Pu-240 source in liquid phase of the fracture continuum. The WINESKIN HST model accounts for sorption of Pu-240 in the rock matrix. A 90% fraction of Pu-240 colloidal transport is accounted for by multiplying the Pu-240 tortuosity factor by 0.10 as described in Section 5.3.4. At 10 years, the WINESKIN HST model shows Pu-240 concentrations approaching 100 MCL within 3Rc. Once the Pu-240 enters the in-situ rock, diffusion, sorption and radioactive decay retard and reduce Pu-240 concentrations over time. By 1,000 years, Pu-240 concentrations near the source remain over the MCL, but the Pu-240 plume has not reached the SZ model interface. As a result, the WINESKIN HST model indicates that Pu-240 will not be a significant radionuclide source for the SZ transport model.

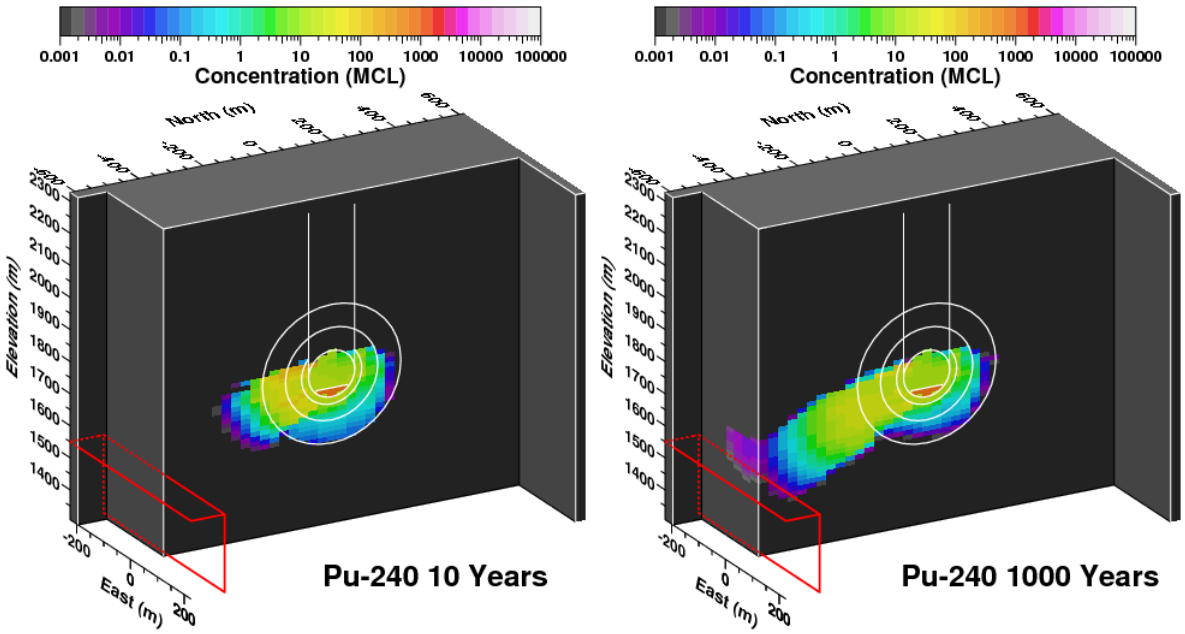

Figure 6.22 WINESKIN HST model simulation of Pu-240 concentration at 10 and 1,000 years for base case transport parameters and initial 1.5Rc distribution of a mean Pu-240 source in the liquid phase of fractures. The model Rc of 72 m is derived from maximum announced yield (USDOE, 2015) and Pawloski (1999) as detailed in Section 2.7.2.

6.4 Sensitivity Studies on Radionuclide Source Flux Concentration to SZ Model for Calibration and Design of the HST

This section provides sensitivity studies on radionuclide source flux to the SZ model, which are useful for improving calibration of flow and transport parameters and design of probability distributions for the HST. The sensitivity parameters illustrated in this section include:

- Radial distance of source distribution in units of cavity radius (Rc) as provided by the spatial ranges given for radionuclide sources in Zavarin et al. (2011).
- Total source term activities for radionuclide isotopes in pCi using the ranges of uncertainty given in Zavarin et al. (2011).
- Three sets of transport mobility parameters identified as low mobility (LoM), base case (Base), and high mobility (HiM) as described in Section 5.4.

Sensitivity to the combined effects of fraction of the source in the melt glass zone and fraction of melt glass released is not illustrated in this section, but is evaluated in the HST model. For most radionuclides sources, the fraction of source released from the melt glass is very small compared to the fraction of source released outside the melt glass. Thus, uncertainty associated with the melt glass source tends to be secondary relative to the sensitivity parameters illustrated in this section.

The sensitivity studies cover eleven radionuclide isotopes: H-3, C-14, Cl-36, I-129, Tc-99, Ni-63, Sr-90, Pu-238, Pu-239, Pu-240, and U-238. As discussed previously, Ni-63 is not included in the list of radionuclide sources given in Zavarin et al. (2011), which includes Am-241. The final CLEARWATER and WINESKIN HST model used for SZ model input will include Am-241. The reason for not having Am-241 HST modeling results in this report is that Am-241 was not included an earlier version of the radionuclide source list developed by LLNL (Zavarin, 2011a), which was subsequently used to generate the CLEARWATER and WINESKIN HST model results given in this report.

6.4.1 Source Flux Concentration Units For Sensitivity Studies

The CLEARWATER and WINESKIN HST models simulate flux of water and radionuclides at the interface with the SZ model boundary (Section 2.1). The resolution of the flux is to 30 m by 30 m in the horizontal plane and 30 m by 15 m in the vertical plane. A vertical flux plane is applied only on the north face of the "stair step" in the SZ model boundary for the WINESKIN HST model (Section 2.1.2).

In lieu of showing every radionuclide flux output at hundreds of locations with time as produced by the HST models, this section examines total radionuclide fluxes to the SZ model boundary. Examination of the total radionuclide fluxes yields the following insights:

- Sensitivity of HST to radionuclide source zone (e.g. melt glass, cavity, 1.5Rc, 3Rc, chimney)
- Effect of constraints on source term distribution.
- Significance of radionuclide sources relative to the MCL.

To improve relevance of total flux to the MCL, concentrations are normalized to the MCL as follows:

$$\text{Concentration} = \left(\frac{\text{total radionuclide flux}}{\text{total water flux}} \right) \Big/ \text{MCL}$$

In this manner, mean radionuclide fluxes across the interface between the HST model and SZ model are scaled to the MCL. This scaling gives some insight into the magnitude of the HST fluxes to relative to the MCL and, importantly, whether the HST model indicates a significant radionuclide source to the SZ model. Furthermore, the concentrations indicated in the sensitivity studies can be compared to observational data to gain insight on calibration of model parameters, particularly parameters that strongly affect radionuclide transport such as Kd, tortuousity, and matrix effective transport porosity. However, concentrations of mean radionuclide fluxes are obviously lower than the maximum concentrations, which should be factored into current and future interpretation of observational data.

For all HST model simulations of radionuclide flux, the radionuclide source values (Table 4.2) are distributed into the radionuclide source zones as described in Section 4. The spatial distribution of radionuclide sources is constrained by Rc ranges as given in Table 4.2. The RST model (Zavarin et al., 2011) prescribes that radionuclide sources outside the melt glass are distributed evenly within the fracture continuum water. Therefore, the HST models distribute the "non-lava" portion of the source term at equal concentration into the fracture continuum within the range of
"non-lava" source zones for the specific radionuclide source.

For simplicity, in all plots of radionuclide flux in this section, the upper range of the fraction of melt glass dissolution, 0.0270, is used. The HST model results indicate that radionuclide fluxes are not very sensitive to the fraction of melt glass dissolution unless the entire source term is distributed into the melt glass only (e.g., where 100% of a plutonium source is in the melt glass).

6.4.2 Transport Sensitivity Cases

Each sensitivity study illustrated in this section includes 18 separate radionuclide transport cases based on the following variables:

- 3 transport mobility cases:
  - Magenta lines = "HiM" (high mobility)
  - Green lines = "Base" (base case)
  - Blue lines = "LoM" = (low mobility)
- 3 source distributions
  - Thick line = mean
  - Thin lines = min and max
- 2 source distribution ranges
  - Dashed line = outer radial limit (Rc units)
  - Solid line = inner radial limit (Rc units)

6.4.3 CLEARWATER

The interface between the SZ model and the CLEARWATER HST model (the "SZ model interface") is a horizontal plane situated at 1,500 m elevation. Based on the CLEARWATER test working point elevation of 1,711 m and the CLEARWATER HST model Rc of 72 m as derived from maximum announced yield (USDOE, 2015) and Pawloski (1999) as detailed in Section 2.7.2, the SZ model interface is located slightly less than 3Rc in the CLEARWATER HST model. As a result, several transport model-related effects can be expected from the CLEARWATER HST model:

- Radionuclide sources distributed to 3Rc can produce radionuclide fluxes to the SZ model domain immediately after time zero.
- Radionuclide sources distributed to 1.5 Rc will be delayed in breakthrough at the SZ model interface relative to sources distributed to 3Rc, but this delay is not necessarily lengthy in time for tracers assuming enhanced fracture permeability to 3Rc (U.S. Congress, 1989).
- Because of the close proximity of the SZ model interface to the outer limits of the CLEARWATER HST model source zones, radionuclide flux concentrations to the SZ model boundary from the CLEARWATER test could be similar to observational data from locations near tests or from tunnel waters derived from sources zones. Therefore, such observational data may be useful to further constrain the CLEARWATER and WINESKIN HST models by focusing on the HST model concentrations for CLEARWATER.

6.4.3.1 Parameter Errors in Low and High Mobility Tracer Case for CLEARWATER Test Sensitivity Analysis

Unfortunately, it was recently discovered that the "low mobility" and "high mobility" transport parameter sensitivity cases for the CLEARWATER HST model were run with some incorrect parameters. The sensitivity studies for the WINESKIN test (Section 6.4.4) were run with the correct parameters. Therefore, the sensitivities between for mobility parameters need to be re-evaluated for the CLEARWATER HST model, which can be done

in a short time. Currently, sensitivities between the "low mobility", "base case", and "high mobility" cases reflect only effects of different flow realizations for the CLEARWATER test.

6.4.3.2 Non-Sorbing Radionuclides

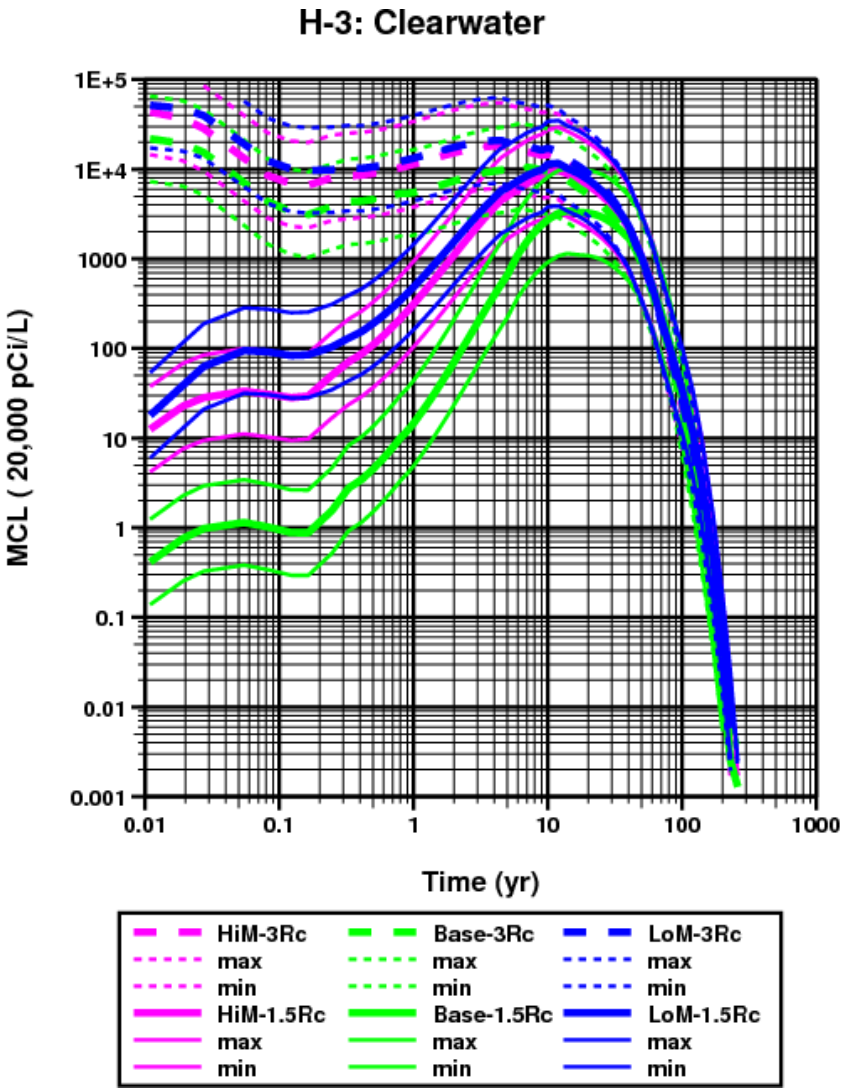

Figure 6.23 Sensitivity study for H-3 transport from CLEARWATER HST model.

For H-3 radionuclide flux concentration to the SZ model interface (Figure 6.23):

- Dashed lines indicate a H-3 source distributed to 3Rc can produce early time H-3 concentrations on the order 1e4 to 1e5 MCL or greater.
- Solid lines show effects of a more compact H-3 source distribution.
- Thin lines reflect uncertainty in H-3 source value.
- Colors show sensitivity to transport mobility cases.

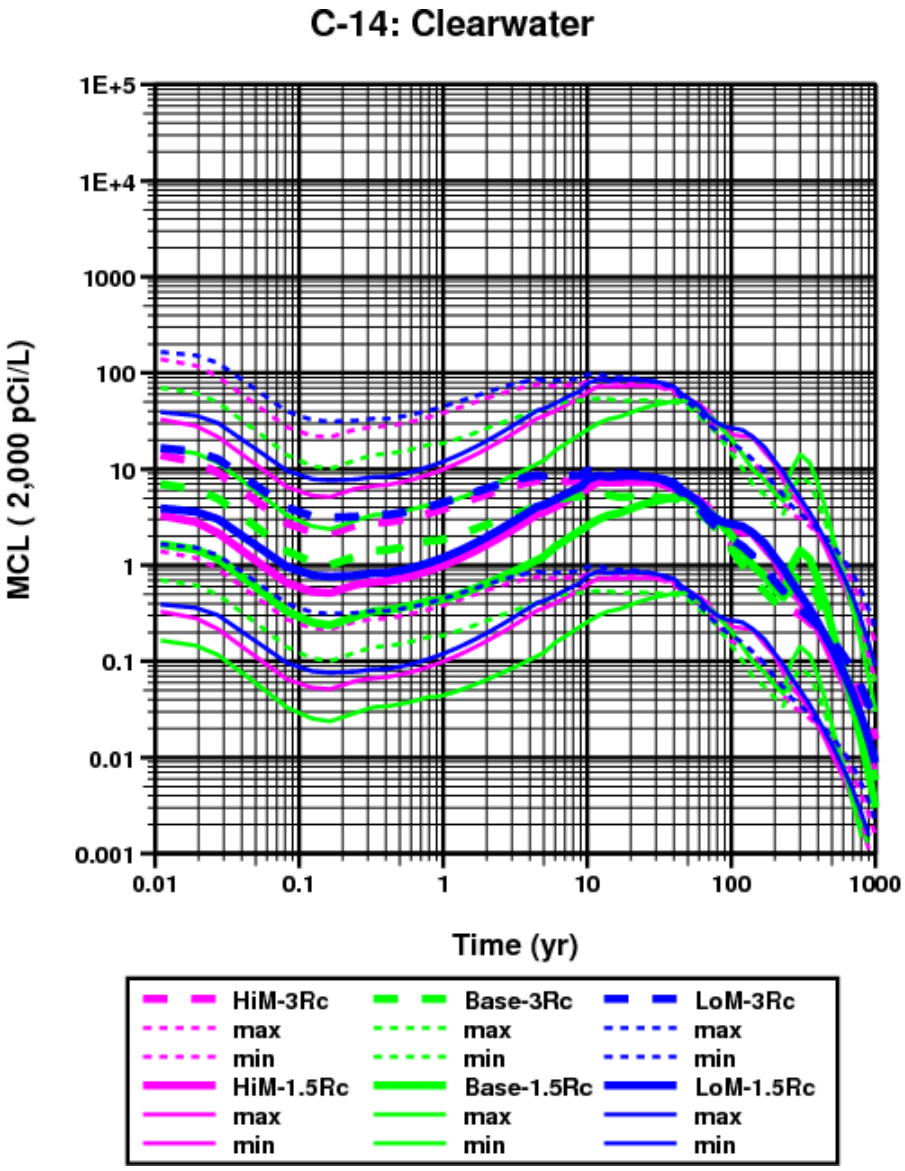

Figure 6.24 Sensitivity study for C-14 transport from CLEARWATER HST model.

For C-14 radionuclide flux concentration to the SZ model interface (Figure 6.24):

- Dashed lines indicate that a C-14 source distributed to 3Rc can produce relatively high radionuclide flux concentrations to the SZ model interface at early times.
- Solid lines show effects of a more compact C-14 source distribution.
- Thin lines reflect uncertainty in C-14 source value.
- Colors show sensitivity to transport mobility cases.
- Importantly, C-14 transport behavior involves more complexities such as those addressed by the 2-D CLEARWATER HST model with thermal, gaseous, and chemical processes (Zavarin et al., 2011).

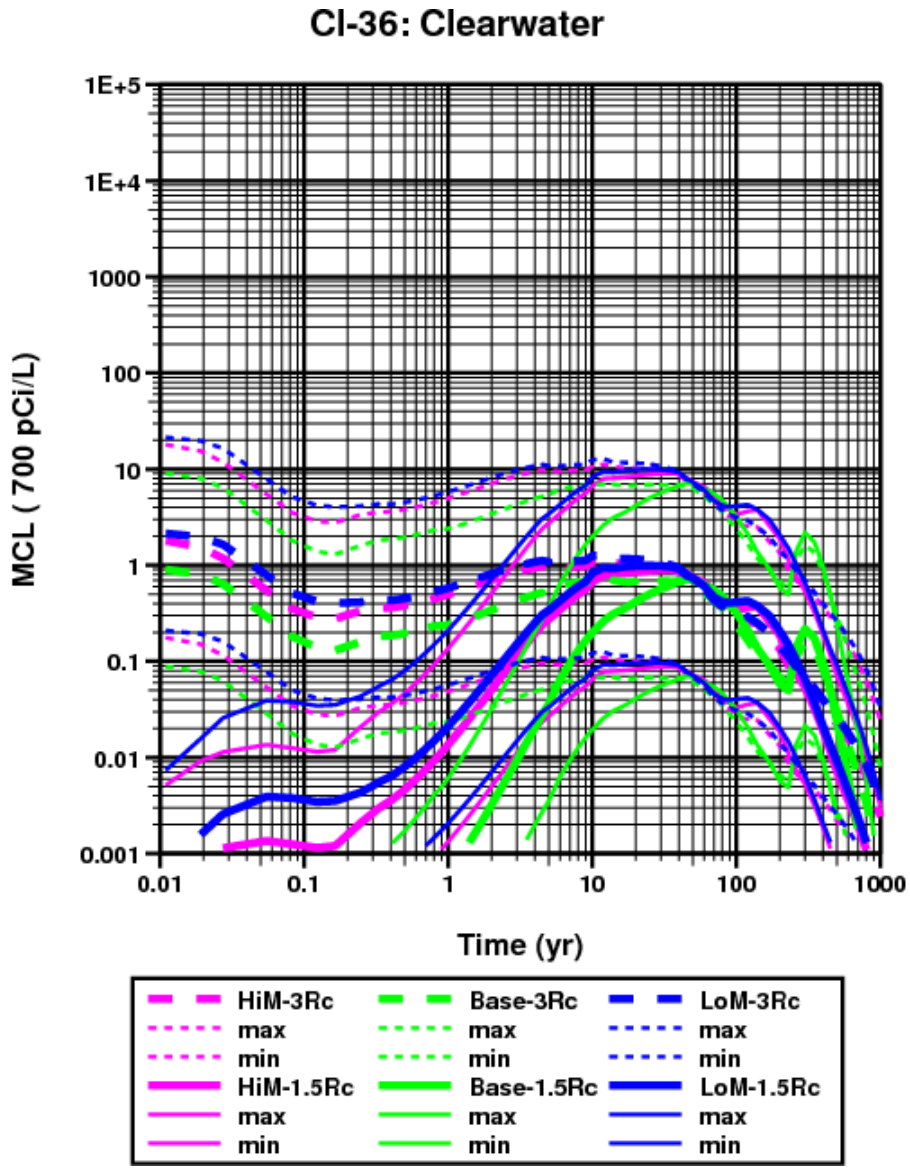

Figure 6.25 Sensitivity study for Cl-36 transport from CLEARWATER HST model.

For Cl-36 radionuclide flux concentration to the SZ model interface (Figure 6.25):

- Dashed lines indicate a Cl-36 source distributed to 3Rc can produce higher radionuclide flux concentrations to the SZ model interface at early times.
- Solid lines show effects of a more compact Cl-36 source distribution.
- Thin lines reflect uncertainty in Cl-36 source value.
- Colors show sensitivity to transport mobility cases.

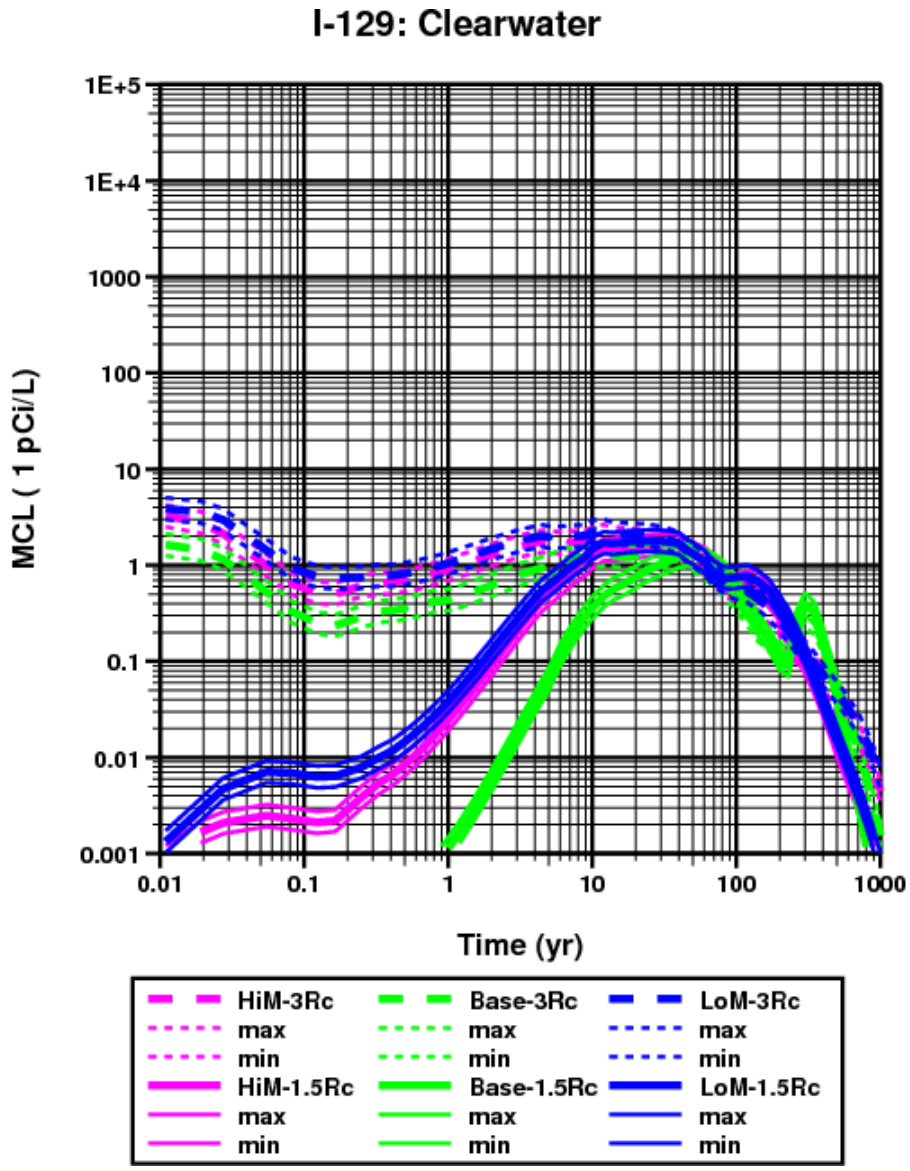

Figure 6.26 Sensitivity study for Cl-36 transport from CLEARWATER HST model.

For I-129 radionuclide flux concentration to the SZ model interface (Figure 6.26):

- Dashed lines indicate an I-129 source distributed to 3Rc can produce relatively high radionuclide flux concentrations to the SZ model interface at early times.
- Solid lines show effects of a more compact I-129 source distribution.
- Thin lines reflect uncertainty in I-129 source value.
- Colors show sensitivity to transport mobility cases.

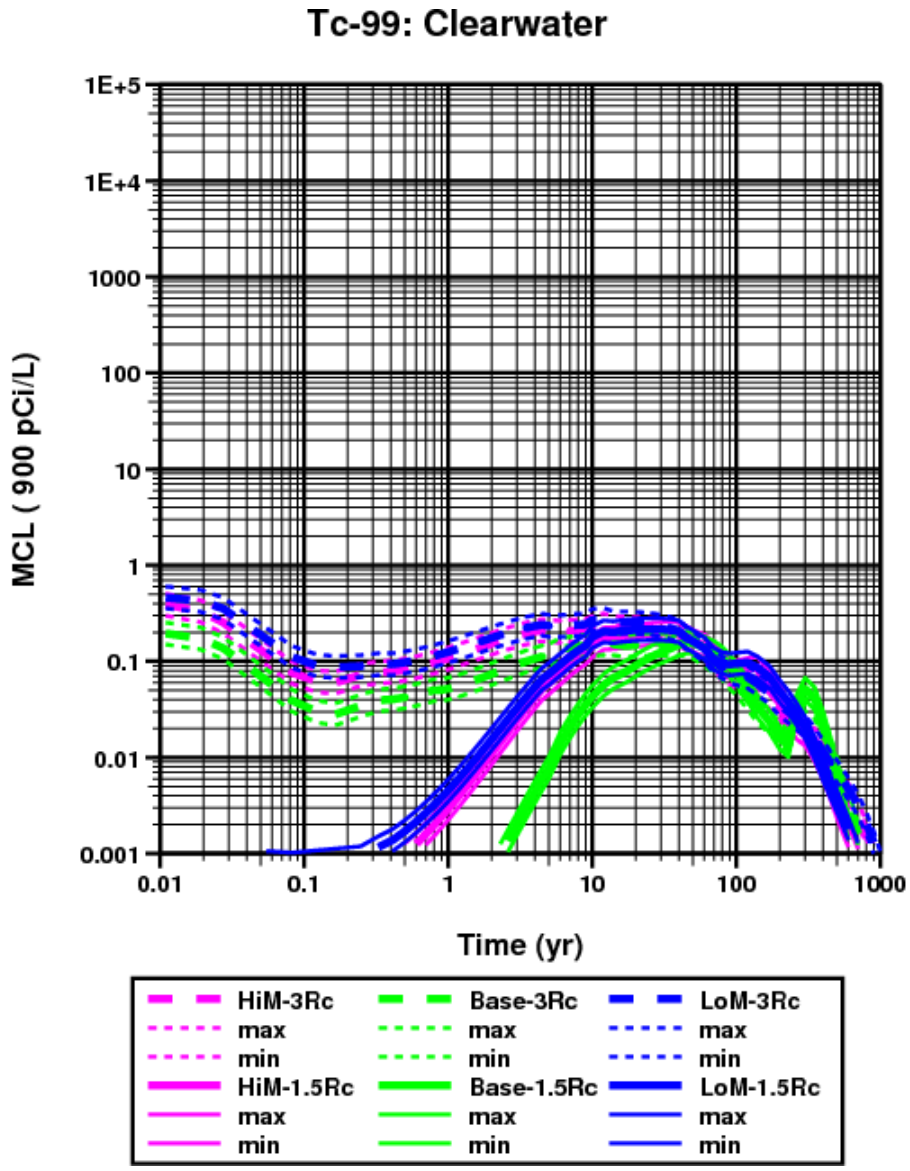

Figure 6.27 Sensitivity study for Tc-99 transport from CLEARWATER HST model.

For Tc-99 radionuclide flux concentration to the SZ model interface (Figure 6.27):

- Dashed lines indicate a Tc-99 source distributed to 3Rc can produce relatively high radionuclide flux concentrations to the SZ model interface at early times.
- Solid lines show effects of a more compact Tc-99 source distribution.
- Thin lines reflect uncertainty in Tc-99 source value.
- Colors show sensitivity to transport mobility cases.

6.4.3.3 Sorbing Radionuclides

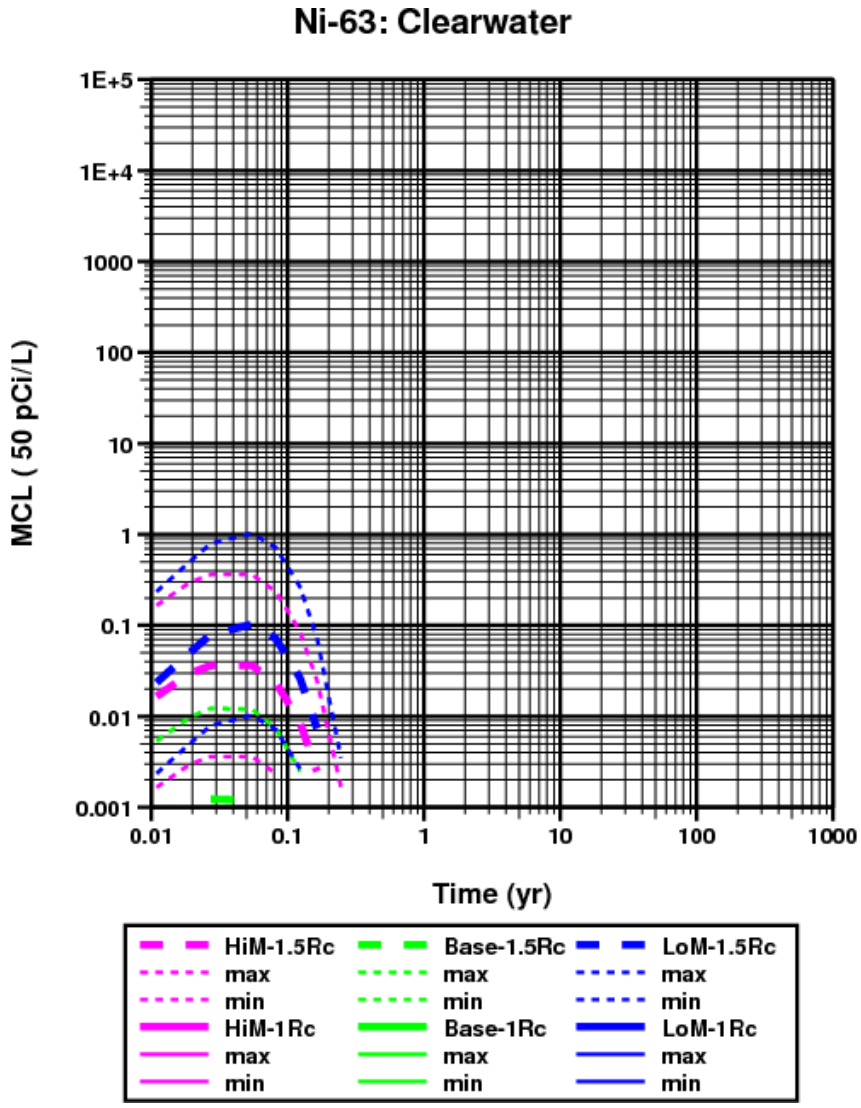

Figure 6.28 Sensitivity study for Ni-63 transport from CLEARWATER HST model.

For Ni-63 radionuclide flux concentration to the SZ model interface (Figure 6.28):

- Dashed lines indicate a Ni-63 source distributed to 1.5Rc can produce early relatively high radionuclide flux concentrations to the SZ model interface at early times assuming a maximal radial distribution. However, these Ni-63 flux concentrations are below the MCL even for high mobility cases, confirming the N-63 is not a significant radionuclide source term (Zavarin et al., 2011).
- Thin lines reflect uncertainty in Ni-63 source value.
- Colors show sensitivity to transport mobility cases.

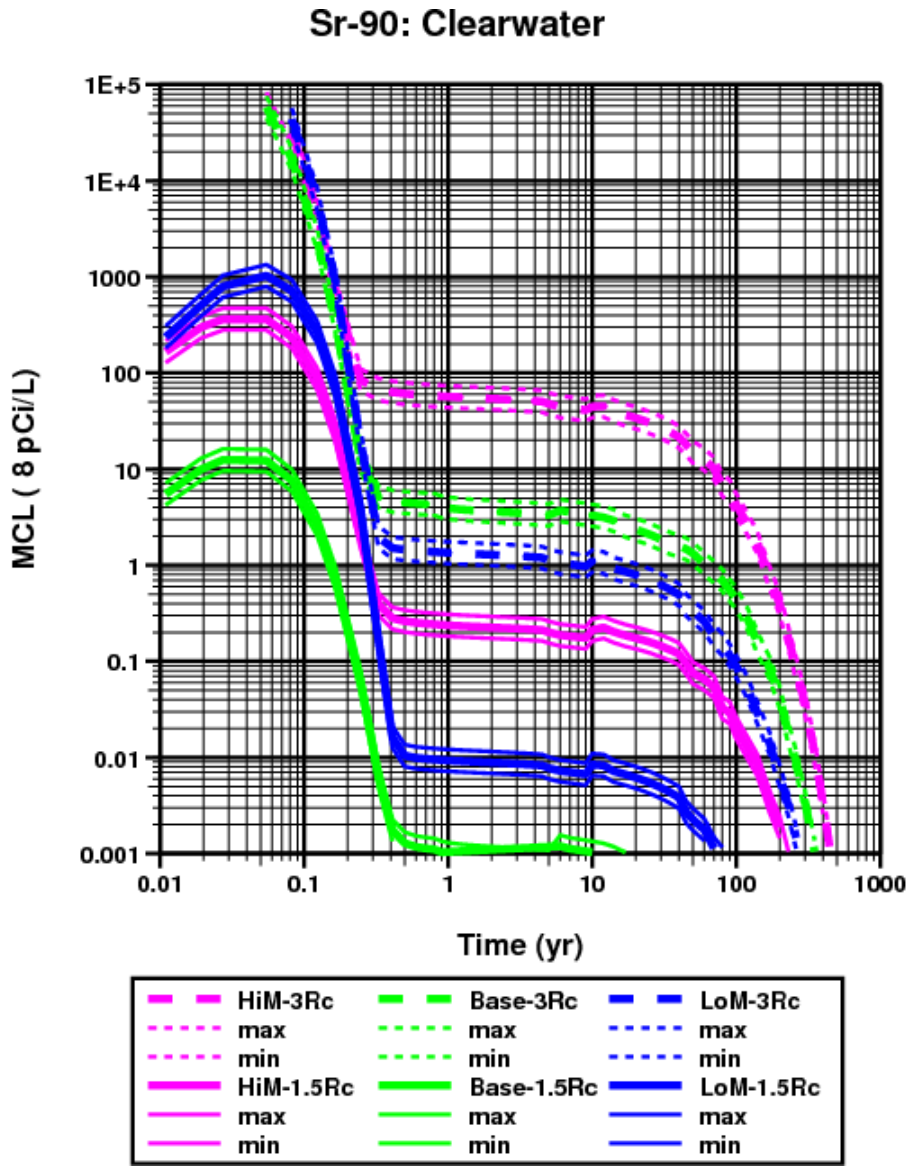

Figure 6.29 Sensitivity study for Sr-90 transport from CLEARWATER HST model.

For Sr-90 radionuclide flux concentration to the SZ model interface (Figure 6.29):

- Dashed lines indicate a Sr-90 source distributed to 3Rc can produce relatively higher radionuclide flux concentrations to the SZ model interface at early times compared to a more compact 1.5Rc source distribution shown by solid lines.
- Thin lines reflect uncertainty in Sr-90 source value.
- Colors show sensitivity to transport mobility cases.

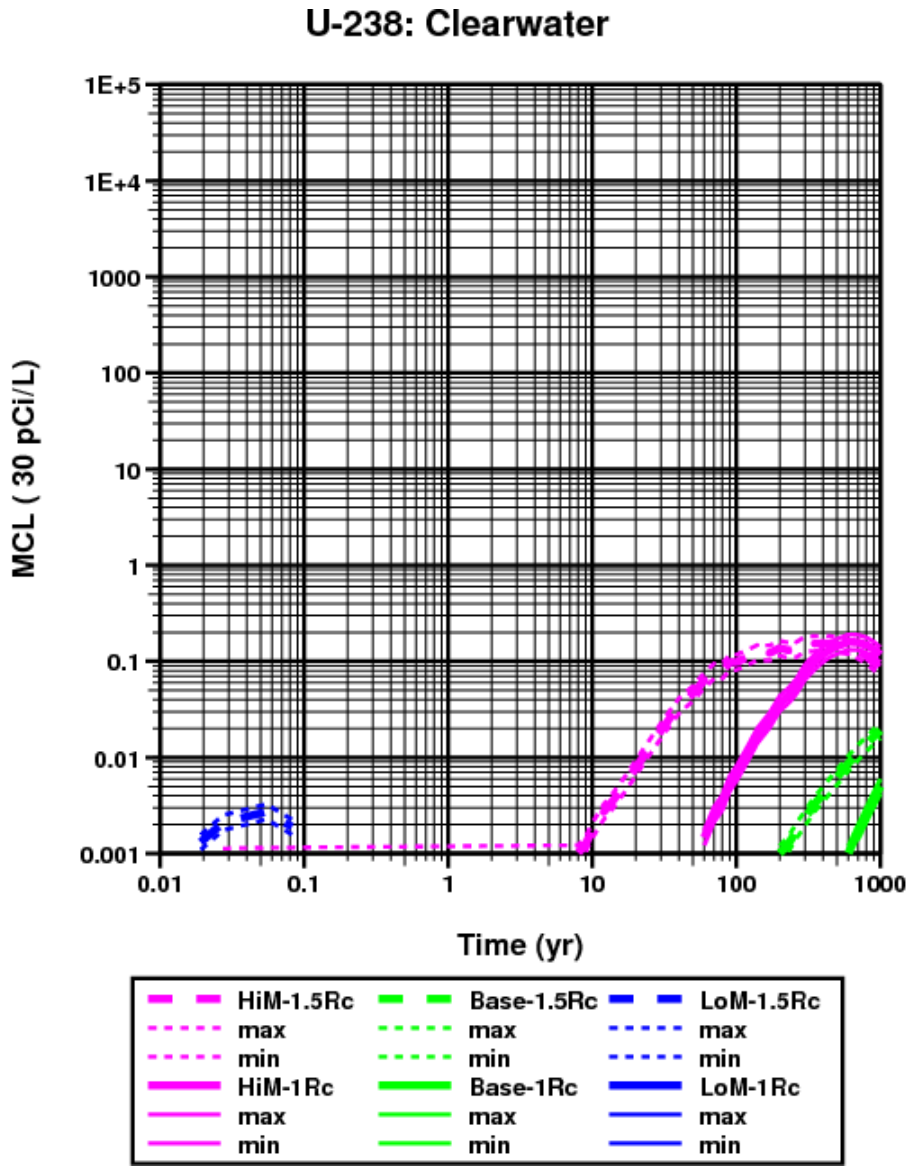

Figure 6.30 Sensitivity study for U-238 transport from CLEARWATER HST model.

For U-238 radionuclide flux concentration to the SZ model interface (Figure 6.30):

- Comparison of dashed lines relative to solid lines show how a U-238 source distributed to 1.5 Rc compared to 1 Rc produces earlier breakthrough to the SZ model interface.
- Thin lines reflect uncertainty in U-238 source value.
- Colors show sensitivity to transport mobility cases.

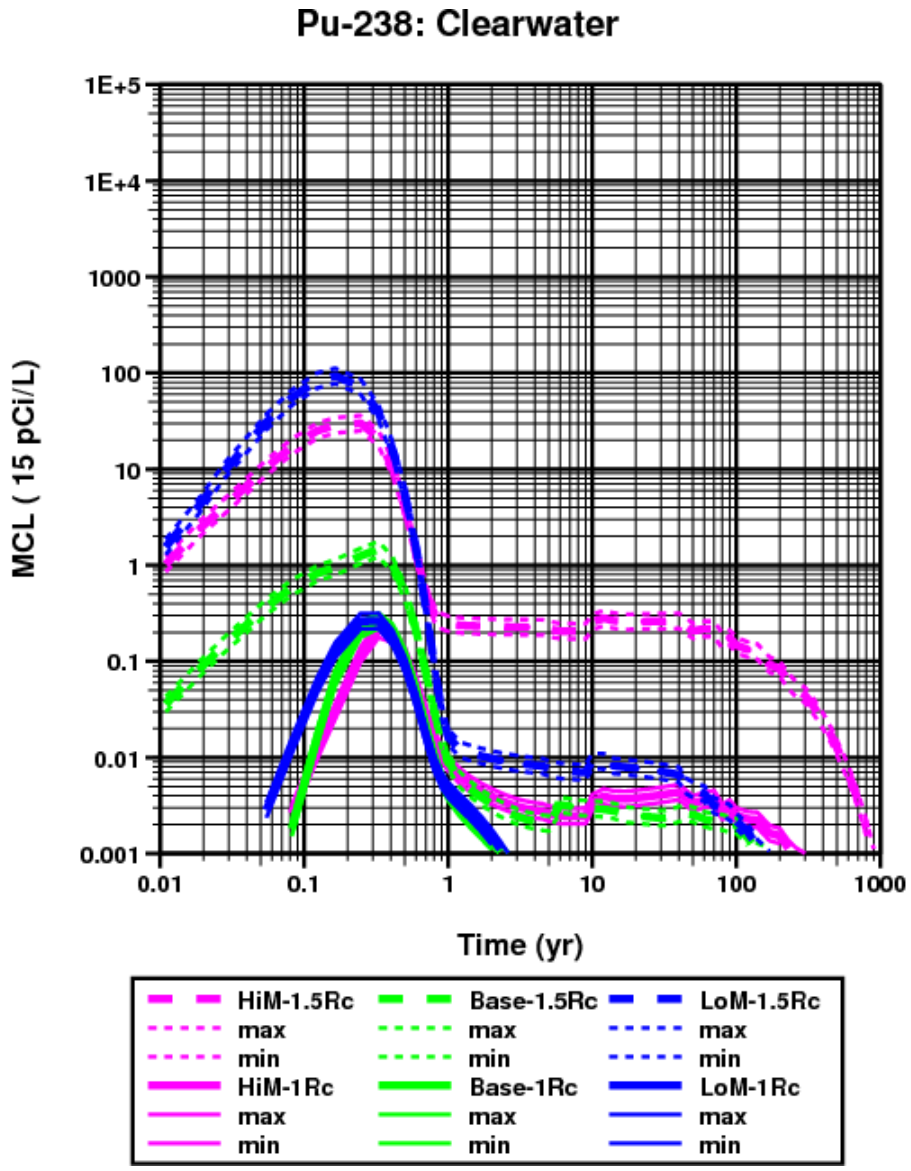

Figure 6.31 Sensitivity study for Pu-238 transport from CLEARWATER HST model.

For Pu-238 radionuclide flux concentration to the SZ model interface (Figure 6.31):

- Comparison of dashed lines relative to solid lines shows how a Pu-238 source distributed to 1.5 Rc compared to1 Rc produces earlier breakthrough and higher concentrations at the SZ model interface.
- Thin lines reflect uncertainty in U-238 source value.
- Colors show sensitivity to transport mobility cases.

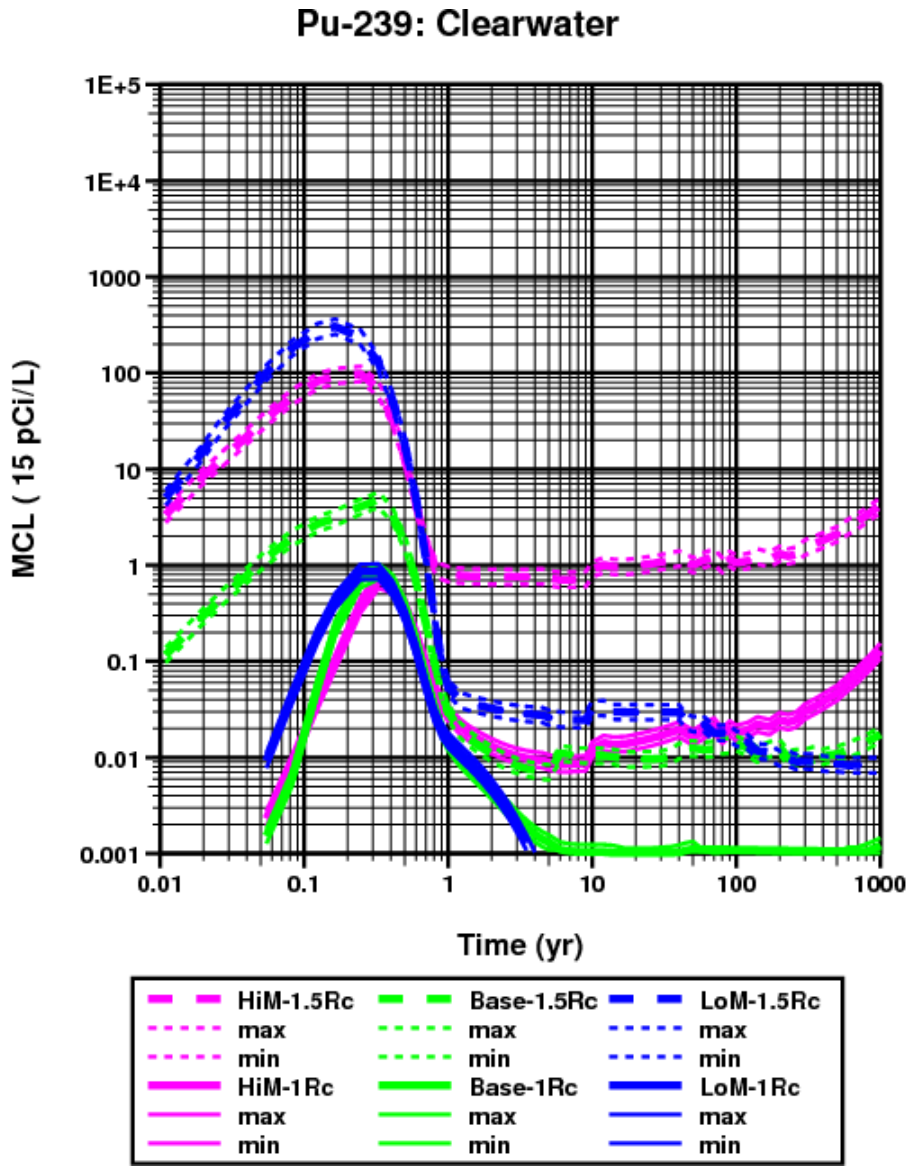

Figure 6.32 Sensitivity study for Pu-239 transport from CLEARWATER HST model.

For Pu-239 radionuclide flux concentration to the SZ model interface (Figure 6.32):

- Comparison of dashed lines relative to solid lines show how a Pu-239 source distributed to 1.5 Rc compared to1 Rc produces earlier breakthrough and higher concentrations at the SZ model interface.
- Thin lines reflect uncertainty in Pu-239 source value.
- Colors show sensitivity to transport mobility cases.

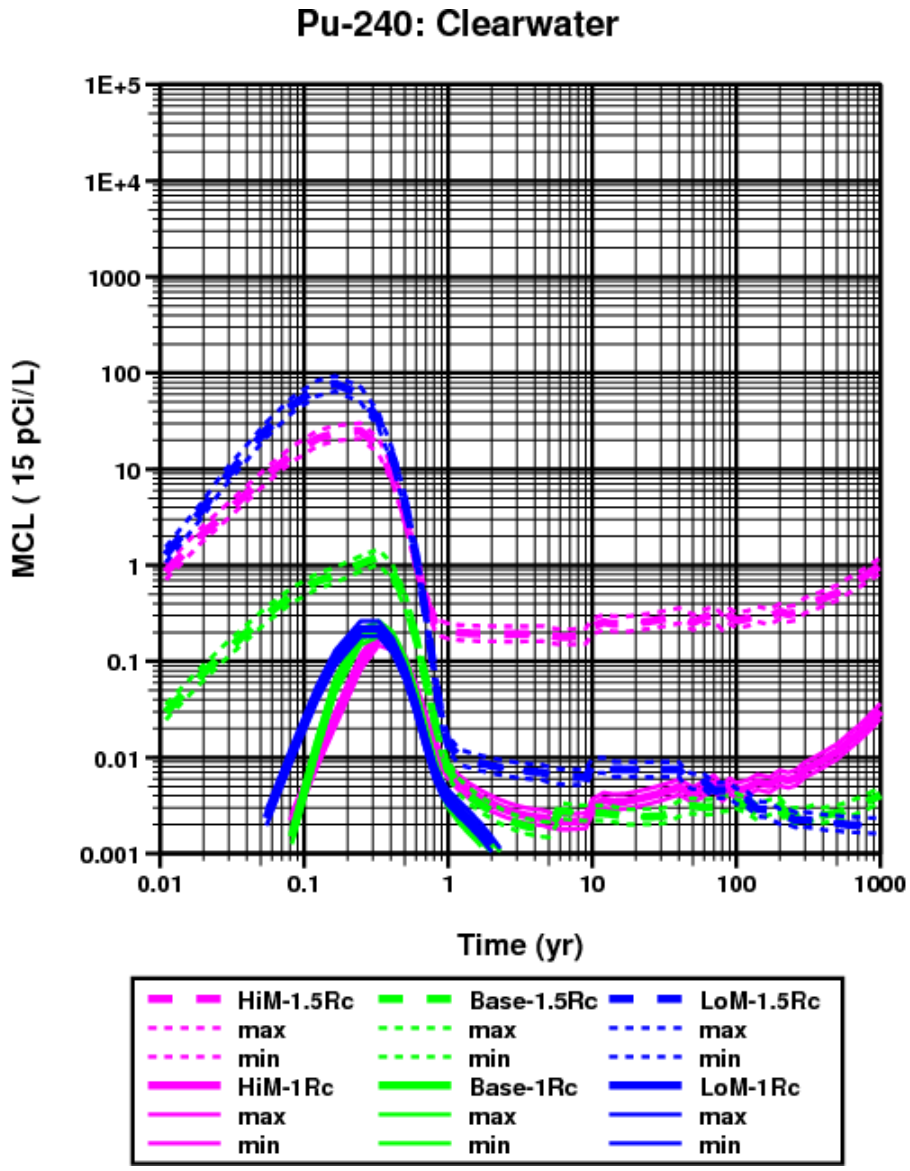

Figure 6.33 Sensitivity study for Pu-240 transport from CLEARWATER HST model.

For Pu-240 radionuclide flux concentration to the SZ model interface:

- Comparison of dashed lines relative to solid lines show how a Pu-239 source distributed to 1.5 Rc compared to1 Rc produces earlier breakthrough and higher concentrations at the SZ model interface.
- Thin lines reflect uncertainty in Pu-240 source value.
- Colors show sensitivity to transport mobility cases.

6.4.4 WINESKIN

The interface between the SZ model and the WINESKIN HST model (the "SZ model interface") is a "stairstep" pair of planes (Section 2.1.2), with the vertical face situated about 475 m south of the WINESKIN test and the horizontal top of the step situated at 1,550 m elevation, which is about 221 meters below the elevation of the WINESKIN test of 1,771 m. The source zones for the WINESKIN HST model are at least 300 m distant from the closest point on the WINESKIN SZ model interface, based on the WINESKIN HST model Rc of 72 m as derived from maximum announced yield (USDOE, 2015) and Pawloski (1999) as detailed in Section 2.7.2. Because the SZ model interface is located relatively distant from the WINESKIN HST model source zones compared to the CLEARWATER HST model sources zones, several transport model-related effects can be expected from the WINESKIN HST model:

- Radionuclide sources distributed out to 3Rc or less will result in a delay time for breakthrough at the SZ model interface.
- Radionuclide sources distributed to 1.5 Rc or less will be delayed in breakthrough relative to sources distributed to 3Rc, but this delay may be less prominent compared to the CLEARWATER test because of the greater distance to the SZ model interface for the WINESKIN test.
- Because of the distance of the SZ model interface between radionuclide source zones and the SZ model interface, which is largely occupied by zeolitic tuffs with sorbing minerals, sorbing radionuclides, such as Ni-63, Sr-90, and Pu species, may not reach the SZ model interface for the WINESKIN test regardless the range of radionuclide mobility parameters. The WINESKIN HST model has a potential to exclude several sorbing radionuclide sources from consideration for regional-scale transport evaluation by SZ models.

6.4.4.1 Non-Sorbing Radionuclides

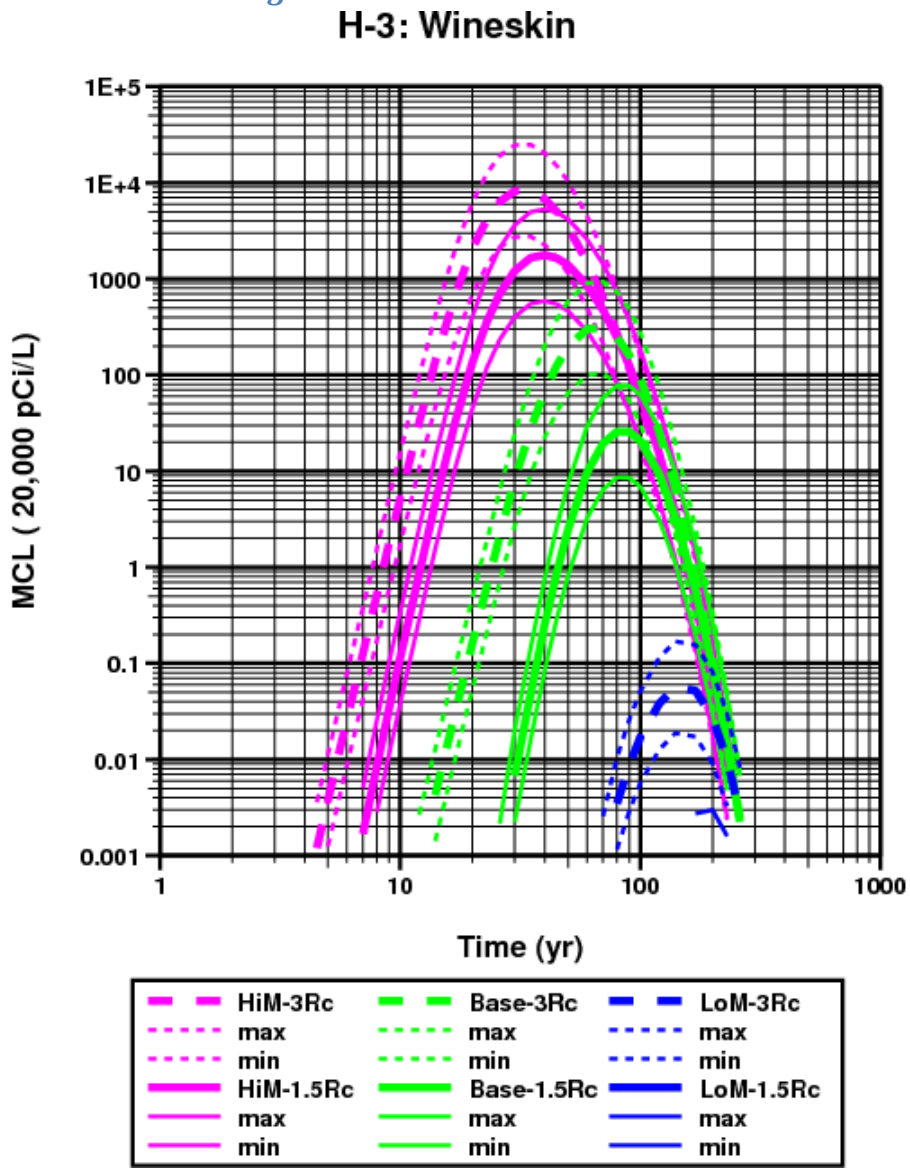

Figure 6.34 Sensitivity study for H-3 transport from WINESKIN HST model.

For H-3 radionuclide flux concentration to the SZ model interface (Figure 6.34):

- Comparison of dashed lines relative to solid lines shows how a H-3 source distributed to 3 Rc compared to 1.5 Rc produces earlier breakthrough and higher peak concentrations at the SZ model interface.
- Thin lines reflect uncertainty in H-3 source value.
- Colors show sensitivity to transport mobility cases.

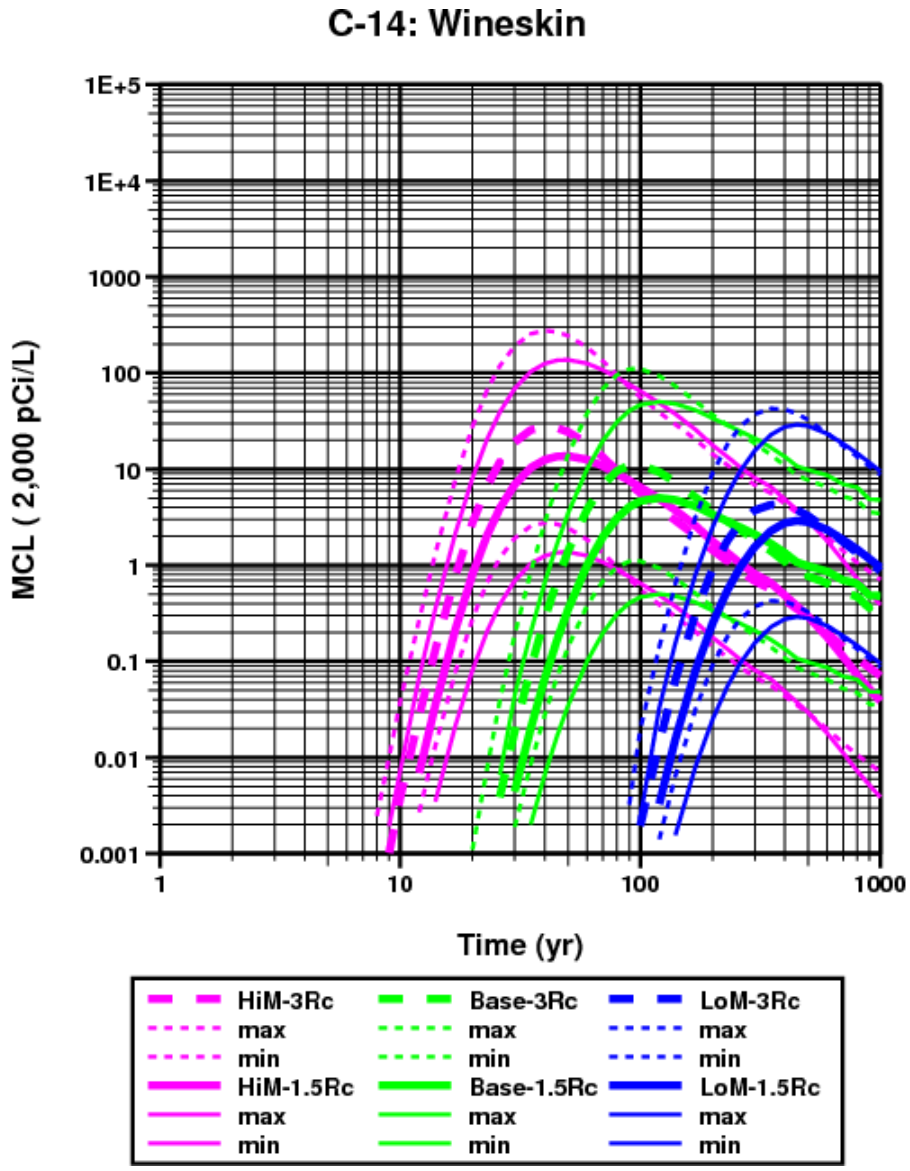

Figure 6.35 Sensitivity study for C-14 transport from WINESKIN HST model.

For C-14 radionuclide flux concentration to the SZ model interface (Figure 6.35):

- Comparison of dashed lines relative to solid lines shows how a C-14 source distributed to 3 Rc compared to 1.5 Rc produces earlier breakthrough and higher peak concentrations at the SZ model interface.
- Thin lines reflect uncertainty in C-14 source value.
- Colors show sensitivity to transport mobility cases.
- Results from 2-D CLEARWATER HST model (Zavarin et al., 2011) including thermal, gaseous, and chemical processes may be used to adjust C-14 source distribution or, possibly, eliminate C-14 as a source term.

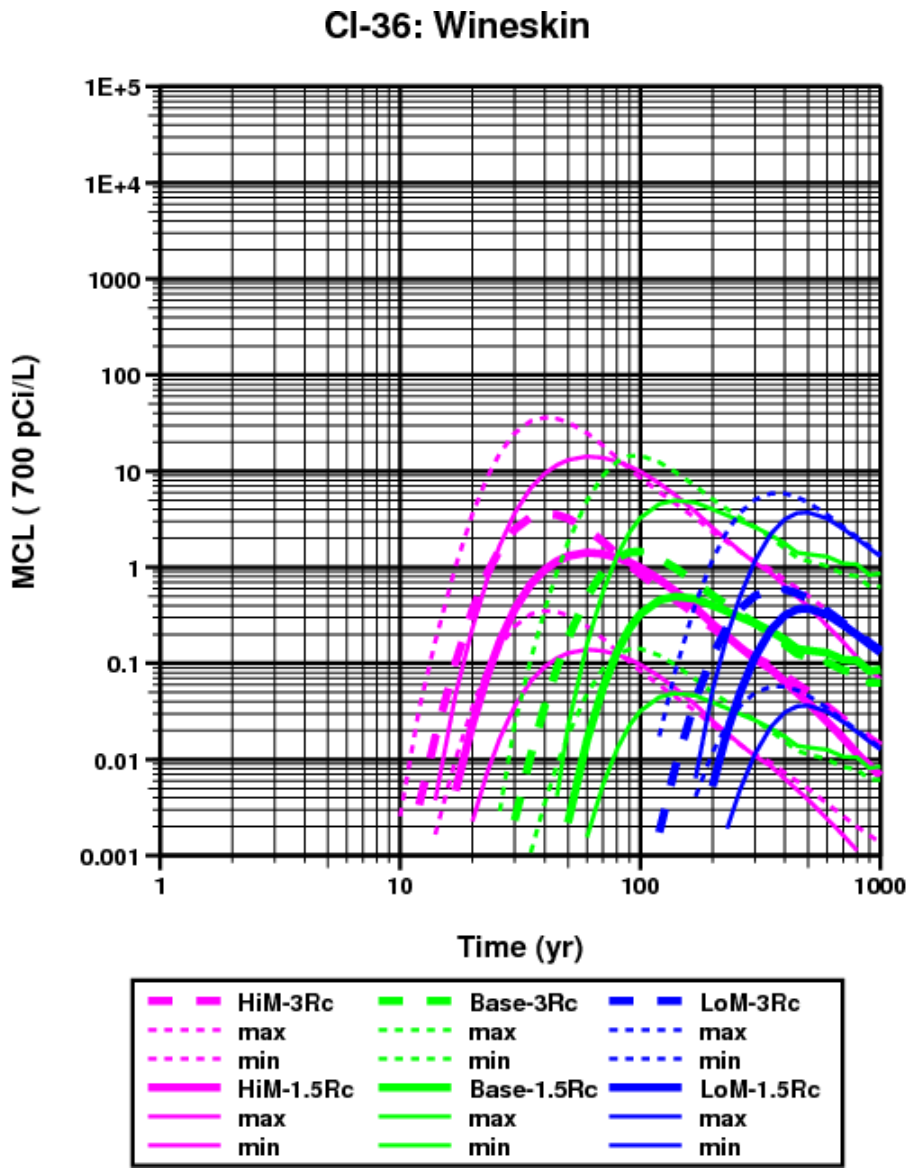

Figure 6.36 Sensitivity study for Cl-36 transport from WINESKIN HST model.

For Cl-36 radionuclide flux concentration to the SZ model interface (Figure 6.36):

- Comparison of dashed lines relative to solid lines shows how a Cl-36 source distributed to 3 Rc compared to 1.5 Rc produces earlier breakthrough and higher peak concentrations at the SZ model interface.
- Thin lines reflect uncertainty in Cl-36 source value.
- Colors show sensitivity to transport mobility cases.

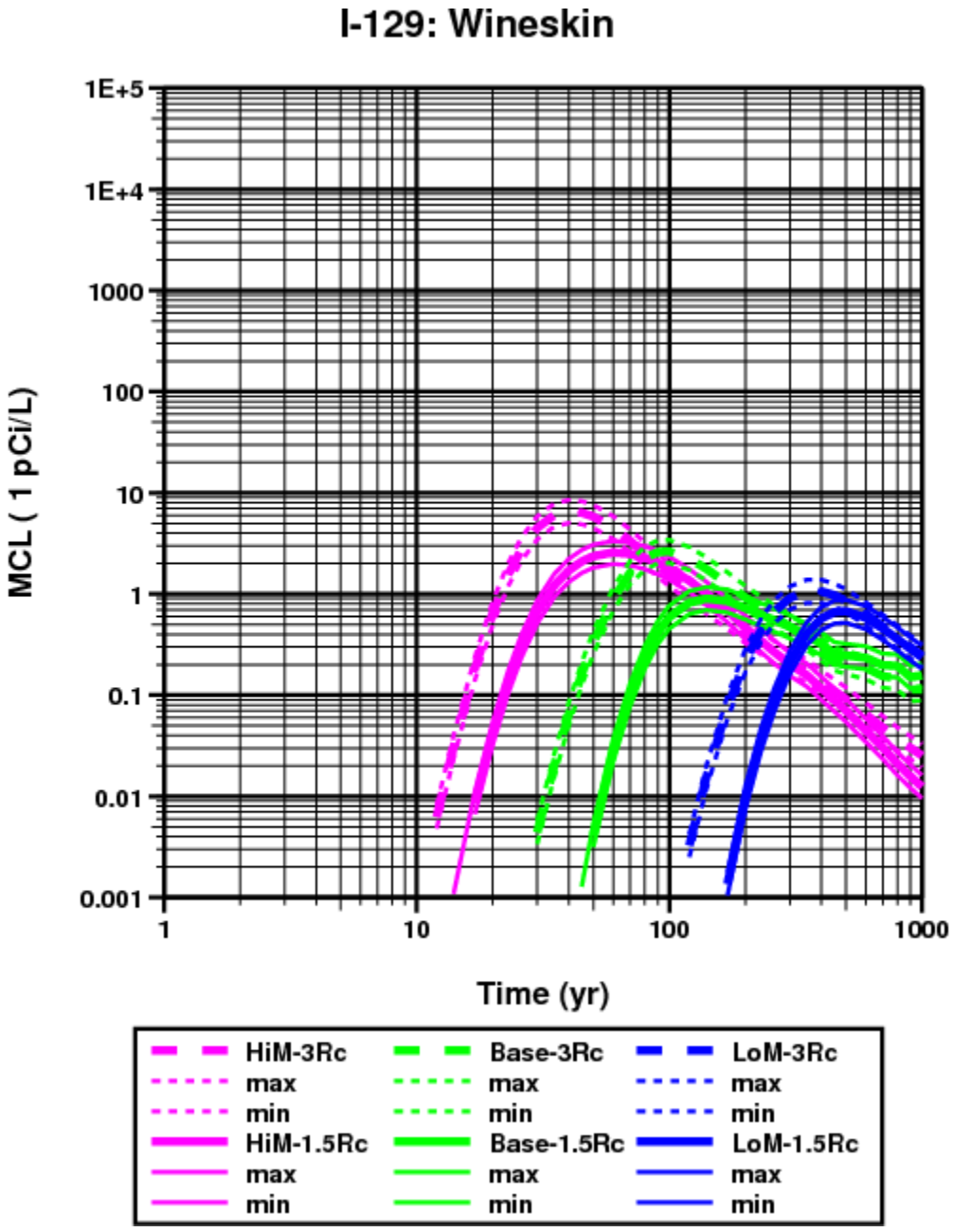

Figure 6.37 Sensitivity study for I-129 transport from WINESKIN HST model.

For I-129 radionuclide flux concentration to the SZ model interface (Figure 6.37):

- Comparison of dashed lines relative to solid lines shows how a I-129 source distributed to 3 Rc compared to 1.5 Rc produces earlier breakthrough and higher peak concentrations at the SZ model interface.
- Thin lines reflect uncertainty in I-129 source value.
- Colors show sensitivity to transport mobility cases.

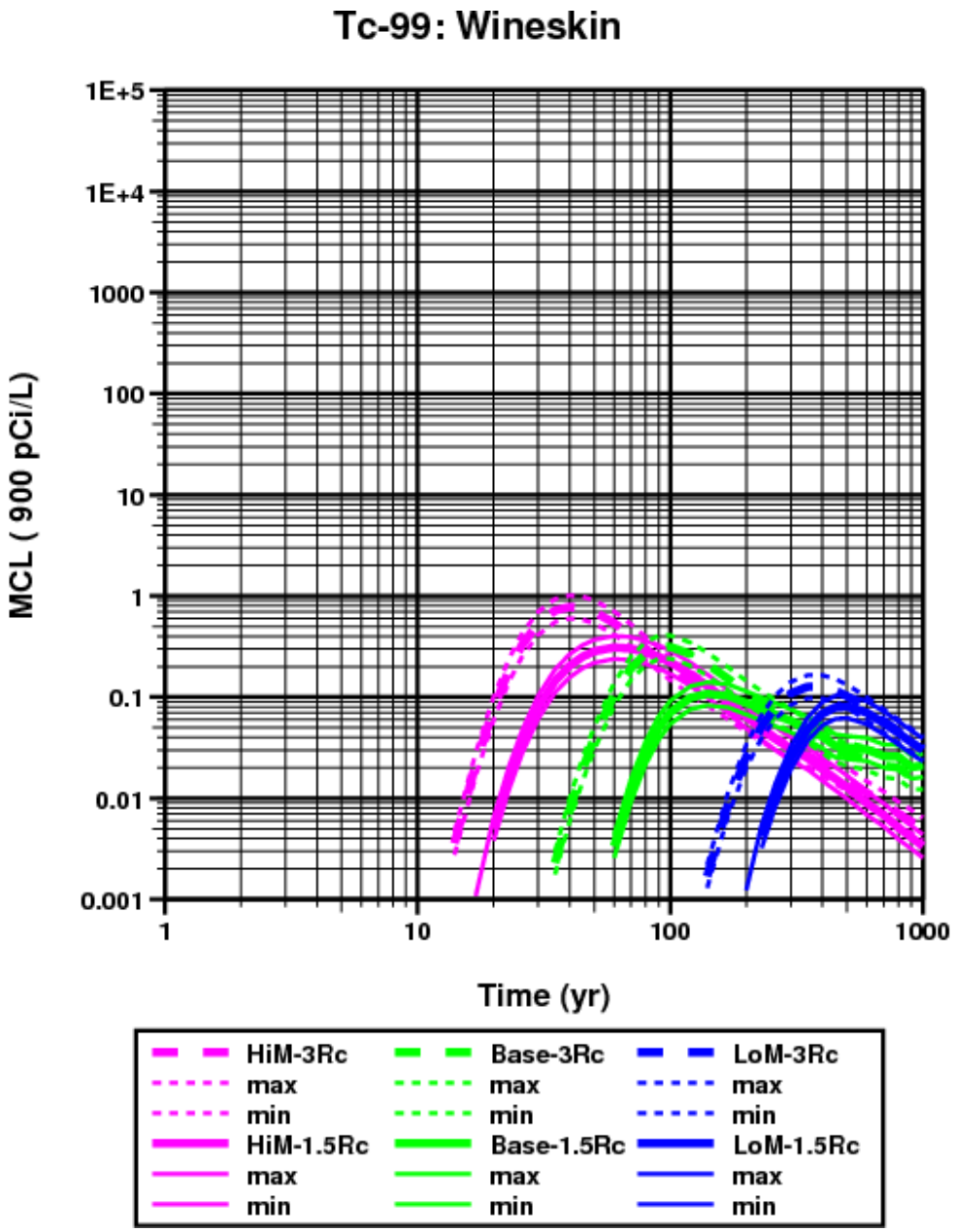

Figure 6.38 Sensitivity study for Tc-99 transport from WINESKIN HST model.

For Tc-99 radionuclide flux concentration to the SZ model interface (Figure 6.38):

- Comparison of dashed lines relative to solid lines shows how a Tc-99 source distributed to 3 Rc compared to 1.5 Rc produces earlier breakthrough and higher peak concentrations at the SZ model interface.
- Thin lines reflect uncertainty in Tc-99 source value.
- Colors show sensitivity to transport mobility cases.

6.4.4.2 Sorbing Radionuclides

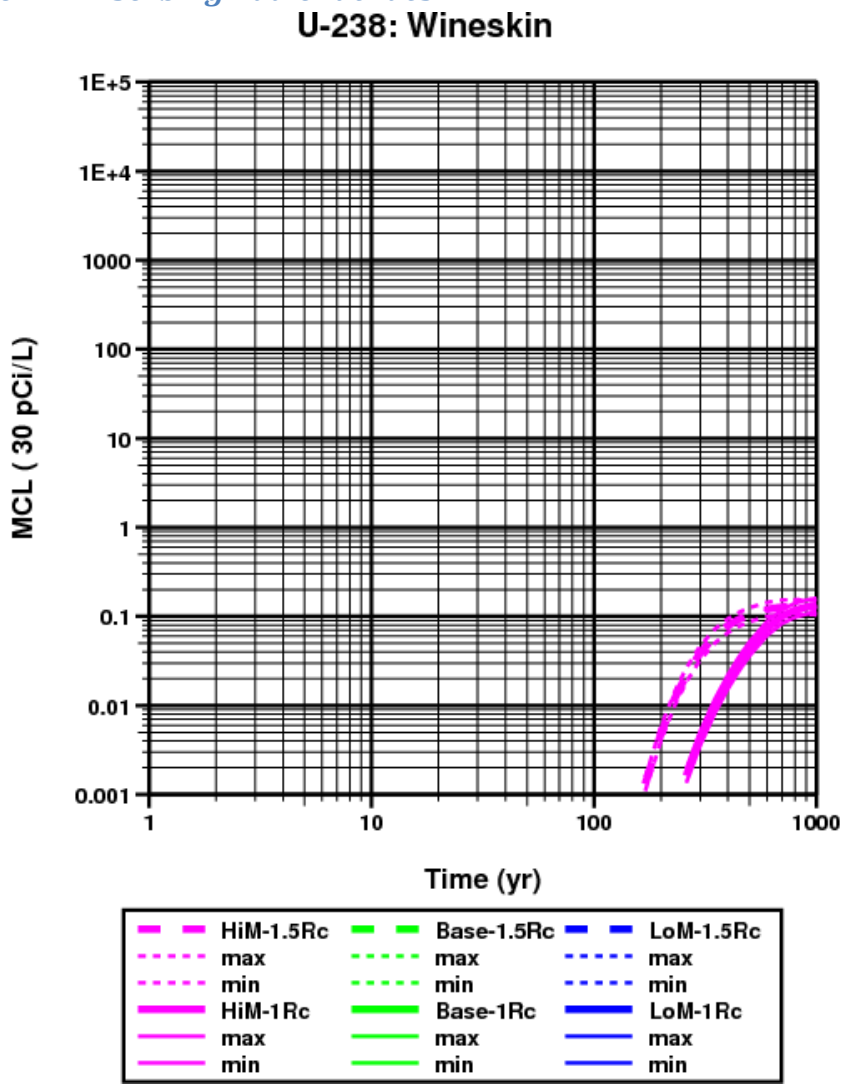

Figure 6.39 Sensitivity study for U-238 transport from WINESKIN HST model.

For U-238 radionuclide flux concentration to the SZ model interface (Figure 6.39):

- Only the high-mobility transport case produces U-238 flux to the WINESKIN SZ model interface.
- Comparison of dashed lines relative to solid lines shows how a U-238 source distributed to 1.5 Rc compared to 1.0 Rc produces earlier breakthrough at the SZ model interface.
- Thin lines reflect uncertainty in U-238 source value.

Sensitivity studies for Ni-63, Sr-90, Pu-238, Pu-239, and Pu-240 are not shown because these radionuclide sources did not reach the SZ model interface for all sensitivity cases.

6.5 Comparison of Observational Data to HST Model Transport

A goal of the CLEARWATER and WINESKIN HST models is produce aqueous concentrations consistent with the available observational data. Radionuclide aqueous concentration data at Rainier Mesa or other NNSS areas with similar test characteristics can be used to help constrain the HST model parameters.

6.5.1 Observational Data

Post-test radionuclide data in source zones for the RAINIER test are presented in Zavarin et al., (2011). These data are used to directly constrain the 2-D RAINIER HST model (Zavarin et al., 2011) and can indirectly help constrain the WINESKIN and CLEARWATER HST models. There are other radionuclide concentration data than the RAINIER data that may be more relevant to the CLEARWATER, WINESKIN, and other Rainier Mesa tests. The RAINIER test was situated in a transition zone between vitric and zeolitic tuff, and most Rainier Mesa tests including CLEARWATER and WINESKIN were situated at least one Rc below the top of the zeolitized tuff (USDOE, 2015; Townsend, 2008).

No radionuclide concentration data are available specifically for the CLEARWATER and WINESKIN tests. Aqueous radionuclide concentration data in drill holes on Rainier Mesa were obtained at locations distant from the CLEARWATER and WINESKIN radionuclide source zones and HST model volume. Thus, no radionuclide concentration data are available to directly constrain early time aqueous concentrations in the CLEARWATER and WINESKIN HST model source zone fractures or to calibrate late-time aqueous concentrations in the in the CLEARWATER and WINESKIN HST model volumes.

Additional radionuclide concentration data that may be useful to constrain the CLEARWATER and WINESKIN HST models include:

- Sr-90 data obtained from 1959 to 1961 following B, C, and E-Tunnel tests.
- Radionuclide concentration data obtained from T, N, and E-Tunnel water, effluent, or ponds.
- Radionuclide concentration data obtained from “hot well” sampling of the BILBY and DALHART tests situated in zeolitic tuffs of Yucca Flat.

To better understand the relevance of the observational data to the HST model, concentrations are given in both as radiologic activity in picocuries per liter (pCi/L) and maximum contaminant limit (MCL), with the MCLs posted in the tables of data.

6.5.1.1 B, C, and E-Tunnel Sr-90 Data Collected From 1959 to 1961

Between 1959 and 1961, Sr-90 data was collected from seeps and exploratory holes associated with B, C, and E-Tunnel tests. These data were analyzed by the USGS at Denver, Colorado using USGS method 13503. Location of the 1959-1961 Sr-90 data associated with the C and E-Tunnel tests is compiled by Hu and Zavarin (2007). A single B-Tunnel Sr-90

datum has no location or test-specific information except that the sample date was preceded by the RAINIER, EVANS, and TAMALPAIS tests. These measured aqueous concentrations indicate that early-time Sr-90 concentrations in fractures can be well above the Sr-90 MCL of 8 pCi/L.

The NEPTUNE test was detonated October 14, 1958 (11/14/58) in C-Tunnel beneath the eastern face of Rainier Mesa. This test was not contained and produced a collapse structure at the ground surface. The measured Rc is 6.1 m (Zavarin, 2014). Several post-test drill holes were drilled into the collapse structure. Sr-90 aqueous concentration was obtained from a seep in the U12c.03-1 shaft and from the U.12.c05 exploratory hole. The distance of these sample locations from the NEPTUNE working point could not be determined.

The LOGAN test was detonated October 16, 1958 (10/16/58) in E-Tunnel. The U-12e.02 post-test exploratory drift was excavated between 73.2 m and 48.8 m of the LOGAN working point location. Assuming a measured Rc of 28.4 m (Boardman et al., 1964; Zavarin, 2014) and considering that sample locations are 58.2m from the working point, the Sr-90 data labeled "U12e.02X191" are located at 2.1Rc and, thus, well within the RST maximum Sr-90 source zone radius of 3Rc. Importantly, these data were obtained from a post-test drift and, thus, may most useful for estimating post-test Sr-90 aqueous concentration within a source zone.

The BLANCA test was detonated October 30, 1958 (11/30/58) in E-Tunnel. Measured Rc is 44.2 m (Boardman et al., 1964; Zavarin, 2014). Sr-90 aqueous concentration data obtained from pre-test E-Tunnel shafts and alcoves are estimated to be located between 3.5 and 4.5 Rc from the nearest test, farther than the expected 3 Rc limit of the HST model Sr-90 source zone. Importantly, the LOGAN and BLANCA tests did not use a "buttonhook" emplacement tunnel design and, rather, a direct tunnel with plugs of sandbags for containment. As a result, the location and magnitude of Sr-90 aqueous concentration data from pre-test shafts for the LOGAN and BLANCA tests may be affected by the test design.

As mentioned above, one Sr-90 aqueous concentration datum was obtained from the U-12B-Tunnel complex. This datum has no specific-Tunnel or shaft location associated with the sample name. Based on the date of sampling, the closest test for the U-12b data could be RAINIER, EVANS, or TAMALPAIS.

Table 6.2 compiles Sr-90 aqueous concentration data with concentrations greater than 3 pCi/L (0.375 MCL) as analyzed by USGS Denver using procedure USGS 13503 (Clebsch, 1960; Clebsch and Barker, 1960; Navarro-Intera, 2013). Additional data have lower Sr-90 concentrations, and these are not listed in Table 6.2. It is not clear how and exactly where sample locations were selected, but preference was given to "cracks" or "seeps" indicating these data are relevant to the "fracture" continuum of the HST model. The data compiled in Table 6.2 are provided to gain insight on maximum Sr-90 concentrations in fractures at

early times in a radionuclide source environment similar to the CLEARWATER and WINESKIN tests. All distances are given by measured Rc from Zavarin (2014).

Table 6.2 Sr-90 aqueous concentration data with concentrations greater than 3 pCi/L (0.375 MCL) analyzed by USGS Denver using procedure USGS 13503.

Tunnel or Hole	Closest Test	Location	Source Description	Depth b.g.s. (m)	Distance to WP (Rc)	Date	Conc (pCi/L)	Conc (MCL)
U12b	?	Tunnel Shaft	Seep	n/a	?	9/28/61	60	7.5
U12c	NEPTUNE	U.12.c05	Exploratory	190.5	?	5/5/61	70	8.8
U12c	NEPTUNE	U12c.03-1	Seep	246.7	?	5/3/61	3.3	0.4
U12e	LOGAN	U12e.02, Alcove B	Seep	n/a	~4Rc	5/5/61	140	17.5
U12e	LOGAN	U12e.02 470 NE	Seep	n/a	5.1 Rc	1/29/59	380	48
U12e	LOGAN	U12e.02 170 NE	Seep	n/a	1.8Rc	5/31/59	3900	490
U12e	BLANCA	U12e 29+35	Drip	n/a	3.7Rc	1/22/59	3.6	0.5
U12e	BLANCA	U12e 19+05	Seep from	n/a	4.4Rc	1/22/59	160	20

6.5.1.2 T-Tunnel Monitoring Data

The U-12t GSP data refer to radionuclide concentrations sampled from the water impounded within T-Tunnel. Compared to E and N-Tunnel discharge monitoring data, the T-Tunnel GSP data produce relatively higher radionuclide concentrations, which may be attributed to many factors. Modeling of T-Tunnel flow, transport, and discharge provides further insights into the T-Tunnel radionuclide monitoring data (Zavarin et al., 2011).

Assuming the impounded T-Tunnel water partially originates from or passes through radionuclide source zones, radionuclide concentrations for U-12t GSP monitoring data may be reflective of radionuclide exchange zones for CLEARWATER or WINESKIN. Interpretation of these data must include consideration of radioactive decay, mixing of sources from different tests, releases from containment vessels, and dilution of impounded tunnel water originating from or passing through source zones (Zavarin et al., 2011). Therefore, the T-Tunnel GSP data may guide either lower or upper bounds for HST model calibration of radionuclide aqueous concentrations in fractures or void space of the radionuclide source zones.

Radionuclide concentrations associated with T-Tunnel have been monitored within seeps and flow in shafts and effluent, and in ponds. The complete set of monitoring data is too voluminous and complex to discuss in this report. Alternatively, maximum concentrations are examined in this report to gain insight on possible HST model concentration upper limits. As discussed earlier, interpretation of these maximum concentration values must consider many complexities not addressed in this report.

Table 6.3 Selected maximum concentrations of HST model radionuclides measured at the U-12t GSP.

Radionuclide	Date	Conc (pCi/L)
H-3	12/1/1993	2.20e7
H-3	6/9/94	6.14e7
H-3	11/30/94	5.68e7
H-3	3/7/95	4.99e7
H-3	6/13/95	5.09e7
H-3	9/5/95	4.79e7
H-3	12/5/95	4.91e7
H-3	9/17/96	4.05e7
H-3	10/14/98	3.12e7
H-3	1999	4.4e+07
H-3	10/6/99	3.27e7
H-3	2/6/01	3.75e7
H-3	10/3/01	3.99e7
H-3	10/9/02	2.2e7
H-3	11/2/06	4.36e7
C-14	1999	75.3
C-14	11/2/06	78.5
Cl-36	1999	31.4
Cl-36	11/2/06	59.2
I-129	11/2/06	0.33
Tc-99	11/2/06	0.183
Pu-238 (total)	11/2/06	6
Pu-239+240 (aq)	11/2/06	35
Pu-239+240 (total)	11/2/06	54
Sr-90	11/2/06	35.2 to 37
U-238	11/2/06	1.164

Table 6.4 Maximum measured concentrations of HST model radionuclides measured at T-Tunnel in GSP, shafts, effluent, or ponds.

Radionuclide	MCL	Date	Location	Concentration (pCi/L)	Concentration (MCL)
H-3	20,000	4/17/87	Pond 1	4.0e8	20,000
C-14	2,000	11/2/06	GSP	78.5	0.048
Cl-36	700	11/2/06	GSP	59.2	0.045
I-I29	1	11/2/06	GSP	0.33	0.33
Tc-99	900	11/2/06	GSP	0.183	0.00020
Pu-238 (total)	15	11/2/06	GSP	6	0.40
Pu-239+240 (aq)	30 (15+15)	11/2/06	GSP	35	1.2
Pu-239+240 (total)	30 (15+15)	11/2/06	GSP	54	1.8
Sr-90	8	7/21/92	GSP	37	4.6
U-238	30	11/2/06	GSP	1.164	0.039

Table 6.4 compiles selected maximum concentrations of HST model radionuclide sources measured in either T-Tunnel GSP, shafts, effluent, or ponds. Of the T-Tunnel radionuclide concentration measurements, the highest concentrations of the HST model radionuclide

sources have been measured at the GSP except for tritium, where highest concentrations were measured in T-Tunnel Pond 1. Tritium concentrations at the T-Tunnel GSP (see Table 6.3) tend to be about an order of magnitude lower than the maximum Pond 1 concentration.

6.5.1.3 N Tunnel Monitoring Data

Table 6.5 compiles maximum concentrations of HST model radionuclide sources measured in either N-Tunnel GSP, shafts, effluent, or ponds. Concentrations of radionuclides from N-Tunnel monitoring data tend to be lower than for T-Tunnel. This may be caused by dilution from water not passing through radionuclide source zones. Modeling of N-Tunnel flow, transport, and discharge provides further insights into the N-Tunnel radionuclide monitoring data (Zavarin et al., 2011).

Table 6.5 Maximum measured concentrations of HST model radionuclides measured at N-Tunnel in GSP, vent hole, shafts, effluent, or ponds.

Radionuclide	MCL	Date	Location	Conc (pCi/L)	Conc (MCL)
H-3	20,000	11/18/92	Pond 3	5.2e7	2,600
C-14	2,000	8/20/08	U12n.10 Vent Hole	150	0.0029
Cl-36	700	10/31/06	U12n.10 Vent Hole	100	0.0045
I-I29	1	10/31/06	U12n.10 Vent Hole	0.99	0.024
Tc-99	900	10/31/06	U12n.10 Vent Hole	0.19	0.0000066
Pu-238	15	1/10/91	Pond 3	0.55	0.037
Pu-239+240	30 (15+15)	5/3/90	Effluent	24	0.80
Sr-90	8	N/A	N/A	ND	N/A
U-238	30	10/30/06	Ext. Drift GSP	0.8983	0.030

6.5.1.4 E-Tunnel Monitoring Data

Maximum radionuclide concentrations from observational data in E-Tunnel show similar patterns to N and T-Tunnel, except for Sr-90 (Table 6.6). Relatively high Sr-90 concentrations are unique to data from B, C, and E-Tunnel as described in Section 6.5.1.1.

Table 6.6 Maximum measured concentrations of HST model radionuclides measured at E-Tunnel in GSP, shafts, effluent, or ponds.

Radionuclide	MCL (pCi/L)	Date	Location	Concentration (pCi/L)	Concentration (MCL)
H-3	20,000	7/15/70	Pond 4	1.15e9	57,500
C-14	2,000	8/23/99	Main GSP	9.4	0.0046
Cl-36	700	8/23/99	South GSP	15.0	0.021
I-I29	1	N/A	N/A	N/A	N/A
Tc-99	900	N/A	N/A	N/A	N/A
Pu-238 (?)	15	1/10/91	Pond 3	0.55	0.037
Pu-239+240 (?)	30 (15+15)	5/3/90	Effluent	24	0.80
Sr-90	8	5/31/59	Inside E-Tunnel	3,900	490
U-238	30	N/A	N/A	N/A	N/A

6.5.1.5 BILBY and DALHART Tests

Radionuclide concentration data pertinent to source zones of NNSS tests are compiled from "hot well" sampling databases relevant to the radionuclide source zones from underground nuclear tests at NNSS (Zavarin, 2011b). Hot well data from the BILBY and DALHART tests of Yucca Flat may be more comparable to the CLEARWATER and WINESKIN tests and other tests on Rainier Mesa because the BILBY and DALHART tests were situated in zeolitic tuffs. Tables 6.7 and 6.8 compile maximum measured concentrations of HST model radionuclides measured in the near field of the BILBY and DALHART tests. The maximum concentrations provide some guidance for plausible upper bounds to modeled radionuclide concentrations in the near field. However, many complexities remain in using the BILBY and DALHART hot well data to directly constrain the HST model, particularly for test-specific processes such as initial source term distribution and re-distribution by test effects, flow transients, sorption, matrix diffusion, and sampling time and location, for example.

Table 6.7 Maximum measured concentrations of HST model radionuclides measured in near field of BILBY test (U-3cn) detonated on 9/13/1963.

Radionuclide	MCL (pCi/L)	Date	Location	Concentration (pCi/L)	Concentration (MCL)
H-3	20,000	10/21/81	U-3cn PS#2	4.6e7	2,300
C-14	2,000	12/09/04	U-3cn PS#2	372	0.19
Cl-36	700	12/18/01	U-3cn PS#2	43.2	0.062
I-I29	1	12/09/04	U-3cn PS#2	0.252	0.25
Tc-99	900	12/18/01	U-3cn PS#2	82.6	0.092
Pu-238	15	N/A	N/A	N/A	N/A
Pu-239+240(?)	30 (15+15)	9/29/77	U-3cn PS#2	85.7	2.9
Sr-90	8	7/01/83	U-3cn PS#2	0.057	0.0071
U-238	30	9/27/77	U-3cn PS#2	27.0	0.90

Table 6.8 Maximum measured concentrations of HST model radionuclides measured in near field of DALHART test (U-4u) detonated on 10/13/1988.

Radionuclide	MCL	Date	Location	Conc (pCi/L)	Conc (MCL)
H-3	20,000	7/02/92	U-4u PS#2A	5.8e7	2,900
C-14	2,000	10/09/03	U-4u PS#2A	326	0.16
Cl-36	700	10/09/03	U-4u PS#2A	29.3	0.042
I-I29	1	10/09/03	U-4u PS#2A	0.132	0.132
Tc-99	900	10/09/03	U-4u PS#2A	35.1	0.039
Pu-238	15	7/21/97	U-4u PS#2A	0.027	0.0018
Pu-239+240 (aq)	30 (15+15)	8/16/99	U-4u PS#2A	1.2	0.040
Sr-90	8	7/21/97	U-4u PS#2A	3.11	0.39
U-238	30	10/09/03	U-4u PS#2A	2.48	0.083

6.5.1.6 Compilation of Maximum Radionuclide Concentrations from Relevant Observational Data

Study of radionuclide concentrations from relevant observational data can be used for two main purposes:

- To decipher trends in the observational data related to source zone concentrations and radionuclide transport processes, and
- To derive plausible lower and upper bounds for HST model concentrations.

Trends in the radionuclide concentration data include:

- H-3 data from GSPs or in hot well data tend to maximize at 2,000 to 3,000 MCL except for sporadic concentration spikes in pond data. H-3 concentrations on the order 1,000 MCL are frequently present in the relevant observational data.
- Maximum H-3 data in ponds are 20,000 MCL or greater, suggesting that maximum initial H-3 concentrations in the fracture continuum of source zones can exceed 10,000 MCL.
- C-14, Cl-36, I-129, Tc-99, and Pu-238 observational data are consistently below the MCL by about one order of magnitude or more except for I-129 at N-Tunnel north.
- Maximum Pu-239+240 concentrations fluctuate above and below the combined MCL of 30 pCi/L.
- Maximum Sr-90 concentrations in observational data are usually below the MCL. However, the highest Sr-90 concentration of 490 MCL is associated with a measurement taken within the Sr-90 source zone in a timeframe within a few years after time zero. Five other similar Sr-90 measurements in the source zone ranged from 7.5 to 48 MCL, and ten more measurements were below the MCL. These

source zone data suggest initial Sr-90 concentrations in fracture zones can be well above the MCL. Observational data not taken directly from a Sr-90 source zone or taken many years after time zero indicate Sr-90 concentrations fall below the MCL with time and distance from the source zones. An exception is T-Tunnel GSP data, which include a maximum Sr-90 concentration of 4.6 MCL. It is possible that high Sr-90 concentrations in T-Tunnel GSP data could be associated with release beyond a T-tunnel containment vessel, such as the MIGHTY OAK test (U.S. Congress, 1989).

- U-238 observational data consistently fall one to two or more magnitudes below the MCL.

Table 6.9 compiles maximum radionuclide concentrations from relevant observational data discussed in this section.

Table 6.9 Compilation of maximum radionuclide concentrations from relevant observational data.

Radionuclide	MCL (pCi/L)		Concentration (MCL)				
		E-Tunnel	N-Tunnel South	N-Tunnel North	T-Tunnel	BILBY	DALHART
H-3	20,000	800 (portal) 57,500 (pond)	2,600 (GSP)	313 (vent hole)	20,000 (pond) 3,070 (GSP)	2,300	2,900
C-14	2,000	0.0046	0.0029	0.075	0.048	0.19	0.16
Cl-36	700	0.021	0.0045	0.143	0.045	0.062	0.042
I-I29	1	*	0.024	0.99	0.33	0.25	0.132
Tc-99	900	*	0.0000066	0.00021	0.00020	0.092	0.039
Pu-238	15	0.037	0.037	*	0.40	N/A	0.0018
Pu-239+240 (aq)	30 (15+15)	0.80	0.80	*	1.2	2.9	0.040
Sr-90	8	490	N/A	*	4.6	0.0071	0.39
U-238	30	0.04	0.030	0.0026	0.039	0.90	0.083

6.5.2 HST Model Transport Predictions Related to Observational Data

As mentioned above, comparison of the available observational data for radionuclides to HST model transport predictions involves many complexities. Nonetheless, some general interpretations can be made in light of HST model transport predictions:

- For H-3, initial or early-time fracture concentrations of over 10,000 MCL appear plausible for source zones, and concentrations of over 1,000 MCL can persist within and beyond the source zones for many years. The current CLEARWATER and WINESKIN HST model produces transport predictions that bracket H-3 observational data. Further refinement of the HST models can largely rely on H-3 calibration to abundant H-3 observational data. For example, matrix effective transport porosity can be fine-tuned to be consistent with H-3 observational data.

- For C-14, the observational data suggest that concentrations will decline below the MCL within and beyond the source zones in a timeframe of several years or more after time zero. The current 3-D CLEARWATER and WINESKIN HST models consistently overpredict C-14 concentration data relative to observational data, which is not surprising because the model does not include thermal effects, gas-phase transport, and pH-dependent gas-liquid phase equilibrium, which result in a spatially extensive re-distribution of early-time C-14 aqueous phase concentrations and partitioning into the gas phase. The CLEARWATER 2-D HST model includes the thermal, gas phase, and chemical processes that lower early-time aqueous phase C-14 concentrations (Zavarin et al., 2011).
- For Cl-36, I-129, Tc-99, the current 3-D CLEARWATER and WINESKIN HST models tend to overpredict but still bracket observational data.
- For Sr-90, the current 3-D CLEARWATER and WINESKIN HST model produces initial source concentrations well above the MCL, consistent with the E-Tunnel observations. Modeled Sr-90 confirms that matrix diffusion and sorption will reduce Sr-90 concentrations below the MCL within short distances beyond the source zones, which is consistent with observational data.
- For Pu-238, Pu-239, and Pu-240, current 3-D CLEARWATER and WINESKIN HST models indicate Pu species concentrations can be well above the MCL near the source zones, but Pu species mobility remains limited even with tortuosity factors reduced by an order of magnitude to account for 90% colloidal transport. Maximum observed aqueous concentrations for Pu species are slightly above the MCL, with most observed concentrations below the MCL. Several of the HST model parameter sets explored in the sensitivity studies (Section 6.4) produce Pu species concentrations near or below the MCL at the SZ model interface for the CLEARWATER test.
- For U-238, the current 3-D CLEARWATER and WINESKIN HST model produces concentrations below that MCL that are consistent with the observational data.
- For Ni-63, which has no observational data to compare to, the current 3-D CLEARWATER and WINESKIN HST model produces concentrations outside the melt glass zone well below the Ni-63 MCL, which confirms current reasoning to exclude Ni-63 from the current HST model list of radionuclide sources (Zavarin et al., 2011).

6.5.3 Issues to Consider

For the purpose of producing HST model results that are consistent with the observational data, several issues affect use of the observational radionuclide concentration data to constrain the CLEARWATER and WINESKIN HST models:

- None of the observational radionuclide concentration data include direct or indirect observations attributable to the CLEARWATER and WINESKIN tests.

- The CLEARWATER and WINESKIN tests have two of the three highest announced yield ranges on Rainier Mesa and, therefore, initial radionuclide source magnitudes are higher for CLEARWATER and WINESKIN than for most other Rainier Mesa tests.
- Part of the strategy of HST modeling is to purposely evaluate model cases with more "conservative" parameters and conceptual models, such as the "high-mobility" set of transport parameters. Such "conservative" cases help substantiate elimination of certain radionuclide sources to the SZ model if the resulting radionuclide fluxes for "conservative" cases are found to have concentrations below the MCL with consistency to observational data.

6.6 Description of HST Model Inputs for the SZ Model

The HST model inputs for the SZ model include water fluxes and radionuclide fluxes and concentrations as a function of time. Water fluxes are given in units of m^3/s, radionuclide fluxes are given in pCi/s, and radionuclide concentrations are given in pCi/L. Time units are given in seconds and years.

The HST model inputs for the SZ model are compiled in digital data files not included in this report. Data formats can be modified, if needed.

7 Conclusions and Recommendations

7.1 Conclusions

7.1.1 Hydrogeologic Conceptualization and Modeling

- The hydrostratigraphic framework model (HFM) provides a plausible means to distribute in-situ rock properties for the CLEARWATER and WINESKIN HST models based on the spatial distribution of hydrostratigraphic units (HSUs) (Section 2.3).
- The NET-INFIL3 recharge model provided by Los Alamos National Laboratory is readily integrated into the CLEARWATER and WINESKIN HST models. The HST models integrate unsaturated and saturated flow processes from ground surface to the base of the Tertiary volcanic sequence and, thus, avoid difficulties in using a separate model to redistribute recharge to the saturated zone (Section 2.4.1).
- Calibration of potentiometric head in the CLEARWATER HST model to regional aquifer water levels and the perched water level at U12q (Fenelon et al., 2008) provides validation of the hydrogeologic conceptual model (Chapter 2).
- While the WINESKIN HST model had no perched water levels measurements to calibrate to, the rock properties used to calibrate head in the CLEARWATER model provided a plausible flow conditions for the WINESKIN HST model. For example, simulated pre-test perched water levels for six flow realizations based on six NET-INFIL3 realizations at WINESKIN were near or below the test location and within

the Tertiary volcanics, consistent with observations during drilling of the emplacement hole U12r (Sections 3.6 and 3.7).

- The HST models produced saturation conditions in both matrix and fracture continua in the perched zone with pressure heads consistent with observations elsewhere on Rainier Mesa (Sections 3.6 and 3.7).
- The dual-continuum flow model, which can address transitions from matrix to fracture dominated flow, indicates that recharge redistribution with lateral flow components can occur above the interface between porous-flow dominated vitric tuffs and fracture-flow dominated zeolitic tuffs (Section 3.8).
- Discharge boundary conditions allowing for lateral flow in welded tuff and drainage at the vitric-zeolitic tuff interface were found to be instrumental in flow calibration (Sections 2.4 and 3.8). The drainage boundary for the vitric-zeolitic tuff interface allowed for lateral flow along the vitric-zeolitic tuff interface and, thus, can be viewed as a means for allowing for recharge redistribution at the vitric-zeolitic tuff interface.
- Consideration by the CLEARWATER and WINESKIN HST models of lateral flow in the Redrock Valley aquifer (RVA) and other welded tuff aquifers maintains consistency with other UGTA technical efforts: (1) the USGS's characterization of predevelopment groundwater conditions in the Timber Mountain–Pahute Mesa regional volcanic aquifer (Fenelon et al., 2008), which includes components of lateral flow near CLEARWATER, WINESKIN, and other Rainier Mesa test locations near B, E, G, and N-Tunnels, as shown in Figure 3.2 and (Section 3.1.3) (2) the SZ model's hydrogeologic conceptual model for flow in the regional volcanic aquifer, and (3) revised interpretation of the lateral extent of the RVA (NSTec, 2009a) shown in Figure 3.3 (Section 3.1.4).
- Test altered zones are essential to realistic implementation of the RST for HST and flow and transport models (Section 2.7). Observations of test altered zones at Rainier Mesa and other NNSS test locations indicate substantial enhancement of permeability, porosity, and surface area between fractures and matrix (Sections 3.4.4 and 3.5.3).

7.1.2 Rock Properties

- An effort was made to correct and constrain matrix hydraulic property data for permeability, porosity, and van Genuchten model parameters (Appendices B and C). Consideration of revised stratigraphic and hydrostratigraphic interpretation of data from hole RME #1 (Section 3.4.1.2) affects assignment of data to model rock units used in HST and flow and transport models. The results of this effort to better constrain matrix property data facilitated calibration of the flow model to observed saturation and potentiometric head (Sections 3.6 and 3.7).

- A subset of the corrected matrix property data used in the CLEARWATER and WINESKIN HST models is also being used for T-Tunnel flow and transport modeling. Modeled matrix properties are similar between the CLEARWATER and WINESKIN HST models and the T-Tunnel flow and transport model, resulting in consistent model parameters across LLNL and DRI modeling efforts.
- Fracture permeability of TCU rocks is not well constrained by data (Section 3.4.2 and Appendix A). However, flow model calibration using the corrected matrix properties as fixed model parameters resulted in reasonable TCU fracture permeability values (Section 3.5.3). Fracture permeability ranges estimated in CLEARWATER and WINESKIN HST modeling fell within fracture permeability ranges independently determined in T-Tunnel flow and transport modeling.
- The test altered zones can be expected to have enhanced permeability and porosity (U.S. Congress, 1989). Unfortunately, no direct measurements of the key properties of fracture permeability and porosity are available specific to Rainier Mesa tests (Section 3.4.4). The CLEARWATER and WINESKIN HST models rely on measurements from granitic tests to address test-related permeability enhancement in in-situ rocks. However, the lack of data on test-altered rock properties for Rainier Mesa further contributes to uncertainty for both HST and flow and transport modeling.

7.1.3 HST Model Source Term Implementation

- Considering that the CLEARWATER and WINESKIN tests were located in the LTCU, similar to most N and T-Tunnel tests, the CLEARWATER and WINESKIN HST models provide an example for source term implementation for the N and T-Tunnel flow and transport models (Chapter 4).
- HST model source zone definitions are designed to provide a simple framework for addressing uncertainty in the spatial distribution of the radionuclide sources (Section 4.2).
- Use of a fracture-matrix dual continuum model mesh enabled selective partitioning of the initial source term distribution into fractures of the test altered zones, water in the void space between cavity and chimney rubble, and melt glass between rubble blocks (Section 4.3). This avoids an unrealistic assumption that the source term is initially distributed uniformly throughout fractures, matrix, and rubble material in the exchange zone.

7.1.4 Transport Processes and Properties

- The dual-continuum model enables integration of matrix and fracture transport processes while maintaining contrasting properties of matrix and fracture materials, which is of particular importance in the TCU separating the test locations from the regional aquifer. Given fractures with relatively high permeability accompanied by

lack of data and knowledge on sorption processes in contrast to matrix materials with low permeability and abundant data on *Kd* in matrix materials, the dual-continuum fracture-matrix model is essential to simultaneous assessment of both (1) potential for rapid contaminant migration in fracture dominated flow system and (2) bulk radionuclide retardation in fractured rocks through fracture-matrix interaction (Sections 5.1 and 5.2).

- Conceptualization of diffusion processes between fracture and matrix materials is a key component to assessment of radionuclide transport processes and uncertainty in the HST models (Sections 5.3 and 5.4).
- Estimation and calibration of the "effective matrix transport porosity" is a key parameter for assessing the effective volumes and length scales that radionuclide sources penetrate into matrix materials (Sections 5.3 and 6.4).

7.1.5 HST Modeling Results

- Transport in fractures dominates HST model radionuclide fluxes at the interface between the HST and SZ models.
- Both the CLEARWATER and WINESKIN HST models indicate that the non-sorbing radionuclide sources (H-3, C-14, Cl-36, I-129, and Tc-99) are mobile through the fracture-matrix system, including tuff confining units. Non-sorbing radionuclide sources have the potential to provide significant fluxes across the interface between the HST and SZ models for both CLEARWATER and WINESKIN HST models (Sections 6.3.2, 6.3.3, 6.4.3 and 6.4.4).
- Both the CLEARWATER and WINESKIN HST models indicate that the strongly sorbing radionuclide sources (Ni-63, Pu-238, Pu-239, Pu-240, and Sr-90) are largely immobilized in the zeolitic tuff test settings by fracture-matrix interaction combined with matrix *Kd* properties (Sections 5.2, 6.3 and 6.4).
- The current WINESKIN HST model assumes impermeable granitic rock underlies the test-altered zones based on the current SZ flow model conceptualization. Under this assumption, the granitic portion of the test-altered zone experiences relatively stagnant flow conditions, which combined with lower sorption coefficients (Kds), leads to relatively higher radionuclide concentrations over time compared to other test-altered zones (Sections 6.3.3 and 6.4.4).
- Because of the close proximity of the SZ model interface to the CLEARWATER radionuclide source zones, the more strongly sorbing radionuclide sources – Sr-90, Pu-238, Pu-239, and Pu-240 – may produce radionuclide fluxes to the SZ model interface above the MCL for certain HST model parameter sets. However, the current HST model indicates these strongly sorbing radionuclides would not reach the regional volcanic aquifer. Further work is needed to assess sorbing radionuclide flux at the SZ model interface at CLEARWATER. In both the CLEARWATER and WINESKIN HST models, the U-238 radionuclide source is mobile in the fracture-

matrix system and produces low concentration flux at the interface with the SZ model. However, the HST models indicate that concentrations of U-238 at the SZ model interface could approach or exceed the U-238 MCL only for the CLEARWATER test (Sections 6.3.3.8 and 6.4.3.3).

- Current HST modeling of Ni-63, a radionuclide which is not included in the current list of radionuclides for HST and flow and transport modeling assessment at Rainier Mesa (Zavarin et al., 2011), confirms that Ni-63 is not a radionuclide source of concern for HST and flow and transport assessment.

7.1.6 Implementation of the HST into the SZ Model

- The planar interfaces defined between the HST and SZ models for flux transfer facilitate integration of the complex HST model processes as practical inputs to the SZ model (Section 2.1).
- The definition of "time zero" for the CLEARWATER and WINESKIN HST models is assigned to the time of the detonation (Section 5.5). This is based on the relatively short timeframe of approximately 1 day for most of the test-related transients in source term re-distribution to subside (Zavarin et al, 2011) compared to the 1,000-year timeframe of HST and SZ modeling.
- The HST models produce water flux inputs for the SZ model that account for transients in water flow resulting from inclusion of test-altered zones.
- For the CLEARWATER HST model, some grid cells of the "3Rc" radionuclide source zone slightly overlap the concurrent SZ model domain (Section 4.2) based on the HST model Rc of 72 m as derived from maximum announced yield (USDOE, 2015) and Pawloski (1999), as detailed in Section 2.7.2. However, all of the CLEARWATER HST model grid block centers including these lowermost grid cells remain above the current SZ model interface elevation of 1,500 meters. Thus, although all radionuclide sources in the CLEARWATER HST model are centered above the SZ model domain at time zero (Section 5.5), any downward flux from the lowermost cells of a "3Rc" radial distribution will contribute to flux into the SZ model domain.

7.2 Recommendations

7.2.1 Hydrogeologic Conceptualization

- Given the presence of laterally extensive welded tuff aquifers in the vicinity of Rainier Mesa tunnel and vertical shaft tests, consideration should be given to lateral flow and transport processes in assessment of radionuclide migration on Rainier Mesa (Section 3.8).
- Consideration should be given in HST, flow and transport, and SZ models for the potential for recharge redistribution with lateral flow components at the vitric-zeolitic tuff interface and storage of groundwater in vitric tuffs at the base of

synclinal structures. Consideration of the transition of flow properties from matrix to fracture flow and the structural characteristics of the vitric-zeolitic interface can improve flow calibration in the perched zone, provide an explanation for post-test filling of cavity and chimney with water at T-Tunnel, and enable consideration of redistribution of recharge by a lateral flow mechanism (Section 2.4.4).

- More uncertainty in infiltration rates than provided by the NET-INFIL3 model could be addressed because the HST models were robust to different recharge models (Section 3.9).
- HST and flow and transport models can calibrate saturation and potentiometric head to the observations on Rainier Mesa (Sections 3.6 and 3.7). In conjunction with matrix property data, flow calibration helps constrain fracture permeability (Section 3.5).

7.2.2 Rock Properties

- Matrix hydraulic property data should be carefully evaluated to help constrain flow conditions for HST, flow and transport, and SZ models (Section 3.4 and Appendices A, B, C, and D).
- Enhancement of permeability and porosity in test-altered zones should be considered in HST, flow and transport, and SZ models (Sections 2.7 and 3.4).
- The SZ model should include properties to account for the 3Rc extent of the test-altered zone for the CLEARWATER test, which overlaps with the SZ model domain assuming the HST model Rc of 72 m as derived from maximum announced yield (USDOE, 2015) and Pawloski (1999) (Section 2.7).

7.2.3 HST Model Source Term Implementation

- The geometry and rock properties of test altered zones need to be considered in implementation of the RST for HST and flow and transport models (Sections 2.7 and Chapter 4).
- Flow and transport models can use the CLEARWATER and WINESKIN HST model as an example for source term implementation.
- The HST model source zone definitions (Section 4.2) can be used by flow and transport models to account for spatial variation in the distribution of the radionuclide sources,
- The flow and transport models should initialize the source term in a fracture-like continuum, as done for the CLEARWATER and WINESKIN HST models, to ensure that the source term is not unrealistically distributed as uniform concentration through matrix materials (Section 4.3).

7.2.4 Transport Processes and Properties

- Further HST modeling work is needed to assess uncertainties in the effects of matrix diffusion, sorption, and colloidal transport. The preliminary modeling results show a large sensitivity to these transport mobility parameters (Section 6.4). Assessment of colloidal processes may require additional HST model refinements and parameter sets.
- The SZ model assessment of radionuclide transport will need to pay careful attention to effects of fracture-matrix interaction. Based on the HST modeling results, the strong influences of fracture-matrix interactions on radionuclide transport can be expected to persist into the SZ model domain.
- While some of the current HST model parameters sets produce radionuclide concentrations that are comparable to observational data, further refinement of HST model parameters could be justified by observational data (Section 6.5).

7.2.5 Implementation of the HST into the SZ Model

- The HST model results indicate that the SZ model should focus on assessment of the non-sorbing radionuclide sources because the strongly sorbing radionuclides are practically immobile beyond the radionuclide source zones, and U-238 concentrations at the interface between the HST and SZ model tend to be lower than the MCL (Sections 6.3 and 6.4).
- While the HST models include transient flow resulting from property changes in test-altered zones after the time zero, it may be reasonable for the SZ model to assume steady state water flux at the interface between the HST and SZ model domains. However, the radionuclide fluxes should be derived directly from radionuclide mass or curie fluxes and not the product of concentration and water flux (Section 6.6).
- For the CLEARWATER test, it may be better to implement the HST model radionuclide fluxes at the interface of the RVA rather than a 1,500 m horizontal elevation. This would avoid a need to address initialization of the source term into the SZ model without detailed evaluation of important processes of fracture-matrix interaction, matrix diffusion, and sorption.

7.3 Acknowledgments

Mavrik Zavarin provided important technical input on *Kd*, RST models, and matrix-fracture interactions. Tim Vogt provided valuable assistance in importing the HFM to the HST model domains. Gayle Pawloski provided useful technical review comments. Andrew Tompson provided Figures 1.1 and 1.2.

8 References

Boardman, C. R. (1966), Some Characteristics of the HARD HAT Chimney and Surrounding Wall Rock, URCL-50177, Lawrence Radiation Laboratory, Livermore, CA.

Boardman, C. R., D.D. Rabb, and R.D. McArthur (1964), Responses of Four Rock Medium to Contained Nuclear Explosions, Journal of Geophysical Research, v. 69, n. 16, p. 3459-3469.

Boardman, C. R., D.D. Rabb, and R.D. McArthur (1965) Contained Nuclear Detonations in Four Media – Geological Factors in Cavity and Chimney Formation, UCRL -7711 Lawrence Radiation Laboratory, CA.

Boardman, C. R., and J. Skrove (1966), Distribution in fracture permeability of a granitic rock mass following a contained nuclear explosion, UCRL-14292 Rev. II, Lawrence Radiation Laboratory, CA.

Borg, I. Y. (1971), Some Shock Effects in Granodiorite to 270 Kbar at the PILE DRIVER Site, UCRL-73377, Lawrence Livermore Laboratory, Livermore, CA.

Borg, I. Y. (1973), Comparison of shock effects in granitic rock recovered from the Monique event Algeria and the PILE DRIVER event, Nevada National Security Site, UCRL-51349, Lawrence Livermore Laboratory, Livermore, CA.

Borg, I. Y., R. Stone, H.B. Levy, and L.D. Ramspott (1976), Information pertinent to the migration of radionuclides in ground water at the Nevada National Security Site Part 1: Review and Analysis of Existing Information, UCRL-52078, Lawrence Livermore Laboratory, Livermore, CA.

Bowen, S. M., D.L. Finnegan, J.L. Thompson, C.M. Miller, P.L. Baca, L.F. Olivas, C.G. Geoffrion, D.K. Smith, W. Goishi, B.K. Esser, J.W. Meadows, N. Namboodiri, and J.F. Wild (2001), Nevada National Security Site Radionuclide Inventory, 1951-1992, LA-13859-MS, Los Alamos National Laboratory, Los Alamos, NM.

Brethauer, G. E., J.E. Magner, and D.R. Miller (1980), Statistical Evaluation of Physical Properties in Area 12, Nevada Test Site Using the USGS/DNA Storage and Retrieval System, USGS-474-309, U.S. Geological Survey.

Carle, S. F., R.M. Maxwell, G.A. Pawloski, D.E. Shumaker, A.F.B. Tompson, and M. Zavarin (2007), Evaluation of the Transient Hydrologic Source Term for the Cambric Underground Nuclear Test at Frenchman Flat, Nevada National Security Site, UCRL-TR-226916, Lawrence Livermore National Laboratory, CA.

Carle, S. F., M. Zavarin, Y. Sun, and G.A. Pawloski (2008), Evaluation of Hydrologic Source Term Processes for Underground Nuclear Tests in Yucca Flat, Nevada National Security Site: Carbonate Tests: LLNL-TR-403485, Lawrence Livermore National Laboratory, CA.

Carle, S. F., Y. Hao, and A. Tompson (2014), Quality Assurance of NUFT Code for Underground Test Area (UGTA) Activities: LLNL-TR-657855, Lawrence Livermore National Laboratory, Livermore, CA.

Carroll, R. D. (1990), Electrical Logging and Electrical Properties of Rocks in Rainier Mesa Area, Nevada National Security Site, Nevada, Open-File Report 90-31, U.S. Geological Survey.

Clebsch, A. (1960), Ground Water in the Oak Spring Formation and Hydrologic Effects of Underground Nuclear Explosions at the Nevada Test Site, Trace Elements Investigations Report TEI-759, U.S. Geological Survey, Washington, D.C.

Clebsch, A., and F.B. Barker (1960), Analyses of Ground Water from Rainier Mesa, Nevada Test Site, Nye County, Nevada, Trace Elements Investigations Report TEI-763, U.S. Geological Survey, Washington, D.C.

Cherry, J. T., D.B. Larson, and E.G. Rapp (1968), Computer Calculations of the Gasbuggy Event, UCRL-50419, Lawrence Radiation Laboratory, CA, Livermore, CA.

Ebel, B.A., and J.R. Nimmo (2009), Estimation of unsaturated zone travel times for Rainier Mesa and Shoshone Mountain, Nevada National Security Site, Nevada using a source-responsive preferential-flow model: U.S. Geological Survey Open-File Report 2009-1175, 74 p.

Ebel, B.A., and J.R. Nimmo (2009), Simple estimation of fastest preferential contaminant travel times in the unsaturated zone: Application to Rainier Mesa and Shoshone Mountain, Nevada: Hydrology and Earth System Sciences Discussions, v. 7, no. 3, p. 3879-3930.

Ege, J. R., R.D. Carroll, J.E. Magner, and D.R. Cunningham (1980), U.S. Geological Survey Investigations in the U12n.03 Drift, Rainier Mesa, Area 12, Nevada Test Site, Open-File Report 80-1074, U.S. Geological Survey.

Fenelon, J. M., R.J. Laczniak, and K.J. Halford (2008), Predevelopment Water-Level Contours for Aquifers in the Rainier Mesa and Shoshone Mountain Area of the Nevada National Security Site, Nye County, Nevada, Scientific Investigations Report 2008-5044, U.S. Geological Survey.

Fredrich, J. T., J.W. Martin, R.B. Clayton (1995), Induced pore pressure response during undrained deformation of tuff and sandstone, Mechanics of Materials, v. 20, p. 95-104.

Hu, M. Q., and M. Zavarin (2007), Evaluation of the Rainier Mesa/Shoshone Mountain CAU HST Transport Parameters Based on Solid and Water Sampling, UCRL-MI-234814, Lawrence Livermore National Laboratory, Livermore, CA.

Kwicklis, E., G. WoldeGabriel, and M. Sulley (2008), written communication: Analysis of core-scale hydrologic and mineralogic data from boreholes UE12t #1 and RME #1 at Rainier Mesa, Nevada National Security Site, LA-UR-XXXX, Los Alamos National Laboratory, Los Alamos, NM.

Kwicklis, E., Z. Lu, H. Viswanathan, D. Leavitt, and N. Becker (2009), oral and written communication: Unsaturated-zone flow and transport models of the N-tunnel area of Rainier Mesa, presentation at Preemptive Review, March 18, 2009, Desert Research Institute, Las Vegas, NV.

Kwicklis, E. (2010a), oral and written communication: June 2010 Rainier Mesa Technical Integration Meeting, Lawrence Livermore National Laboratory, Livermore, CA.

Kwicklis, E. (2010b), written communication: Comments on "A numerical investigation of soil-bedrock interface flow impedance" by D.M Reeves and Rishi Parashar, November 2010 Rainier Mesa Technical Integration Meeting.

Maxwell, R. M., R.L. Detwiler, Q. Hu, A.F.B. Tompson, S. Kollet, and S.K. Roberts (2008), Evaluation of Hydrologic Source Term Processes for Underground Nuclear Tests in Yucca Flat, Nevada National Security Site: Saturated Tests, LLNL-TR-403429, Lawrence Livermore National Laboratory, Livermore, CA.

Mcnab, W. W. (2008), Evaluation of Hydrologic Source Term Processes for Underground Nuclear Tests in Yucca Flat, Nevada Test Site: Unsaturated Tests and the Impact of Recharge, LLNL-TR-403360, Lawrence Livermore National Laboratory, Livermore, CA.

Moreno, L., and J. Crawford (2009), Can we used tracer tests to obtain data for performance assessment of repositories for nuclear waste?, Hydrogeology Journal, v. 17, p. 1067-1080.

Murray, W. A. (1980), Permeability testing of fractures in Climax Stock Granite, NTS, UCRL-8523, Lawrence Livermore National Laboratory, Livermore, CA.

Navarro (2017a), written communication: Case Study Analyses of Radionuclide Transport in Variably Saturated Media at Rainier Mesa. Las Vegas, NV.

Navarro (2017b), written communication: HFM-Prime: Revisions to A Hydrostratigraphic Model and Alternatives for the Groundwater Flow and Contaminant Transport Model of Corrective Action Unit 99: Rainier Mesa/Shoshone Mountain, Nye County, Nevada. Las Vegas, NV.

Navarro-Intera, LLC. (2013), written communication: "UGTA Geochemistry Database," UGTA Technical Data Repository Database Identification Number UGTA-4-129. Las Vegas, NV.

Neretnieks, I. (1980), Diffusion in the Rock Matrix: An Important Factor in Radionuclide Retardation?, Journal of Geophysical Research, v. 85, n. B8, p. 4379-4397.

NNSA (2006), Completion Report for Well ER-12-4, Corrective Action Unit 99: Rainier Mesa-Shoshone Mountain, DOE/NV-1208, National Nuclear Security Administration.

Nilson, R. H. (1989), Gas-flow acceptance of a fractured permeable medium, in 5th Symposium on Containment of Nuclear Explosions, Sept 19-21, 1989, C. Olsen ed., p. 231-252.

Nitao, J. J. (2000a), Reference Manual for the NUFT Flow and Transport Code, Version 3.0, UCRL-MA-130651 REV 1, Lawrence Livermore National Laboratory, Livermore, CA.

Nitao, J. J. (2000b), User's Manual for the USNT Module of the NUFT Code, Version 3.0, UCRL-MA-130643-REV-2, Lawrence Livermore National Laboratory, Livermore, CA.

Nitao, J. J. (2004), User's Manual for the US1P Module of the NUFT Flow and Transport Code, unpublished report, Lawrence Livermore National Laboratory, Livermore, CA.

Nitao, J. J. (2005), User's Manual for the US1C Module of the NUFT Flow and Transport Code, unpublished report, Lawrence Livermore National Laboratory, Livermore, CA.

Norris, A. E., R.D. Aquilar, B.P. Bayhurst, D.L. Bish, M.R. Cisneros, W.R. Daniels, C.J. Duffy, R.D. Golding, S.L. Jensen, S.D. Knight, F.O. Lawrence, S. Maestas, A.J. Mitchel, P.Q. Oliver, N.A. Raybold, R.S. Rundberg, G.M. Thompson, E.N. Treher, B.J. Travis, G.R. Walter, R.G. Warren, and K. Wolfsberg (1982), Geochemistry Studies Pertaining to the G-Tunnel Radionuclide Migration Field Experiment, LA-9332-MS, Los Alamos National Laboratory, Los Alamos, NM, 43p

NSTec (2007), A Hydrostratigraphic Model and Alternatives for the Groundwater Flow and Contaminant Transport Model of Corrective Action Unit 99: Rainier Mesa-Shoshone Mountain, DOE/NV/25946-146, Nye County, Nevada, National Security Technologies, LLC, Las Vegas, NV.

NSTec (2009a), written communication: Comparison of RVA Extent; HFM (2007) vs Revision (2009), Unpublished data, undated, National Security Technologies, LLC, Las Vegas, NV.

NSTec (2009b), written communication: Geology and Hydrogeology of Rainier Mesa Exploratory #1, unpublished data dated April 16, 2009, National Security Technologies, LLC, Las Vegas, NV.

NSTec (2010), written communication: Structure Map of the Top of Zeolitization in the Rainier Mesa Vicinity, unpublished data dated August 25, 2010, National Security Technologies, LLC, Las Vegas, NV.

NSTec (2011), written communication: Thoughts on the Redrock Valley Aquifer in the Rainier Mesa Area, November 17, 2011, National Security Technologies, LLC, Las Vegas, NV.

Patch, D., and K. Lie (1975), Gas Flow Calculations for the MING BLADE Chimney – Preliminary Calculational Results, publisher unknown (Cover missing)

Pawloski, G. A. (1999), Development of Phenomenological Models of Underground Nuclear Tests on Pahute Mesa, Nevada National Security Site – BENHAM and TYBO, UCRL-ID-136003, Lawrence Livermore National Laboratory, Livermore, CA.

Pawloski, G. A., A.F.B. Tompson, and S.F. Carle (2001), Evaluation of the Hydrologic Source Term from Underground Nuclear Tests on Pahute Mesa at the Nevada National Security Site: The CHESHIRE Test, UCRL-ID-147023, Lawrence Livermore National Laboratory, Livermore, CA.

Prothro, L B., (2008), Analysis of Fractures in Cores from the Tuff Confining Unit beneath Yucca Flat, Nevada National Security Site, DOE/NV/25946-351, National Security Technologies LLC, Las Vegas, NV.

Reeves, M. R., (2008), Fracture and Matrix Characteristics at T-Tunnel, Rainier Mesa, NNSS, presented June 9, 2008 at Lawrence Livermore National Laboratory, Livermore, CA.

Russell, C. E., R.H. French, R.A. Nicholson, J.S. Miller, and S. Benner (2003), Evaluation of Monitoring Data from Impounded Water within U12n and U12t Tunnel Rainier and

Aqueduct Mesas, Nevada National Security Site, Letter Report, Desert Research Institute, NV.

Short, N. M., (1966), Effects of Shock Pressures from a Nuclear Explosion on Mechanical and Optical Properties of Granodiorite, Journal of Geophysical Research, v. 71, n. 4, p. 1195-1215.

Stoller-Navarro (2006a), Phase I Hydrologic Data for the Groundwater Flow and Contaminant Transport Model of Correction Action Unit 97: Yucca Flat/Climax Mine, Nevada National Security Site, Nye County, Nevada, S-N/99205-077, Stoller-Navarro Joint Venture, Las Vegas, NV.

Stoller-Navarro (2006b), Analysis of FY 2005/2006 Hydrologic Testing and Sampling Results for Well ER-12-4, Nevada National Security Site, Nye County, Nevada, S-N/99205-083, Stoller-Navarro Joint Venture, Las Vegas, NV.

Stoller-Navarro (2007a), U12n and U12t Tunnels Preliminary Data Report Groundwater Sampling February 2007, Stoller-Navarro Joint Venture, Las Vegas, NV.

Stoller-Navarro (2007b), Phase I Contaminant Transport Parameters for the Groundwater Flow and Contaminant Transport Model of Corrective Action Unit 97: Yucca Flat/Climax Mine, Nevada National Security Site, Nye County, Nevada. S-N/99205-096, Stoller-Navarro Joint Venture, Las Vegas, NV.

Stoller-Navarro (2008a), Phase I Hydrologic Data for the Groundwater Flow and Contaminant Transport Model of Correction Action Unit 99: Rainier Mountain/Shoshone Mountain, Nevada Test Site, Nye County, Nevada. S-N/99205—103, Stoller-Navarro Joint Venture, Las Vegas, NV.

Stoller-Navarro (2008b), Phase I Contaminant Transport Parameters for the Groundwater Flow and Contaminant Transport Model of Corrective Action Unit 99: Rainier Mesa/Shoshone Mountain, Nevada National Security Site, Nye County, Nevada. S-N/99205-102, Stoller-Navarro Joint Venture, Las Vegas, NV.

Thordarson, W. (1965), Perched Ground Water in Zeolitized-Bedded Tuff, Rainier Mesa and Vicinity, Nevada National Security Site, Nevada, TEI-862, U.S. Geological Survey, 98p.

Tompson, A. F. B. (ed.), S.F. Carle, Q. Hu, W.W. Mcnab, G.A. Pawloski, S.K. Roberts, D.E. Shumaker, Y. Sun, and M. Zavarin (2010), written communication: On the Evaluation of Hydrologic Source Term Behavior for Underground Nuclear Tests Conducted at Rainier Mesa and Shoshone Mountain, Nevada Test Site, Interim Working Draft Report, Lawrence Livermore National Laboratory, Livermore, CA.

Townsend, D. R., and M.J. Townsend (2004), Underground Test Area Geology Task to Construct Database of Drill-Hole and Stratigraphic Information for the Rainier Mesa Area, Status Report for Work Conducted in Fiscal Year 2004, Bechtel Nevada and Peer Consultants, Inc., Las Vegas, NV.

Townsend, D. R., M. Townsend, M., and B.L. Ristvet (2007), A Geotechnical Perspective on Post-Test Data for Underground Nuclear Tests Conducted in Rainier Mesa, DTRIAC-SR-07-002, DOE/NV/25946-269, Defense Threat Reduction Agency, Kirtland AFB, NM.

Townsend, D. R. (2008), Documentation Report for Rainier Mesa Test Information Compiled for the UGTA Project, Wastren Advantage Incorporated, prepared for National Security Technologies, LLC, Las Vegas, NV.

Townsend, M. J. (2009), Xcel spreadsheet named "RM_Rock_all_data_rev1.xlsx" dated April 2009, National Security Technologies, LLC, Las Vegas, NV.

U.S. Congress (1989), The Containment of Underground Nuclear Explosions, Office of Technology Assessment OTA-ISC-414 (Washington D.C.: US Government Printing Office, October 1989) 85p.

USDOE (2015), United States Nuclear Tests, July 1945 through September 1992, DOE/NV--209-REV 16, National Nuclear Security Administration Nevada Field Office, U.S. Department of Energy, Las Vegas, NV.

van Genuchten, M. Th. (1980), A closed-form equation for predicting the hydraulic conductivity of unsaturated soils, Soil Science Society of America Proceedings, 44(5), p. 892-898.

van Genuchten, M. Th., F.J. Leij, and S.R. Yates (1991), The RETC code for quantifying hydraulic functions of unsaturated soils, EPA/600/2-91-065, Robert S. Kerr Environmental Research Laboratory, Office of Research and Development, U.S. Environmental Protection Agency, Ada, OK.

Winograd, I.J., and W. Thordarson (1975), Hydrogeologic and Hydrochemical Framework, South-Central Great Basin, Nevada-California, with Special Reference to the Nevada Test Site, USGS-PP-712-C. Denver, CO: U.S. Geological Survey.

Zavarin, M. (2011a), written communication: Excel spreadsheet with Kd values and uncertainties for radionuclide classes and hydrostratigraphic and hydrogeologic units.

Zavarin, M. (2011b), written communication: Excel spreadsheets Rainier Mesa tunnel radionuclide concentration data and hot well concentration data.

Zavarin, M. (2014), Yields and Cavity Radii of Underground Nuclear Tests with Specified Yields Reported in DOE/NV—209-REV 15 (2000), LLNL-TR-664664, Lawrence Livermore National Laboratory, Livermore, CA.

Zavarin, M., S. Roberts, P. Reimus, and M. Johnson (2007), Summary of Radionuclide Reactive Transport Experiments in Fractured Tuff and Carbonate Rocks from Yucca Flat, Nevada Test Site, UCRL-TR-225271, Lawrence Livermore National Laboratory, Livermore, CA.

9 Appendix A: Hydrologic and Transport Property Data Compiled from UGTA Program Sources

Stoller-Navarro (2006, 2007, 2008a and b) provide compilations of hydrologic and transport property data relevant to the Rainier Mesa and Shoshone Mountain (RM/SM) areas. These data support parameter assignment for the CLEARWATER and WINESKIN HST and other flow and transport models. Additional attention must be paid to assignment of properties for dual-continuum models such as the CLEARWATER and WINESKIN HST models. This section focuses on the relevant data compiled by the UGTA program sources including fracture-matrix properties.

9.1 RM/SM Hydraulic Conductivity Data

Stoller-Navarro (2008a) provides analysis of hydraulic conductivity ranges for hydrogeologic units (HGUs). These hydraulic conductivity ranges will be used in the Rainier Mesa/Shoshone Mountain SZ model (Chen, 2010). Stoller-Navarro (2008a) points out that bias toward higher permeabilities results from well completions focusing on more productive intervals and testing of fractured interval within an otherwise low-conductivity formation. The Stoller-Navarro (2008a) hydraulic conductivity ranges will be used to help bound fracture permeability in HST modeling, particularly in welded tuff aquifers (WTAs).

Permeability data specific to Rainier Mesa or Shoshone Mountain is limited. Table 9.1 compiles permeability data obtained from Rainier Mesa from pumping, slug, and laboratory scale tests. Rainier Mesa data specific to the tuff confining unit (TCU) hydrogeologic unit (HGU) are absent, including the argillic tuff confining unit (ATCU) hydrostratigraphic unit (HSU). Thordarson (1965) provides average and range values for "interstitial permeability", which is relevant to estimation of matrix permeability but not fracture permeability. Direct data measurements of TCU bulk permeability at RM do not exist.

Table 9.1 Permeability data for HGUs derived from hydraulic conductivity values (converted at 20°C) given by Stoller-Navarro (2008a) specific to Rainier Mesa and Shoshone Mountain.

HGU	Count	Permeability (m^2)			Hydraulic Conductivity (m/day)		
		Geometric Mean	Min	Max	Geometric Mean	Min	Max
Pumping-Scale Data							
WTA	6	4.8E-12	4.2E-13	1.4E-11	3.2	0.35	12
LCA3	9	2.4E-13	1.3E-15	1.5E-12	0.20	0.0011	1.6
UCCU	2	5.9E-16	3.8E-16	9.2E-16	5.0e-4	3.2e-4	7.8e-4
Slug Test-Scale Data							
LCA3	2	7.4E-13	5.7E-13	9.8E-13	0.63	0.48	0.83
UCCU	3	9.0E-15	2.6E-15	8.2E-14	0.010	0.0022	0.069
Laboratory-Scale Data							
LCA3	2	8.2E-18	3.6E-18	2.4E-17	7.8e-6	3.0e-6	2.0e-5

9.2 NNSS Hydraulic Conductivity Data

In lieu of the few hydraulic conductivity data local to Rainier Mesa, Stoller-Navarro (2008a) recommends use of NNSS-wide data in estimation of bulk permeability for Rainier Mesa HGUs. Table 9.2 shows NNSS-wide permeability data (converted from hydraulic conductivity at 20°C) for HGUs present on Rainier Mesa.

While cautioning that permeability of the zeolitic tuff (TCU) was not directly measured, Thordarson (1965) estimated fracture transmissivity "ranges from 10 to 100 gpd per foot for a 500-foot-thick section" which corresponds to a hydraulic conductivity range of 0.0008 to 0.008 m/day. This range is more in line with the mean hydraulic conductivity of 0.0035 m/day from slug test data for the NNNS-wide hydraulic conductivity data. The Thordarson (1965) estimates suggest a mean hydraulic conductivity of 0.11 m/day for the TCU based on NNSS data could be at least one to two orders of magnitude too high for Rainier Mesa.

Table 9.2 Permeability data for HGUs derived from hydraulic conductivity values (converted at 20°C) given by Stoller-Navarro (2008a) as obtained from NNSS-wide data.

HGU	Count	Permeability (m^2)			Hydraulic Conductivity (m/day)		
		Geometric Mean	Min	Max	Geometric Mean	Min	Max
Pumping-Scale Data							
WTA	79	1.9e-12	1.4e-14	6.5e-11	1.6	0.012	55
TCU	71	1.4e-13	1.1e-17	2.6e-11	0.11	9.5e-6	22
LCA3	9	2.4E-13	1.3E-15	1.5E-12	0.20	0.0011	1.6
LCCU	1	5.9E-16	-	-	0.0062	-	-
UCCU	2	5.9e-17	3.8e-17	9.3e-17	5.0e-4	3.2e-4	7.8e-4
GCU	1	3.8e-16	-	-	0.0032	-	-
Slug Test-Scale Data							
VTA	11	2.2e-15	1.4e-16	1.7e-13	0.0019	1.2e-4	0.15
WTA	170	5.4e-15	3.6e-18	1.4e-12	0.0046	3.1e-6	1.2
TCU	86	4.1e-15	1.1e-18	1.2e-12	0.0035	1.0e-6	0.02
LCA3	2	7.4E-13	5.7E-13	9.8E-13	0.63	0.48	0.83
UCCU	3	9.0E-15	2.6E-15	8.2E-14	0.010	0.0022	0.069
GCU	3	8.2E-14	7.6e-16	1.7e-12	0.069	6.5e-4	1.4
Laboratory-Scale Data							
VTA	210	4.2e-16	2.1e-20	4.7e-8	3.5e-4	1.8e-8	40,000
WTA	531	5.0e-17	8.7e-21	3.8e-10	4.3e-5	7.4e-9	320
TCU	201	2.6e-17	4.0e-20	2.4e-14	2.2e-5	3.4e-8	0.02
LCA3	4	7.3e-18	3.6e-18	2.4e-17	6.2e-6	3.0e-6	2.0e-5
LCCU	30	3.3e-19	3.4e-20	2.4e-17	2.8e-7	2.9e-8	2.0e-5

9.3 Matrix Porosity

Stoller-Navarro (2008b) provides data on matrix porosity for HSUs on Rainier Mesa (see Table 9.3). Effective porosity factors are given by Stoller-Navarro (2008a and b) to account for the fraction of voids transmitting water. Therefore, it is reasonable for HST, N- and T-

Tunnel, or SZ flow and transport models to implement matrix porosity as less than the mean measured porosity.

Consistency of the effective porosity factors can be checked by comparison to volumetric saturation from van Genuchten models (van Genuchten, 1980) derived for the mobile water (Section 3.4.1.4). A calculated effective porosity factor is determined by dividing the volumetric saturation by the measured porosity. In all HSUs porosity, effective porosity factor, and van Genuchten model values are available (TM-LTVA, LVTA, BRCU, LTCU, OSBCU, and ATCU), the calculated effective porosity is within the range of the effective porosity factor estimates for matrix materials from Stoller-Navarro (2008a and b). Therefore, mean HST model matrix porosity estimates based on van Genuchten model fitting are consistent with combined SZ model matrix porosity data and effective porosity estimates.

Table 9.3 Matrix porosity data and effective porosity factor estimates from Stoller-Navarro (2008a, b) compared with mean water content for fitted mobile saturated water content van Genuchten models. Calculated effective porosity is obtained by the ratio of van Genuchten mobile saturated water content and mean matrix porosity

HSU	N	Matrix Porosity			Effective Porosity Factor	Saturated Volumetric Water Content	Calculated Effective Porosity Factor
		Mean	Min	Max			
AA	100	30.9	21.0	56.2	0.8-1.0	-	-
TM-WTA	110	21.9	5.7	54.1	-	-	-
TM-LVTA	799	41.0	0.8	70.8	0.8-1.0	35.3	0.86
SWA	0	-	-	-	-	-	-
UTCU1	237	36.7	13.6	53.6	0.5-0.8	-	-
LVTA	38	46.6	32.8	61.0	0.8-1.0	41.1	0.88
BRA	41	17.6	1.7	46.7	-	-	-
BRCU	946	35.6	6.0	51.3	0.5-0.8	26.4	0.75
LTCU	4607	35.5	2.3	58.0	0.5-0.8	26.4	0.74
TUBA	12	16.3	12.6	22.9	-	-	-
OSBCU	657	32.3	12.9	51.0	0.5-0.8	25.8	0.80
RVA	0	-	-	-	-	-	-
ATCU	20	28.1	20.5	35.6	0.5-0.8	16.2	0.58
LCCU1	28	5.5	1.0	23.0	0.5-0.9	-	-
LCA3	14	6.4	2.6	17.7	-	-	-
MGCU	18	1.3	0.0	3.3	-	-	-

9.4 Fracture Properties

9.4.1 Fracture Porosity

Stoller-Navarro (2007) provides effective porosity estimates for the fracture-flow controlled welded tuff aquifer (WTA) hydrogeologic units (HGU) on Rainier Mesa. Prothro (2008) gives values of average open fracture spacing of 5.0 m and average aperture of 1.1

mm based on four boreholes in the tuff confining units (TCU) of Yucca flat. A mean fracture porosity of 0.00022 (2.2e-4) is derived from these values. Based on fracture spacing and aperture data from individual boreholes, TCU fracture porosity values vary from 5.0e-5 to 5.7e-4. Prothro (2008) did not observe open fractures in the ATCU, suggesting that fracture permeability and porosity, if non-zero, are very low in the ATCU relative to the LTCU and OSBCU. These porosity ranges are compiled in Table 9.4 as possible representative estimates of effective porosity for the fractured WTA and TCU HGUs.

Table 9.4 Estimates of effective porosity for fractured HGUs on Rainier Mesa.

HGU	Effective Porosity for Fractured HGUs		
	Min	Max	Mean
TCU	0.00005	0.00057	0.00022
WTA	0.0001	0.006	0.003

9.4.2 Fracture Spacing and Frequency

In the CLEARWATER and WINESKIN HST models, fracture spacing or frequency is considered in estimation of both fracture porosity and interfacial area per unit volume in TCU and WTA HGUs.

Reeves (2008) reports mean fracture spacings of 12 m vertical and 50 m horizontal for Rainier Mesa Tertiary volcanics, which is mostly composed of a TCU tuff confining unit within the T-Tunnel flow and transport model domain. These mean fracture spacings correspond to 0.08/m vertical and 0.02/m horizontal fracture frequencies, with a mean fracture frequency of 0.05/m.

Wolfsberg et al. (2002) report a fracture spacing range of 0.57 to 1.86 m in welded tuffs of Pahute Mesa, which corresponds to fracture frequencies of 0.54 to 1.8 m^{-1}. Therefore, for welded tuffs on Rainier Mesa, a fracture frequency of 1.0 m^{-1} is assigned as a reasonable base case estimate.

9.4.3 Fracture Aperture

Fracture porosity, ϕ, can be related to the product of fracture frequency, f, aperture, a, and a dimensionality factor, β, by

$$\phi = \beta f a$$

Therefore, average fracture aperture can be estimated from fracture porosity and fracture frequency by

$$\bar{a} = \frac{\phi}{\beta f}$$

If the fracture sets are oriented in three dimensions, a dimensionality factor of three may be applied to account for three-dimensional effects (CRWMS M&O, 2000). The dimensionality factor may be set to as low as unity to represent fractures occurring in parallel planes (Wolfsberg et al., 2002). Given preferentially oriented horizontal and vertical sets of fractures, the dimensionality of fractures in the TCU is estimated at 2. Considering that joints and fractures in welded tuffs are oriented in multiple planes, the dimensionality of WTA fractures is estimated at 3. Table 9.5 shows estimates of mean fracture aperture for HGUs derived from fracture porosity, mean fracture frequencies, and dimensionality factors.

Table 9.5 Estimates of fracture aperture and interfacial area per unit volume for HGUs derived from fracture porosity and mean fracture frequencies, fracture apertures, and dimensionality factors.

HGU	Porosity	Mean Fracture Frequency (m^{-1})	Dimensionality β	Mean Aperture (m)	Area (m^2/m^3)
TCU	0.00022	0.05	2	0.0022	0.2
WTA	0.0030	1.0	3	0.001	6.0

9.4.4 Fracture Area

The dual continuum model assigns an interfacial area per unit volume between the fracture and matrix continua. For the TCU and WTA units, the interfacial area per unit volume is derived from the fracture frequency and dimensionality

$$A = 2 f\beta$$

where the factor of 2 accounts for the surficial area on both sides of a planar fracture. Table 9.5 includes estimates of fracture interfacial area per unit volume.

9.5 Specific Storage

The few data on specific storage at Rainier Mesa (see Table 9.6) are limited to the WTA and LCA3 HGUs (Stoller-Navarro, 2008a). However, Stoller-Navarro (2008a) warns that specific storage data with values over 1E-4 are unreliable. Considering the mean values of specific storage of 5.65E-2 and 3.77 E-1 for the WTA and LCA3 HGUs at Rainier Mesa are much greater than 1E-4, the Rainier Mesa specific storage data presented in Stoller-Navarro (2008a) are unreliable.

Alternatively, the NUFT flow and transport code directly accounts for specific storage as a function of rock and fluid compressibility. Compressibility of water and air is modeled by NUFT as a function of pressure and temperature. Compressibility is specified for rock type. Data and estimates of compressibility for Rainier Mesa rocks are compiled later in this report (Section 12.3).

Table 9.6 Mean specific storage values for RM/SM HGUs from Stoller-Navarro (2008a).

HGU	Count	Mean
WTA	5	5.65E-2
LCA3	6	3.77E-1

9.6 Tortuosity

Stoller-Navarro(2008b) compiles NNSS tortuosity and porosity data by rock type. These data can be used to estimate mean and range for tortuosity of hydrogeologic units (HGUs) based on rock types and porosities at Rainier Mesa (Table 9.7).

Table 9.7 Tortuosity data compiled in Stoller-Navarro (2008b).

Rock Type	HGU	Porosity Range	Estimated Tortuosity		
			Min	Mid-Range	Max
Welded Tuff	WTA	0.18-0.23	0.02	0.10	0.4
Zeolitized Bedded Tuff	TCU	0.24-0.26	0.02	0.10	0.6
Crystalline Granitic	GCU	0.01-0.02	0.0001	0.001	0.01
Carbonate	CA	0.05	0.03	0.10	0.2

Stoller-Navarro(2008b) infers tortuosity ranges for HGUs based on correlation statistics with porosity (Table 9.8). These porosity-based tortuosity ranges encompass more HGUs than covered by direct measurements of tortuousity. However, the porosity-based ranges of tortuosity have unrealistically high variability for modeling field scale transport considering high variability of porosity between different rock samples of much smaller scale than model grid block size.

Table 9.8 Tortuosity values inferred from correlation statistics with porosity by Stoller-Navarro (2008b).

HGU	Estimated Tortuosity		
	5%	Mean	95%
AA	0.024	0.21	0.63
CA	0.00017	0.026	0.33
CCU	0.000255	0.031	0.35
GCU	0.000001	0.0030	0.17
TCU	0.0037	0.025	0.66
VTA	0.061	0.31	0.70
WTA	0.0067	0.12	0.53

9.7 Effective Porosity In Fractured Flow Systems

Effective porosity as presented in Stoller-Navarro (2008b) refers to the transport model parameter value of porosity used to calculate average flow velocity for advective transport. At the larger scales used in transport modeling, effective porosity for HGUs with fracture-controlled flow is affected by the aperture size distribution, fracture roughness, and tortuous flow. Based on tracer tests, the effective porosity for modeling transport in a fracture-controlled flow system can be expected to be about one order of magnitude larger than fracture porosity calculated from hydraulic conductivities and fracture spacings using cubic law and parallel plate assumptions (Stoller-Navarro, 2007).

9.8 References

Chen, Y., (2010), written communication.

CRWMS M&O (2000), Probability distribution for flowing interval spacing. Yucca Mountain Analysis and Model Report, TDR-NBS-HS-000003, Rev 0.0, Office of Civilian Radioactive Waste Management, Las Vegas, NV.

Prothro, L B., (2008), Analysis of Fractures in Cores from the Tuff Confining Unit beneath Yucca Flat, Nevada National Security Site, DOE/NV/25946-351, National Security Technologies LLC, Las Vegas, NV.

Reeves, M. (2008), Fracture and Matrix Characteristics at T-Tunnel, Rainier Mesa, NNSS, presentation on June 9, 20008 at Lawrence Livermore National Laboratory.

Stoller-Navarro (2006), Phase I Hydrologic Data for the Groundwater Flow and Contaminant Transport Model of Correction Action Unit 97: Yucca Flat/Climax Mine, Nevada National Security Site, Nye County, Nevada. S-N/99205-077, Stoller-Navarro Joint Venture, Las Vegas, NV.

Stoller-Navarro (2007), Phase I Contaminant Transport Parameters for the Groundwater Flow and Contaminant Transport Model of Corrective Action Unit 97: Yucca Flat/Climax Mine, Nevada National Security Site, Nye County, Nevada. S-N/99205-096, Stoller-Navarro Joint Venture, Las Vegas, NV.

Stoller-Navarro (2008a), Phase I Hydrologic Data for the Groundwater flow and Contaminant Transport Model of Corrective Action Unit 99: Rainier Mesa/Shoshone Mountain, Nevada National Security Site, Nye County, Nevada, Stoller-Navarro Joint Venture, Las Vegas, NV.

Stoller-Navarro (2008b), Phase I Contaminant Transport Parameters for the Groundwater Flow and Contaminant Transport Model of Corrective Action Unit 99: Rainier Mesa/Shoshone Mountain, Nevada National Security Site, Nye County, Nevada. S-N/99205-102, Stoller-Navarro Joint Venture, Las Vegas, NV.

Thordarson, W. (1965), Perched Ground Water in Zeolitized-Bedded Tuff, Rainier Mesa and Vicinity, Nevada National Security Site, Nevada, TEI-862, U.S. Geological Survey, 98p.

Wolfsberg, A., L. Glascoe, G. Lu, A. Olson, P. Lichtner, M. McGraw, T. Cherry, and G. Roemer (2002), TYBO/BENHAM: Model Analysis of Groundwater Flow and Radionuclide Migration from Underground Nuclear Tests in Southwestern Pahute Mesa, Nevada, LA-13977, Los Alamos National Laboratory, Los Alamos, NM.

10 Appendix B: Corrections to Matrix Ksat and Van Genuchten Property Data of Kwicklis et al. (2008)

A fundamental question for flow and transport modeling at Rainier Mesa is:

Why is groundwater "perched" in the volcanic rocks?

At the regional scale, perched conditions require the bulk vertical hydraulic conductivity of the volcanic rocks to be less than the recharge rate near the base of the perched zone of saturation. Within the tuff confining unit, where bulk permeability is controlled by fractures and faults (Thordarson, 1965; Townsend, 2008), two hydrogeologic conditions are required near the base of the perched zone of saturation:

1. Fault and fracture flow is restricted at the base of the volcanic section either by lack of vertical interconnectivity or plugging by clay and secondary minerals.
2. The hydraulic conductivity of matrix materials is considerably less than the average recharge rate.

The section focuses on the second condition by taking a closer look at data for saturated hydraulic conductivity (Ksat) and other unsaturated flow parameters used to characterize matrix flow at Rainier Mesa. It will be shown that direct use of new data from Kwicklis et al. (2008) may lead to overestimation of Ksat and, subsequently, inability for flow models to simulate perched conditions.

Data for van Genuchten (1980) model parameters - Ksat, alpha, n or m, residual saturation, and saturated volumetric water content – given in Kwicklis et al. (2008) are re-examined prior to HST modeling to address heterogeneity within matrix rock properties in hydrostratigraphic units (HSUs) and to probe causes for difficulty in matching modeled flow conditions with hydrologic observations of perched groundwater. Heterogeneity can reduce bulk vertical hydraulic conductivity, for which the harmonic mean is commonly used in model parameterization. Perching requires hydraulic conductivity below the recharge rate, so lack of model calibration to perching behavior could be explained by model parameters based on permeability measurements that are erroneously high.

Matrix Ksat is particularly important to HST model calibration at Rainier Mesa. In Kwicklis et al. (2008), estimates of Ksat from core samples were obtained from two methods: rigid wall and flexible wall. Kwicklis et al. (2008) indicate that Ksat was overestimated for some data obtained using the flexible wall method. Inaccuracy of flexible wall Ksat data directly affects interpretation of Ksat data from UE12t#1 core for which only the flexible wall method was applied, whereas both rigid-wall and flexible-wall methods were applied to RME#1 core. Additionally, we find that consideration of standard errors in moisture

retention curve-fitting can indicate erroneous alpha parameter data which consequently affects estimation of correlation between alpha and Ksat (van Genuchten et al., 1991).

With consideration of the corrections to Ksat described in this section, matrix hydraulic conductivity estimates are sufficiently lower than described in Kwicklis et al. (2008). This analysis contributes to explaining why perched conditions exist in the volcanic rocks at Rainier Mesa.

10.1 Purpose

The purpose of re-interpreting matrix hydrologic property data from Kwicklis et al. (2008) includes several objectives:

- Correct Ksat for UE12t#1 data to account for error in flexible-wall method noted by Kwicklis et al. (2008)
- Consider standard error in Van Genuchten model alpha values to establish correlation between Ksat and alpha (van Genuchten et al., 1991)
- Check for consistency in alpha and Ksat values between RME#1 and UE12t#1 data.
- Provide a basis for reducing uncertainty and establishing consistent matrix properties in HST, N and T-Tunnel, and SZ flow and transport models
- Address heterogeneity in HST modeling by defining subunits with equal or more refined spatial resolution than HSUs.
- Develop tables of hydraulic properties for HST, N and T-Tunnel, and SZ flow and transport model rock units derived from data.

10.2 Methods

To re-interpret matrix hydrologic property data from Kwicklis et al. (2008), the following methods are applied:

1. Use of RME#1 alpha and rigid-wall Ksat data to establish correlation between Ksat and alpha (see Figures 10.3, 10.3 and 10.5) including consideration of standard error in the alpha parameter
2. Checking of consistency between different lithologies such as-non-welded, welded", and other tuff and carbonate lithology descriptors (Figures 10.3, 10.4 and 10.5).
3. Comparison of UE12t#1 flexible-wall Ksat and alpha data to RME#1 Ksat-alpha correlation to identify suspect Ksat data values for UE12t#1 core.
4. Use of Ksat-alpha correlation from RME#1 core data to correct suspect UE12t#1 Ksat if corresponding alpha data have low standard error.
5. Highlight all alpha, Ksat, and lithologic data values that are suspect (use color in tables)
6. Combine RME#1 and UE12t#1 data to estimate properties for stratigraphic units, hydrostratigraphic units, and HST model rock units.

10.3 Mean Values Upscaling of Hydraulic Property Data

Many methods and approaches are advocated for averaging and upscaling of hydraulic property data, particularly hydraulic conductivity and permeability (K). It is widely understood that:

- Effective or "block-averaged" K will be bounded by the harmonic and arithmetic means.
- The harmonic mean is the effective K for a 1-D flow system.
- The geometric mean is intermediate between harmonic and arithmetic mean.

The geometric mean is widely used as effective K for lateral flow in groundwater models. The geometric mean K yields an effective K for a 2-D randomly heterogeneous media with log-K normal distribution and 3-D spatially uncorrelated cell values (Wen and Gomez-Hernandez, 1996).

The harmonic mean provides a lower bound to an effective K derived from multiple data. The harmonic mean is the effective K for a 1-D flow system. As such, the harmonic mean is a representative effective K for uniform downward flow in a horizontally layered system. Therefore, the harmonic mean is representative of a lower bound for bulk vertical K (K_z) in HSU or stratigraphic units composed of layered ash-fall tuffs on Rainier Mesa.

10.4 RME#1 Data

10.4.1 Comparison of Rigid-and Flexible-Wall Ksat Data to Alpha

The RME#1 matrix property data include Ksat data measured by both rigid-wall and flexible-wall methods. Comparison of Ksat values from these different data methods indicates that the flexible-wall data tend to underestimate Ksat. Furthermore, consideration of correlation of Ksat to alpha and standard error in the alpha parameter estimation indicates that alpha may often be overestimated (Kwicklis et al., 2008).

Figure 10.1 compares duplicate RME#1 flexible and rigid-wall Ksat data for the same depth intervals. Comparison of the differences between rigid and flexible-wall data values from the same core depth locations is indicated by deviation from the blue line representing equal Ksat values. For most data, Ksat for the flexible wall method exceeds Ksat for the rigid wall method. Cases where the K data differ by more than an order of magnitude are labeled as "suspect". The flexible wall Ksat data are more likely biased high given that twelve of thirteen suspect data pairs result from higher values from the flexible wall Ksat. The one suspect data pair with a higher rigid wall Ksat could be a result of an erroneous rigid wall Ksat measurement. Considering the different Ksat methodologies used, many of the UE12t#1 flexible-wall Ksat data values are likely overestimated, as suggested by Kwicklis et al. (2008) based on comparison of RME#1 flexible and rigid-wall data.

Figure 10.2 compares rigid wall Ksat data with the alpha parameter derived by the RETC code for fitting of a van Genuchten model for effective saturation as a function of capillary pressure – the "moisture retention curve" (van Genuchten et al., 1991; Kwicklis et al., 2008). Importantly, the RETC code produces a standard error the alpha parameter, which for many cases exceeds the alpha parameter itself; in these cases, the alpha data are labeled as "suspect". The remaining data exhibit a correlation between Ksat and the alpha parameter, which was been previously examined in Kwicklis et al. (2008).

Although Kwicklis et al. (2008) used correlation of Ksat and alpha to evaluate measurement consistency, no consideration was given to estimated error of the alpha parameter. In Figure10.2, the blue and red horizontal lines represent standard error in alpha parameter measurement calculated from the RETC inversion code of van Genuchten et al. (1991). Alpha standard error is given in raw alpha units, which are preserved on the log10[alpha] scale in Figure 10.2. In some cases, the alpha standard error is greater than the alpha value estimate, which leads to an unlimited lower extent to the alpha standard error as plotted on a log scale. Alpha values with large standard error (represented by the red horizontal lines in Figure 10.2) could be orders of magnitude lower within the bounds of the measurement uncertainty. Without consideration of alpha standard error, an analysis of Ksat-alpha correlation can spuriously support overestimation of Ksat values.

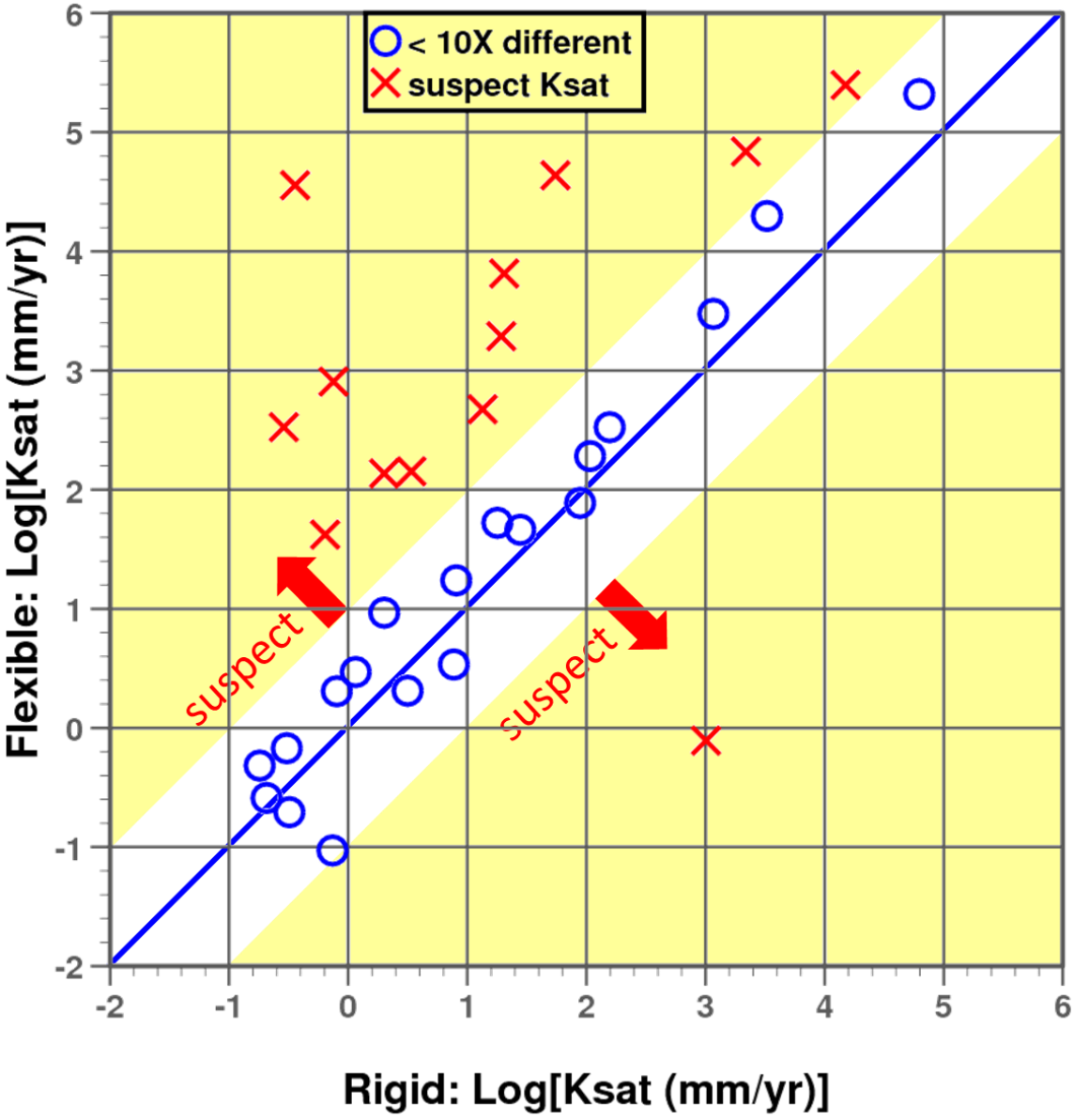

Figure 10.1 Comparison of RME#1 flexible and rigid-wall Ksat data. Rigid-wall Ksat values are consistently lower than flexible wall values Ksat. This indicates UE12t#1 flexible-wall Ksat data are often too high, as suggested by Kwicklis et al. (2008). Data pairs differing by a factor of 10 or more are labeled "suspect".

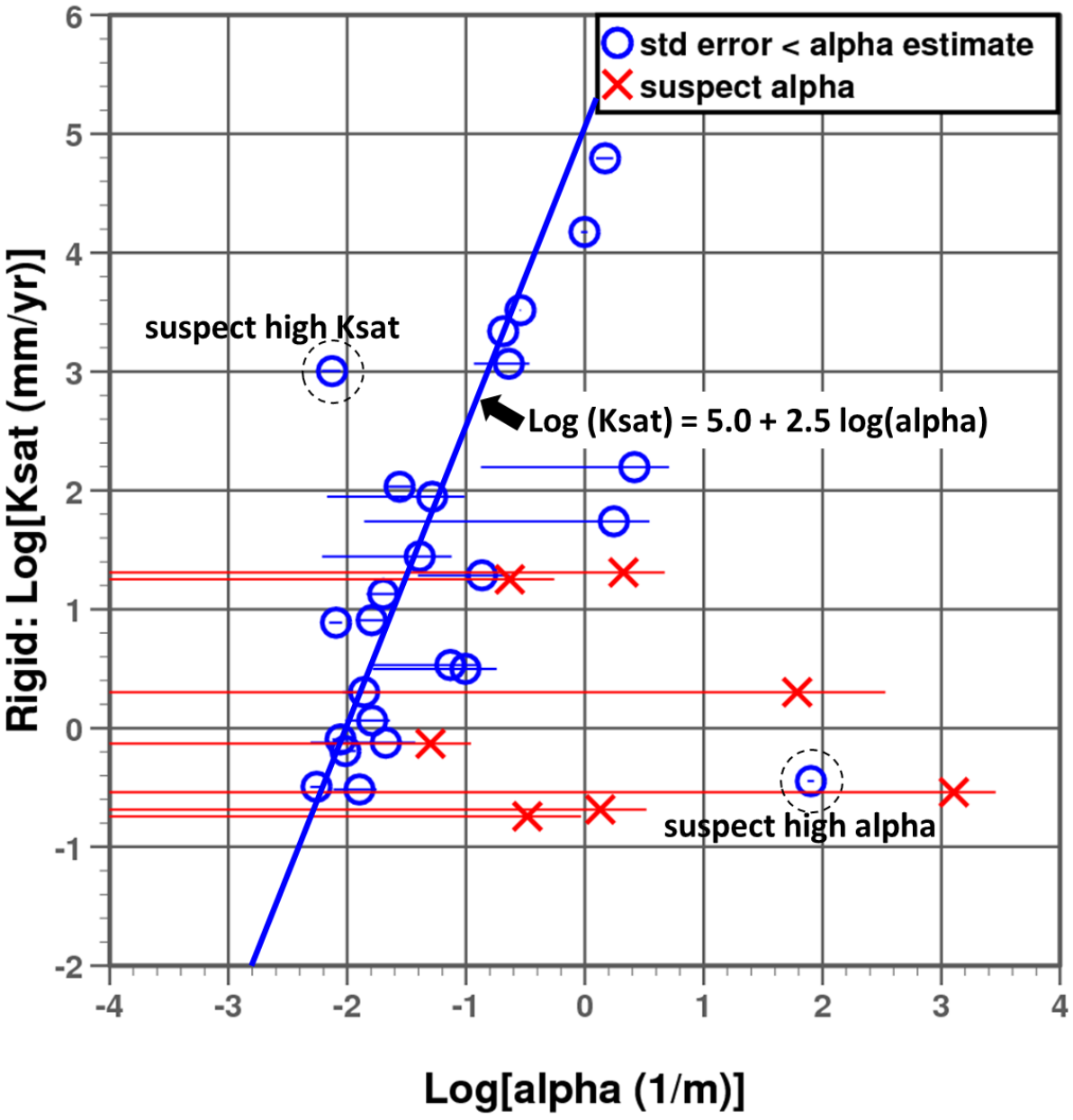

Figure 10.2 Correlation plot of Ksat and alpha highlighting "suspect" alpha values based on high standard error. Correlation fit of log (Ksat) = 5.0 + 2.5 log(alpha) considers variable standard error of alpha and suspect data.

10.4.2 Relationship of Ksat and Alpha to Lithology

It is reasonable to expect Ksat and alpha to depend on lithology, particularly where the different lithologies have different pore structures as is the case for volcanic rocks on Rainier Mesa. Using the lithologic description in Kwicklis et al. (2008), the lithology of the volcanic cores can be generally divided into non-welded (usually zeolitic), welded, vitric,

and argillic tuffs. Non-welded tuffs comprise most of the data. Lithologic descriptions from Kwicklis et al. (2008) are abbreviated as follows:

NWT = non-welded tuff
PWT = partially-welded tuff
MST = moderately welded tuff
WT = welded tuff
PT = pumiceous tuff
AS = arkosic sandstone:
bedded with alternating sandy and pebbly layers, matrix filled with clay
RWT = reworked tuff
SS = sandstone
VSiSS = tuff volcaniclastic silty sandstone
V = vitrophyre
VT = vitric tuff

To isolate effects of lithology, Ksat and alpha data are first evaluated within the data described as non-welded tuffs by Kwicklis et al. (2008), who provided "fit by eye" lines for four data subsets:

1. UE-12t#1, Flexible wall $\log(Ksat) = 5.18 + 2.08\log(alpha)$
2. UE-12t#1, Flexible wall $\log(Ksat) = 5.71 + 2.71\log(alpha)$
   (excluding data with dewpoint potentiometer measurements)
3. RME#1, Flexible wall $\log(Ksat) = 5.11 + 2.43\log(alpha)$
4. RME#1, Rigid wall $\log(Ksat) = 4.56 + 2.21\log(alpha)$

Figure 10.3 compares RME#1 rigid-wall Ksat and alpha for cores described as non-welded tuffs. These data indicate Ksat ranges from 0.2 to 1000 mm/yr and alpha ranges from 0.005 to 0.20 m^{-1} in non-welded tuffs. A Ksat-alpha trend line of $\log(Ksat)=5.0 + 2.5\log(alpha)$ is estimated using "fit by eye" at with consideration of standard error in alpha (horizontal bars). This fit is within a range of models given by Kwicklis et al. (2008) for different data subsets. As discussed below, the $\log(Ksat)=5.0 + 2.5\log(alpha)$ model also provides a reasonable fit to all Ksat alpha data subsets (including welded tuffs) with consideration of standard error in alpha and underestimation of Ksat by the flexible wall method.

Figure 10.4 compares RME#1 rigid-wall Ksat and alpha for cores described as welded tuffs. Alpha data for welded tuffs in RME#1 tend to have large standard error. With consideration of standard error in alpha, the Ksat-alpha correlation of $\log(Ksat)=5.0 + 2.5\log(alpha)$ for non-welded tuffs also provides a reasonable fit to the data for welded tuffs. These data indicate Ksat ranges from 0.2 to 3 mm/yr for welded tuffs. With consideration of the large standard error in alpha and a Ksat-alpha trend line of $\log(Ksat)=5.0 + 2.5\log(alpha)$, these data indicate alpha for welded tuff ranges from 0.004 to 0.02 m^{-1}.

Figure 10.5 compares RME#1 rigid-wall Ksat and alpha for cores described as vitric, pumiceous, reworked, (arkosic) sandstone, or volcaniclastic tuffs. With the exception of one outlier, the Ksat-alpha correlation of $\log(Ksat)=5.0 + 2.5\log(alpha)$ provides a reasonable fit to the Ksat alpha data considering standard error because the line passes

within or near the variable standard error bars for all of the data. For tuffs in non-zeolitized HSUs (TM-LVTA and LVTA1) including vitric, pumiceous, and sandstone tuffs, Ksat ranges from 2000 to 60,000 mm/yr and alpha ranges from 0.2 to 1.5 m^{-1}. For tuffs in argillic units, Ksat ranges from 0.3 to 0.8 mm/yr and alpha is about 0.01 m^{-1}, considering standard error in alpha and a Ksat-alpha trend line of $\log(Ksat)=5.0 + 2.5 \log(alpha)$. The alpha value for the "Tot, V(volcaniclastic), RVA" datum is suspect.

Figure 10.6 compares Ksat determined by rigid-wall method, flexible-wall method, and correlation with alpha based on RME#1 rigid-wall Ksat and alpha data. Red crosses are alpha-based Ksat with high standard error in Ksat. As illustrated in Figure 10.1, the RME#1 data show rigid-wall Ksat tends to be lower than flexible-wall Ksat as pointed out by Kwicklis et al. (2008). Alpha-based Ksat based on the alpha-Ksat trend line correlation established in Figures 10.3, 10.4 and 10.5 tends to be close to rigid wall for measured Ksat for alpha values with low standard error (green crosses) and high relative to measured Ksat for alpha values with high standard error (red crosses). This suggest that erroneously high Ksat values are associated with van Genuchten data having high standard error in alpha.

The determination of Ksat values that are erroneously high is important to establishment of model parameters capable of explaining the perched groundwater conditions observed at Rainier Mesa. Ksat values lower than the recharge rate, estimated at 24 mm/yr by Russell (1987), have potential for producing perched conditions. Erroneously high Ksat data could lead to overestimation of Ksat matrix model permeability or hydraulic conductivity. Most of the rigid-wall Ksat data fall below the recharge rate, whereas most of the flexible-wall Ksat data fall above the recharge rate. This suggests strict reliance on flexible-wall Ksat data for model parameters, such as using only Ksat values derived from UE12t#1 data given in Kwicklis et al. (2008), could lead to overestimation of Ksat and failure to produce perched conditions in variably saturated flow models of Rainier Mesa.

10.4.3 Corrected Hydrologic Property Data for RME#1

Table 10.1 summarizes corrected hydrologic property data for RME#1 using lithologic descriptions from NSTec (2009), with suspect data for Ksat and alpha highlighted in color. Suspect alpha values are distinguished by high standard error in the fitting of the moisture retention curve data. The data are organized by HGU, HSU, and stratigraphic unit to facilitate relationship to HST, N and T-Tunnel, and flow and transport model units. Alteration is determined from XRD in Kwicklis et al. (2008) with terminology from NSTec (2009). For HST modeling, it is important to evaluate clay content (e.g., given by XRD) rather than rely entirely on predominate mineralogic alteration (e.g., zeolitic in the TCU) because most radionuclide classes have far higher sorption to clay compared to zeolite (Zavarin et al., 2011).

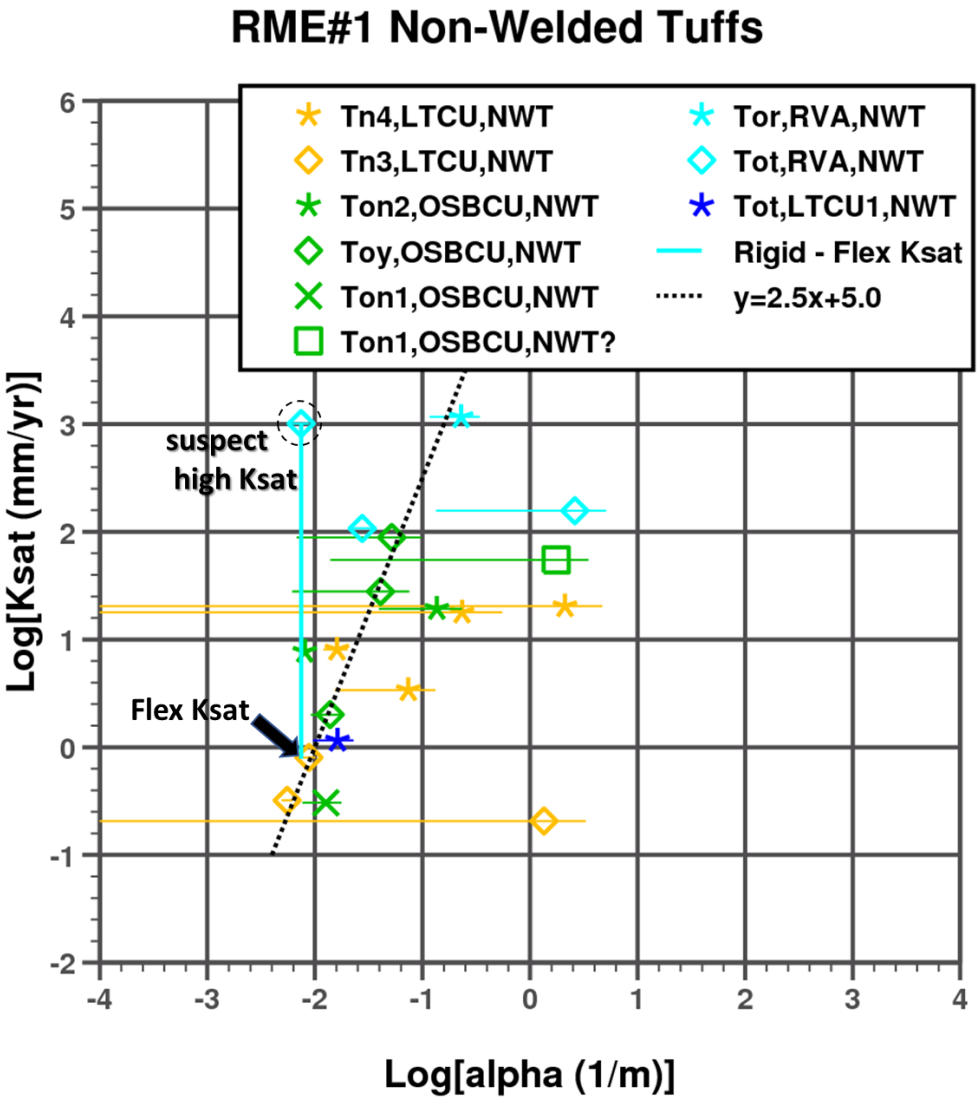

Figure 10.3 RME#1 rigid-wall Ksat and alpha for cores described as non-welded tuffs. These data indicate Ksat ranges from 0.2 to 1000 mm/yr and alpha ranges from 0.005 to 0.20 m^{-1} in non-welded tuffs. Ksat-alpha trendline is estimated at log(Ksat)=5.0+2.5log(alpha) considering standard error in alpha (horizontal bars). The vertical bar for one of the "Tot, RVA, NWT" data represents an unusual large positive discrepancy between rigid and flexible wall Ksat estimates.

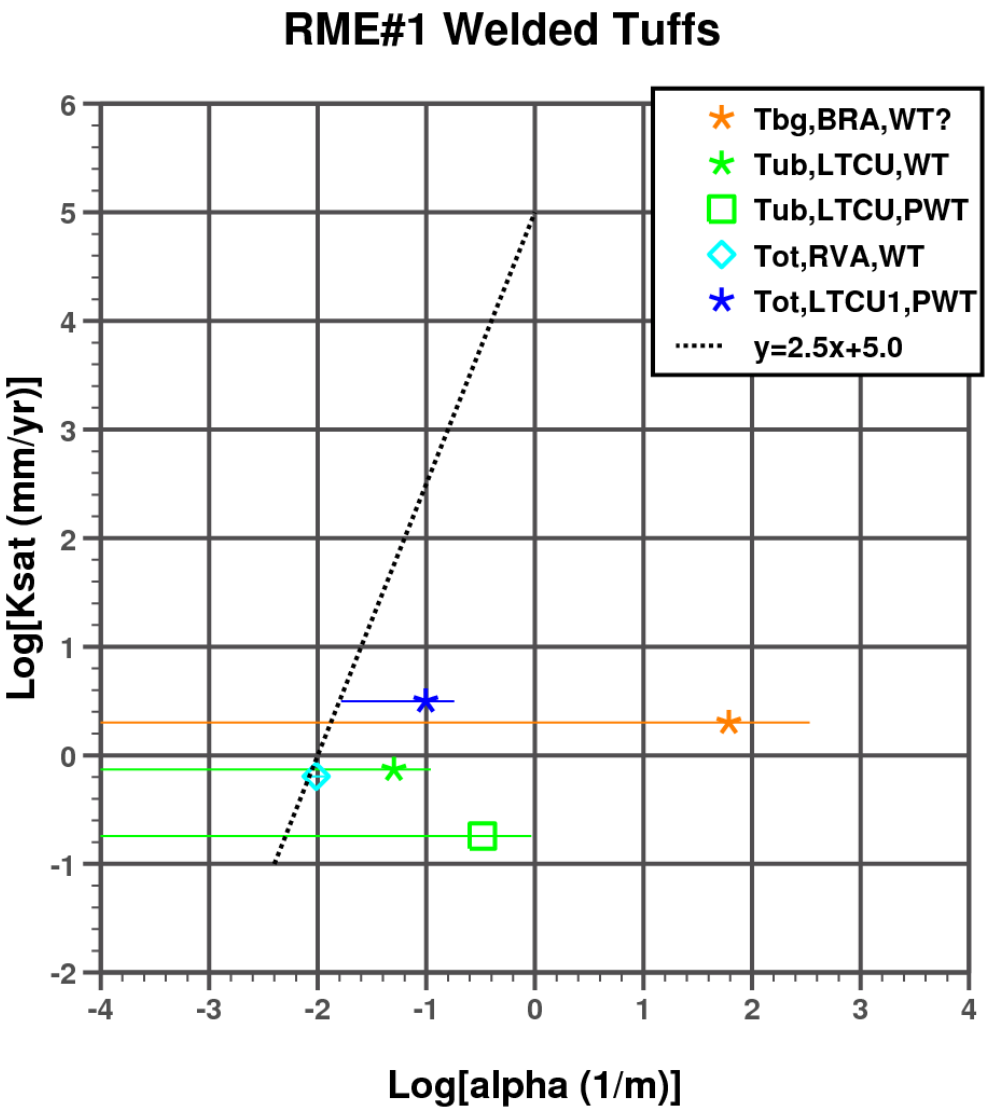

Figure 10.4 RME#1 rigid-wall Ksat and alpha for cores described as welded tuffs. These data indicate Ksat ranges from 0.2 to 3 mm/yr for welded tuffs. With consideration of standard error in alpha and a Ksat-alpha of log(Ksat)=5.0+2.5log(alpha), these data indicate alpha for welded tuff ranges from 0.004 to 0.02 m^{-1}.

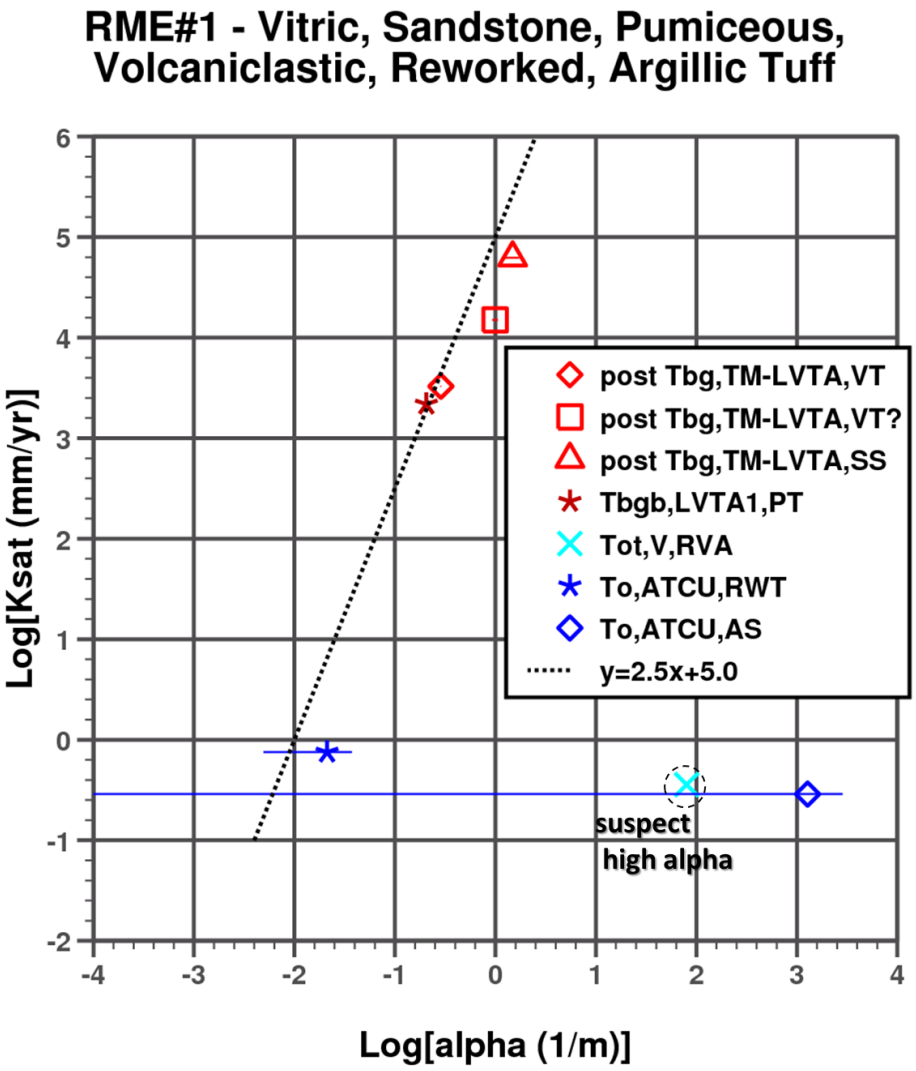

Figure 10.5 RME#1 rigid-wall Ksat and alpha for cores described as vitric, pumicieous, reworked, (akosic) sandstone, or volcaniclastic tuffs. For tuffs in non-zeolitized HSUs (TM-LVTA and LVTA1) including vitric, pumiceous, and sandstone tuffs, Ksat ranges from 2000 to 60,000 mm/yr and alpha ranges from 0.2 to 1.5 m^{-1}. For tuffs in argillic units, Ksat ranges from 0.3 to 0.8 mm/yr and alpha is about 0.01 m^{-1}, considering standard error in alpha and a Ksat-alpha trendline estimated at log(Ksat)=5.0+2.5log(alpha). The alpha value for the Tot, V(volcaniclastic), RVA datum is suspect.

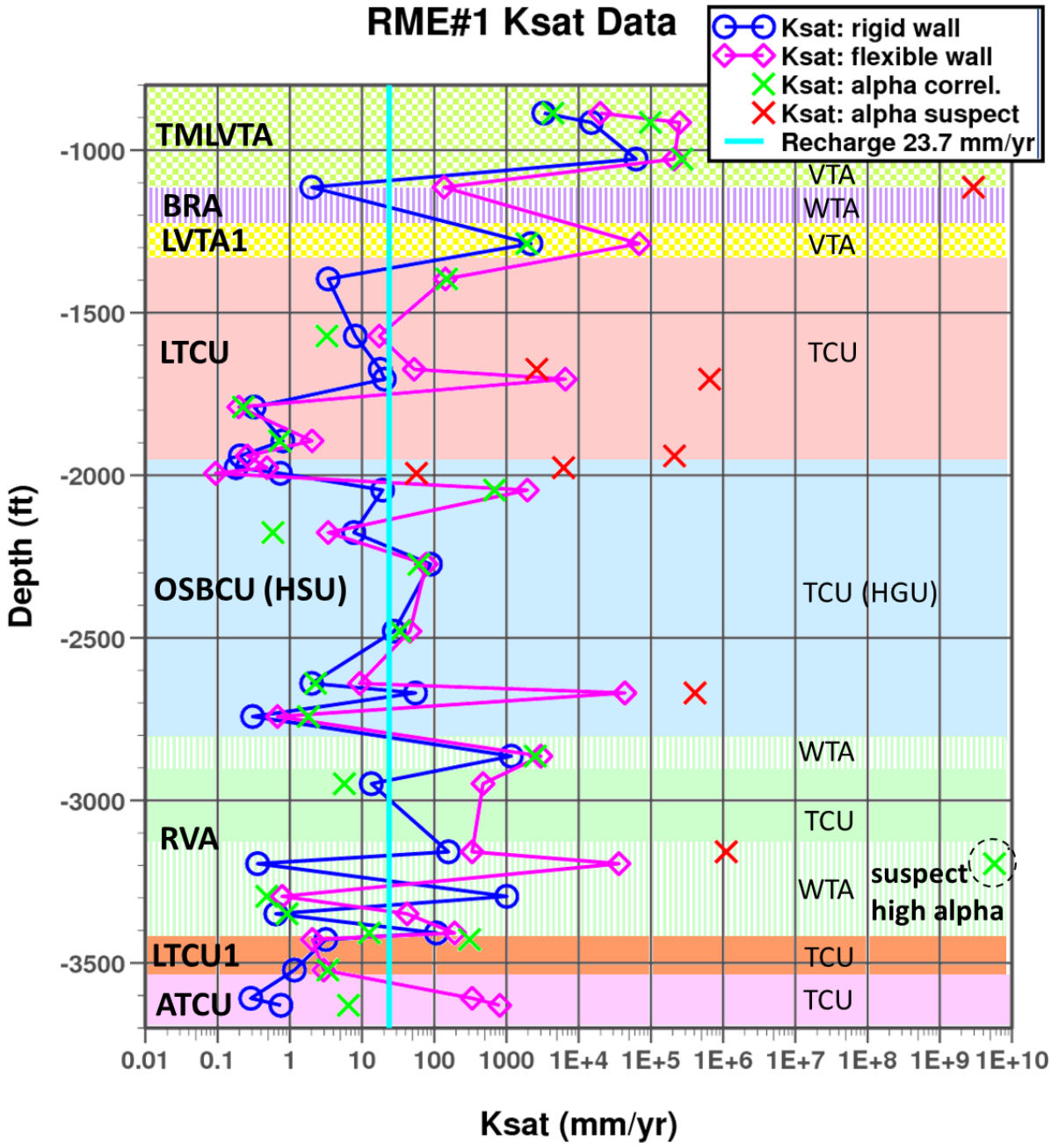

Figure 10.6 Comparison of Ksat determined by rigid-wall method (blue circles), flexible-wall method (magenta diamonds), and correlation with alpha (green and red crosses) based on RME#1 rigid-wall Ksat and alpha data. Red crosses are alpha-based Ksat with high standard error in Ksat. Rigid-wall Ksat tends to be lower than flexible-wall Ksat. Alpha-based Ksat tends to be close to rigid wall Ksat (blue) for low alpha standard error (green) and high relative to rigid wall Ksat for high standard error (red). Ksat values lower than recharge rate (23.7 mm/yr) shown by vertical light blue line have potential for producing perched conditions. Depth ranges for HSUs and HGUs are color-coded.

Table 10.1 RME#1 hydrologic property data of Kwicklis et al. (2008) compared to HGU, HSU and stratigraphic units, lithology from NSTec (2007), and alteration from Kwicklis et al. (2008).

Depth (ft)	HGU	HSU	Strat	Lith	Alt	Rigid Wall Ksat (cm/s)	Alpha (m^{-1})	$\frac{StdErr}{Ksat}$	*n*	θ*r*	θs
886.3	VTA	TM-LVTA	Post Tbg	NWT/ PWT	GL	1.04E-05	2.87E-1	0.01	4.59	0.044	0.365
915.0						4.75E-05	9.93E-1	0.06	1.74	0.042	0.420
1027.6						1.98E-04	1.48E+0	0.16	1.77	0.048	0.297
1114.2	WTA	BRA	Tbg	PWT/ DWT	ZC	6.35E-09	6.12E+1	4.54[b]	1.04	0	0.231
1287.7	VTA	LVTA1	Tbgb	BED	GL	6.92E-06	2.06E-1	0.03	2.55	0.083	0.368
1396.3	TCU	LTCU	Tn4	BED/ RWT	ZC	1.08E-08	7.39E-2	0.79	1.24	0	0.221
1571.9						2.56E-08	1.61E-2	0.25	1.31	0	0.295
1674.3						5.67E-08	2.34E-1	1.36[b]	1.27	0	0.315
1704.5						6.47E-08	2.11E+0	1.22[b]	1.18	0	0.198
1790.1			Tn3	BED/ RWT	ZC	1.02E-09	5.52E-3	0.11	1.40	0	0.203
1894.4						2.54E-09	8.80E-3	0.14	1.77	0	0.266
1940.3					ZC	6.54E-10	1.35E+0	1.44[b]	1.18	0	0.306
1976.6			Tub	NWT	,	5.72E-10	3.29E-1	1.82[b]	1.15	0	0.258
1994.					AR	2.34E-09	5.03E-2	1.18[b]	1.22	0	0.245
2045.6		OSBCU	Ton2	BED/ RWT	ZC	6.12E-08	1.36E-1	0.71	1.29	0	0.282
2176.4						2.44E-08	8.06E-3	0.12	1.81	0	0.242
2273.6			Toy	NWT/ RWT	ZC	2.81E-07	5.19E-2	0.87	1.45	0	0.265
2479.6					, AR	8.84E-08	2.08E-2	0.85	1.50	0	0.311
2640.2					ZC	6.36E-09	1.39E-2	0.34	1.58	0	0.259
2669.6			Ton1	BED/ RWT	AR	1.74E-07	1.75E+0	0.99[b]	1.23	0	0.255
2742.1						9.66E-10	2.18E-2	0.39	1.27	0	0.188
2864.0	WTA	RVA	Tor	PWT/ MWT	nr	3.69E-06	2.29E-1	0.49	1.45	0	0.268
2948.7	TCU	RVA	To	BED	ZC	4.26E-08	2.01E-2	0.27	1.81	0	0.135
3158.2	WTA	RVA	Tot	DWT	nr	4.97E-07	2.36E+0	0.95[b]	1.30	0.012	0.285
3194.8						1.13E-09	8.00E+1[c]	0.06	1.01	0	0.073
3295.3						3.20E-6[a] (2.48E-9)	7.45E-3	0.18	1.66	0	0.090
3349.0						2.03E-09	9.65E-3	0.23	1.67	0	0.138
3408.0						3.40E-07	2.76E-2	0.26	1.73	0	0.262
3428.0	TCU	LTCU1	Tot	PWT/ NWT	ZC	1.00E-08	9.88E-2	0.83	1.23	0	0.256
3522.0						3.66E-09	1.62E-2	0.41	1.31	0	0.226
3608.8		ATCU	To	BED/ RWT	AR	9.33E-10	1.27E+3	1.24[b]	1.02	0	0.160
3630.4						2.39E-09	2.11E-2	0.77	1.21	0	0.093

a. Ksat suspected too high; vertical bar represents difference from flexible wall Ksat, which is usually higher than rigid wall Ksat; Alpha of 7.45E-03, flexible- wall Ksat of 2.48E-09, and saturated water content are indicative of a welded tuff.

b. Standard error of alpha measurement is high, which leads to overestimation of alpha and uncertainty in *n*.

c. Alpha suspected too high; however vitrophyre lithology (Kwicklis et al., 2008) may have unique properties.

10.5 UE12t#1 Data

10.5.1 Use of Ksat-Alpha Correlation to Correct Overestimation of Ksat

In lieu of using erroneous Ksat measurements, Ksat can be estimated through correlation with alpha; however, the standard error of the alpha measurement should be considered. The analysis of RME#1 hydrologic data in Section 10.4 establishes a correlation between alpha and Ksat measured by the rigid-wall method, which in some cases is more reliable than the flexible wall method used exclusively for UE12t#1 Ksat measurement. Since the RME#1 data indicate Ksat measured by the flexible-wall method are often overestimated, it is reasonable to conclude that some Ksat values from UE12t#1 measured by the flexible-wall method are also overestimated, as indicated by Kwicklis et al. (2008).

The Ksat-alpha correlation established by the RME#1 alpha and rigid-wall Ksat data can be used to evaluate possible overestimation of Ksat by the UE12t#1 flexible-wall data. Overestimation of Ksat will be indicated by UE12t#1 Ksat values corresponding to alpha values with low standard error and falling well above the Ksat-alpha correlation line established from RME#1 data. For data suspected of overestimating Ksat, it is reasonable to use an alpha value with low standard error to estimate Ksat through the Ksat-alpha correlation relationship established from RME#1 rigid-wall Ksat data (Section 10.4.1).

Figure 10.7 compares five UE12t#1 Ksat and alpha data for lithologies described as bedded and non-welded tuffs (Kwicklis et al., 2008). The three non-welded data in the lower left cluster fall within the RME#1 Ksat range of 40 to 120 mm/yr and alpha range of 0.025 to 0.6 m^{-1} in non-welded tuffs. The upper right cluster suggest bedded tuff in the TCU have higher Ksat of 30,000 to 40,000 mm/yr and alpha of 0.5 to 0.6 m^{-1}. Only one of these five data, a non-welded tuff in the Tn4 stratigraphic unit and BRCU HSU, shows significantly higher Ksat relative to the Ksat-alpha correlation established from RME#1 data. Therefore, for most (but not all) of the UE12t#1 Ksat data in cores described as bedded and non-welded tuffs (Kwicklis et al., 2008), the flexible-wall Ksat estimates are not suspected of being erroneously high.

Figure 10.8 compares UE12t#1 flexible-wall Ksat and alpha for cores described as welded tuffs (Kwicklis et al., 2008). Most data lie above and well to the left of the y=2.5x+5.0 correlation line, suggesting greater overestimation of Ksat by the flexible-wall method in welded tuffs compared to bedded or non-welded tuffs. For Tn3 units and older, an alpha range of 0.008 to 0.01 m^{-1} is consistent with the RME#1 data with an alpha range of 0.004 to 0.02 m^{-1}. In TM-LVTA and Tn4 units, alphas of about 0.3 m^{-1} and relatively high flexible-wall Ksat values of greater than 10,000 mm/yr are consistent with bedded tuff properties from RME#1 data. Tmr welded tuffs show higher alpha and Ksat compared to older welded tuffs. Therefore, for most of the UE12t#1 Ksat data in rocks described as welded tuffs

(Kwicklis et al., 2008), the flexible-wall Ksat estimates are suspected of being erroneously high.

Figure 10.9 compares UE12t#1 rigid-wall Ksat and alpha for cores described as vitric, pumiceous, or argillic tuffs and carbonate (Kwicklis et al., 2008). The alpha range of 0.4 to 1.8 m^{-1} for TM-LVTA and LVTA1 HSUs is consistent with the RME#1 alpha range 0.2 to 1.5 m^{-1} for the same HSUs. ATCU Ksat values from UE12t#1 data are over three-orders of magnitude higher than from RME#1 data. These UE12t#1 data for vitric, pumiceous, and argillic tuffs suggest that Ksat tends to be overestimated by the flexible wall method.

For LCA3 properties, alpha in breccia has high standard error and, therefore, Ksat is suspect. A single Ksat datum for LCA3 matrix (~28 mm/yr), though relatively low compared to most flexible-wall Ksat data, is likely overestimated by the flexible-wall method. For carbonate rocks, Ksat does not appear to be correlated to alpha in the same manner as for volcanic rocks.

10.5.2 Corrected Hydrologic Property Data for UE12t#1

Table 10.2 summarizes hydrologic property data for UE12t#1, with six suspect data for Ksat, alpha and core description highlighted in red. Suspect alpha values are distinguished by high standard error in the fitting of the moisture retention curve data. The data are organized by HGU, HSU, and stratigraphic unit to facilitate relationship to HST, N and T-Tunnel, and SZ flow and transport model units. Ksat values are given for both flexible wall data and derivation from correlation with alpha. Suspect Ksat values derived from alpha correlation are highlighted in red. Considering standard error of alpha, Ksat-alpha correlation, and amount of decrease in Ksat value relative to flexible wall data, Ksat estimation based on alpha correlation is recommended for 11 of the 27 UE12t#1 Ksat data.

Table 10.3 repeats the summary of hydrologic properties for UE12t#1 and includes lithology from NSTec (2007), alteration from XRD in Kwicklis et al. (2008), and alteration terminology from NSTec (2007). For HST modeling, it is important to evaluate clay content (e.g., given by XRD) rather than rely entirely on predominate mineralogic alteration (e.g. zeolitization) because most radionuclide classes have far higher sorption to clay compared to zeolite.

Figure 10.10 compares UE12t#1 Ksat data determined from flexible-wall data (magenta) and alpha correlation with low standard error (green) and high standard error (red). The comparison indicates Ksat is overestimated by flexible-wall data for some but not all UE12t#1 data. Some data with large standard error in alpha may be accurate, as indicated by consistency to other data.

Alpha correlation-based Ksat values for zeolitized Ton2, Tn3, and Tn4 stratigraphic units in UE12t#1 are frequently about one order-of-magnitude lower than flexible wall Ksat.

Accurate estimation of Ksat in Ton2, Tn3, and Tn4 is particularly relevant to HST and other flow and transport models because all N and T-tunnel tests are located within zeolitized tuffs in these stratigraphic units.

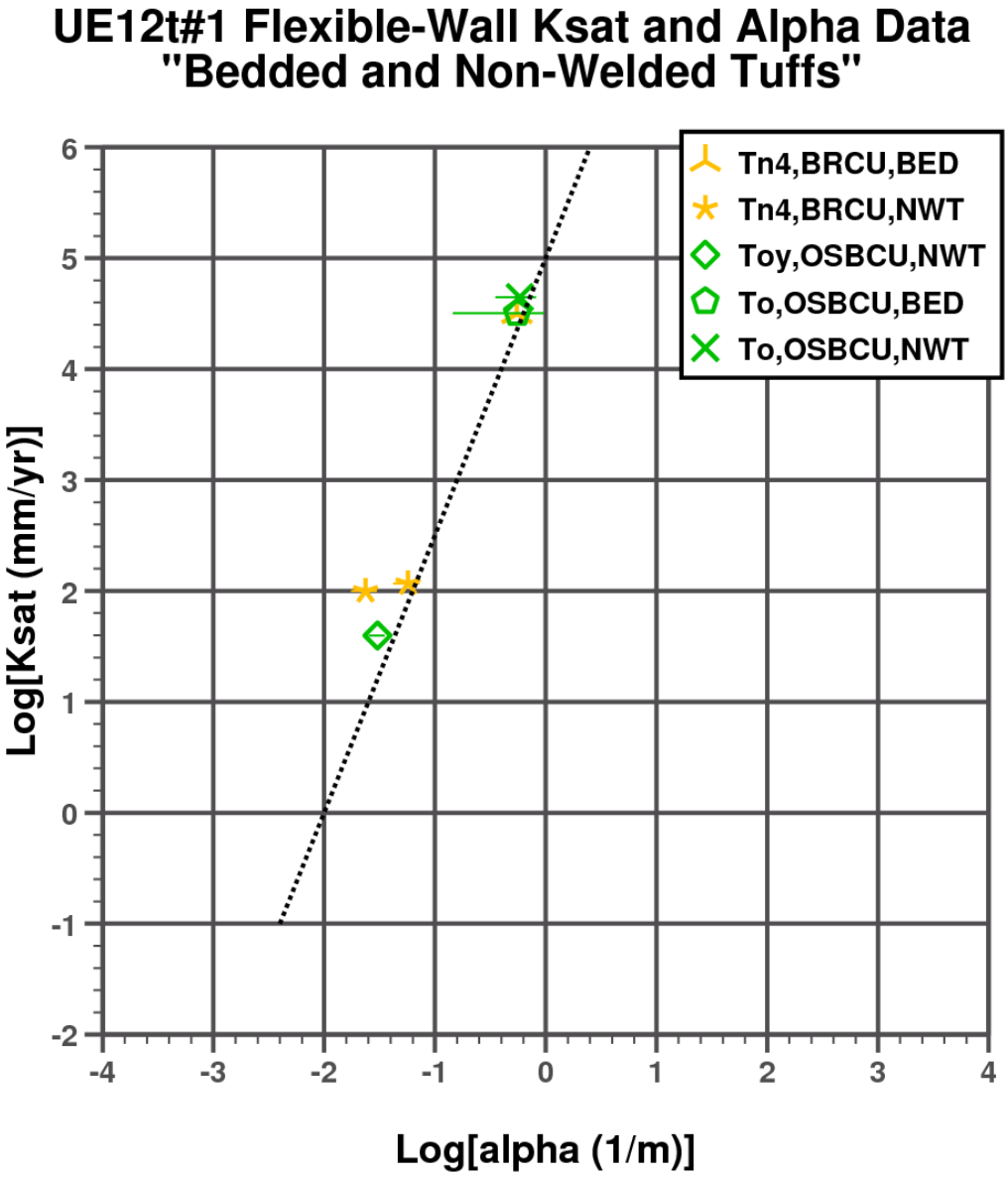

Figure 10.7 UE12t#1 flexible-wall Ksat and alpha for cores described as non-welded or bedded tuffs. The three non-welded data in the lower left cluster fall within the RME#1 Ksat range of 40 to 120 mm/yr and alpha range of 0.025 to 0.6 m^{-1} in non-welded tuffs. The upper right cluster suggest some intervals of bedded tuff in the TCU have higher Ksat of 30,000 to 40,000 mm/yr and alpha of 0.5 to 0.6 m^{-1}. A Ksat-alpha trendline (dotted line) of log(Ksat)=5.0+2.5log(alpha) provides reasonable fit to the data.

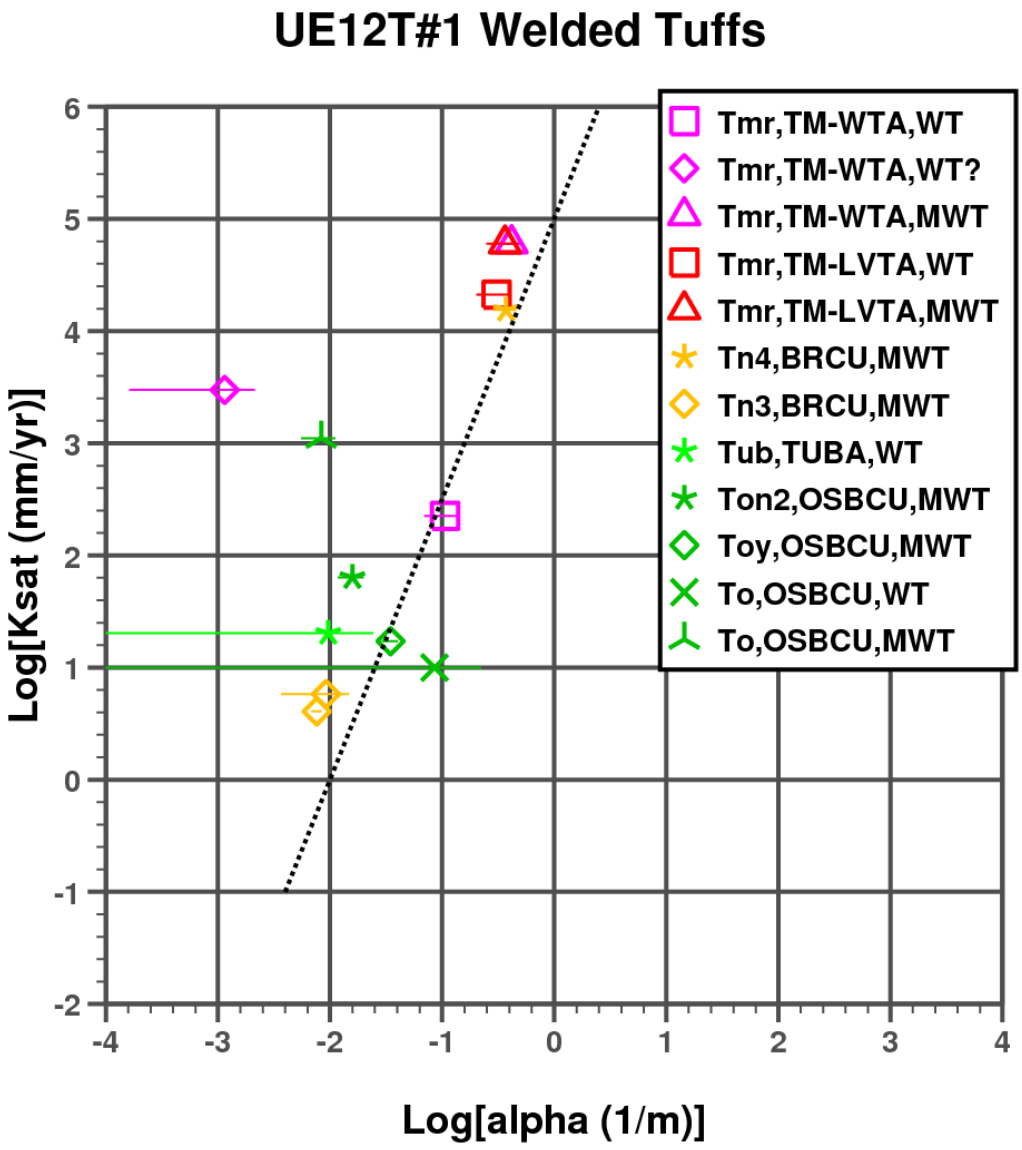

Figure 10.8 UE12t#1 flexible-wall Ksat and alpha for cores described as welded tuffs. Most data lie to the left of a Ksat-alpha trendline (dotted line) of log(Ksat)=5.0+2.5log(alpha), suggesting overestimation of Ksat by the flexible-wall method. For Tn3 units and older, alpha range of 0.008 to 0.01 m^{-1} is consistent with the RME#1 data. In TM-LVTA and Tn4 units, alphas of about 0.3 m^{-1} and high flexible-wall Ksats are consistent with bedded tuff properties from RME#1 data. Tmr welded tuffs show higher alpha and Ksat compared to older welded tuffs.

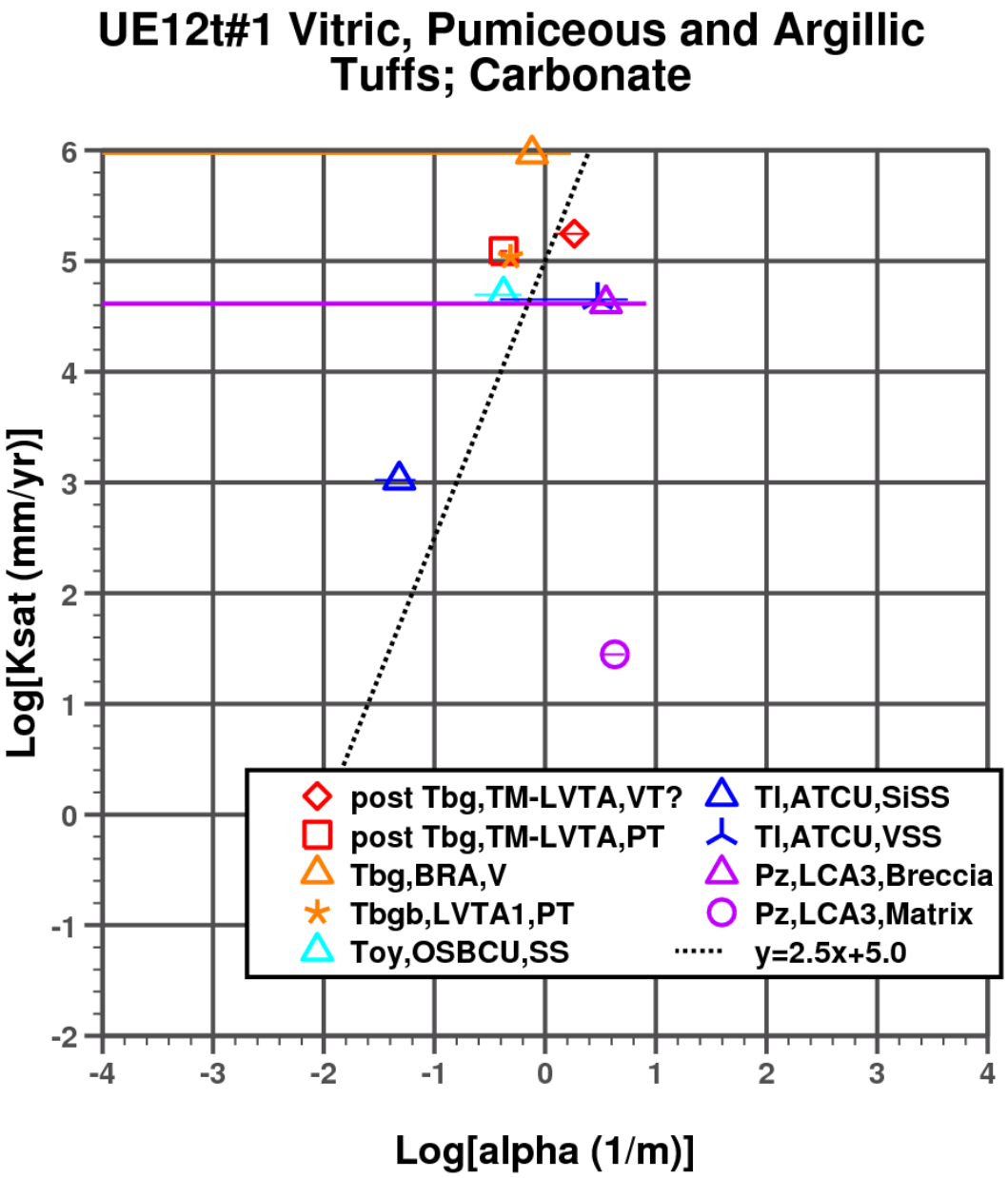

Figure 10.9 UE12t#1 rigid-wall Ksat and alpha for cores described as vitric, pumiceous, or argillic tuffs and carbonate. The alpha range of 0.4 to 1.8 m^{-1} for TM-LVTA and LVTA1 HSUs is consistent with the RME#1 alpha range 0.2 to 1.5 m^{-1} for the same HSUs. UE12t#1 Ksat data for the ATCU are over three-orders of magnitude higher than in RME#1. For LCA3 properties, alpha in breccia has high standard error and, therefore, Ksat is suspect. The single Ksat datum for LCA3 matrix (~28 mm/yr), though low, is likely overestimated by the flexible-wall method. Considering standard error, the a (Ksat)=5.0+2.5log(alpha) trendline is generally consistent with the data except for carbonate (LCA3) matrix.

Table 10.2 UE12t#1 Hydrologic property data and core description from Kwicklis et al. (2008) compared to HGU, HSU, and stratigraphy.

Depth (ft)	HGU	HSU	Strat	Core Descr	Ksat (cm/s)		Alpha (m^{-1})	Std Err	*n*	θ*r*	θ*s*
					FLEX	Based on alpha					
34.9	WTA	TM-WTA	Tmr	MWT	1.91E-4[b]	*3.6E-5*[d]	4.17E-1	0.2	1.47	0	0.322
193.6				WT	7.14E-7	*1.2E-6*	1.06E-1	0.35	1.68	0.030	0.090
267				WT?	9.48E-6[b]	*1.4E-11*	1.15E-3	0.86[c]	1.38	0	0.026
321.7	VTA	TM-LVTA		WT[a]	6.72E-5[b]	*1.6E-5*[d]	3.01E-1	0.34	2.59	0.057	0.227
365.4				MWT[a]	1.90E-4[b]	*2.5E-5*[d]	3.64E-1	0.32	2.48	0.045	0.301
391.5			Post Tbg	VT?	5.60E-4	*1.5E-3*	1.84E+0	0.35	1.88	0.040	0.396
608.8				PT	3.89E-4[b]	*3.7E-5*[d]	4.22E-1	0.08	2.45	0.031	0.464
736	WTA	BRA	Tbg	V	2.95E-3[b]	*1.6E-4*	7.62E-1	1.24[c]	1.14	0	0.023
790.0	VTA	LVTA1	Tbgb	PT	3.45E-4[b]	*5.2E-5*[d]	4.87E-1	0.18	2.21	0.046	0.454
940.0	TCU	BRCU	Tn4	MWT[a]	4.89E-5	*2.7E-5*	3.73E-1	0.23	2.93	0.108	0.169
1030.2				NWT	3.71E-7	*2.5E-7*	5.71E-2	0.27	1.30	0	0.263
1134				BED	9.96E-5	*7.1E-5*	5.50E-1	0.13	1.76	0.076	0.310
1155				NWT	3.16E-7[b]	*2.7E-8*[d]	2.37E-2	0.26	1.49	0	0.381
1260.1			Tn3	MWT	1.84E-8[b]	*2.6E-9*[d]	9.22E-3	0.6	1.30	0	0.254
1376.2				MWT	1.29E-8[b]	*1.6E-9*[d]	7.60E-3	0.1	1.75	0	0.277
1463.0	WTA	TUBA	Tub	WT	6.43E-8[b]	*2.9E-9*	9.65E-3	1.52[c]	1.50	0	0.039
1561.5	TCU	OSBCU	Ton2	WT	2.02E-7[b]	*1.0E-8*[d]	1.58E-2	0.26	1.57	0	0.271
1651.3			Toy	SS	1.57E-4[b]	*3.6E-5*[d]	4.21E-1	0.45	1.25	0	0.342
1738.5				NWT	1.26E-7	*5.1E-8*	3.03E-2	0.17	1.62	0	0.281
1851.4				MWT[e]	5.44E-8	*7.1E-8*	3.47E-2	0.16	1.44	0	0.328
1917.6			To	NWT[a]	1.41E-4	*8.3E-5*	5.84E-1	0.4	1.27	0	0.229
1950.0				BED	1.01E-4	*7.2E-5*	5.54E-1	0.74	1.18	0	0.230
2057.9				MWT	3.51E-6[b]	*2.0E-9*[d]	8.34E-3	0.34	1.44	0	0.134
2150.9				WT	3.17E-8[b]	*6.8E-7*	8.58E-2	1.62[c]	1.17	0	0.155
2193.1		ATCU	Tl	VSS	1.43E-4[b]	*4.9E-3*	2.98E+0	0.87[c]	1.12	0	0.245
2195.6				SiS	3.34E-6[b]	*1.6E-7*[d]	4.81E-2	0.4	1.29	0	0.234
2206.2	CA	LCA3	Pz	B	1.31E-4[b]	*7.5E-3*	3.54E+0	1.31[c]	1.06	0	0.151
2251.1				matrix	8.88E-8	*1.2E-2*[f]	4.26E+0	0.22	1.28	0.010	0.053

a. Lithology suspect; alpha and Ksat similar to vitric or bedded tuff.

b. Ksat suspected too high; Ksat value is at least 3 times greater than Ksat based on RME#1 correlation with alpha using rigid wall data. Suggest using Ksat based on alpha correlation, unless standard error of alpha measurement is too high.

c. Standard error of alpha measurement is high; causes overestimation of alpha, overestimation of Ksat predicted by correlation with alpha, and greater uncertainty in ***n***.

d. Ksat values based on RME#1 correlation of alpha to rigid-wall Ksat data; recommended to avoid overestimation of Ksat from UE12t#1 flexible-wall Ksat data.

e. Lithology suspect; alpha, Ksat , and θ_s similar to NWT

f. Alpha for this carbonate rock sample is high relative to volcanic rocks.

Table 10.3 UE12t#1 Hydraulic property data with relation to HST model rock units distinguished by HGU, HSU, stratigraphy, lithology (NSTec, 2007) and alteration determined by XRD (Kwicklis et al., 2009) using terminology of NSTec (2007).

Depth (ft)	HGU	HSU	Strat	Lith	Alt	Ksat (cm/s)	Alpha (m^{-1})	Std	n	θr	θs
34.9	WTA	TM-WTA	Tmr	MWT	nr	*3.6E-5*[b]	4.17E-1	0.2	1.47	0	0.322
193.6				DWT		7.1E-7	1.06E-1	0.35	1.68	0.030	0.090
267.0						*error*	1.15E-3[a]	0.86	1.38	0	0.026
321.7	VTA	TM-LVTA	Tmr	PWT/ NWT	nr	*1.6E-5*[b]	3.01E-1	0.34	2.59	0.057	0.227
365.4						*2.5E-5*[b]	3.64E-1	0.32	2.48	0.045	0.301
391.5			post Tbg	BED/ RWT	GL	5.6E-4	1.84E+0	0.35	1.88	0.040	0.396
608.8						*3.7E-5*[b]	4.22E-1	0.08	2.45	0.031	0.464
736.0	WTA	BRA	Tbg	DWT /VIT	nr	*error*	7.62E-1[a]	1.24	1.14	0	0.023
790.0	VTA	LVTA1	Tbgb	BED	GL	*5.2E-5*[b]	4.87E-1	0.18	2.21	0.046	0.454
940.0	TCU	BRCU	Tn4	BED/ RWT	ZC	4.89E-5	3.73E-1	0.23	2.93	0.108	0.169
1030.2						3.71E-7	5.71E-2	0.27	1.30	0	0.263
1134					OP	9.96E-5	5.50E-1	0.13	1.76	0.076	0.310
1155					ZC	*2.7E-8*[b]	2.37E-2	0.26	1.49	0	0.381
1260.1			Tn3	BED/ RWT	ZC	*2.6E-9*[b]	9.22E-3	0.6	1.30	0	0.254
1376.2						*1.6E-9*[b]	7.60E-3	0.1	1.75	0	0.277
1463.0	WTA	TUBA	Tub	DWT	nr	*error*	9.65E-3[a]	1.52	1.50	0	0.039
1561.5	TCU	OSBCU	Ton2		ZC	*1.0E-8*[b]	1.58E-2	0.26	1.57	0	0.271
1651.3			Toy		AR	*3.6E-5*[b]	4.21E-1	0.45	1.25	0	0.342
1738.5					ZE	1.26E-7	3.03E-2	0.17	1.62	0	0.281
1851.4						5.44E-8	3.47E-2	0.16	1.44	0	0.328
1917.6			To	BED/ RWT	AR	1.41E-4	5.84E-1	0.4	1.27	0	0.229
1950.0						1.01E-4	5.54E-1	0.74	1.18	0	0.230
2057.9				PWT	AR	*2.0E-9*[b]	8.34E-3	0.34	1.44	0	0.134
2150.9				BED/ RWT	ZC	*error*	8.58E-2[a]	1.62	1.17	0	0.155
2193.1		ATCU	Tl	PCL	AR	*error*	2.98E+0[a]	0.87	1.12	0	0.245
2195.6						*1.6E-7*[b]	4.81E-2	0.4	1.29	0	0.234
2206.2	CA	LCA3	Pz	DM	AR	*error*	3.54E+0[a]	1.31	1.06	0	0.151
2251.1			Pz			8.88E-8	4.26E+0	0.22	1.28	0.010	0.053

a. Standard error of alpha measurement is high, which leads to overestimation of alpha and Ksat predicted by correlation with alpha and uncertainty in N.

b. Ksat values based on RME#1 correlation of alpha to rigid-wall Ksat data; recommended to avoid overestimation of Ksat from UE12t#1 flexible-wall Ksat data.

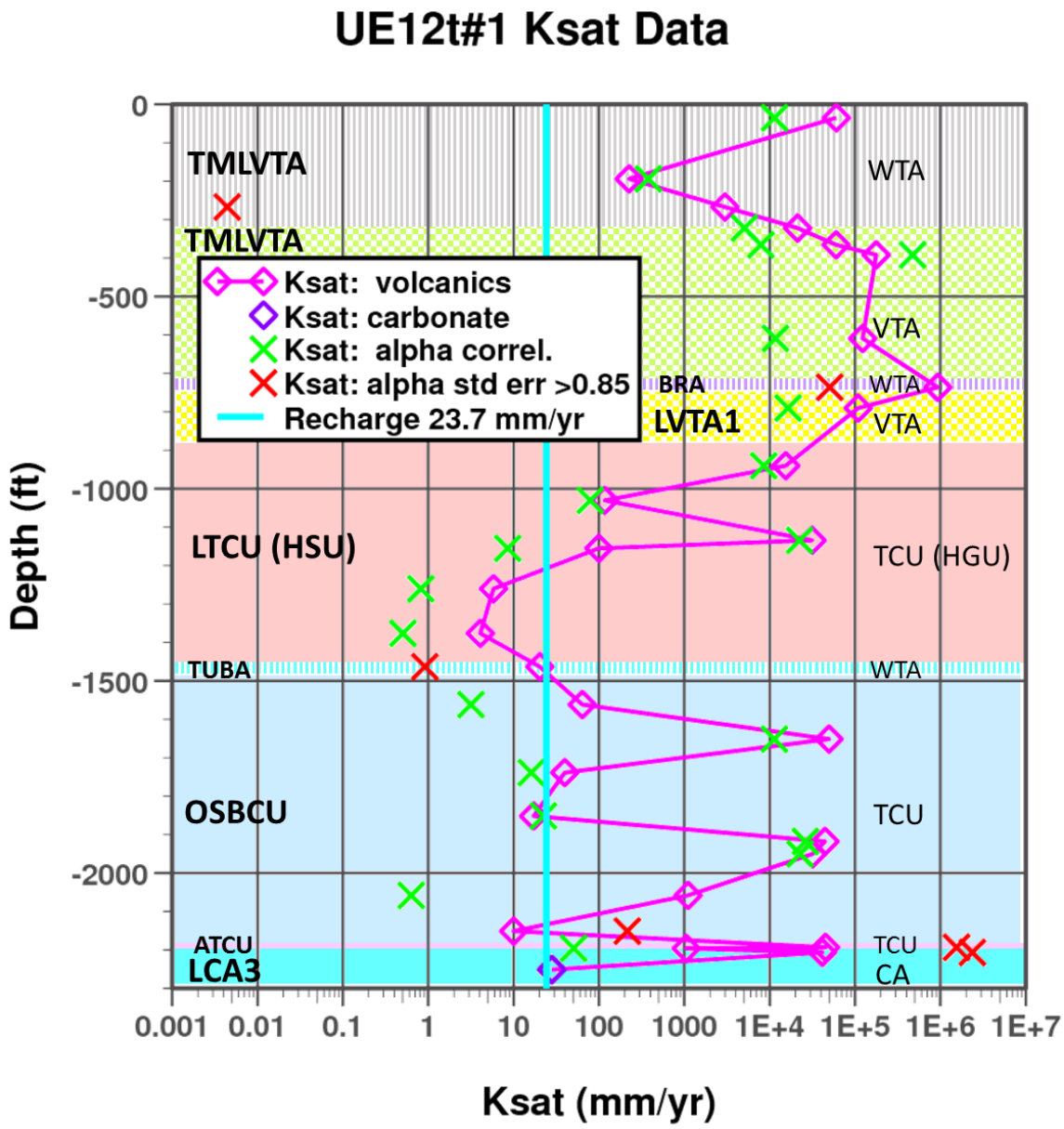

Figure 10.10 Comparison of Ksat determined by flexible-wall method (magenta) with alpha based Ksat (green) through correlation of RME#1 rigid-wall Ksat and alpha data. Red crosses are alpha-based Ksat with high standard error in Ksat. Alpha-based Ksat tends to be lower than flexible wall Ksat, suggesting flexible-wall Ksat data for UE12t#1 tends to overestimate Ksat. Unlike RME#1, alpha-based Ksat does not tend to be high relative to measured Ksat for alpha values with high standard error. Light blue vertical line represents estimate of recharge rate on Rainier Mesa (Russell, 1987). Depth ranges for HSUs and HGUs are color-coded.

10.6 Conclusions

- The Ksat-alpha correlation established from RME#1 rigid-wall Ksat data with consideration of standard error in alpha extends to all volcanic lithologies except vitrophyre and does not extend to carbonate rocks.
- Alpha values for "non-welded" (predominantly zeolitized ash-fall) tuffs are consistent between RME#1 and UE12t#1 (compare Figures 10.3 and 10.6).
- Alpha values for "welded" tuffs are consistent between RME#1 and UE12t#1 in units Tn3 and older (compare Figures 10.4 and 10.7).
- Some core described as "non-welded" tuffs (e.g. in Tn4 and To in UE12t#1) and "welded" tuffs (e.g. in TM-LVTA in UE12t#1) have properties similar to bedded or vitric tuffs (much higher K and alpha). This may be explained by differences in terminology between Kwicklis et al. (2008) and NSTec (2007).
- For non-welded (predominately zeolitized ash fall) tuffs, combined RME#1 and UE12t#1 data indicate Ksat ranges from 0.2 to 1000 mm/yr and alpha ranges from 0.005 to 0.20 m^{-1}. The RME#1 Ksat data suggest non-welded units such as Tn4, Tn3, Ton2 could be more tightly constrained in Ksat and alpha compared to bulk HSU properties.
- For welded tuffs in units Tn3 and older, combined RME#1 and UE12t#1 data indicate Ksat ranges from 0.2 to 3 mm/yr, and alpha ranges from 0.004 to 0.02 m^{-1}.
- For vitric, pumiceous, and sandstone tuffs of the TM-LVTA and LVTA1, an alpha range of 0.2 to 1.8 m^{-1} and a Ksat range of to 2,000 to 300,000 mm/yr are consistent between RME#1 and UE12t#1 data (see Figures 10.4 and 10.7). Based on two data, the LVTA1 could be constrained to an alpha range of 0.2 to 0.5 m^{-1} and a Ksat range of 2,000 to 10,000 mm/yr.
- Ksat data for argillic tuffs are over three orders of magnitude lower in RME#1 (less than 1 mm/yr) compared to UE12t#1 (greater than 1000 mm/yr). Interpretation of these data for application of model parameters can have a strong effect on modeled flow behavior in the perched zone (e.g., whether perching can occur, or whether vertical or lateral flow is dominant).
- Data for core from "vitrophyre" lithology is probably not representative of bulk matrix properties of aquifer units in HSUs (i.e. BRA, RVA).
- Correlation of alpha and Ksat at RME#1 indicates that the flexible-wall method tends to overestimate Ksat at UE12t#1 for some but not all data. For about half of the flexible-wall Ksat data, a typical overestimation is about 1 order of magnitude and is high as 3 orders of magnitude (see Figure 10.10).

10.7 Recommendations

- Use alpha parameter standard error estimates from the RETC van Genuchten model parameter inversion code (van Genuchten et al., 1991) to help identify suspect alpha

values. For example, some standard errors are greater than the alpha value, providing immediate insight that measurement error in alpha (and addition to Ksat) affects interpretation of correlation between Ksat and alpha.

- For model parameter estimation, such as establishing Ksat and van Genuchten property distributions or effective values, use only Ksat or alpha values with text colored in black or blue in Tables 10.1,10.2, and 10.3
- Where alpha-based Ksat is significantly lower (~3x) than flexible-wall Ksat at UE12t#1, use the alpha-based Ksat (highlighted in blue, Table 10.3). However, do not use an alpha-based Ksat for the six UE12t#1 data with high standard error in alpha (highlighted in red, Table 10.3).
- Do not combine "welded tuff" data for Tmr (TMWTA and TMLVTA) with older welded tuffs (BRA, TUBA, and RVA).
- Do not use "vitrophyre" data in establishing bulk BRA and RVA properties.
- Heterogeneities within TCUs can be attributed, in part, to contrasting properties for lithologic characteristics of ash-fall, (partially) welded, and bedded tuffs.

10.8 Implications of UE12t#1 Ksat Corrections for Flow and Transport and HST Modeling

A reduction of Ksat values based on alpha correlation of UE12t#1 data has implications for modeling perched conditions. Perching conditions require hydraulic conductivity below the recharge rate. A recharge rate of 23.7 mm/yr estimated by Russell (1987) and commonly used in flow and transport models at RM indicates that perching requires a layer with hydraulic conductivity less than 23.7 mm/yr or 7.6e-10 m/s. Comparing alpha-based and flexible-wall Ksat estimates, the alpha-based Ksat causes a majority of UE12t#1 Ksat estimates to fall below a 23.7 mm/yr (or 7.6e-10 m/s) threshold related to the recharge rate, whereas the majority of flexible-wall Ksat data are greater than 23.7 mm/yr (see Figure 10.9). Therefore, model permeability estimates based on UE12t#1 Ksat values including corrections derived from Ksat-alpha correlation are more likely to produce perching conditions in variably saturated flow models.

10.9 Revised Parameters for Stratigraphic Units

The matrix property data in Kwicklis et al. (2008) have been used extensively in HST and N and T-Tunnel flow and transport model development and could be used in SZ model development. However, unlike the CLEARWATER and WINESKIN HST models and the N-Tunnel flow and transport model, rock property units for the T-Tunnel flow and transport model are based on stratigraphic units. This section compiles the Ksat and van Genuchten parameter data and corrections with respect to stratigraphic units. In this section, revised mean matrix Ksat and van Genuchten parameter values for stratigraphic units are compiled as an alternative to values given in Kwicklis et al. (2008) to account for:

- Revised hydrostratigraphy and stratigraphy for RME#1 (NSTec, 2009)
- Consideration of dehydration effects on zeolite and smectite minerals (Appendix C)
- Greater accuracy of rigid-wall Ksat data compared to flexible wall Ksat data (see Appendix B)
- Consideration of standard error in parameters of the van Genuchten model (see Appendix B)
- Use of Ksat-alpha correlation to reduce some Ksat estimates derived from UE12t#1 flexible-wall Ksat data (See Appendix B).
- Addition of harmonic mean Ksat to estimate lower bound of vertical permeability (K_z) useful for investigating the range of possible vertical and lateral flow characteristics in the Tertiary volcanics.

10.9.1 Ksat

Using the same methods used in Appendix B and Section 3.4.1.3 for HSUs, Table 10.4 compares mean Ksat values in stratigraphic units derived from core data (Kwicklis et al., 2009) with revised Ksat values developed from the analysis in Appendix B. As for HSUs, revised Ksat parameter values for stratigraphic units include both geometric and harmonic mean to provide plausible ranges of effective matrix properties for lateral and vertical flow directions in anisotropic media such as the layered and bedded volcanic sequences on Rainier Mesa.

As for HSUs, differences relative to Kwicklis et al. (2008) in interpretation of the number of data (N) within each stratigraphic unit results from both: (1) differences in criteria for excluding data (see Appendix B), and (2) use of re-interpreted RME#1 stratigraphy (NSTec, 2009). Revised geometric mean Ksat values are generally reduced in stratigraphic units by accounting for effects of overestimation of Ksat by flexible-wall data from UE12t#1, but can also be raised as result of revised RME#1 stratigraphy (NSTec, 2009), as follows.

- Ksat in the Tmr unit is reduced by 72%.
- The composite “pre-Tmr, post-Tbg” stratigraphic unit results in averaged effective values for vitric tuffs spanning TM-LVTA, LVTA1, and LVTA2 hydrostratigraphic units.
- Revised Ksat for Tbg is representative of a matrix Ksat for welded tuff.
- Revised Ksat for Tbgb is representative of a vitric tuff.
- Ksat values for stratigraphic units predominately within zeolitized or argillic tuff or confining units – Tn4, Tn3, Tub, Ton2, Ton2, To, Tf, and Ttl - are reduced by 20 to 85%.
- The Tot unit spans both aquifer (RVA) and confining (LTCU1) units. Models using stratigraphic units for distributing properties (e.g., the T-Tunnel flow and transport

model) may need to extract data values appropriate to the corresponding hydrostratigraphic units.

Table 10.4 Mean Ksat parameter values for hydrostratigraphic units (HSUs) derived from Kwicklis et al. (2008) compared to mean values derived from rigid-wall data and correlation with alpha. "N" denotes number of data within stratigraphic unit included in mean calculations.

Strati-graphic Unit	Mean Ksat (Kwicklis et al., 2008)			Mean Ksat (using rigid-wall data and correlation with alpha)						
	N	(m^2)	(mm/yr)	N	(m^2)		(mm/yr)		(m/s)	
		Geom.	geom		Geom	harm	geom	harm	geom	harm
Tmr	4	3.72E-14	11,500	4	1.03E-14	2.66E-15	3,180	825	1.01E-7	2.61E-8
pre-Tmr	2	4.77e-13	147,500	5	7.41E-14	3.37E-14	22,900	10,400	7.27E-7	3.31E-7
Tp	1	1.06e-14	3,280							
Tpc	1	4.85e-14	15,000							
Tcbs	1	2.02e-13	62,400							
Tbg	2	2.79e-16	-	1	6.47E-18	6.47E-18	2.00	2.00	6.35E-11	6.35E-11
Tbgb	1	3.53e-13	109,000	2	1.93E-14	1.24E-14	5,990	3,850	1.90E-7	1.22E-7
Tn4	7	5.21e-16	161	8	2.95E-16	3.99E-17	91.4	12.3	2.90E-9	3.91E-10
Tn3	4	5.09e-18	1.57	5	1.51E-18	1.30E-18	0.466	0.403	1.48E-11	1.28E-11
Tub	2	6.20e-18	1.91	2	1.18E-18	9.37E-19	0.365	0.29	1.16E-11	9.19E-12
Ton2	3	3.14e-17	9.69	3	2.51E-17	1.94E-17	7.77	6.02	2.46E-10	1.91E-10
Toy	3	1.05e-15	-	6	1.88E-16	3.08E-17	58.1	9.54	1.84E-9	3.02E-10
Ton1	3	8.65e-17	26.7	2	1.32E-17	1.96E-18	4.09	0.606	1.30E-10	1.92E-11
Tor	5	1.59e-17	4.90	1	4.04E-15	4.04E-15	1,250	1,250	3.96E-8	3.96E-8
To	6	4.73e-16	146	6	1.20E-16	3.04E-18	37.3	0.940	1.18e-9	2.98E-11
Tot	0	-	-	7	1.22E-17	3.30E-18	3.78	1.02	1.20E-10	3.24E-11
Tf	3	2.37e-17	7.32	-	-	-	-	-	-	-
Ttl	5	6.86e-16	212	1	1.63e-16	1.63e-16	50.5	50.5	1.60E-9	1.60e-9
Pz	**1**	**9.08e-17**	**28.0**	**1**	**9.08E-17**	**9.08E-17**	**28.0**	**28.0**	**8.88E-10**	**8.88E-10**

As discussed in Appendix B, Section 10.4, the harmonic mean provides a lower bound to the effective or upscaled "block averaged" hydraulic conductivity or permeability. Considering that permeability is usually lower in the vertical (z) direction than the horizontal (x) direction, the ratio of the geometric to harmonic mean provides an estimate of the anisotropy ratio (K_x:K_z).

The anisotropy ratio in zeolitic or argillic tuff confining units, particularly the To and Ton1 stratigraphic units which occur extensively at the base of the Tertiary volcanic section, is pivotal in establishing whether groundwater perching can occur in the Tertiary volcanic section of Rainier Mesa. Revised Ksat values in the To and Ton1 stratigraphic units are 37.3 mm/yr and 4.09 mm/yr for the geometric mean and 0.940 and 0.606 mm/yr for the harmonic mean as compared to 146 and 26.7 mm/yr for the geometric mean values in Kwicklis et al. (2008). The revised To and Ton1 harmonic mean Ksats of 0.940 and 0.606 mm/yr can justify adjustment of anisotropy ratios (K_x:K_z) to enable perching to occur for a typical recharge rate of 24 mm/yr (Russell, 1987). All of the remaining stratigraphic units

that typically comprise zeolitized tuff confining units, including Tot, Ton2, Tub, Tn3, and Tn4, have revised harmonic mean Ksat values of 9.54 mm/yr or less, indicating these units can also potentially sustain perching conditions for typical recharge rates on Rainier Mesa.

10.9.2 Van Genuchten Parameters

Table 10.5 shows revised van Genuchten model parameters for stratigraphic units. As for HSUs, differences with respect to van Genuchten parameters in Kwicklis et al. (2008) result from combined effects of:

- Zeolite and smectite dehydration (Appendix C),
- Revised RME#1 stratigraphy (NSTec, 2009), and
- Criteria for removing erroneous data (Appendix B).

These differences in van Genuchten parameters will have secondary effects on flow compared to the differences in Ksat.

Table 10.5 Mean van Genuchten model parameter values for stratigraphic units including corrections for zeolite and smectite dehydration described in Appendix C.

HSU	alpha			n		m		Volumetric Water Content		
	N	geom		Arith	geom	arith	geom	N	Arith	
		(m-1)	(Pa-1)						Residual	Saturated
Tmr	4	0.264	2.69E-5	2.06	2	0.51	0.5	4	0.033	0.235
pre-Tmr post-Tbg	5	0.8	8.17E-5	2.16	1.43	0.54	0.3	5	0.041	0.388
Tbg	0	-	-	-	-	-	-	1	0	0.231
Tbgb	2	0.317	3.23E-5	2.38	2.37	0.58	0.58	2	0.065	0.411
Tn4	6	0.083	8.49E-6	1.67	1.59	0.4	0.37	8	0.023	0.269
Tn3	4	0.008	7.80E-7	1.55	1.54	0.36	0.35	5	0	0.261
Tub	0	-	-	-	-	-	-	2	0	0.252
Ton2	3	0.026	2.64E-6	1.56	1.54	0.36	0.35	3	0	0.265
Toy	6	0.043	4.43E-6	1.47	1.47	0.32	0.32	6	0	0.298
Ton1	1	0.022	2.23E-6	1.27	1.27	0.21	0.21	2	0	0.222
Tor	1	0.229	2.34E-5	1.45	1.45	0.31	0.31	1	0	0.268
To	5	0.065	6.62E-6	1.38	1.36	0.28	0.27	6	0	0.164
Tot	5	0.020	2.04E-6	1.52	1.51	0.34	0.34	7	0.002	0.190
Tl	1	0.048	4.91E-6	1.29	1.29	0.22	0.22	1	0	0.234
Pz	1	4.26	4.35E-4	1.28	1.28	0.22	0.22	1	0.01	0.053

10.10 References

Kwicklis, E., G. WoldeGabriel, and M. Sulley (2008), written communication: Analysis of core-scale hydrologic and mineralogic data from boreholes UE12t #1 and RME #1 at Rainier Mesa, Nevada National Security Site, Los Alamos National Laboratory, Los Alamos, NM.

NSTec (2007), A Hydrostratigraphic Model and Alternatives for the Groundwater Flow and Contaminant Transport Model of Corrective Action Unit 99: Rainier Mesa-Shoshone Mountain, Nye County, Nevada, DOE/NV/25946-146, National Security Technologies LLC, Las Vegas, NV.

NSTec (2009), Geology and Hydrogeology of Rainier Mesa Exploratory #1, Unpublished data dated April 16, 2009 by National Security Technologies, LLC, Las Vegas, NV.

Russell, C. E. (1987), Hydrogeologic Investigations of Flow in Fractured Tuffs, Rainier Mesa, Nevada National Security Site, Masters Thesis, University of Nevada, Las Vegas. 104 p.

Wen, X., and J.J. Gomez-Hernandez (1996), Upscaling Hydraulic Conductivity in Heterogeneous Porous Media: An Overview, Journal of Hydrology, v. 193, p. 9-32.

van Genuchten, M. Th. (1980), A closed-form equation for predicting the hydraulic conductivity of unsaturated soils, Soil Science Society of America Proceedings, 44(5), p. 892-898.

van Genuchten, M. Th., F.J. Leij, and S.R. Yates (1991), The RETC code for quantifying hydraulic functions of unsaturated soils, EPA/600/2-91-065, Robert S. Kerr Environmental Research Laboratory, Office of Research and Development, U.S. Environmental Protection Agency, Ada, OK.

Zavarin, M., W.W. McNab, S.F. Carle, D.E. Shumaker, C. Lu, Y. Sun, and G.A. Pawloski, Q. Hu, S.K. Roberts, and A.F.B. Tompson (2011), Hydrologic Source Term Processes and Models for Underground Nuclear Tests at Rainier Mesa and Shoshone Mountain, Nevada Test Site, LLNL-TR-483852-DRAFT, Lawrence Livermore National Laboratory, Livermore, CA.

11 Appendix C: Correction of Rock Property Data for Mineral Hydration Using XRD and Relative Humidity Box Data

11.1 Purpose

Methods for measurement of rock properties such as grain density, porosity, and water content do not necessarily consider the effects water molecules incorporated into the molecular structures of zeolite and smectite minerals. From a hydrological point of view, the structural water is immobilized and, therefore, is not "water content" to porous flow. From a mineralogy point of view, the structural water constitutes the "hydrated" portion of a hydrous mineral grain structure. The extent of hydration in zeolite and smectite minerals depends on temperature and humidity, with mineral hydration decreasing as temperature increases and mineral hydration increasing as humidity increases.

At the Nevada National Security Site (NNSS) and Yucca Mountain in southern Nevada, USA, massive, variably saturated zeolitized ash-fall tuffs typically contain on the order 50% zeolite. Argillic tuffs typically contain 20% or more smectite (up 64% in this study) and may also contain 10% to well over 50% zeolite by mass. Considering that hydrated zeolite and smectite minerals contain about 13% to 20% water molecules by mass, the mass fraction of structural water can easily constitute several percent total mineral mass.

The temperature and humidity dependence of zeolite and smectite hydration affects measurement of rock properties because the *in situ* rock and rock property measurement environments differ. Historically, different methods have been used to measure rock properties at the NNSS and Yucca Mountain. The various methods expose the rock samples to different ranges of temperature and humidity and, thus, impart variability in hydration of zeolite or smectite minerals. The hydration effects will cause variability in estimates of specific gravity or grain density, porosity, and water content depending on the testing method

The impact of hydration effects on rock property measurements has been recognized at Yucca Mountain in consideration for long term storage of nuclear waste and at NNSS for siting of locations for underground nuclear tests. For example, in a comparison of laboratory techniques in determining bulk properties of tuffaceous rocks from Yucca Mountain, Boyd et al. (1995) conclude:

Absolute values for the bulk properties of zeolitized tuff are immeasurable due to the complex nature of their dehydration behavior.

Martin et al (1993) pointed out the difficulties presented by zeolites in applying standard water and gas pycnometry techniques to rock property measurements:

Zeolites are capable of adsorbing liquid, vapors, and gases. This adsorptive capability presents a challenge to the physical properties measurement of rocks containing large zeolite fractions. Such errors are introduced in both water and gas pycnometry procedures. …These errors are magnified in calculating the degree of porosity and saturation from measured densities. For instance, if accurate measurements are made for as-received and dry bulk density, but with a grain density error of 10%, the resulting calculated gas-filled porosity could vary by as much as an order of magnitude. ["Gas-filled porosity" is the portion of the porosity not saturated with water.]

At NNSS, many underground nuclear tests were located in zeolitic ash fall tuffs including 56 of 61 underground nuclear tests on Rainier Mesa (Townsend, 2008; USDOE, 2015). This study focuses on rock properties for rock samples obtained from drill holes RME #1 and UE12t#1 on Rainier Mesa, NNSS (Kwicklis et al., 2008), which are being used to establish matrix hydraulic properties for various radionuclide transport models (this report; Kwicklis et al, 2007; Reeves, 2008a and b; Kwicklis et al., 2011; Zavarin et al., 2011; Navarro, 2017). These rock samples were evaluated by D.B. Stephens and Associates, Inc. using ASTM methods 854 for grain density, D7623-09 for porosity, and D2216 for gravimetric water content, and D6836-02 for volumetric water content and van Genuchten parameters (ASTM 2002, 2005, 2006, 2009). Importantly, these rock samples also include additional data useful for evaluating zeolite and smectite hydration:

- The analyses include a "relative humidity box" (RH box) measurement to establish "residual" water content.
- All but two samples were analyzed for mineral content using X-Ray Diffraction (XRD) methods.

This study confirms that the presence of smectite and zeolite minerals introduces error in grain density, porosity, and saturation measurement using standard ASTM methods without consideration of hydration and volume swelling effects. Importantly, either RH box or XRD measurements can be used to correct for zeolite and smectite hydration effects, yielding very similar results. This study's regression-based linear functions of hydration and smectite and zeolite content using RH box and XRD data yield estimates of water loss from heating and drying consistent with other studies. The XRD data provide means to verify that corrections using the more commonly available RH box data are accurate.

11.2 Background

Water may be bound in volcanic tuffs either physically or chemically within minerals. For example in Yucca Mountain tuffs, Vaniman et al. (2001) give weight percentages of water in minerals identified by XRD at standard measurement conditions either as [1] physically bound in glass (3%) and opal-CT(6%) or [2] chemically bound at saturated conditions in smectite (20%) and the zeolites clinoptilolite (16.6%) and mordenite (13.2%). It is widely

recognized that changes in humidity, temperature, and pressure affect the amount of bound water in smectite and zeolite.

11.2.1 Previous NNSS and Yucca Mountain Rock Property Studies

Zeolite hydration properties have long been recognized as affecting evaluation of grain density, porosity, and water content measurements at NNSS (Catalano, 1969; Knowlton and McKague, 1976; Knowlton et al, 1981; McKague et al, 1991; Martin et al., 1993) and Yucca Mountain (Kranz et al., 1989; Nelson and Anderson, 1992; Boyd et al., 1995; Bish et al., 2003). For Yucca Mountain rocks, the thermal and humidity dependency of mineral hydration has been studied for smectite by Bish (1988) and for zeolite by Wolfsberg et al., (1980), Bish (1993), and Carey and Bish (1996). Thermodynamic equilibrium models for zeolite have been derived by Carey and Bish (1996) and Wilkin and Barnes (1999).

At Rainier Mesa, NNSS, thousands of rock property data generated for characterization of underground nuclear test sites and analog site testing for Yucca Mountain over decades by different entities including private contractors (TerraTek, Holmes & Narver Inc., Nevada Testing Labs Ltd., D.B. Stephens & Associates, Inc.), government agencies (U.S. Army Waterways Experimentation Station and the U.S. Geological Survey), and National Laboratories (Lawrence Livermore, Los Alamos, and Sandia). Grain density, porosity, and water content measurements have been evaluated using several different techniques dating back to the late 1950s (e.g., Diment et al., 1958; Diment et al., 1959; Byers, 1962; Ege et al., 1980; Moss and Haseman, 1983; McKague et al., 1991; Martin et al., 1993; Kwicklis et al, 2008).

In hydrological modeling studies, porosity data are needed for model parameterization. If the modeling studies include unsaturated conditions, additional model parameters and calibration information may rely on saturation data derived from water content, porosity, and grain density data. If the rocks include smectite and zeolite minerals, additional understanding will be needed about the porosity, grain density, and water content measurement techniques and the effects of mineral hydration. For example, prior to detonation of the first underground nuclear "RAINIER", a nonsensical saturation range of 95% to 138% was estimated for altered tuffs in the "Tos7c" stratigraphic unit (Diment et al., 1959). However, by accounting for smectite and zeolite hydration using correction approaches derived from this study, the resulting saturation range is 77% to 93% (Zavarin et al., 2011), which is more realistic considering the RAINIER test location was located in unsaturated conditions about 150 m above the local shallow water table (Thordarson, 1965).

11.2.2 Importance of LANL Data Set

The rock property data set from Rainier Mesa examined in this study was obtained from Los Alamos National Laboratory (LANL), with measurements taken and physical properties

determined by D.B. Stephens & Associates, Inc. (Kwicklis et. al., 2008). These data are particularly important to ongoing radionuclide transport studies at Rainier Mesa for several reasons:

1. The core were obtained from two drill holes in two key areas – N-Tunnel and T-Tunnel – over a vertical extent that spans the entire Tertiary volcanic section. Importantly, ongoing models of radionuclide transport are focused on the entire Tertiary volcanic section, and two of four modeling efforts are focused on the N and T-Tunnel areas (Kwicklis, 2007; Kwicklis et al., 2011; Reeves, 2008a and b). Most previous rock property data from Rainier Mesa were obtained from near-horizontal tunnels and are, therefore, clustered within a small fraction of the entire vertical volcanic section.
2. In addition to measurements of the physical properties of particle density, dry bulk density, wet bulk density, porosity, and saturation, the measurements by D.B. Stephens & Associates, Inc. also include moisture content as a function of pressure head used to derive van Genuchten parameters for modeling pressure and hydraulic conductivity as function of saturation (van Genuchten, 1980; van Genuchten et al., 1991). Van Genuchten model parameters are needed for the various unsaturated flow modeling efforts at Rainier Mesa.
3. X-ray Diffraction (XRD) measurements were obtained on most of the same core segments used to measure physical properties, providing mineral composition including mass fraction of zeolite and smectite. The availability of mineral composition data enables analysis of the effects of smectite and zeolite hydration on measurement of physical properties using standard methods of the American Society of Testing and Materials (ASTM).

11.2.3 Hydrated Zeolite and Smectite

Total water content measured in rocks may include three components:

- Mobile water in the connected pore structure.
- Immobile water physically bound in “dead-end” or enclosed pores.
- Structural water either adsorbed or incorporated into mineral structures.

This study is focused on effects “structural water” – water that is chemically bonded to mineral structures - on physical property measurements.

Zeolite minerals are hydrated aluminosilicates with a unique open molecular framework created by interconnecting tetrahedrons of silicon and aluminum atoms bounded to four oxygen atoms (Martin et al., 1993). The openings within the framework contain cations (e.g., Ca^{+2}, Na^{+1}, K^{+1}, and Mg^{+2}) and molecules of H_2O as structural water.

Smectites are swelling clays that incorporate water into an interlayered mineral framework. The crystallographic position and the density of the interlayer water varies with water content (Bish, 1988; Richards, and Bouazza, 2007).

11.2.4 ASTM Methods

The hydration effects of structural water in zeolites and smectites are not considered in several ASTM methods used to characterize variably saturated rocks, particularly the ASTM 854 method used to determine grain or particle density (ASTM, 2006) and the ASTM 2216 method to determine moisture content (ASTM, 2005). Subsequent calculation of moisture retention by the ASTM D6836-2 method (ASTM, 2002) and porosity by the ASTM D7623 method is also affected by hydration effects and the results of using the ASTM 2216 and ASTM 854 methods.

11.2.4.1 ASTM 854

The ASTM 854 method uses water pycnometry to measure specific gravity of solid material, which involves drying of the solid followed by water immersion of the solid. Difficulty with using water pycnometry to produce accurate measurements of grain density in zeolitic tuff has been known since there early 1960s (Dickey and Monk, 1963). The specific gravity measurement is used in conjunction with water density and dry bulk density measurements to derive particle density and porosity estimates. Specific gravity is defined by the ratio of solid to water density or mass within a fixed volume (V):

$$G_S = \left(\frac{M_S}{M_{W(T)}} \right)_V \qquad (11.1)$$

where:

M_S = mass of dry solid in volume V.

$M_{W(T)}$ = mass of water at temperature T in volume V.

In water pycnometry, two mass measurements are made in addition to M_S with the intention to determine the mass of water displaced by the solid volume of M_S.

- $\{M_P + M_{W(T)}\}$ = the mass of the pycnometer including the portion of water, $M_{W(T)}$, that will be displaced by the solid.
- $\{M_S + M_P\}$= mass of the solid and mass of the pycnometer (includes the portion of water not displaced by the solid).

$M_{W(T)}$ is determined by keeping the water level in the vessel the same in both measurements (before and after immersion of M_S). The grain density is calculated by

subtracting out the mass of the pycnometer vessel (M_P) from the two measurements of the mass of the pycnometer vessel with and without the solid.

$$G_S = \frac{\{M_S\}}{\{M_S\}+\{M_P + M_{W(T)}\}-\{M_S + M_P\}} = \left(\frac{M_S}{M_{W(T)}}\right)_V \tag{11.2}$$

In ASTM 854, the specific gravity measurement operates under two main assumptions that do not consider mineral hydration/dehydration processes:

- The solid sample is dried by oven heating to 105 °C.
- The volume of the water displaced by an *oven dried* solid sample immersed in water is assumed equivalent to the volume of the solid.

Hydrous minerals such as zeolite and smectite will not honor these two assumptions implicit to the ASTM 854 method because:

- Oven heating to 105 °C releases water adsorbed or incorporated into zeolite and smectite minerals (McKague et al., 1975; McKague et al., 1982; Martin et al., 1993). The hydrous component of water in these minerals is, in effect, erroneously treated by the ASTM 854 method as mobile water from the pore structure.
- Oven-dried zeolite and smectite minerals will rehydrate upon immersion in water (Martin et al., 1991; Martin et al., 1993). The rehydration processes for zeolite and smectite minerals structure are erroneously ignored by ASTM 854 in estimation of the volume of water displaced by mineral grains. During rehydration, zeolite and smectite minerals adsorb and incorporate water into the mineral structure, thereby decreasing the volume of water displacement. Additionally, smectite swells from rehydration, increasing the volume of water displacement.

Following ASTM 854, the particle density or density of the solid material, ρ_S, is related to the grain density by

$$\rho_S = \rho_{W(T)} G_S \tag{11.3}$$

where $\rho_{W(T)}$ is the density of water at the measurement temperature *T*.

11.2.4.2 ASTM D2216

The ASTM method D2216 determines the ratio of the mass of water to the mass of solid, often referred to as moisture content by mass, w_M, from

$$w_M = \frac{\{M_M + M_C\}-\{M_D + M_C\}}{\{M_D + M_C\}-\{M_C\}} = \frac{M_M - M_D}{M_D} \tag{11.4}$$

where:

M_M = mass of moist sample

M_D = mass of dried sample

M_C = mass of container

Notably, the ASTM method D2216 specifies that "a standard temperature of $110 \pm 5^{\circ}C$ is used to determine these masses." However, the mass of hydrous components of zeolite and smectite minerals will not stay constant between the different temperature and humidity conditions of the *in situ* rocks and an oven setting of $110 \pm 5^{\circ}C$.

11.2.4.3ASTM D6836-02

ASTM D6836-02 includes five methods (A, B, C, D, and E) to determine soil water moisture and pressure characteristic curves. The five methods enable determination of moisture content at different suction pressure ranges. The results from different methods can be combined for fitting of a mathematical function to the soil water characteristic curve data (van Genuchten, 1980) using, for example, the RETC code (van Genuchten et al., 1991).

In application to volcanic rock samples at Rainier Mesa, the analysis for moisture content given in Kwicklis et al. (2008) applied a combination of three ASTM D6836-02 methods performed by D.B. Stephens and Associates, Inc.:

- Hanging column
- Pressure plate
- Thermocouple psychometry (dewpoint potentiometer).

Water retention curves are typically plotted as functions of pressure head and volumetric moisture content.

In ASTM D6836-02, development of saturation-dependent models for permeability and capillary pressure, involves conversion of gravimetric water content θ_M of a moist sample to volumetric water content by

$$\theta_M = \frac{\rho_B}{\rho_w} w_M \qquad (11.5)$$

where

ρ_B = bulk density

ρ_w = density of water

The bulk density is determined by

$$\rho_B = \frac{M_S}{V_B} \qquad (11.6)$$

where

M_S = mass of solid (including structural water)

V_B = bulk volume

11.2.4.4 ASTM D7623-09

ASTM D7623-09 relates porosity, ϕ, to sample volume, V, dry solid mass, M_S, and particle density, ρ_S, by

$$\phi = \frac{V - \frac{M_S}{\rho_S}}{V} \qquad (11.7)$$

where ρ_S is determined using ASTM 854 using Equation (11.3).

11.2.5 Relative Humidity Box

In addition to ASTM D6836 methods, D.B. Stephens and Associates, Inc. included measurements of moisture content given in Kwicklis et al. (2008) using the "relative humidity box" or vapor equilibration method to determine moisture content at high matric potential (Karathanasis and Hajek, 1982). The relative humidity (RH) box data are indicative of the difference in moisture content between "oven dried" conditions and conditions of room temperature with RH=1. The relative humidity box data help establish "residual saturation" assumed for the van Genuchten (1980) soil water characteristic function. This study considers use of the RH box measurement to correct for the effects of mineral hydration on rock property measurements.

11.3 Methods for Correcting for Swelling and Mineral Hydration

11.3.1 Swelling

Volume swelling of altered tuffs is known to be affected by saturation and the state of hydration as affected by humidity, temperature, and pressure. Carr et al. (1975) recognized presence of smectite as a swelling clay within tuffaceous rocks at NNSS. Ege et al. (1980) identified swelling clays in the U12n.03 drift of N-Tunnel, Rainier Mesa, NNSS. At Yucca Mountain, Kranz et al. (1989) and Blacic (1993) investigate long term swelling

affects in zeolitized tuffs undergoing dehydration and rehydration at elevated temperatures and confining pressures (up to 55 MPa). For argillized and zeolitized nonwelded tuffs, Salve and Oldenberg (2001) determined that swelling of smectite is the likely cause of decline of fault permeability in a transient, in situ flow experiments at Yucca Mountain. However, these prior works on rocks similar to zeolitized and argillized tuffs at Rainier Mesa do not analyze effects of swelling associated with ASTM rock property measurement techniques.

In analysis of kaolinite/smectite mixtures, Likos and Lu (2006) analyze volume change in smectite as a function of humidity, showing volumetric change as high as 102 percent for a case of 100% smectite. Therefore, the volume of sample containing smectite is expected to increase between the time after oven drying at 105 °C and the subsequent two steps of (1) humidification by the RH Box measurement and (2) re-saturation during suction pressure-moisture content testing. A swelling effect is evident if measurement of volumetric moisture content at saturated conditions exceeds the measurement of total porosity. If the volume of the sample is only measured prior to either humidification or re-saturation and not after re-saturation, the clay swelling effects are not factored in.

The RME#1 and UE12t #1 data show some evidence for swelling effects in comparison of porosity and volumetric water content at saturated conditions:

- Volumetric water content at saturated conditions exceeds porosity for nearly two thirds (22 of 38) of data in the altered tuffs.
- The amount which volumetric water content exceeds porosity at saturation conditions trends greater with increasing smectite content.

For the sample containing the greatest smectite content (64%), the ASTM methods produce a volumetric moisture content of 44.6% at saturated conditions compared to a porosity of 26.9%, indicating an unrealistically high saturation of 166%. For the sample with the next highest smectite content (34%), the ASTM methods produce a volumetric moisture content of 31.5% and a porosity of 23.0%, indicating a saturation of 137%.

A simple correction approach is implemented for clay swelling, assuming sample volume changes between the states of "as-received" (or oven-dried) and "saturated" conditions. Discrepancy between volumetric water content and porosity is attributed to swelling of the sample volume upon reaching saturated conditions. A change in sample bulk volume in going to a hydrated state, $\Delta V_{B,H}$, is assumed linearly related to smectite content using the sample with 64% smectite content as a single calibration point, yielding

$$\Delta V_{B,H} = 0.28 \chi_{Sm} \qquad (11.8)$$

where χ_{Sm} is the mass fraction of smectite as given from data in Kwicklis et al. (2008). Figure 11.1 compares smectite mass fraction with the difference between saturated volumetric moisture content and porosity for two cases (1) with no swelling considered, and (2) using Equation (11.8) as a volume correction factor for swelling. With the correction factor, the saturated volumetric moisture content is more realistically near or below the porosity, such that the corrected volumetric content minus porosity is more near or below zero. Alternatively, it would be advisable to re-measure sample volume after re-saturation. In any case, the correction factor used here is only a simple empirical model applied to the data examined in this report.

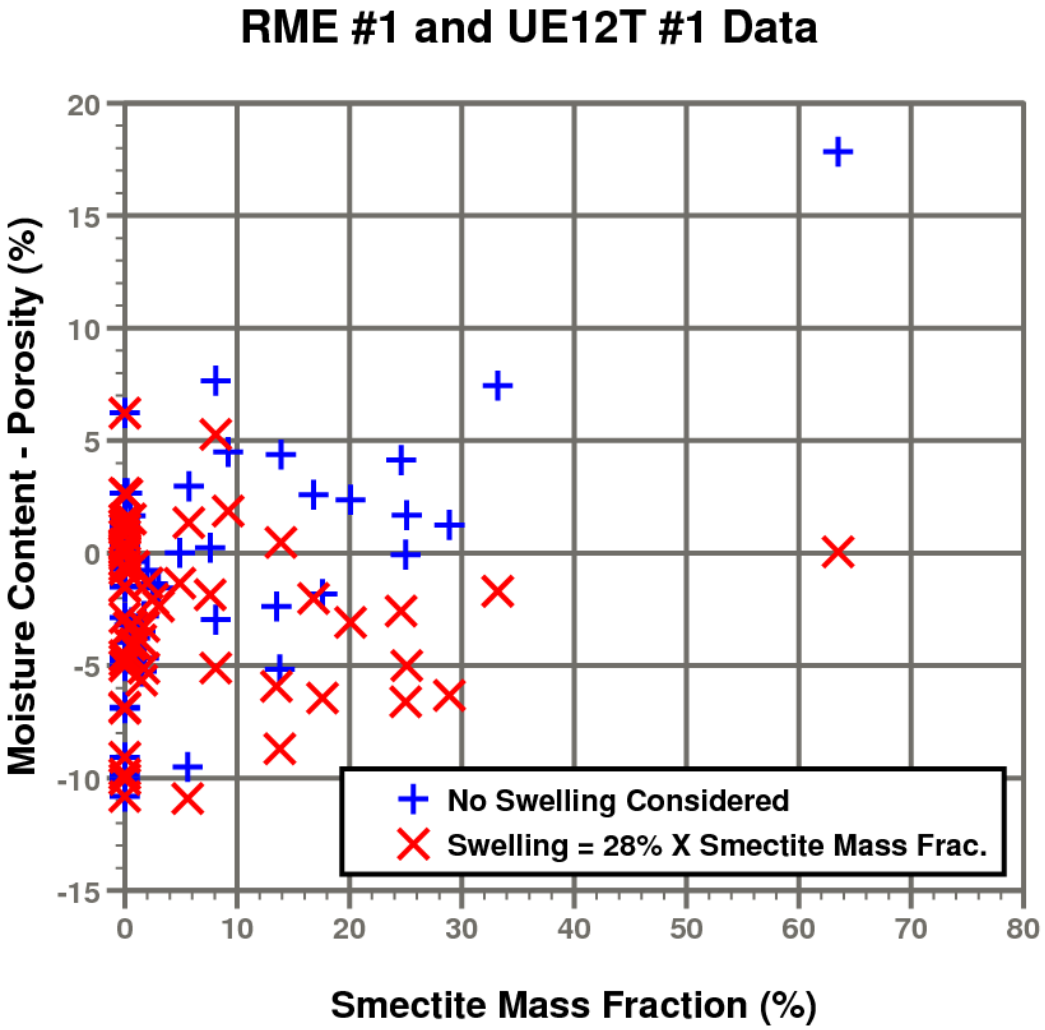

Figure 11.1 Comparison of smectite mass fraction to difference between volumetric moisture content and porosity for two cases (1) with no swelling effect considered, and (2) adding a volume swelling correction factor proportional to smectite mass fraction.

11.3.2 Use of XRD Data to Determine Grain Density

Quantitative X-ray diffraction (XRD) methods yield the mass fraction of minerals in the solid material (Chipera and Bish, 1989; Chipera and Bish, 2002). XRD data combined with individual mineral grain densities can be used to estimate and XRD- derived solid grain density ρ_{XRD} as follows:

$$\rho_{XRD} = \frac{\sum_{i}^{N} X_{i,XRD}}{\sum_{i}^{N} \frac{X_{i,XRD}}{\rho_i}} \qquad (11.9)$$

where:

$X_{i,XRD}$ = mass fraction of mineral *i*, determined by XRD

ρ_i = grain density of mineral *i*.

Kwicklis et al. (2008) provide XRD data for samples from Rainier Mesa, NNSS. Nelson and Anderson (1992) provide mineral grain density values. We use these XRD data and mineral grain density values to calculate XRD-derived grain density. Differences in grain density derived by XRD and ASTM 845 directly relate to the fraction of structural water removed from an oven-dried sample.

11.3.3 Use of RH Box Data

The relative humidity (RH) box measures the change in mass of a sample before and after being exposed to specified water vapor pressure and temperature. An RH box measurement obtained from an oven-dried sample increases in mass largely due to hydration of smectite and zeolite. If RH box conditions are set to a vapor pressure corresponding to a relative humidity of 1.0 at the *in situ* rock temperature, the RH box measurement approximates the difference in water content between *in situ* and oven-dried conditions. This difference in water content is closely related to the fraction of structural water removed from an oven-dried sample, as occurs for the ASTM 845 and ASTM D2216 methods.

Karathanasis and Hajek (1982) used RH box measurements to infer the quantity of smectite from the mass of water vapor incorporated into rock samples. This implies RH Box data can be used to infer the quantity of water vapor adsorbed and incorporated into both smectite and zeolite minerals in volcanic tuffs. Comparison of RH box measurements

to XRD measurements of smectite and zeolite mass fractions provides direct means to determine how well RH box measurements can quantify water contained in hydrous minerals.

11.3.4 Corrections to ASTM Methods

11.3.4.1 Specific Gravity from ASTM 854

The water pycnometry technique used in ASTM 854 will not produce accurate specific gravity or grain density measurements if the mineral solid includes hydrous minerals such as smectite or zeolite. To correct inaccuracies resulting from hydrous minerals, Equation (11.1) must be modified to account for the mass of water adsorbed and incorporated into the hydrous minerals by adding this hydrous mass to the solid mass (in numerator) and the mass of water displaced by the solid (in denominator):

$$G_S = \frac{M_{S,D} + \Delta M_H}{M_{W(T)} + \Delta M_H} \qquad (11.10)$$

where ΔM_H is the change in mass of water adsorbed or incorporated into hydrous minerals relative to $M_{S,D}$, the oven-dried mass measurement. ΔM_H can be estimated from either XRD or RH box data as described below.

11.3.4.2 Gravimetric Water Content from ASTM D2216

To account for hydrous minerals in determination of gravimetric water content, w_M, of a moist solid sample of mass $M_{S,M}$, Equation(11.4) is modified to

$$w_M = \frac{M_{S,M} - \left(M_{S,D} + \Delta M_H\right)}{M_{S,D} + \Delta M_H}$$

where ΔM_H is the mass of structural water adsorbed into hydrous minerals relative to the oven-dried state of the $M_{S,D}$ measurement. Again, ΔM_H can be estimated from either XRD or RH box data.

11.3.4.3 Volumetric Water Content from ASTM D6836

Considering hydrous minerals and swelling, Equation (11.6) for bulk density is modified relative to an oven-dried state by

$$\rho_B = \frac{M_{S,D} + \Delta M_H}{V_{B,D} + \Delta V_{B,H}}$$

where $V_{B,D}$ is the volume at oven dried (or as received) conditions, and $\Delta V_{B,H}$ is the change in bulk volume between the volume at oven dried conditions (or as received conditions) and hydrated conditions. Equation (11.5) for conversion of gravimetric to volumetric water content is modified to correct for hydrous minerals and swelling by

$$\theta_M = \frac{M_M - \left(M_{S,D} + \Delta M_H\right)}{\rho_w \left(V_{B,D} + \Delta V_{B,H}\right)}$$

11.3.4.4 Porosity from ASTM D7263-09

To address mineral hydration and swelling effects, the porosity calculation from Equation (11.7) is modified by

$$\phi = \frac{V_{B,D} + \Delta V_{B,H} - \dfrac{M_{S,D} + \Delta M_H}{\rho_{W(T)} G_S}}{V_{B,D} + \Delta V_{B,H}} \qquad (11.11)$$

where G_S is determined from Equation (11.10).

11.3.5 Mineral Hydration Correction Model

The correction for mineral hydration and dehydration developed in this study uses a linear model in which the mass fraction of the hydrous component of the rock, $X_{H,mineral}$, depends on smectite (*Sm*) and zeolite (*Ze*) mineral mass fractions determined by XRD:

$$X_{H,\mathrm{mineral}} = aX_{Sm} + bX_{Ze} + c\left(1 - X_{Sm} - X_{Ze}\right) \qquad (11.12)$$

where *a*, *b*, and *c* are coefficients and X_{Sm} and X_{Ze} are the mass fractions of smectite and zeolite as determined by XRD. The "*c*" coefficient represents a positive background value to account for hydration of non-smectite and non-zeolite minerals.

11.3.5.1 Use of XRD Data for Smectite and Zeolite

XRD data provide estimates of X_{Sm} and X_{Ze} and mass fractions for other minerals. Figures 11.2 and 11.3 show the XRD smectite and zeolite content for the RME#1 and UE12t#1 data in units of mass fraction. The zeolite and smectite abundance data from RME#1 and UE12t#1 reveal important aspects of the vertical profiles of hydrostratigraphic and hydrogeologic units (HSUs and HGUs) at Rainier Mesa (NSTec, 2007). These include location of the upper level of pervasive zeolitization at the top of LTCU and increased clay content within deeper horizons of the tuff confining units (TCUs), particularly within the OSBCU and ATCU HSUs. The wide variability in smectite and zeolite content with depth at

Rainier Mesa highlights the need to account for mineral hydration and dehydration effects in measurement of grain density, porosity, and water content.

The model change in mass for the mineral hydration correction inferred from smectite and zeolite content, $\Delta M_{H,\min eral}$, is calculated relative to the dry solid mass, $M_{S,D}$ by

$$\Delta M_{H,\min eral} = M_{S,D} \frac{X_{H,\min eral}}{1 - X_{H,\min eral}} \tag{11.13}$$

where model-predicted values of $X_{H,mineral}$ are derived from Equation (11.12). $\Delta M_{H,\min eral}$ derived from Equation (11.13) is used in estimation of grain density based on modified ASTM 854 formula for grain density (Equation 11.8) based on estimates of ΔM_H from smectite and zeolite content only (Equation 11.13):

$$G_{S,\min eral} \cong \frac{M_{S,D} + \Delta M_{H,\min eral}}{M_{W(T)} + \Delta M_{H,\min eral}} \tag{11.14}$$

For the mineral hydration correction model based on smectite and zeolite content, the coefficients *a*, *b*, and *c* in Equation (11.12) are estimated by non-linear regression using a model independent parameter estimation code (Doherty, 2008) with the objective to minimize the root-mean-squared difference of grain density derived from XRD data (Equation 11.9) and the modified ASTM 854 formula (Equation 11.14) with hydration correction (Equation 11.13).

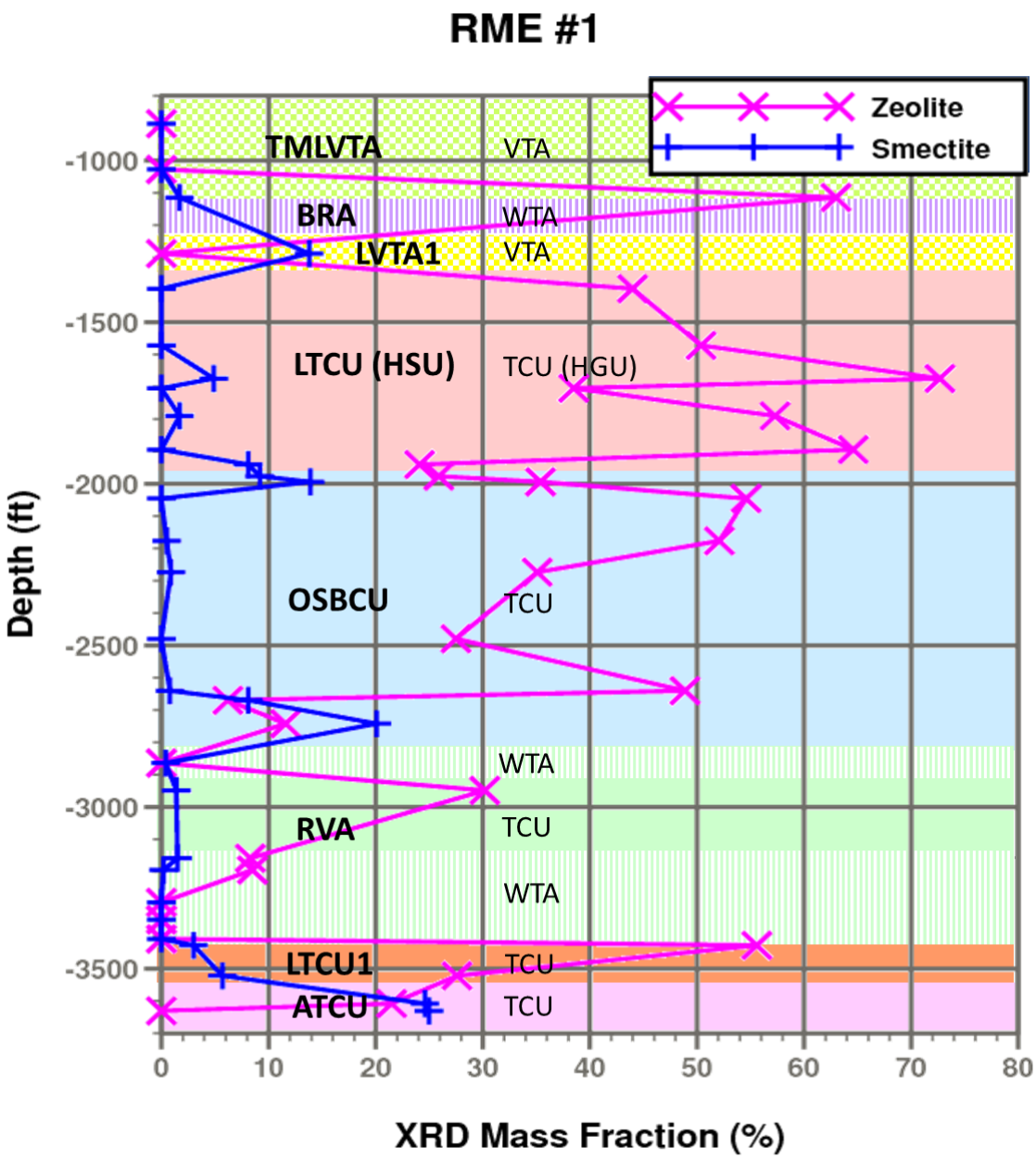

Figure 11.2 Smectite and zeolite XRD mass fraction data for drill hole RME#1.

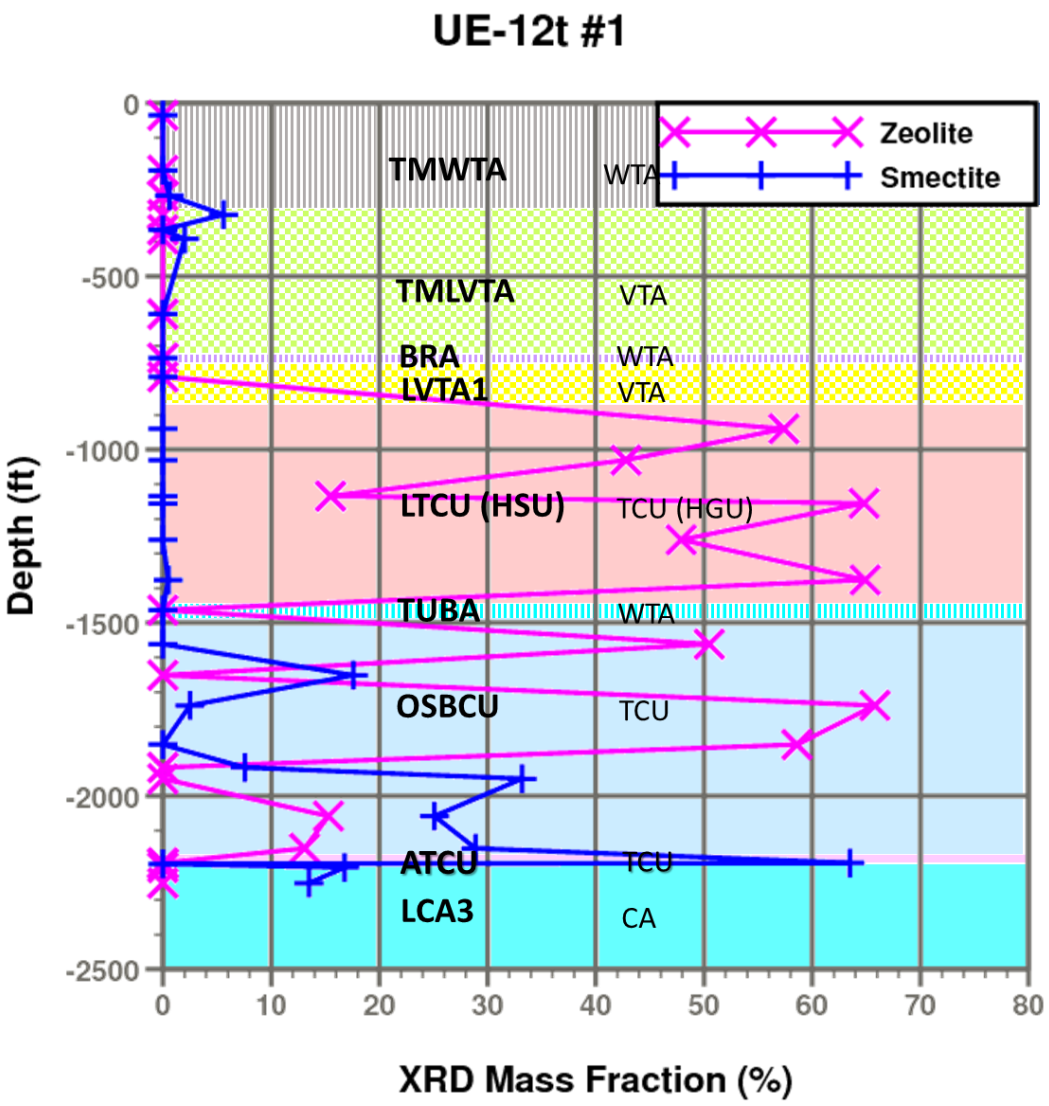

Figure 11.3 Smectite and zeolite XRD mass fraction data for drill hole UE-12t#1.

11.3.5.2 Use of RH Box Data

RH box data measure the change in mass of water adsorbed or incorporated onto the mineral structure between oven dried conditions and room temperature at 1.0 humidity. The RH box data may be presented either as a change in mass, $\Delta M_{H,RH}$, or in terms of a change in volumetric water content, $\Delta\theta_{RH}$ irrespective of whether the water is mobile or not. If the RH box data are given in units of volumetric water content, $\Delta M_{H,RH}$ is determined from

$$\Delta M_{H,RH} = \frac{\Delta\theta_{RH} M_{W(T)}}{1-\Delta\theta_{RH}} \tag{11.15}$$

where $M_{W(T)}$ is the measured mass of water at temperature T in the volume V of the solid sample. Based on RH box data, $\Delta M_{H,RH}$ from Equation (11.15) is used to estimate ΔM_H and grain density using the modified ASTM 854 formula (Equation 11.10):

$$G_{S,RH} = \frac{M_S + \Delta M_{H,RH}}{M_{W(T)} + \Delta M_{H,RH}} \tag{11.16}$$

The RH box data can be used to estimate the coefficients for the linear smectite-zeolite mineral hydration correction model (Equation 11.12) by setting the objective function to minimize the root-mean-squared difference between modeled grain density and grain density including corrections from RH Box data (Equation 11.16).

11.4 Results

The results for correcting for effects of zeolite and smectite hydration on measurement of grain density, porosity, and water content of rocks from Rainier Mesa, NNSS, Nevada, using ASTM methods are summarized here. Comparison of results of applying the hydration model and to grain density, porosity, and water content measurements focuses on comparison of values obtained from the ASTM standard methods with measurements derived from XRD data, RH box data, and ASTM values corrected for dehydration and rehydration. The results show that XRD mineral, RH box, and corrected ASTM measurements are consistent with each other and collectively different from measurements derived directly from the ASTM method.

Non-linear regression results using three data sets yielded similar results for the linear hydration model (Equation 11.8):

1. XRD mineralogic content data only:
   $X_{H,\mathrm{mineral}} = (12.6\% \pm 2.2\%)X_{Sm} + (5.5\% \pm 1.0\%)X_{Ze} + (0.6\% \pm 0.8\%)(1 - X_{Sm} - X_{Ze})$
2. RH Box data only:
   $X_{H,RH} = (10.5\% \pm 1.5\%)X_{Sm} + (5.5\% \pm 0.7\%)X_{Ze} + (0.4\% \pm 0.3\%)(1 - X_{Sm} - X_{Ze})$
3. Combined mineralogic and RH Box data:
   $X_{H,\mathrm{mineral+RH}} = (10.6\% \pm 1.1\%)X_{Sm} + (5.5\% \pm 0.5\%)X_{Ze} + (0.4\% \pm 0.2\%)(1 - X_{Sm} - X_{Ze})$

Uncertainties in the regression coefficients overlap mean values using all three data sets. The model derived from combined XRD mineral and RH Box data is used for subsequent values labeled as “corrected.”

Properties data labeled as “RH Box” use the raw RH Box values to estimate a composite hydration correction for grain density (Equations 11.14 and 11.15). This enables comparison to a situation where only RH box data are available with no mineral content

data such as XRD, similar to the approach of Karanthanasis and Hajek (1982) for estimation of smectite content directly from RH box data.

In comparison of ASTM with corrected grain density, porosity, and water content measurements, the following terms are used to label the different measurement results:

- "XRD" estimates particle density from mineral grain densities and XRD mass fractions.
- "ASTM" derives all measurements from ASTM methods as described in Section 11.2.4.
- "Corrected" assumes a mineral hydration correction model $X_{H,\mathrm{min}eral+RH} = 10.6\% X_{Sm} + 5.5\% X_{Ze} + 0.4\%(1 - X_{Sm} - X_{Ze})$ based on the composite XRD and RH box data.
- "RH Box" uses the raw relative humidity box measurement value to estimate mineral mass gained by rehydration from a "dry" state.

11.4.1 Particle Density

Figures 11.4 and 11.5 compare particle density measurement results for RME#1 and UE12t#1 data. The ASTM 854 method measurements of particle density are consistently higher compared to the other measurements where zeolite or smectite content is high (see Figures 11.2 and 11.3). Within the zeolitized ash fall tuffs, particle densities determined from XRD, corrected, and RH Box data average particle densities average 0.120, 0.119, and 0.088 g/cm^3 or 4.8%, 4.5%, and 3.5% less, respectively, that the ASTM values. For zeolitic rocks at Yucca Mountain, similar discrepancies are seen for grain density determined gravimetrically with heating to a dry state as compared to XRD (Nelson and Anderson, 1992).

Figure 11.6 compares particle density derived from XRD data with the other values obtained from (1) ASTM 854 directly, (2) ASTM 854 corrected for smectite and zeolite content, and (3) ASTM 854 corrected using relative humidity (RH) box data. The ASTM values without corrections are consistently higher than particle densities determined directly from XRD data. The corrected particle densities using smectite and zeolite content or RH box data show more consistency with the XRD data.

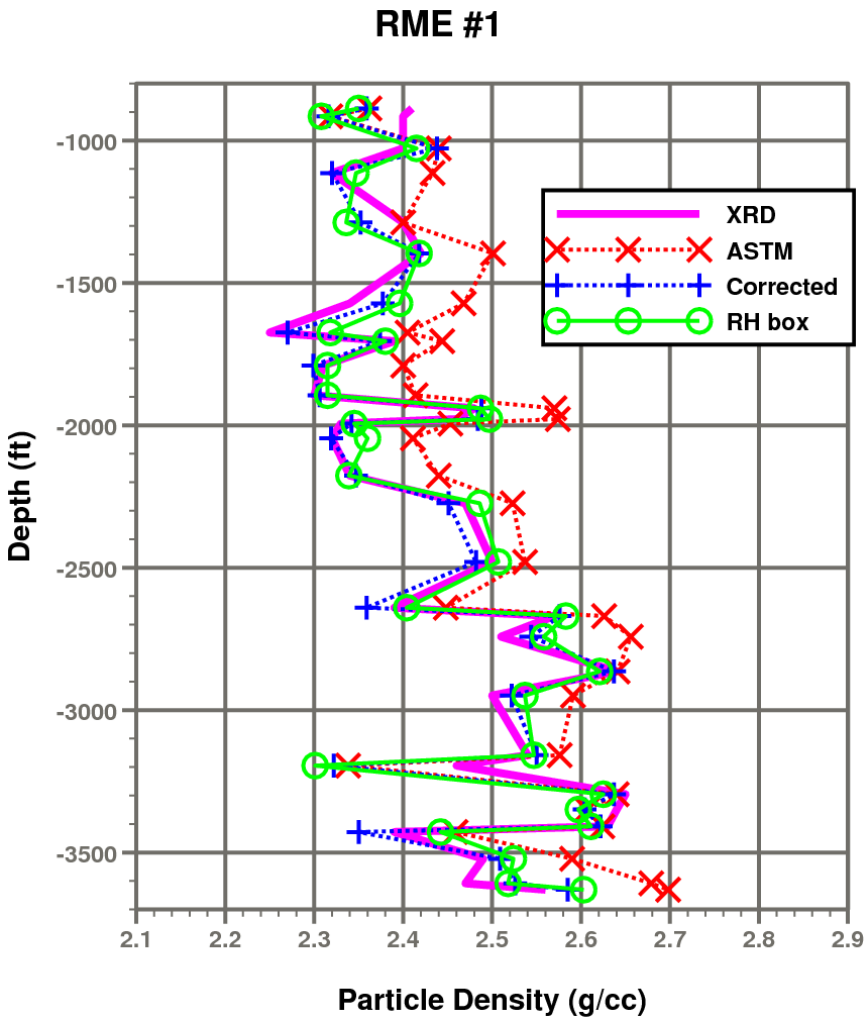

Figure 11.4 RME#1 particle density derived from XRD, ASTM, ASTM corrected for hydration (corrected), and RH box measurements.

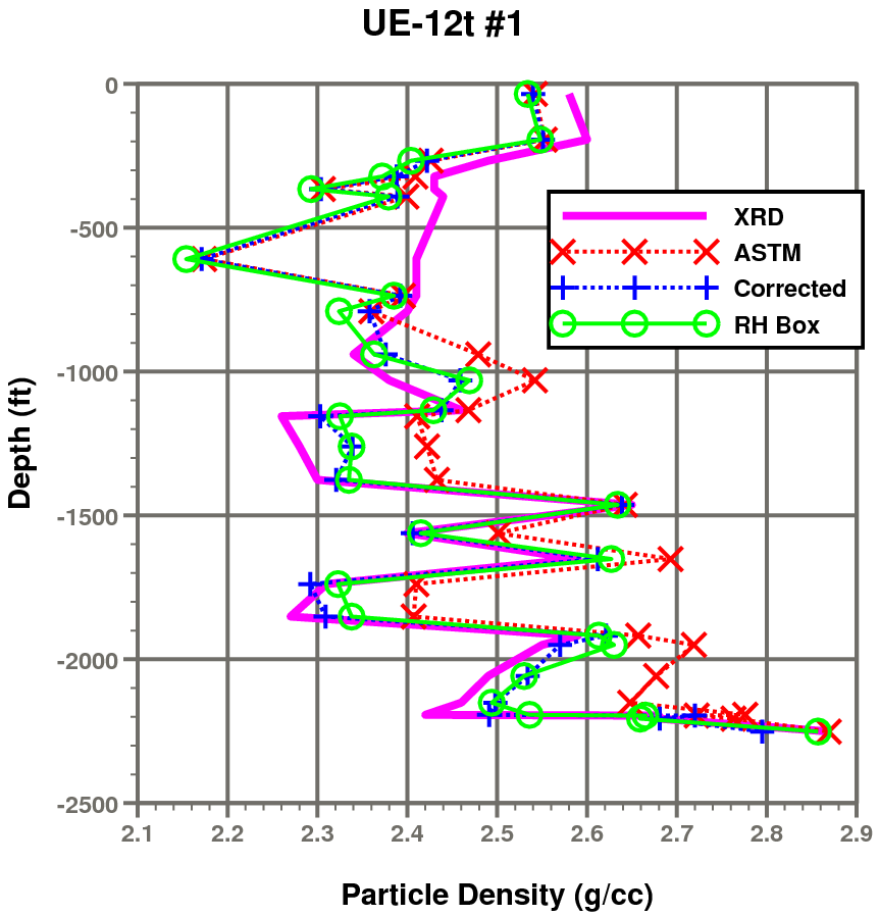

Figure 11.5 UE-12t #1 particle density derived from XRD, ASTM, ASTM corrected for hydration (corrected), and RH box measurements.

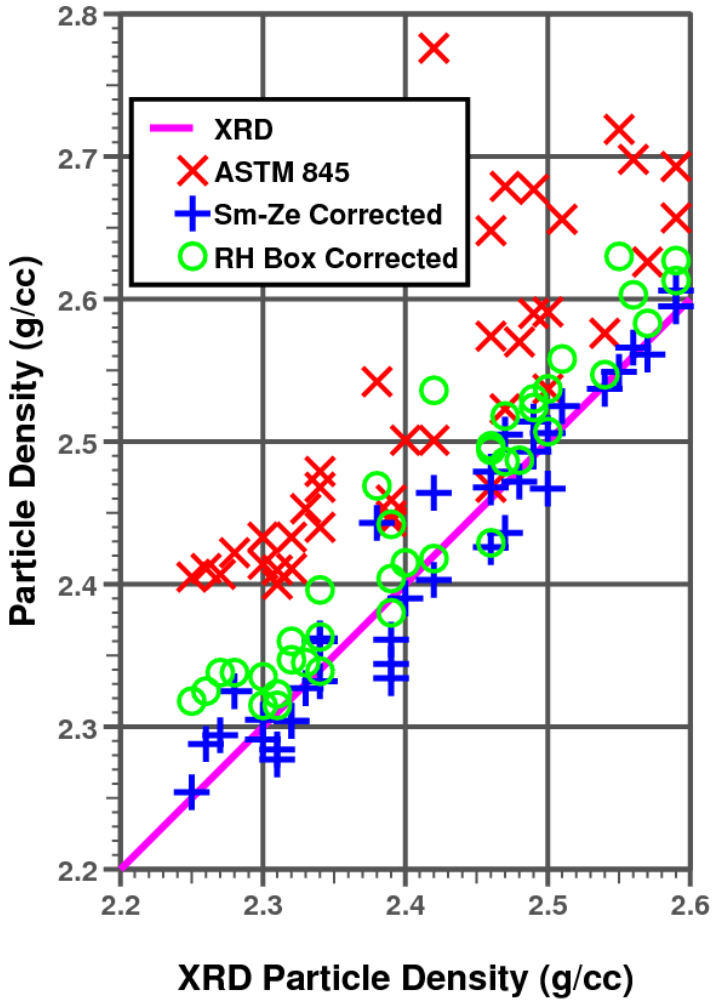

Figure 11.6 Comparison particle density derived from XRD data with values obtained from ASTM method, ASTM corrected for smectite and zeolite content, and ASTM corrected using relative humidity (RH) box data.

11.4.2 Porosity

Porosity, ϕ, defined here refers to "total porosity" or the total volume of voids per unit bulk volume of the rock. Since the ASTM methods use an oven dry value for both bulk and particle density, an error propagates into the ASTM porosity estimate. Porosity values given in Kwicklis et al. (2008) are calculated from Equation (11.5) of ASTM D7623-9, while corrected and RH Box porosity values are calculated from Equation (11.11) with consideration of mineral hydration.

Figures 11.7 and 11.8 compare the ASTM and corrected porosity estimates for RME#1 and UE-12t#1 data. The dehydration corrections generally reduce porosity estimates by 5% or less. While a 5% correction may seem small, the correction can easily represent 15% of the pore space. Improved accuracy of porosity estimates become important for estimating water and gas saturation, particularly for gas saturation where water content is high, such as in zeolitized and argillized tuffs at Rainier Mesa (Thordarson, 1965; Carroll, 1990; Townsend, 2008).

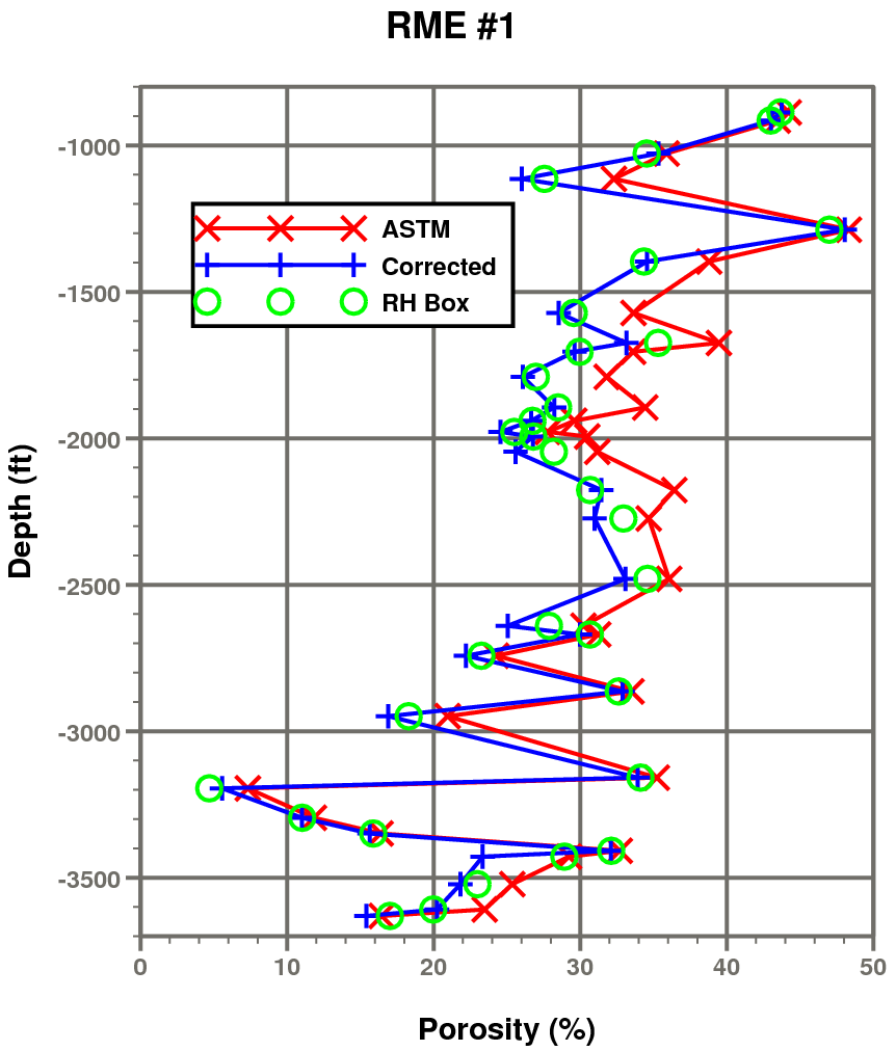

Figure 11.7 Comparison of ASTM and hydration corrected porosity measurements for RME#1 data.

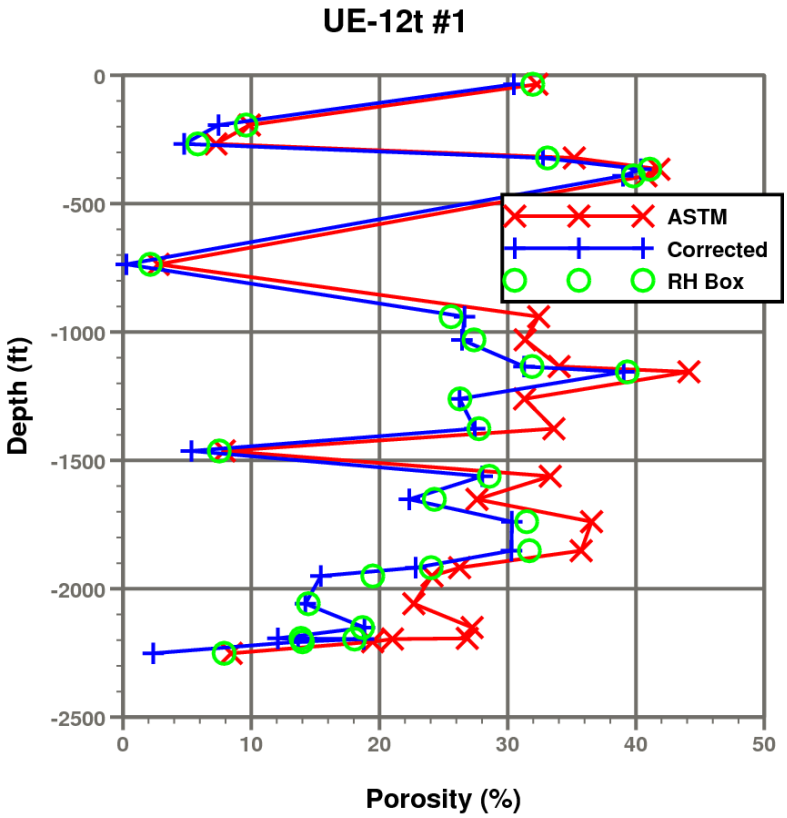

Figure 11.8 Comparison of ASTM and hydration corrected porosity measurements for UE12t#1 data.

11.4.3 Volumetric Moisture Content

Smectite and zeolite hydration and swelling effects cause volumetric moisture content to be overestimated by ASTM methods. Figures 11.9 and 11.10 compare volumetric moisture content derived from ASTM and ASTM corrected for hydration by XRD smectite and zeolite (corrected) and RH Box measurements and swelling using Equation (11.6). The water contents corrected by XRD or RH Box measurements are consistent, whereas the ASTM method produces higher values in zeolitized or argillized zones.

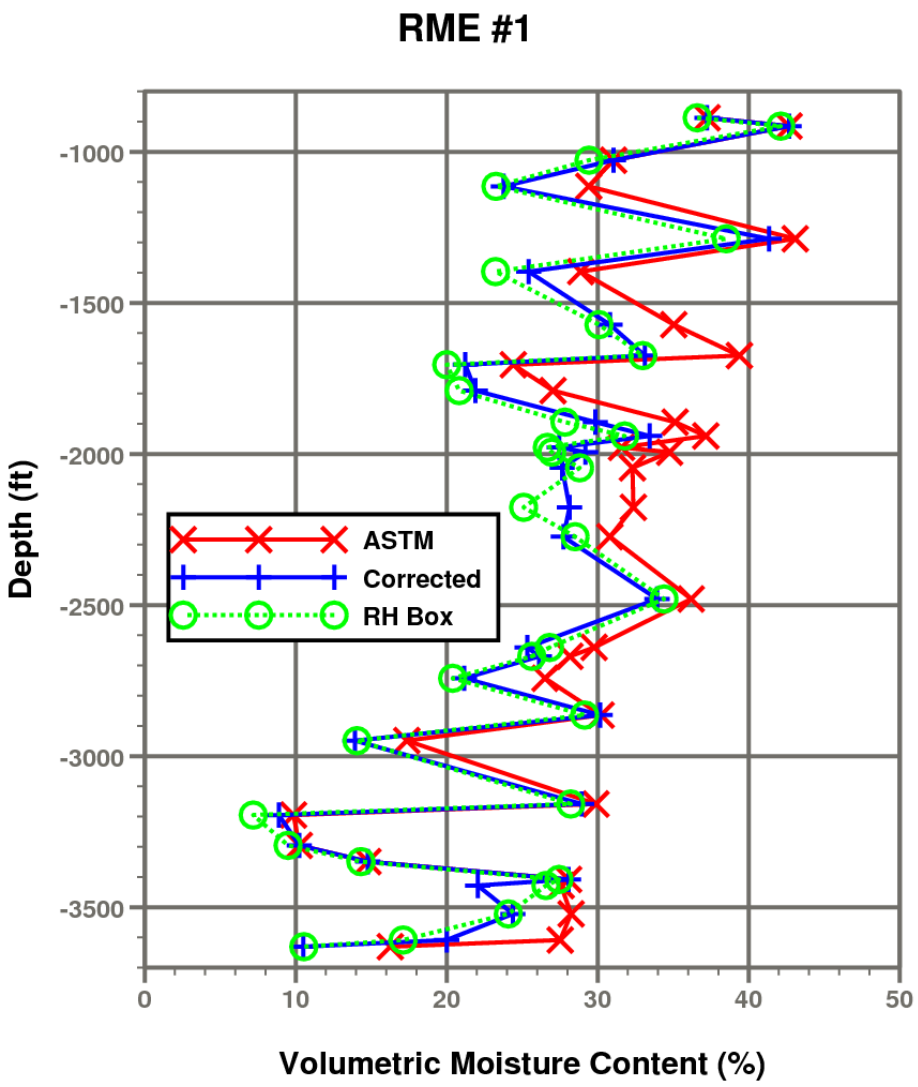

Figure 11.9 Comparison of volumetric moisture content derived from ASTM and ASTM corrected for hydration by XRD smectite and zeolite (corrected) and RH-Box measurements for RME#1 data.

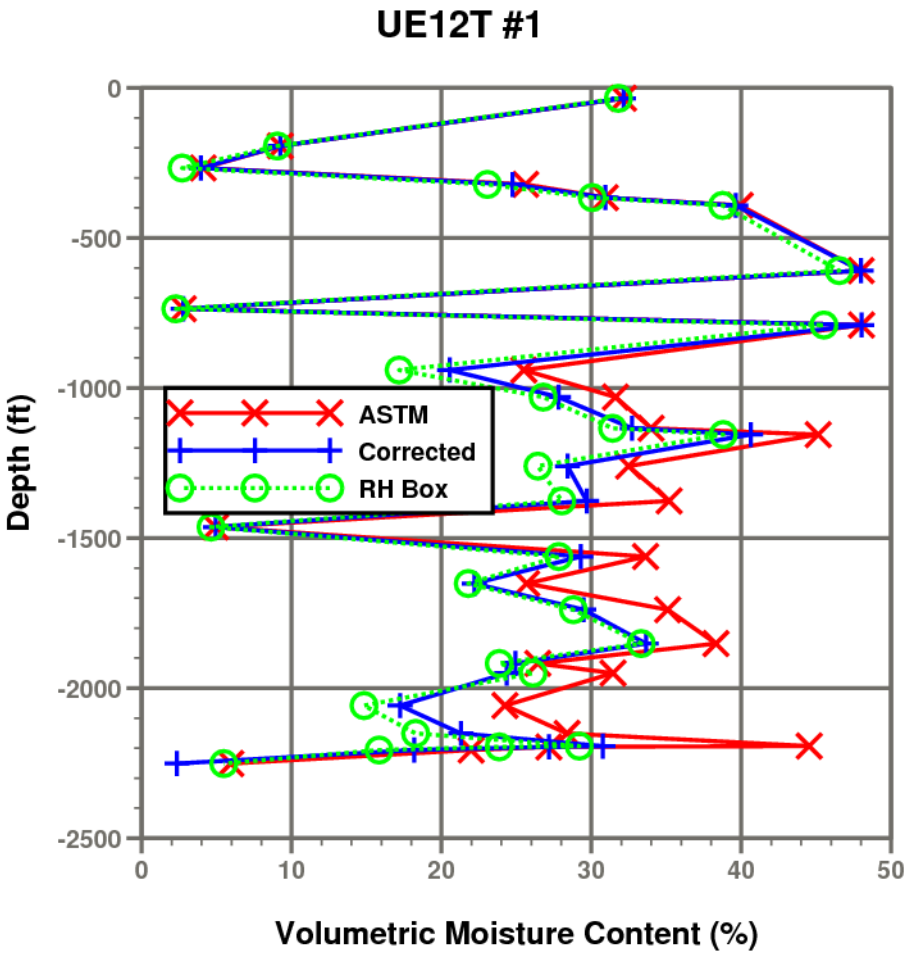

Figure 11.10 Comparison of volumetric moisture content derived from ASTM and ASTM corrected for hydration by XRD smectite and zeolite (corrected) and RH-Box measurements for RME#1 data.

As discussed in Sections 11.3.1 and 11.3.4.3, volumetric swelling associated with hydration of smectite can affect the sample bulk volume measurement in used calculation in the volumetric moisture content. If the bulk volume measurement of the sample was obtained from a dehydrated state, subsequent comparison of measurement of volumetric moisture content at a saturated state with porosity can reveal inconsistencies indicating saturation well over 100%. Realistically, volumetric moisture content at saturated conditions should be less than or equal to porosity, considering that a portion of the porosity can be unavailable to mobile water. Other measurement errors can contribute to saturation calculations over 100%, but swelling effects are likely to have a larger impact if smectite content is high.

Using the XRD data in Kwicklis et al. (2008), Equation (11.11) accounts for effects of mineral hydration and swelling on porosity by using grain density calculation directly from mineral content using Equation (11.9) with corrections for effects of clay swelling on sample volume from Equation (11.8) and hydrated mineral mass from Equation (11.12). This porosity estimate calculated with corrections from XRD data is expected to be more accurate than porosity calculated without such corrections. Accordingly, volumetric moisture content at the saturated state should be similar or less than porosity. Improved accuracy in volumetric moisture content measurement should be evident by values of volumetric moisture content at saturated conditions that are near or less than porosity.

For 38 samples within intervals of the zeolitized and argillized tuffs, Figure 11.11 compares porosity calculated with XRD corrections to volumetric moisture content at saturated conditions for three calculations:

1. Use of ASTM 854 as derived from Equation (11.5)
2. Corrected volumetric water content accounting for mineral hydration using the clay swelling model (Equation 11.8) and the smectite-zeolite linear hydration model (Equation 11.12)
3. Corrected volumetric water content accounting for mineral hydration using the clay swelling model (Equation 11.8) and RH box data to determine hydrated mineral mass.

The comparison in Figure 11.11 illustrates how strict use of ASTM 854 leads to frequent overestimation of volumetric water content. Incorporation of corrections based on either XRD or RH Box data in combination with recognition of clay swelling effects produces more realistic and accurate volumetric water content estimates.

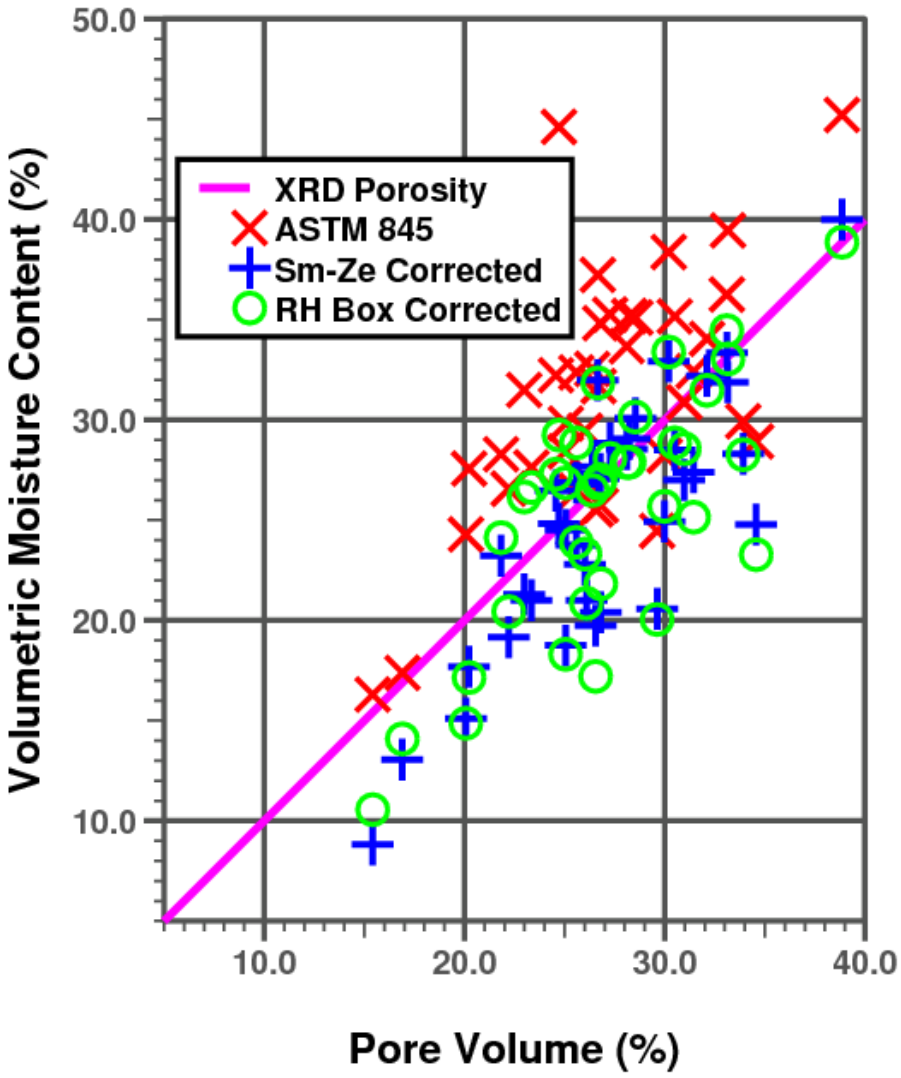

Figure 11.11 Comparison of pore volume derived from XRD porosity corrections with volumetric moisture content at saturated conditions derived from ASTM 854 and corrections using the smectite-zeolite hydration model and RH Box data combined with the clay swelling model.

11.5 Conclusions

- Users of grain density, porosity, and water content data or other properties derived thereof should be aware that smectite and zeolite minerals will affect common methods used to calculate density, porosity, and water content.

- ASTM methods can underestimate dry bulk density and overestimate particle density, porosity, and *mobile* water content because of zeolite and smectite dehydration.

- ASTM calculations of rock properties can be corrected for effects of zeolite and smectite if XRD or RH box data are available.
- Many radionuclide transport pathways at NNSS and Yucca Mountain are situated in zeolitized and argillic tuffs and, therefore, transport model parameters relying on rock property data can be affected by the methods used to calculate density, porosity, and water content.
- It is possible to correct for mineral hydration/dehydration effects on rock property measurements of grain density, porosity, and water content by using either data for mineralogic content , particularly zeolite and smectite, or the "Relative Humidity Box" measurement used to measure "residual" water content.

11.6 References

ASTM (2002), D 6836-02 Standard Test Methods for Determination of the Soil Water Characteristic Curve for Desorption Using a Hanging Column, Pressure Extractor, Chilled Mirror Hygrometer, and/or Centrifuge, American Society for Testing and Materials.

ASTM (2005), D 2216-05 Standard Test Methods for Laboratory Determination of Water (Moisture) Content of Soil and Rock by Mass, Test Method D 2216, American Society for Testing and Materials.

ASTM (2006), D 854-06 Standard Test Methods for Specific Gravity of Soil Solids by Water Pycnometer, American Society for Testing and Materials.

ASTM (2009), D 7263-09 Standard Test Methods for Laboratory Determination of Density (Unit Weight) of Soil Specimens, American Society for Testing and Materials.

Bish, D. L. (1988), Smectite Dehydration and Stability: Applications to Radioactive Waste Isolation at Yucca Mountain, Nevada, LA—11023-MS, Los Alamos National Laboratory, Los Alamos, NM.

Bish, D. L. (1993), Thermal Behavior of Natural Zeolites, LA-UR 93-2881 and Conf-9306100—5, Los Alamos National Laboratory, Los Alamos, NM.

Bish, D.L., D.T. Vaniman, S.J. Chipera, and W.J. Carey (2003), The distribution of zeolites and their effects on the performance of a nuclear waste repository at Yucca Mountain, Nevada, U.S.A., American Mineralogist, v. 88, p. 1889-1902.

Blacic, J. D. (1993), Hydration Swelling Effects on Time-Dependent Deformation of Zeolitized Tuff, Journal of Geophysical Research, v. 98, n. B9, p. 15,909-15,917.

Boyd, P. J., R.J. Martin, and R.H. Price (1994), An Experimental Comparison of Laboratory Techniques in Determining Bulk Properties of Tuffaceous Rocks, Sand92-0119, Sandia National Laboratories, Albuquerque, NM.

Byers, F. M., Jr. (1962), Porosity, density, and water content data on tuff of the Oak Spring Formation from the U12e tunnel system, Nevada Test Site, Nye County, Nevada.

Carey, W. J., and D.L. Bish (1996), Equilibrium in the clinoptilolite-H2O system, American Mineralogist, v. 81, p. 952-962.

Carr, W. J., C.H. Miller, and H.W. Dodge (1975), Geology, physical properties, and surface effects at Discus Thrower Site, Yucca Flat, Nevada Test Site, TID—26912.

Carroll, R. D. (1990), Electrical Logging and Electrical Properties of Rocks in Rainier Mesa Area, Nevada National Security Site, Nevada, Open-File Report 90-31, U.S. Geological Survey.

Catalano, E. (1969), Comments on Some of the Physical Chemical Questions Associated with the Analysis of Water in Earth Materials, UCRL-50630, Lawrence Radiation Laboratory, Livermore, CA.

Chipera, S. J., and D.L. Bish (1989), Quantitative X-Ray Diffraction Analyses of Samples Used for Sorption Studies by the Isotope and Nuclear Chemistry Division, LA—11669-MS, Los Alamos National Laboratory, Los Alamos, NM.

Chipera, S. J., J.W. Carey, and D.L. Bish (1997), Controlled-Humidity XRD Analyses: Application to the Study of Smectite Expansion/Contraction, Advances in X Ray Analysis, Issue 39, p. 713-72.

Chipera, S. J., and D.L. Bish (2002), FULLPAT: a full-pattern quantitative analysis program for X-ray powder diffraction using measured and calculated patterns, Journal of Applied Crystallography, v. 35, p. 744-749

Dickey, D. D., and E.F. Monk (1963), Determining Density and Porosity of Tuff Containing Zeolites, Geological Survey Professional Paper 475-B, p. B169-B170, U.S. Geological Survey, Washington, D.C.

Diment, W. H., R.E. Wilcox, G.V. Keller, E. Dobrovolny, F.C. Kraceck, J.C. Roller, L. Peselnick, E.C. Robertson, A.H. Lachenbruch, and C.M. Bunker (1958), Properties of Oak Spring Formation in Area 12 at the Nevada Test Site, Open-File Report 59033, U.S. Gelogocial Survey,

Diment, W. H., V. R. Wilmarth, R. E. Wilcox, A. Clebsch, G. E. Manger, C. C. Hawley, G. V. Keller, E. C. Robertson, L. Peselnick, C. M. Bunker, D. L. Healey, M. F. Kane, E. F. Roth,

S. W. Stewart, J. C. Roller, W. H. Jackson, H. W. Oliver, P. E. Byerly and D. R. Mabey (1959), Geologic Effects of the Rainier Underground Nuclear Explosion, Trace Element Investigation Report 355, United States Geological Survey.

Doherty, J. (2008), PEST, Model Independent Parameter Estimation—User manual (5th ed.): Brisbane, Australia, Watermark Numerical Computing, accessed October 1, 2009, at *http://www.pesthomepage.org/Downloads.php*.

Ege, J. R., R.D. Carroll, J.E. Magner, and D.R. Cunningham (1980), U.S. Geological Survey Investigations in the U12n.03 Drift, Rainier Mesa, Area 12, Nevada Test Site, Open-File Report 80-1074, U.S. Geological Survey.

Karanthanasis, A. D., and B.F. Hajek (1982), Quantitative Evaluation of Water Adsorption on Soil Clays, Soil Sci. Soc. Am. J., v. 46, p. 1321-1325.

Knowlton, G. D., and H.L. McKague (1976), A Study of the Water Content in Zeolitic Tuffs from the Nevada Test Site, UCRL-78013, Lawrence Livermore Laboratory, Livermore, CA.

Knowlton, G. D., T.R. White, and H.L. McKague (1981), Thermal Study of Types of Water Associated with Clinoptilolite, Clays and Minerals, v. 29, n. 5, p. 403-411.

Kranz, R. L., D.L. Bish, and J.E. Blacic (1989), Hydration and Dehydration of Zeolitic Tuff from Yucca Mountain, Nevada, Geophysical Research Letters, v. 16, n. 10, p. 1113-1116.

Kwicklis, E. (2007), oral and written communication: Unsaturated Flow and Transport Models for the U12n Tunnel complex, presented at Rainier Mesa/Shoshone Mountain flow and transport modeling Pre-emptive review, September 21, 2007.

Kwicklis, E., H. Viswanathan, Z. Dai, D. Levitt, and Z. Lu (2011), oral and written communication: Flow and Transport Model for the N-Tunnel Complex, Rainier Mesa, NNSS, presentation to the Rainier Mesa pre-emptive review committee by Ed Kwicklis, March 15-16, 2011, Desert Research Institute, Las Vegas, NV.

Kwicklis, E., G. WoldeGabriel, and M. Sulley (2008), Analysis of core-scale hydrologic and mineralogic data from boreholes UE12t #1 and RME #1 at Rainier Mesa, Nevada National Security Site, LA-UR-XXXX, Los Alamos National Laboratory, Los Alamos, NM.

Likos, W. J., and N. Lu (2006), Pore-scale analysis of Bulk Volume Change from Crystalline Interlayer Swelling in Na+ and Ca2+ - Smectite, Clays and Clay Minerals, V. 54, n. 4, p. 516-529.

Martin, J. W., C. W. Felice, and R.T. DeVan (1991), The Effects of Zeolitized Tuff on Grain Density Determinations, in Rock Mechanics as a Multidisciplinary Science, A. A. Bakema, Rotterdam, Netherlands.

Martin, J. W., C.W. Felice, and S.J. Green (1993), Grain Density of Zeolitized Tuff- TerraTek Investigations Volume II, TR93-48, TerraTek, Inc., Salt Lake City, UT.

McKague, H. L., N.W. Howard, and L.D. Ramspott (1975), A Method for Measuring the Powder Density of Hygrospopic Minerals, Abstracts with Program 7, Rocky Mountain Section, Geological Society of America, p. 629.

McKague, H. L., N.W. Howard, L.D. Ramspott, and P. Turner (1982), Background and Procedures of Grain Density Technique for LLNL Containment Program, UCID-19574, Lawrence Livermore Laboratory, Livermore, CA.

McKague, H. L, J.R. Hearst, and R.L. Ward (1991), Nuclear Magnetic Resonance Determination of the Non-Pore Water Content of Zeolitic Tuffs and its Application to Correction of Epithermal-Neutron-LC G-Derived Water Content, UCRL-JC-106893, Lawrence Livermore National Laboratory, Livermore, CA.

Moss, M., and G.M. Haseman (1983), A Proposed Model for the Thermal Conductivity of Dry and Water-Saturated Tuff, SAND83-0535C, Sandia National Laboratory, Albuquerque, NM.

Navarro (2017), written communication: Case Study Analyses of Radionuclide Transport in Variably Saturated Media at Rainier Mesa. Las Vegas, NV.

Nelson, P. H., and L.A. Anderson (1992), Physical Properties of Ash Flow Tuff from Yucca Mountain, Nevada, Journal of Geophysical Research, v 97, n B5, p. 6823-6841.

NSTec (2007), A Hydrostratigraphic Model and Alternatives for the Groundwater Flow and Contaminant Transport Model of Corrective Action Unit 99: Rainier Mesa-Shoshone Mountain, Nye County, Nevada, DOE/NV/25946-146, National Security Technologies LLC, Las Vegas, NV.

Reeves, M. R. (2008a), Fracture and Matrix Characteristics at T-Tunnel, Rainier Mesa, NNSS, presented June 9, 2008 at Lawrence Livermore National Laboratory, Livermore, CA.

Reeves, M. R. (2008b), written communication, spreadsheet “Matrix_All.xls”.

Richards, S., and A. Bouazza (2007), Determination of particle density using water and gas pycnometry, Geotechnique, v. 57, n. 4, p. 403-406.

Salve, R., and C.M. Oldenburg (2001) Water flow within a fault in altered nonwelded tuff, Water Resources Research, v. 37, n. 12, p. 3043-3056.

Thordarson, W. (1965), Perched Ground Water in Zeolitized-Bedded Tuff, Rainier Mesa and Vicinity, Nevada National Security Site, Nevada, TEI-862, U.S. Geological Survey, 98p.

Townsend, D. R. (2008), written communication: Documentation Report for Rainier Mesa Test Information Compiled for the UGTA Project, Wastren Advantage Incorporated, prepared for National Security Technologies, LLC, Las Vegas, NV.

USDOE (2015), United States Nuclear Tests, July 1945 through September 1992, DOE/NV--209-REV 16, National Nuclear Security Administration Nevada Field Office, U.S. Department of Energy, Las Vegas, NV.

van Genuchten, M. Th., (1980), A closed-form equation for predicting the hydraulic conductivity of unsaturated soils, Soil Science Society of America Proceedings, 44(5), p. 892-898.

van Genuchten, M. Th., F.J. Leij, and S.R. Yates (1991), The RETC code for quantifying hydraulic functions of unsaturated soils, EPA/600/2-91-065, Robert S. Kerr Environmental Research Laboratory, Office of Research and Development, U.S. Environmental Protection Agency, Ada, OK.

Vaniman, D. T., and D.L. Bish (1993), The Importance of Zeolites in the Potential High-Level Radioactive Waste Repository at Yucca Mountain, Nevada, LA-UR 93-2326 and Conf-9306100—2, Los Alamos National Laboratory, Los Alamos, NM.

Vaniman, D. T, S.J. Chipera, D.L. Bish, W.J. Carey, S.S. and Levey (2001), Quantification of unsaturated-zone alteration and cation exchange in zeolitized tuffs at Yucca Mountain, Nevada, USA, Geochimica et Cosmochimica Acta, v. 65, n. 20, p. 3409-3433.

Wilkin, R. T., and H.I. Barnes (1999), Thermodynamics of hydration of Na and K-clinoptilolite to 300C, Phys Chem Minerals, v. 26, p. 468-476.

Zavarin, M., W.W. McNab, S.F. Carle, D.E. Shumaker, C. Lu, Y. Sun, and G.A. Pawloski, Q. Hu, S.K. Roberts, and A.F.B. Tompson (2011), Hydrologic Source Term Processes and Models for Underground Nuclear Tests at Rainier Mesa and Shoshone Mountain, Nevada Test Site, LLNL-TR-483852-DRAFT, Lawrence Livermore National Laboratory, Livermore, CA.

12 APPENDIX D: Thermal and Mechanical Rock Property Data and Parameters

Rock properties of thermal conductivity, heat capacity, and compressibility are needed for the non-isothermal groundwater flow and transport simulations used in hydrologic source term (HST) modeling (Zavarin et al., 2011). Rock compressibility properties are used in the isothermal groundwater flow and transport simulations for the CLEARWATER and WINESKIN HST models described in this report. The HST models use the non-isothermal unsaturated flow and transport code "NUFT", for which supporting documentation includes further description of the rock property parameters (Nitao 2000a and b, 2004, 2005). Thermal conductivity, heat capacity, and compressibility data relevant to Rainier Mesa rocks are compiled below, and parameter values for HSUs and stratigraphic units and sub-units are given in Sections 12.4 and 12.5.

12.1 Thermal Conductivity

Linear models of correlation between thermal conductivity and porosity in "dry" and "saturated" conditions are established from thermal conductivity and pore fraction data from Diment et al. (1958, 1959) shown in Figure 12.1 and 12.2 and summarized in Table 12.1. The same linear functions fit data for "bedded" and "welded tuff" (which removes dependency on degree of welding) in dry and saturated conditions:

$$K_{dry}^{T} = 0.98 - 1.39\emptyset$$

$$K_{sat}^{T} = 1.0 - 0.61\emptyset$$

Linear functions also fit data for "friable tuff"

$$K_{dry}^{T} = 0.84 - 1.39\emptyset$$

$$K_{sat}^{T} = 0.96 - 0.96\emptyset$$

Zimmerman and Finley (1987) compiled thermal conductivity data from G-Tunnel core samples (Figure 12.3). This data set is smaller in number relative to the Diment et al. (1958) thermal conductivity data set. The linear functions above fit the Zimmerman and Finley (1987) data also.

In the development of thermal conductivity/porosity relationships, Diment et al. (1958) estimated porosity gravimetrically with respect to a "dry" state, which was oven dried at 105 ^{o}C. An oven dried state is not the same as zero saturation state considering mineral hydration effects (see Appendix C, this report). The measurement technique used to

estimate porosity values used in Diment et al. (1958) is detailed in Diment et al. (1959) and corresponds more closely to a measurement of the difference in volumetric water content between a "dry" and "saturated" state, not porosity. Therefore, in estimating thermal conductivity from RME#1 and UE12t#1 rock property data, the linear models are applied to measurements of volumetric water content.

In the NUFT simulation code, a thermal conductivity is needed for an *in situ* dry (not oven-dried) and saturated states corresponding to simulated saturation (S) values of 0.0 (S=0) and 1.0 (S=1). The S=0 state includes the structural water associated with smectite and zeolite minerals. If "oven dried" data are used to parameterize water content, a correction is needed to estimate thermal conductivity at the S=0 or "dry" state. If the volumetric water content data from drill holes RME#1 and UE12t#1 given in Kwicklis et al. (2008) is to be used for estimation of thermal conductivity at S=0 and S=1 states, two issues should be considered: (1) water content data in Kwicklis et al. (2008) is measured relative to an oven-dried state ($\theta_{sat} - \theta_{dry}$), and (2) the hydrated mineral portion of water content ($\theta_{S=0} - \theta_{dry}$) relative to an oven dry state can be estimated using techniques describe in Appendix C. We will estimate thermal conductivity in the S=0 state from a linear interpolation of thermal conductivities for "dry" and "sat" states, using differences in water content at S=1 and S=0 states relative to an oven dry state

$$K_{S=0}^{T} = K_{dry}^{T} + \frac{\theta_{S=0} - \theta_{dry}}{\theta_{sat} - \theta_{dry}} \left[K_{sat}^{T} - K_{dry}^{T} \right] .$$

This thermal conductivity estimation model includes consideration of the mineral hydration effects of smectite and zeolite, which were not considered in previous comparison of thermal conductivity to porosity by Diment et al. (1958) and to measurement of porosity in Diment et al. (1959).

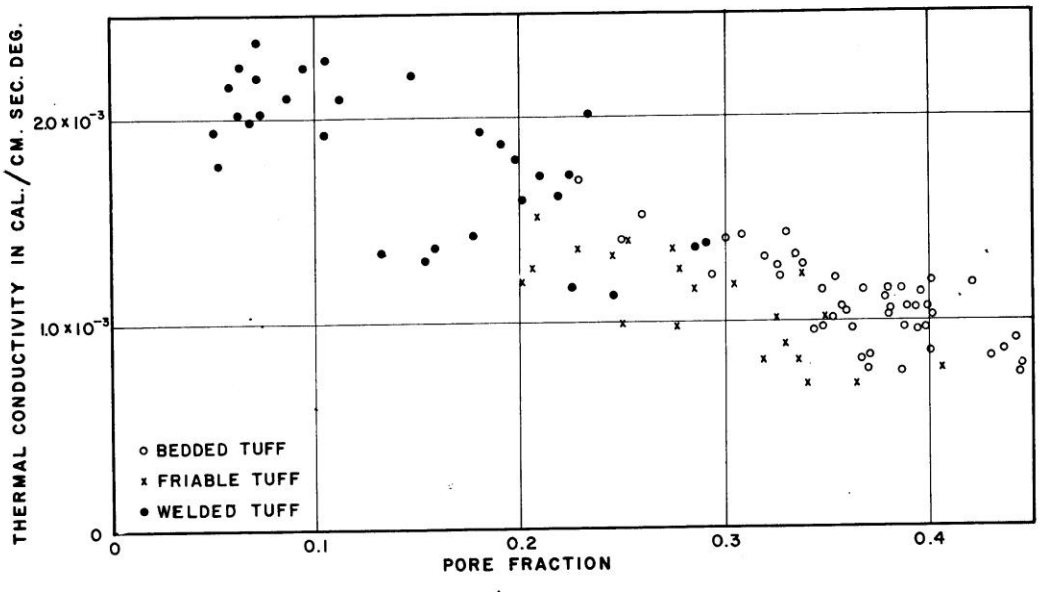

Figure 12.1 Thermal conductivity of dry Rainier Mesa tuffs (Diment et al., 1958).

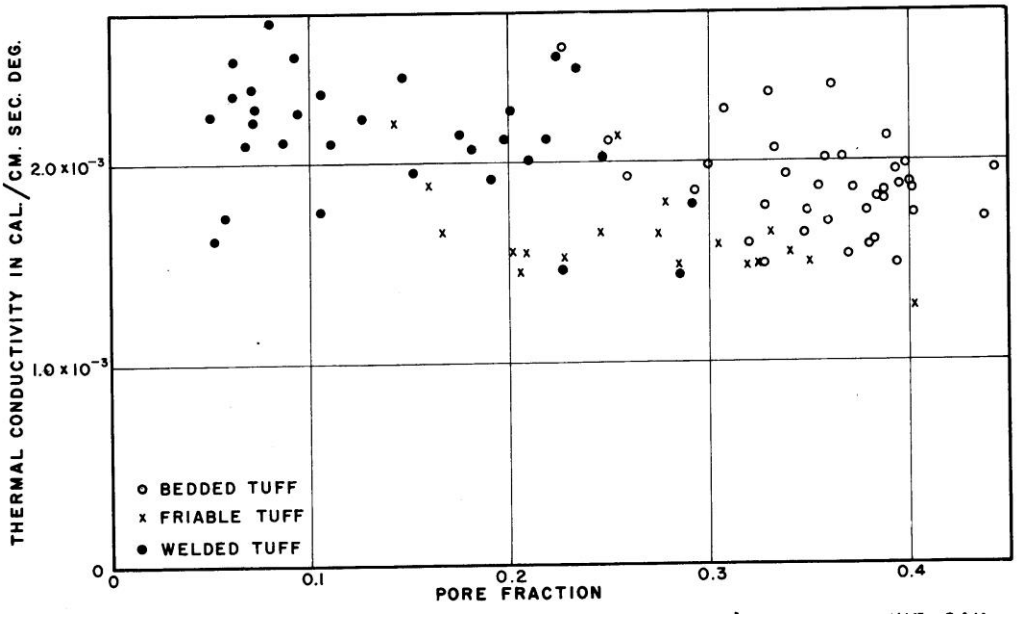

Figure 12.2 Thermal conductivity of saturated welded tuffs (Diment et al., 1958).

Table 12.1 Dry and saturated thermal conductivity estimates for tuffs on Rainier Mesa from (Diment et al., 1958).

Lithology	Dry Thermal Conductivity		Saturated Thermal Conductivity	
	cal/cm-sec-°C	W/m-°C	cal/cm-sec-°C	W/m-°C
Welded Tuff (porosity <0.12)	0.0021	0.879	0.00225	0.941
Welded Tuff (porosity >0.12)	0.0016	0.669	0.00215	0.900
Vitric (friable)Tuff	0.0011	0.460	0.0016	0.669
Zeolitized (bedded) Tuff	0.0011	0.460	0.0019	0.795

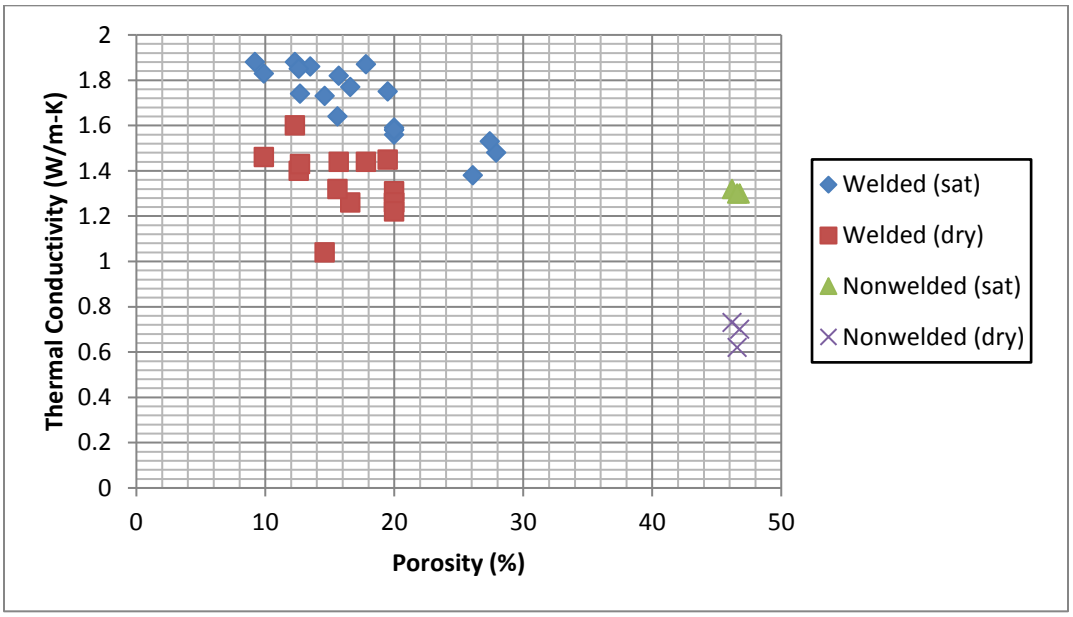

Figure 12.3 Thermal conductivity data from G-Tunnel compiled by Zimmerman and Finley (1987).

12.2 Heat Capacity

12.2.1 Measurements

Direct measurements of heat capacity for Rainier Mesa rocks are limited. Specific heat of dry vitric tuff (Table 12.2) was measured at different temperatures by Warner and Violet (1959). Zimmerman (1983) conducted thermal modeling of rocks in G-Tunnel using properties shown in Table 12.3 including heat capacity for welded and non-welded tuffs.

Table 12.2 Specific heat of dry vitric tuff measured at different temperatures by Warner and Violet (1959).

Specific heat at different temperatures									
25 °C		100 °C		200 °C		400 °C		600 °C	
Cal/g/°C	J/kg-°K	Cal/g/°C	J/kg-°K	Cal/g/°C	J/kg-°K	Cal/g/°C	J/kg-°K	Cal/g/°C	J/kg-°K
0.1804	755	0.2106	881	0.2360	987	0.2714	1136	0.3008	1259

Table 12.3 Model parameters used by Zimmerman (1983), including heat capacity.

Rock (Tbg in G-Tunnel)	Thermal Conductivity W/m-K		Heat Capacity KJ/m^3-K; J/kg-K		Bulk Density kg/m^3	Porosity %
	saturated	dry	saturated	dry		
Welded Tuff	1.80	1.44	2478; 1116	1858; 837	2220	0.15
Nonwelded Tuff	1.30	0.66	2964; 2245	1105; 837	1320	0.45

12.2.2 Estimation from XRD

Another approach to estimation of heat capacity is to use the mass fractions of minerals and mineral heat capacities to estimate the composite heat capacity of rock (Bechtel SAIC, 2004). Heat capacity can be estimated from the XRD data for RME#1 and UE12t#1 (Kwicklis et al., 2008) combined with grain and bulk density estimates (Appendix C).

12.3 Compressibility

Rock compressibility data for core from Rainier Mesa are compiled in Brethauer et al. (1980) for Rainier Mesa tuffs in general and for vitric tuffs by Fredrich et al. (1995). Table 12.4 compiles available compressibility data with respect to HGUs, HSUs, and stratigraphic unit.

.

Table 12.4 Compressibility data from Brethauer et al. (1980) and Fredrich et al. (1995) with respect to HGUs, HSUs, and stratigraphic unit.

HGU	HSU	Stratigraphic unit	Compressibility (Pa^{-1})
WTA	TM-WTA	Tmr	-
VTA	TM-LVTA	Tmr	4e-9
		Post Tbg	-
WTA	BRA	Tbg	-
VTA	LVTA1	Tbgb	4e-9
TCU	LTCU	Tn4	7.7e-10
		Tn3	9.7e-10
			2.6e-10
WTA	TUBA	Tub	7.8e-11
TCU	OSBCU	Ton2	8.3e-11
		Toy	8.5e-10
			6.7e-10
		Ton1	-
		To	-
WTA	RVA	Tor	-
TCU		To	-
WTA		Tot	-
TCU	LTCU1	Tot	1.2e-9
	ATCU	To	-
		Tl	-
CA	LCA3	Pz	-

12.4 Thermal Properties Derived from RME#1 and UE12t #1 Data

Estimates of heat capacity and thermal conductivity for RME #1 and UE12t #1 rock property data (Kwicklis et al., 2008) can be derived from the following relationships in rock properties:

- Thermal conductivity correlated to porosity, rock type, and saturation (Section 12.1)
- Heat capacity derived from XRD mineralogic mass fractions (Section 12. 2)
- Solid density with correction for smectite and zeolite content (Section 11)

Tables 12.5 and 12.6 compile thermal rock property data for RME #1 and UE12t #1 data with respect to depth, HGU, HSU, and stratigraphic unit. Saturated thermal conductivities are consistent with average saturated thermal conductivities given for NNSS rock units by Gillespie (2005) and Stoller-Navarro (2006).

Table 12.5 RME#1 heat capacity and thermal conductivity estimates derived from rock property and XRD data (Kwicklis et al., 2008) and thermal conductivity data of Diment et al. (1958), Zimmerman and Finley (1987), and Thomas et al, (1973). Volumetric water content and solid density values are corrected for mineral hydration and swelling effects as described in Appendix C. Hydrogeologic units, hydrostratigraphy and stratigraphy are given according to NSTec (2009).

Depth (ft)	HGU	HSU	Strat	Volumetric (%) Water Content		Solid Dens. (kg/m3)	Heat Cap. 20C (J/kg-K)	Thermal Conductivity (W/m-C)	
				"dry"	mobile			S_l=0	S_l=1
886.3	VTA	TM-LVTA	Post Tbg	37.32	36.92	2349	786	0.713	1.324
915.0				42.76	42.36	2306	NA	0.547	1.209
1027.6				31.10	30.63	2427	NA	0.905	1.455
1114.2	WTA	BRA	Tbg	29.46	22.80	2304	977	1.379	1.806
1287.7	VTA	LVTA1	Tbgb	43.17	39.41	2339	796	0.586	1.200
1396.3	TCU	LTCU	Tn4	28.93	24.78	2403	884	1.349	1.812
1571.9				35.11	30.09	2362	910	1.175	1.729
1674.3				39.46	31.88	2254	1001	1.088	1.670
1704.5				24.47	20.57	2361	851	1.482	1.872
1790.1			Tn3	27.08	21.01	2284	942	1.442	1.837
1894.4				35.19	29.06	2291	969	1.193	1.728
1940.3				37.24	31.99	2472	822	1.113	1.700
1976.6			Tub	32.23	26.48	2468	837	1.277	1.767
1994.0				34.83	27.30	2327	892	1.230	1.733
2045.6		OSBCU	Ton2	32.37	26.88	2304	917	1.268	1.766
2176.4				32.43	27.40	2332	936	1.257	1.765
2273.6			Toy	30.88	27.00	2436	852	1.284	1.786
2479.6				36.26	33.36	2467	828	1.100	1.713
2640.2				29.82	24.51	2344	920	1.343	1.800
2669.6			Ton1	28.22	24.93	2561	739	1.355	1.821
2742.1				26.47	19.16	2525	788	1.484	1.845
2864.0	WTA	RVA	Tor	30.29	29.65	2624	691	1.242	1.794
2948.7	TCU		To	17.39	13.05	2506	833	1.710	1.967
3158.2	WTA		Tot	29.94	28.31	2537	762	1.271	1.798
3194.8				9.88	8.18	2312	785	1.891	2.067
3295.3				10.25	9.55	2624	699	1.858	2.062
3349.0				14.81	14.15	2592	699	1.716	2.001
3408.0				28.13	27.59	2609	696	1.306	1.822
3428.0	TCU	LTCU1		27.63	21.01	2334	905	1.435	1.829
3522.0				28.29	23.22	2493	827	1.386	1.820
3608.8		ATCU	To	27.57	17.69	2505	834	1.498	1.830
3630.4				16.30	8.82	2566	796	1.806	1.981

Table 12.6 UE12t#1 heat capacity and thermal conductivity estimates derived from rock property and XRD data (Kwicklis et al., 2008) and thermal conductivity data of Diment et al. (1958), Zimmerman and Finley (1987), and Thomas et al. (1973). Volumetric water content and solid density values are corrected for mineral hydration and swelling effects as described in Appendix C.

Depth (ft)	HGU	HSU	Strat	Volumetric (%) Water Content		Solid Dens. (kg/m^3)	Heat Cap. 20C (J/kg-K)	Thermal Conductivity (W/m-C)	
				"dry"	mobile			S=0	S=1
34.9	WTA	TM-WTA	Tmr	32.21	31.69	2532	675	1.181	1.768
193.6				9.26	8.57	2544	684	1.888	2.076
267.0				4.11	3.28	2415	729	2.053	2.147
321.7	VTA	TM-LVTA		25.66	23.88	2381	774	1.098	1.570
365.4				30.98	30.58	2299	775	0.908	1.458
391.5			Post Tbg	40.00	39.05	2384	770	0.640	1.267
608.8				48.08	47.81	2168	793	0.382	1.097
736.0	WTA	BRA	Tbg	2.78	2.08	2387	795	2.094	2.163
790.0	VTA	LVTA1	Tbgb	48.12	47.78	2352	800	0.382	1.096
940.0	TCU	BRCU	Tn4	25.54	19.74	2364	935	1.485	1.857
1030.2				31.68	27.07	2447	865	1.273	1.775
1134.0				34.05	32.20	2430	758	1.149	1.743
1155.0				45.22	39.99	2292	964	0.868	1.593
1260.1			Tn3	32.55	27.68	2329	907	1.251	1.763
1376.2				35.26	28.84	2309	971	1.196	1.727
1463.0	WTA	TUBA	Tub	4.94	4.21	2631	675	2.024	2.134
1561.5	TCU	OSBCU	Ton2	33.68	28.55	2395	907	1.221	1.748
1651.3			Toy	25.74	20.41	2600	723	1.469	1.855
1738.5				35.17	28.50	2281	962	1.203	1.728
1851.4				38.38	32.92	2299	960	1.082	1.685
1917.6			To	26.47	23.77	2611	736	1.397	1.845
1950.0				31.50	21.31	2554	727	1.382	1.777
2057.9				24.29	15.11	2519	812	1.587	1.874
2150.9				28.43	18.75	2483	794	1.468	1.818
2193.1		ATCU	Tl	44.62	24.82	2469	783	1.151	1.601
2195.6				27.22	26.57	2711	837	1.336	1.835
2206.2	CA	LCA3	Pz	22.02	16.51	2667	818	1.588	1.904
2251.1				5.96	1.28	2782	1825	5.1[z]	5.5

12.5 Thermal and Mechanical Properties for RAINIER HST Process Model

The RAINIER HST model addresses heterogeneities within HSU and stratigraphic units (Zavarin et al., 2011). Additionally, the RAINIER test hydrogeologic setting characterization for the HST modeling uses older stratigraphic nomenclature with "Tos" prefixes. Table 12.7 compiles the thermal and compressibility data discussed above into estimates for thermal and compressibility parameters for the RAINIER HST model rock units.

Table 12.7 Compilation of thermal and compressibility data for estimation for thermal and compressibility parameters for the RAINIER HST process model rock units.

HGU	HSU	Strat	NUFT Rock Type	Solid Density (kg/m^3)	Heat Cap. at 20C (J/kg-K)	Thermal Conductivity (W/m-C)		Com-pres-sibility	Corres-ponding HST Facies
						S=0.0	S=1.0	(Pa^{-1})	
WTA	TM-WTA	Tmr	Tmr3	2532	675	1.18	1.77	*7.8e-11*	Tmr-M
			Tmr2	2480	707	1.97	2.11	*7.8e-11*	Tmr-D
VTA	TM-LVTA	Tmr	Tmr1	2340	775	1.00	1.51	4e-9	Tmr-V
		Post Tbg	Tos7-1,2,4,8,9,10	2361	786	0.71	1.33	4e-9	VTA-n
TCU	BRCU	Post Tbg	Tos7-3,5,6,7	2353	913	1.19	1.74	*7.7e-10*	Tn4-Z
WTA	BRA	Tbg	Tos6	2509	728	1.82	2.04	*7.8e-11*	RVA-W
VTA	LVTA1	Tbgb	Tos5	2346	798	0.47	1.15	4e-9	LVTA
TCU	LTCU/ BRCU	Tn4	Tos4	2353	913	1.19	1.74	7.7e-10	Tn4-Z
		Tn3	Tos3	2303	947	1.27	1.76	9.7e-10	Tn3-Z
TCU	OSBCU	Ton2	Tos2	2344	920	1.25	1.76	8.3e-11	Ton2

12.6 References

Bechtel SAIC (2004), Heat Capacity Analysis Report, ANL-NBS-GS-000013 REV 01, Bechtel SAIC Company, LLC, Las Vegas, NV.

Brethauer, G. E., J.E. Magner, and D.R. Miller (1980), Statistical Evaluation of Physical Properties in Area 12, Nevada Test Site Using the USGS/DNA Storage and Retrieval System, USGS-474-309, U.S. Geological Survey.

Diment, W. H., R. E. Wilcox, G. V. Keller, E. Dobrovolny, F. C. Kracek, J. C. Roller, L. Peselnick, E. C. Robertson, A. H. Lachenbruch and C. M. Bunker (1958), Properties of Oak Spring Formation in Area 12 at the Nevada National Security Site, Trace Elements Investigations Report, United States Geological Survey, Denver, CO.

Diment, W.H., V.R. Wilmarth, F.A. McKeown, D.D. Dickey, T. Botinelly, E.N. Hinrichs, C.H. Roach, F.M. Byers, G.A. Izett, and G.R. Johnson (1959), Geological Survey

Investigations in the U12b.01 Tunnel, Nevada Test Site, Trace Elements Memorandum Report 998, U.S. Geological Survey, Denver, CO.

Fredrich, J. T., J.W. Martin, R.B. Clayton (1995), Induced pore pressure response during undrained deformation of tuff and sandstone, Mechanics of Materials, v. 20, p. 95-104.

Gillespie, D. (2005), Temperature Profiles and Hydrologic Implications for the Nevada National Security Site Area, DOE/NV/13609-40; Publication No. 54211, Desert Research Institute, Las Vegas, NV.

Kwicklis, E., G. WoldeGabriel, G., and M. Sulley (2008), Analysis of core-scale hydrologic and mineralogic data from boreholes UE12t #1 and RME #1 at Rainier Mesa, Nevada National Security Site, LA-UR-XXXX, Los Alamos National Laboratory, Los Alamos, NM.

Nitao, J. J. (2000a), Reference Manual for the NUFT Flow and Transport Code, Version 3.0, UCRL-MA-130651 REV 1, Lawrence Livermore National Laboratory, Livermore, CA.

Nitao, J. J, (2000b), User's Manual for the USNT Module of the NUFT Code, Version 3.0, UCRL-MA-130643-REV-2, Lawrence Livermore National Laboratory, Livermore, CA.

Nitao, J. J. (2004), User's Manual for the US1P Module of the NUFT Flow and Transport Code, unpublished report, Lawrence Livermore National Laboratory, Livermore, CA.

Nitao, J. J. (2005), User's Manual for the US1C Module of the NUFT Flow and Transport Code, unpublished report, Lawrence Livermore National Laboratory, Livermore, CA.

NSTec (2009) Geology and Hydrogeology of Rainier Mesa Exploratory #1, Unpublished data by National Security Technologies, LLC, dated April 16, 2009.

Prothro, L B. (2008), Analysis of Fractures in Cores from the Tuff Confining Unit beneath Yucca Flat, Nevada National Security Site, National Security Technologies DOE/NV/25946-351.

Thomas, J., R.R. Frost, and R.D. Harvey (1973), Thermal Conductivity of Carbonate Rocks, Eng Geol, v. 7, p. 3-12.

Stoller-Navarro (2006), Phase I Hydrologic Data for the Groundwater Flow and Contaminant Transport Model of Correction Action Unit 97: Yucca Flat/Climax Mine,

Nevada National Security Site, Nye County, Nevada, S-N/99205-077, Stoller-Navarro Joint Venture, Las Vegas, NV.

Zavarin, M., W.W. McNab, S.F. Carle, D.E. Shumaker, C. Lu, Y. Sun, and G.A. Pawloski, Q. Hu, S.K. Roberts, and A.F.B. Tompson (2011), Hydrologic Source Term Processes and Models for Underground Nuclear Tests at Rainier Mesa and Shoshone Mountain, Nevada Test Site, LLNL-TR-483852-DRAFT, Lawrence Livermore National Laboratory, Livermore, CA.

Zimmerman, R. M. and R.E. Finley (1987) Summary of Geomechanical Measurements Taken in and Around the G-Tunnel Underground Facility, NTS, SAND86-1015 * UC-70, Sandia National Laboratories, Albuquerque, NM.